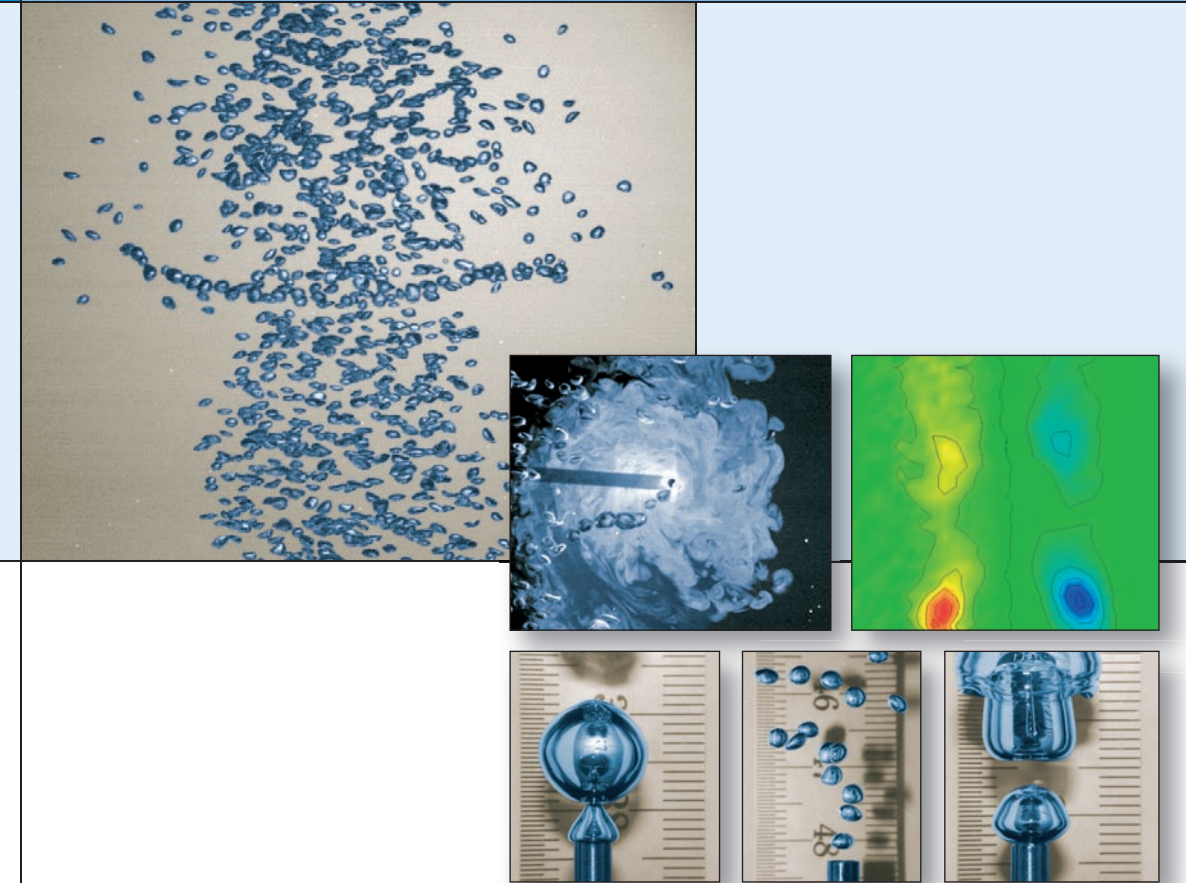


Rade Ž. Milenković

Doctoral Thesis ETH No. 16206

Experimental Investigation of Bubbly Jets

Doctoral Thesis ETH No. 16206



Experimental Investigation of Bubbly Jets

Rade Ž. Milenković

Doctoral Thesis ETH No. 16206

EXPERIMENTAL INVESTIGATION OF BUBBLY JETS

A dissertation submitted to the
SWISS FEDERAL INSTITUTE OF TECHNOLOGY ZURICH

for the degree of

Doctor of Sciences

presented by

Rade Ž. Milenković

Master of Technical Sciences
Graduate Mechanical Engineer

Faculty of Mechanical Engineering,
University of Belgrade

born 24.06.1970

citizen of
Serbia and Montenegro

accepted on the recommendation of

Prof. Dr. George Yadigaroglu, examiner
Prof. Dr. Konstantin Boulouchos, co-examiner
Prof. Dr. Michel Lance, co-examiner
Dr. Beat Sigg, co-examiner

2005

I do not think there is any thrill that can go through the human heart like that felt by the inventor as he sees some creation of the brain unfolding to success... Such emotions make a man forget food, sleep, friends, love, everything.

Nikola Tesla

Preface and Acknowledgment

The story about the basic inspiration, which flashed back from my memory during crucial moments of my doctoral work and was used during the planning of some interesting experiments, begins in the 1990's when, together with a couple of friends and my brother, I enriched my fishing passion by using specially designed lures that suited our favourite rivers and lakes best. Controlling of the moving of these lures brought an incredible feeling of satisfaction and of success when we used them in waters full of predators. It is not only due to their colours and size, but also due to the vibrations and flow structures, periodically created behind them, which enabled some of us to be impressively successful.

Almost 11 years later, thanks to **Professor Dr. George Yadigaroglu, Dr. Beat Sigg** and **Max Fehlmann**, I got the chance to use modern experimental techniques to explore the world of large eddy structures and to metaphorically "fish" bubbles inside them. Even though I did not have enough time to explore all of the magic ideas, the feeling that I made some of them visible to other researchers, brought me full satisfaction.

From the bottom of my heart I would like to thank

Dr. Beat Sigg, who almost daily during the past four years carefully listened, discussed and supported many of my own ideas and solutions. He was always there, day or night, giving his best to answer my scientific and non-scientific questions, to help choosing the right path in the "jungle" of problems that we entered together in October 2001 and to provide me with great confidence in getting to the top of my tree,

Max Fehlmann for his sincere friendship, helpful assistance and technical contributions to the design and erection of the experimental installation, and

Professor Dr. George Yadigaroglu who forced me spontaneously to "wobble" my way of thinking, to bring out some interesting ideas and to explain them properly during famous courses at ETH Zürich and our meetings at PSI Villigen. To work and to discuss with him was a tremendous honour and privilege for me.

I gratefully acknowledge the support of the project by the **Swiss National Science Foundation** and **Paul Scherrer Institut** and wish to express my sincere thankfulness to **Professors Dr. Michel Lance** and **Dr. Konstantin Boulouchos** for their help in the final phases of this work. Many thanks also to **Dr. Jörg Dreier** for his interest and support of this project.

I especially appreciate comments, small favours and advices of my friend **Dr. Ralf Kapulla**. Sometimes it was simply enough to look at his eyes in order to get proper answers on tricky questions.

I would like to thank my wife **Verica D. Milenković** for love, patience, support and encouragement especially during this scientific marathon.

Finally, I should like to express my reverence in the Japanese style to **Professors Dr. Bogosav Vasiljević, Dr. Branislav Jacimović, Dr. Sribislav Genić** and **Dr. Franc Kosi**, who taught me the basics of Thermodynamics, Unit Operations and Heat Transfer at University of Belgrade. Without gaining this knowledge I could have never dreamed of starting any serious work regarding fluid mechanics or heat transfer.

In Umiken, September 2005

Rade Ž. Milenković

Table of Contents

1 Introduction	1
1.1 Motivation, objectives and uniqueness of presented work	1
1.1.1 The effects of deterministic parameters in bubbly jet flow	1
1.1.2 Orderly structures in bubbly jet flow	1
2 Overview and comments on bubbly-flow modelling and experimental investigations	3
2.1 Introduction	3
2.2 Survey of modelling methods	4
2.2.1 Lagrangian-Eulerian (L-E) models	4
2.2.2 Eulerian-Eulerian (E-E) two-fluid models	6
2.2.3 Classification of turbulence modulation	7
2.3 Survey of experimental investigations	7
2.3.1 Experimental investigations of bubbly jets	8
2.3.2 Experiments on jet instabilities and buoyant jets and plumes	8
2.3.3 Experimental results for bubble effects on turbulence and spreading of mixing layers	9
2.4 Conclusions	10
3 Experimental techniques and links to simulations	13
3.1 Particle Image Velocimetry (PIV)	13
3.2 Double Optical Sensors (DOS)	14
3.3 Photographic recordings and image analysis	15
3.4 Laser-Induced Fluorescence (LIF)	18
3.5 Discussion on relationship between bubbly flow modelling and experiments	19
3.5.1 Signal decomposition and filtering	19
3.5.1.1 Mathematical signal decomposition and filtering	20
3.5.1.2 Filtering in DOS	23
3.5.1.3 Physical signal decomposition, phase averaging and filtering	23
3.6 Filtering and scanning characteristics of LES and PIV	25
3.7 Summary and some examples	28
4 Bubbly jet flow conditions	31
4.1 Working principle of the injector	31
4.2 Design and geometrical characteristics of the gas/liquid injector	31
4.3 Parameters and flow conditions in the injector	31
4.4 Flow conditions in the test tank	35

5	Turbulent bubbly jets	37
5.1	Bubble movement and trapping in large eddy structures and the relevant non-dimensional parameters	37
5.1.1	The range of characteristic non-dimensional parameters	40
5.1.2	Bubble trapping condition for "Gaussian" vortex	44
5.2	Development of turbulent bubbly jets, relevant non-dimensional parameters and characteristic regions	50
6	Experimental results for naturally-developing turbulent bubbly jets	55
6.1	Test matrix	56
6.2	Single-phase jets	58
6.3	Effect of bubbles on entrainment and the liquid velocity	59
6.4	Effects of void and Jet Reynolds number on mean and turbulent properties of the liquid	63
6.4.1	Jet region ($y/D = 1.12$)	64
6.4.2	Transition region ($y/D = 3.9$)	67
6.4.3	Discussion	68
6.5	Modeling of the turbulent shear stress in the liquid and turbulence modulation by the bubbles	72
6.5.1	Single-phase jets	73
6.5.2	Bubbly jet	76
7	Bubble clustering and trapping in large vortices: naturally developing vs. triggered jets	81
7.1	Naturally-developing bubbly jet	82
7.1.1	Void fraction and bubble velocity measurement with DOS	82
7.1.2	PIV experimental results	82
7.1.3	Statistical analysis of DOS measurements in the transition region	84
7.2	Triggered bubbly jet	89
7.3	Comparison of bubble velocity measurements by PIV and DOS	91
8	Velocity and bubble concentration fields for triggered bubbly jets	95
8.1	Test matrix	96
8.2	Survey of experimental results for test <i>TF2V1.A</i>	97
8.2.1	PIV experimental results	98
8.2.2	DOS experimental results	100
8.2.3	Correlation of PIV and DOS data	104
8.3	Survey of experimental results for test <i>TTF2V1.B</i>	106
8.3.1	Single-phase jets	106
8.4	Effects of excitation frequency	117
8.4.1	Test f1	117
8.4.2	Test f2	118
8.4.2.1	Phase P_1	119

8.4.2.2	Phase P ₂	124
8.4.3	Test f3	130
8.5	Downstream development and destruction of liquid and bubbly structures	142
8.6	Conclusions on bubble trapping	145
9	LIF visualization tests	147
9.1	Single-phase naturally-developing jets	147
9.2	Naturally-developing bubbly jets	151
9.3	Triggered bubbly jets	151
10	Some experimental results for dilute bubbly jets at low Reynolds number	157
10.1	Test matrix	157
10.2	Experimental results and discussions	157
11	Summary and conclusions	163
11.1	Characteristics of naturally-developing turbulent bubbly jets	163
11.2	Interactions between bubbles and large vortices	166
11.3	Suggestions for future work	167
A	Experimental facility	169
A.1	Water loop, air supply and list of instruments	170
A.2	Tank and traversing system	172
A.3	System for triggering large vortices	173
A.4	Process control and data acquisition systems	174
A.4.1	Process Data Acquisition	176
A.4.2	High-speed data acquisition	176
A.4.3	Photographic measurements	177
A.4.4	System for positioning the sensors (DOS, Thermocouple and PIV cameras)	177
A.4.5	System for feeding the installation with seeding particles	177
A.5	Experimental investigation of bubble formation	178
B	Experimental procedure	181
C	Testing and calibration of the Double Optical Sensors (DOS)	183
C.1	Testing for accuracy, reproducibility and absence of systematic errors	183
C.2	Comparison of volumetric flow rates	183
C.2.1	Test conditions	184
C.3	Adjustment of DOS parameters	187
C.3.1	The offset value (λ)	187
C.3.2	The correction time	188
C.3.3	The bubble velocity	188
C.3.4	Testing of reproducibility	189
C.3.5	Selection of measuring time	190
D	Particle Image Velocimetry (PIV)-Settings and error estimates	191

D.1	General adjustment of PIV system	191
D.1.1	Acquisition scheme	193
D.2	Analysis of PIV images illuminated by backlight	195
D.3	Effects of PIV parameters on time-dependent velocity profiles and <i>rms</i> values	198
D.3.1	Time between laser pulses	198
D.3.2	Application of the window function	202
D.3.3	Testing of reproducibility	205
	Bibliography	206

Abstract

The main motivation for undertaking the present study was an apparent lack of understanding of bubble trapping in eddies in free turbulent shear flows and of the interactions between the fields of bubbles and liquid velocity.

The experiments have been carried out with liquid and bubbly jet flows generated by a gas/liquid injector. Bubbly jet flows are formed by a vertical water jet containing bubbles of various well-controlled sizes and volume fraction. The jet is injected into a water volume contained in a large Plexiglas tank to minimize wall effects. Such flows, with constant inlet flow rate of liquid and gas are called here naturally-developing jets. If the jet flow is periodically excited with controllable frequency and amplitude, it is called triggered jet. The excitation is achieved by periodically modulating the jet shear layer by means of a coaxial water layer injected close to the jet exit through a separate annular nozzle. Two-camera Particle Image Velocimetry (PIV), Double Optical Sensor (DOS) and Laser-Induced Fluorescence (LIF) were the main experimental techniques used. A variety of flow conditions defined by non-dimensional parameters such as the Jet Reynolds number, the Froude number, the Trapping parameter, the Jet Richardson number, bubble size distribution, void fraction, triggering frequency and amplitude etc. can be adjusted.

The main goal of these investigations is to show the characteristics of large coherent structures in turbulent periodically-excited jets and those of naturally-developing bubbly jets. Periodical excitation of the jet with frequencies in the neighborhood those of natural instabilities is applied to systematically create large coherent structures and to demonstrate their importance. When bubbles enter vortex rings, they can be trapped if certain conditions are fulfilled. A clear indication of bubble trapping is the generation of a bubble ring that travels with the same velocity as the confining vortex. In order to study trapping phenomena, simultaneous two-phase PIV and shadowgraphy were applied for tracking the large vortices and bubble structures.

In addition, the bubbly jet experiments aim at the understanding of the influence of the void fraction on shear-layer spreading (velocity, bubble concentration and passive or active scalars), bubble dispersion, turbulent properties and entrainment. In the region of inertia-dominated flow, the effect of the bubbles on the mixing processes is much less pronounced than in the transition region. Integration of the liquid flow in the jet shows that bubbles affect entrainment in the inertial region of the jet. Turbulence produced in the injector also enhances entrainment, particularly in case of smaller Reynolds jet number.

Experiments with periodically excited jets were carried out because information on size and development of the large-eddy structures is very difficult to obtain in case of naturally-developing flows. In order to quantify the interaction between bubbles and the large vortices that are formed in the shear layer, the following phase-averaged quantities were determined by PIV: azimuthal liquid vorticity field, vertical velocity of liquid and bubbles, vertical velocity of both vortex ring and bubble ring. The azimuthal liquid-vorticity field provides information on intensity, size, shape and position of large vortices in the flow field. These data are used to calculate the Vortex Trapping parameter and the Vortex Froude number needed for checking if the condition for bubble trapping is fulfilled. Furthermore, data at different phases within the triggering periods are acquired and analyzed, in order to show how flow properties vary in the flow field.

The DOS results indicate clustering of the bubbles in coherent vortex structures, with a periodic variation of void fraction during the excitation period. Results also show a time-dependence of the bubble velocity during an excitation period. Sequential measurements at a number of different positions in the jet enable determining the coherent part of the bubble field properties.

Keywords: Bubbly jet, Excited jet, Coherent structures, Jet forcing, Particle Image Velocimetry, Optical probes, Phase averaging, Space and time filtering, Simultaneous PIV and shadowgraphy.

Kurzfassung

Wichtigste Beweggründe für die Inangriffnahme der vorliegenden experimentellen Arbeit waren das ungenügende Verständnis der Wechselwirkungen zwischen Blasen und Flüssigkeitsgeschwindigkeitsfeld in blasenhaltigen freien Scherströmungen im allgemeinen und des Blaseneinfangs in Wirbeln im besonderen.

Die Experimente wurden in einphasigen, flüssigen sowie zweiphasigen, blasenhaltigen axialsymmetrischen Jetströmungen durchgeführt, welche in einem Gas-Flüssigkeitsinjektor erzeugt wurden. Ein spezielles Ziel war dabei, Blasen mit möglichst uniformer Grösse zu erzeugen und den Blasenanteil gut unter Kontrolle zu halten. Der Jet wurde in einem grossen, wassergefüllten Plexiglastank durch vertikales Einschiessen durch den Tankboden gebildet. Die Grösse des Tanks war ausreichend, um den Wandeffekt zu minimieren. Bei gleichmässiger, ungestörter Einströmung entstand ein sogenannter natürlicher Jet und bei periodischer Modulation der Strömung ein angeregter Jet. Die Anregung wurde durch eine dünne Schichtströmung erzeugt, die direkt ausserhalb der Düse und koaxial dazu injiziert und dabei mit wählbarer Amplitude und Frequenz moduliert wurde. Für beide Jettypen konnten eine Reihe von Strömungsparametern variiert werden, welche die dimensionslosen Parameter Jet-Reynoldszahl, Froudezahl, Trappingparameter und Jet-Richardsonzahl sowie Grösse und Volumenanteil der Blasen und die Anregungscharakteristiken bestimmten.

Zur Analyse der Wechselwirkungen von Blasen und Flüssigkeitsströmung war es nötig, die Eigenschaften von Geschwindigkeits- und Blasenfeldern in natürlichen Jets und insbesondere jene der kohärenten Strukturen, welche bei angeregten Jets entstehen, möglichst genau zu untersuchen. Gut ausgebildete kohärente Strukturen bilden sich, wenn die Anregungsfrequenz in der Nähe einer natürlichen Instabilität liegt. Wenn auf diese Weise genügend grosse und stabile Wirbel erzeugt wurden, liess sich beobachten, dass Blasen in diesen Wirbeln gefangen wurden. Ein klares Anzeichen für den Blaseneinfang ist die Bildung von Blasenringen um den Jet, die sich mit der gleichen Geschwindigkeit wie die grossen Wirbelringe fortbewegen. Solche Einfangphänomene konnten mittels simultaner Zweiphasen-PIV und Schattenphotographie sichtbar gemacht werden. Neben der Visualisierung von Wirbel- und Blasenfeldstrukturen zielten die Versuche auch darauf ab, den Einfluss des Blasenanteils und anderer Jeteinlassbedingungen auf die Ausbreitung des Jets (Verteilung von Geschwindigkeit, Blasenkonzentration und passive Skalare) zu bestimmen. Im Gebiet der trägheitsdominierten Strömung war der Effekt der Blasen auf Mischprozesse weniger ausgeprägt als in der Übergangsregion zur auftriebsdominierten Strömung. Zunehmende Blasenkonzentration hatte eine Vergrösserung des Flüssigkeitsentrainments, das durch Integration der gemessenen Geschwindigkeitsverteilung bestimmt wurde, zur Folge. Auch die vom Injektor produzierte Turbulenz beeinflusste die Jetausbreitung, besonders für kleine Reynoldszahlen.

Experimente mit periodisch angeregten Jets und synchronisierter Datenerfassung wurden insbesondere deswegen durchgeführt, weil sie im Gegensatz zu natürlichen Jets erlauben, quantitativ genaue, reproduzierbare Information über die Entwicklung grosser Wirbelstrukturen zu erhalten. Ausserdem lässt sich dabei die Methode der Phasenmittelung einsetzen, mit deren Hilfe sich der kohärente Anteil der Geschwindigkeitsfeldschwankungen leicht ermitteln lässt. Die Methode wurde in Zusammenhang mit PIV (Bestimmung der zweidimensionalen Verteilungen von Vortizität und Geschwindigkeit von Flüssigkeit und Blasen), Photographie (Visualisierung von Blasenfeldern und Ringen) sowie mit der DOS (Lokaler Blasenanteil und Blasen- geschwindigkeit) eingesetzt. Die Messungen erlauben, die Wechselwirkung zwischen Blasen und Flüssigkeit zu quantifizieren, da die Messung der Vortizitätsverteilung in einer Schnittebene durch die Jetsymmetrieachse gestattet, Intensität, Grösse und Lage der Wirbel zu ermitteln, womit dann der Trappingparameter und die Wirbel-Froudezahl, welche das Einfangen von Blasen charakterisieren, berechnet werden können. Synchronisation der Datenerfassung mit der Jetanregung sowie Phasenmittelung ermöglichten relativ detaillierte Daten über die periodischen, kohärenten Teile der Geschwindigkeits- und Blasenfelder zu bestimmen, um so die Entwicklung der Felder aufzuzeigen. Mit der DOS Technik liess sich so punktuell die periodische Variation von Blasendichte und Geschwindigkeit bestimmen, so dass durch Ausmessen der Blasencharakteristiken an verschiedenen Punkten ein Schnittbild des kohärenten Teils der Blasenfeldeigenschaften resultiert.

Schlüsselwörter: Blasenhaltiger Jet (Freistrah), angeregter Jet, kohärente Strukturen, Particle Image Velocimetry (PIV), Doppelte Optische Sonde (DOS), Phasenmittelung, Simultane PIV und Schattenphotographie.

List of Symbols

Symbol	Unit	Description
A	m^2	Cross section
a, b	m	Radii of the elliptical vortex
B_0	m^4/s^3	Buoyancy flow at the nozzle exit
C_d	–	Drag coefficient
$C_{d\Gamma}$	–	Drag coefficient that corresponds to the terminal rise velocity
$C_{Fr}, C_\Gamma, C_{St}, C_Q, C_f$	–	Constants
C_l	–	Lift coefficient
C_m	–	Added mass coefficient
d	m	Bubble diameter
D	m	Jet diameter, Outer diameter of the jet nozzle
d_{nio}	m	Outer diameter of capillaries
d_{nii}	m	Inner diameter of capillaries
d_{to}	m	Outer diameter of water tubes
d_{ti}	m	Inner diameter of water tubes
D_v	m	Vortex diameter
D_1	m	Inlet diameter of the jet nozzle
Eo	–	Eötvös or Bond number
f	Hz	Excitation frequency
$\widehat{F}(t, x)$	–	Combined filtered component
$F(t, x)$	–	Signal function
$\widetilde{F}(t, x)$	–	Space-filtered value
$\widehat{F}(t, x)$	–	Time-filtered value
$\overline{F}(t, x), \overline{\overline{F}}$	–	Long-term time average
f_{coh}	–	Coherent part of the signal
f_{incoh}	–	Incoherent part of the signal
$f_t(t, x)$	–	Fluctuating component in case of time filtering
$f_{tx}(t, x)$	–	Fluctuating component in case of combined filtering
$f_x(t, x)$	–	Fluctuating component in case of space filtering
Fr_b	–	Bubble Froude number
Fr_{jet}	–	Jet Froude number
Fr_v	–	Froude number of the large vortices
Fr_0	–	Froude number at the jet exit
Fr_ω	–	Vortex Froude number
g	m/s^2	Acceleration due to gravity
$G_t(t, t')$	–	Time filter function
$G_x(x, x')$	–	Space filter function
$H(t)$	–	Heavyside function
I_c	1	Light intensity
k	m^2/s^2	Turbulent kinetic energy
k_L	m^2/s^2	Time-averaged kinetic energy of the liquid
k_{win}	–	Coefficient for Gaussian window function (PIV)
L	m	Length scale

Symbol	Unit	Description
Mo	—	Morton number
M_0	m^4/s^2	Momentum flow at the nozzle exit
N	—	Number of bubbles
N_{ep}	—	Number of recordings per excitation period
N_{ai}	—	Number of acquired images
$P(x, y)$	—	Position in the flow field
P_a, P_b, P_n	—	Pixel value
p_N	Pa	Pressure at normal conditions
p_0	Pa	Pressure at injector exit
Q_G	Nm^3/s	Gas flow rate
Q_{Lea}	m^3/s	External liquid flow rate
Q_{Lin}	m^3/s	Internal liquid flow rate
Q_{Ltot}	m^3/s	Total liquid flow rate
Q_0	m^3/s	Volume flow at the nozzle exit
\dot{Q}_{air}	m^3/s	Measured air flow rate
r, φ, z	—	Cylindrical coordinates
R_v	m	Vortex radius
Re_b	—	Bubble Reynolds number
Re_{jet}	—	Jet Reynolds number
Re_T	—	Bubble Reynolds number with V_T as characteristic velocity
Ri_0	—	Jet Richardson number at the jet exit
S	—	Nondimensional shear rate
St	—	Strouhal number
St_T	—	Stokes number
$StdevV_L, (\overline{\tilde{v}_L^2})^{1/2}$	m/s	Standard deviation of vertical velocity component of the liquid
t	s	Time
T	s	Period, total measurement time
T_N	K	Temperature at normal conditions
T_0	K	Fluid temperature at nozzle exit
U, V	m/s	Horizontal and vertical velocity components
U_L, \overline{U}_L	m/s	Time-averaged horizontal velocity component of the liquid
U_φ	m/s	Circumferential velocity
V_B, \overline{V}_B	m/s	Time-averaged vertical velocity component of the bubbles
V_{Gin}	m/s	Gas velocity inside the capillaries
V_{jet}	m/s	Superficial liquid velocity at the jet exit
V_L, \overline{V}_L	m/s	Time-averaged vertical velocity component of the liquid
V_{Lin}	m/s	Liquid velocity inside the tubes
V_T	m/s	Terminal bubble rise velocity
$VarU_L, \overline{\tilde{u}_L^2}$	m^2/s^2	Variance of horizontal velocity component of the liquid
$VarV_L, \overline{\tilde{v}_L^2}$	m^2/s^2	Variance of vertical velocity component of the liquid
$\dot{V}_{air,DOS}$	Nm^3/s	Volumetric flow rate estimated by DOS
$\dot{V}_{air,AFC}$	Nm^3/s	Volumetric flow rate measured by AFC
\mathbf{V}_B	m/s	Bubble velocity vector
\mathbf{V}_L	m/s	Liquid velocity vector
\mathbf{W}	m/s	Relative velocity, $\mathbf{W} = \mathbf{V}_B - \mathbf{V}_L$

Symbol	Unit	Description
Δt	s	Time difference
Δt_{fl}	s	Time of flight
Δt_{las}	s	Time interval between two laser shots
Δt_{res}	s	Bubble residence time
x, y, z	–	Coordinates
x_c, y_c	–	Coordinates of the vortex centre
$\Delta x, \Delta y$	m	Average particle displacement
$\{F\}_\varphi$	–	Phase-averaged quantity
$\{u_i \cdot u_j\}_\varphi$	–	Phase-averaged Reynolds stress
$\langle u \cdot v \rangle_L, \overline{\tilde{u}_L \cdot \tilde{v}_L}$	m^2/s^2	Turbulent shear stress component resolved by PIV
$\langle j_{air}^{DOS} \rangle_A$	$m^3/(m^2 \cdot s)$	Total volumetric flux
∇	–	Nabla operator

Greek Letters

Symbol	Unit	Description
β	–	Length scale ratio
δ	m	Characteristic length, Shear layer thickness
ϵ	–	Error, statistical error
ϵ_V	–	Displacement accuracy
ε	m^2/s^3	Dissipation rate
ε	%	Void fraction
ε_h	%	Homogenous void fraction
ε_2	%	Void fraction approximation (Section 5.2, Equation 5.71)
Γ	–	Trapping parameter
Γ_ω	–	Vortex Trapping parameter
Δ	m	Interrogation area size, LES mesh size
ν	m^2/s	Kinematic viscosity
ρ	kg/m^3	Density
σ	N/m	Surface tension
λ	1	Offset value
$\tau_{ij,SG}$	N/m^2	Sub-grid stress model in LES
$\tau_{ij,PIV}$	N/m^2	Turbulent shear stress resolved by PIV
φ	–	Phase
ω_z	s^{-1}	Azimuthal vorticity component
ω_o	s^{-1}	Azimuthal vorticity component at the vortex center

Indexes

Symbol Description

0	At the nozzle exit
<i>ai</i>	Acquired Images
<i>air</i>	Air
<i>AFC</i>	Air Flow Controller
<i>B</i>	Bubbles
<i>DOS</i>	Double Optical Sensor
<i>ep</i>	Excitation Period
<i>ex</i>	External
<i>G</i>	gas
<i>h</i>	Homogenous
<i>in</i>	Internal
<i>jet</i>	Jet
<i>L</i>	Liquid
max	Maximum
min	Minimum
<i>part1</i>	First part of image acquisition
<i>part2</i>	Second part of image acquisition
<i>peak</i>	Peak
<i>pt</i>	Pseudo turbulence
<i>res</i>	Residual
<i>rms</i>	Root mean square
<i>tips</i>	Sensor tips
<i>tot</i>	Total
<i>tr</i>	Triggering (Excitation)
φ	Phase

Abbreviations

Symbol	Description
BJ	Bubbly Jet
CFD	Computational Fluid Dynamics
CMFD	Computational Multiphase Fluid Dynamics
DAQ	Data AcQuisition
DOS	Double Optical Sensor
DNS	Direct Numerical Simulation
DS	Downstream DOS Sensor tip
E-E	Eulerian-Eulerian
FV	Field of View
F	Flow
V	Void fraction
HWA	Hot-Wire Anemometer
HFA	Hot-Film Anemometer
LIF	Laser-Induced Fluorescence
LDA	Laser Doppler Anemometry
L-E	Lagrangian-Eulerian
LES	Large Eddy Simulation
MEGAL	Mixed Eulerian Grid-Averaged Lagrangian
PDV	Phase Doppler Velocimetry
PIV	Particle Image Velocimetry
RANS	Reynolds-Averaged Navier Stokes
SP	Single-Phase
SPIW(L)F	Single-phase Internal Water (Liquid) Flow
TTL	Transistor to Transistor Logic
US	Upstream DOS Sensor tip

1 Introduction

Dispersed multiphase flows [13] such as particles or droplets in liquids and gases, bubbles in fluids, etc. are frequently encountered in chemical processes [14], [25], [10] in relation to the discharge of waste materials into the environment [50] and in thermal-hydraulic phenomena which take place in light water reactors [65] or other power plants.

Although progress has been achieved during recent years in the analysis of two-phase flows, mainly because of their increased amenability to numerical simulation, but also due to the availability of more powerful experimental means that enable their detailed study, a number of new needs and challenges have also appeared [65].

In order to contribute to the understanding of complex two-phase phenomena and to provide experimental information, especially regarding coherent vortex structures, a completely new experimental installation was built and extensive experimental research has been conducted at the *Thermalhydraulics Laboratory*, Paul Scherrer Institut (PSI), Switzerland. The project was supported by the *Swiss National Science Foundation*.

1.1 Motivation, objectives and uniqueness of presented work

The main motivation for undertaking the present study was an apparent lack of understanding of bubble trapping in eddies in free turbulent shear flows and of the interactions between the bubble field and liquid flows.

It was decided to investigate these processes in an axisymmetric bubbly jet that is formed by injecting a water-bubble mixture vertically through the bottom of a large water pool. The main objectives of this study are separately presented in the following two sections.

1.1.1 The effects of deterministic parameters in bubbly jet flow

One of the main goals of these experiments is to investigate the basic properties of turbulent bubbly flows using a vertical bubbly jet with variable flow conditions and carefully controlled bubble sizes. In particular, the bubbly jet experiments aim at the understanding of the following phenomena and parametric effects:

- The influence of the void fraction on shear-layer spreading (velocity, bubble concentration and passive or active scalars), bubble dispersion, turbulent properties and liquid entrainment.
- The role of some non-dimensional parameters and boundary conditions characterizing jet development and bubble trapping inside the large vortices. The downstream variation of these parameters is also investigated.

1.1.2 Orderly structures in bubbly jet flow

The main goal of these investigations is to reveal the characteristics of large coherent structures in turbulent, periodically-excited as well as in naturally-developed, *bubbly jet flows*. Periodical excitation of the jet with frequencies in the neighborhood of natural instabilities is applied to systematically create large coherent structures and to demonstrate their importance. When bubbles enter such vortices, they can be trapped if certain conditions are fulfilled.

Therefore, the basic idea of this experiment is to create large orderly structures in a *bubbly jet* with controllable frequency and phase, in order to enable their study by statistical means and to provide clear conditions for studying the interactions between dispersed (bubbles) and the continuous phase (liquid) in two-phase jet flow.

The advantage of this approach is that the generation of both, large orderly vortices with controllable frequency in the shear layer and uniformly-sized bubbles with controlled diameter, are powerful tools for the systematic observation of bubble movements, that are difficult to analyze in naturally-developing two-phase jet flows.

In the triggered-jet experiments, the shear layer at the jet exit is excited by a small external surging flow with controllable frequency and amplitude. At the same time, bubbles are injected in a controllable jet flow and tracked with a novel method developed for this purpose. Simultaneous two-phase PIV and shadowgraphy opens another promising chapter in exploring two-phase flow phenomena.

Thus the interaction between coherent structures and bubbles, as well as the feedback of bubble agglomeration on the development of these structures can be studied.

2 Overview and comments on bubbly-flow modelling and experimental investigations

2.1 Introduction

Dispersed multiphase flows in general constitute classes of fluid flows with universal importance in process and energy technologies as well as in relation to the discharge of waste materials into the environment. In the analysis of two-phase flows of dispersed solid particles, droplets or bubbles in a continuous fluid, the subject of this overview, great progress has been achieved during recent years, mainly because of increased amenability to numerical simulation and to more powerful experimental means.

The emphasis in this overview is put on a special form of gas-liquid flows, i.e. on bubbly flows, which consist of gas bubbles (dispersed phase) within a carrier fluid (continuous phase). This kind of flow frequently occurs in industry, especially in process, chemical and energy technologies.

In gas-liquid systems, topologically different flow regimes may exist. Examples of these flows are the bubbly, annular, slug, stratified and churn flow regimes. The development of advanced theoretical understanding of gas-liquid flow regimes and regime transition phenomena is one of the most tempting tasks to be addressed. Physical and mathematical theories for describing specific types of flow regimes, that include a set of complex equations and the necessary closure laws, have been deeply and successfully explored during the last decades.

A number of computational, theoretical and experimental investigations of quasi-fully-developed flows have already been conducted in order to improve the understanding of very complex multiphase flow phenomena. At first glance, even simplified topological sketches of the mentioned flow patterns open many questions that cannot be easily answered. The mathematical treatment of such multidimensional gas-liquid flows is very complicated and requires e.g.: adequate models for the exchange of mass, momentum and heat between the phases, modelling of turbulence modulation (shear-induced and bubble-induced turbulence) and of turbulence characteristics such as fluctuating velocities, autocorrelation functions, integral scales of turbulence; comprehensive modelling of forces acting on deformed gas flow structures, of feedback between phases and phase interaction; modelling of time-dependent shape and size of gas-liquid flow structures and of effects of surfactants; modelling of the interaction between gas and flow structures, etc.

Another task that arouses the imagination of many scientists is how to develop basic physical principles for predicting transitions of the flow regimes and pattern development in a complex gas-liquid system. Obviously, the development of universal equations that describe all above-mentioned quasi-fully-developed flow regimes could be just a utopian life-dream. Therefore, different approaches have been chosen for the modelling of gas-liquid flows:

- The Direct Numerical Simulation (DNS) with own continuum equations for each of the spatially separated media, equations for interface phenomena and without turbulence modelling.

- The continuous-fluid model, which describes the behavior of either a mixture of the two phases with averaged properties or of two separate interpenetrating fluids (Eulerian-Eulerian Model(E-E)). It uses various types of turbulence modelling and requires extensive experimental information for validating closure equations and assumptions on phase interactions and non-resolved turbulent motion.
- The point-bubble approach, in which the continuous phase is described by Euler equations with a feedback term from the dispersed phase, whereas bubble movement is treated by Lagrange equations containing models for the forces acting on the bubbles (Lagrangian-Eulerian Models (L-E Models). Collision models can account for bubble-bubble interactions. Two-way coupling between the phases can be embedded in the models.

Depending on the kind of decomposition of the field of physical parameters, the following two methods used in two-phase-flow modelling are distinguished:

- The Large Eddy Simulation (LES) resolves the large structures in the flow, whereas the small scales, which are cut off by applying a space filter (see more details in Chapter 3), are modelled by a sub-grid (SG) model.
- The Reynolds-Averaged Navier Stokes (RANS) equations together with different turbulence models.

In order to improve the understanding and to bring forth new ideas on the development of advanced physical theories, simple basic experimental investigations with well-controlled conditions designed for exploring transitional and not only fully-developed flow conditions, in complex gas-liquid systems can be very useful. Multiphase experiments can also play an important role for the formulation and development of closure laws, which represent key components of many computational methods. In the end, experimental results are necessary for code validation and testing of the models. It is very important to show that if computational results are going to be compared with experimental investigations, the chosen formulation of the mathematical equations as well as approximations used for their solutions should be consistent with methods applied during experimental investigations.

Therefore, even though the main focus in research of complex behavior of multiphase systems is on the development of more generalized computational methods like CFD or CMFD (Computational Multiphase Fluid Dynamics) for industrial applications, experimental investigations conducted with advanced and sophisticated techniques will certainly bring forth new ideas and help to establish new theories. In the end, experimental investigations of complex multiphase phenomena cannot be avoided because they have been and they will always be the "*alfa*" and "*omega*" of exploring complex phenomena.

2.2 Survey of modelling methods

2.2.1 Lagrangian-Eulerian (L-E) models

In the combined L-E approach, the continuous phase and the point-bubble movement are simulated by a single-phase CFD method and by Lagrange tracking, respectively. The CFD methods mentioned in the literature usually fall into one of the following classes:

- DNS type L-E approach without turbulence model;
- RANS methods with L-E models using an effective viscosity based on mixing length or turbulence modelling;

- LES type L-E models.

It is usual to distinguish three modelling levels corresponding to different dispersed-phase concentration ranges, i.e. dilute (no feedback), weakly dilute (with feedback on the fluid) and dense (with interaction between particles) [8]. The equations of motion [1], [40], can be generalized to take into account more details of the forces exerted by the continuous phase, of bubble feedback and interaction [12] if sufficiently precise theoretical, numerical or experimental results are available for their description. The method is also applicable to deformed bubbles, but an additional modelling effort is required to account for bubble shape effects. Complications may result because of interaction of the various external field conditions, bubble shape effects (e.g. drag and lift forces depend on shear and relative velocity and are not strictly parallel and normal to the relative velocity vector, respectively) and the detailed dependency of the force exerted by the liquid on the bubble relative velocity. Heat and mass transfer between the phases can also be included, but are not part of the present investigations.

In the frame of this survey only a few of the most interesting and characteristic computational simulations will be mentioned.

In a model for bubble interaction, Delnoij et al. [12] consider spherical, non-deformed bubbles that bounce and separate after collisions, which is probably a fair assumption for small bubbles rising in a water flow at high Reynolds numbers. Furthermore, the calculation of the total force exerted by the liquid on the bubble is simplified by assuming isothermal flow and low void fraction.

In [11] and [12], using DNS, the L-E method is applied to non-deformed spherical bubbles rising in laminar non-uniform liquid flow. The liquid–bubble interaction is modelled by a force term, which accounts for the momentum exchange due to drag, lift and inertial forces exerted by the liquid on the bubbles. Acceleration, velocity and new bubble position can be calculated from the force balance for the bubble. The influence of neighboring bubbles on the bubble under consideration is taken into account by the modified virtual mass coefficient. Possible direct bubble-bubble interactions (collisions) can also be accounted for.

In [31] and [30], time-dependent calculations of bubbly flows with gas hold-up between 0.7 and 3% and bubble mean diameters of 750, 850 and 900 μm were performed, using simultaneous Lagrangian tracking of a large number of bubbles through the flow field, whereas the continuous flow field was calculated by an Eulerian approach. Since the modelling of the turbulence in the liquid phase was done by the standard $k - \varepsilon$ model, this approach belongs to the RANS type of the L-E method. The modification of the liquid turbulence by the bubbles was taken into account by source terms in both k and ε equations. The source term of k , which was originally proposed by Crowe (can be found in the cited publication), takes into account the wake-induced pseudo-turbulence. This term is proportional to the product of the square of the relative velocity and the void fraction, whereas combined effects of bubble size and shape (assumed to be spherical) and relative velocity are taken into account by the bubble response time scale. Therefore, bubble-size and relative-velocity effects on the wake-induced pseudo turbulence are basically incorporated in the model by means of empirical correlations for the drag coefficient.

A very interesting computational method (Mixed Eulerian Grid-Averaged Lagrangian model (MEGAL)), that is based on an averaging operation applied to a Lagrangian-type equation of particle movement for all particles in each grid volume, is presented in [44]. The continuous-phase motion is formulated in classical LES manner, whereas the SG stress term is evaluated by the equation of turbulent kinetic energy, which includes additional terms due to momentum exchange between two phases. Although this method is applied to turbulent two-phase particle flows, the idea may be applied for bubbly flows especially with small bubbles.

Kitagawa et al. [27] performed calculations with a DNS-type of the L-E approach of both bubbly and/or particle flows, proposing some techniques for removing false liquid-phase velocity calculations which are caused by the sudden changes of the local void fraction in the computational grid. Furthermore, when a too-small mesh size is used in order to improve spatial resolution, the computations may collapse due to numerical instability. Since the maximum void fraction was less than 3%, they ignored interactions between bubbles. Application of Gaussian or sine-wave filtering functions for the local void fraction in the control volume ensures more realistic velocity fluctuations of the liquid phase than conventional simple methods do. Even though they did not apply any bubble-bubble interaction models, some bubble clustering was generated by the local pressure gradients. Bubble velocity and local void fraction are weakly correlated, i.e. the bubble velocity decreases as the local void fraction increases.

2.2.2 Eulerian-Eulerian (E-E) two-fluid models

The Eulerian-Eulerian models essentially treat the dispersed phase also as a continuous phase and use volume-averaged mass- and momentum conservation equations to describe the time evolution of both, the gas and the liquid phase. Generally, they need less computational time than L-E models but, because of difficulties in deriving constitutive laws, more or less accurate empirical equations have to be used for the closure relations. Basic issues are related to the modelling of inter-phase momentum exchange and of the turbulence. Models for inter-phase momentum exchange, which are introduced in the source term in Eulerian-type equations for the liquid, are further related with the modelling of the forces acting on the bubbles. While some models for these forces contain empirical correlations e.g. for the drag coefficient, others contain constants that need to be adjusted and quantities that can be measured by means of various experimental techniques. The effect of the bubble size is usually taken into consideration by correlations for drag coefficients and in some turbulent models for pseudo-turbulence.

Usually, E-E models used in the literature can be classified as follows:

- Reynolds-averaged E-E models, using an effective viscosity based on mixing length or $k - \epsilon$ turbulence modelling;
- LES type E-E models, where the so-called SG stress term must be modelled.

Depending on the type of used averaging methods, calculated quantities such as liquid-phase velocity distributions and turbulence as well as distribution of the bubble density and velocity can be compared with appropriately obtained experimental results.

The Reynolds-averaged type of the Eulerian method is most frequently used for numerical simulations of bubbly flows in bubble columns ([45], [47], [55], [3] and [62]), whereas the LES type E-E models was for instance applied in simulations of confined bubbly plumes, jets and mixing layers ([43]).

In general, Eulerian methods, which have been developed during the last decades, provide mainly results for statistical properties and the spatial distribution of local statistical variables. If practical calculations for industrial problems are to be carried out, these methods, accompanied with specified closure relations, need to be improved. Theoretical bases of closure laws will offer a constant challenge in the future.

An extensive review on flow patterns in bubble columns with a focus on transient flow structures, including summaries of previous experimental and computational work, is presented in [26] and [25].

2.2.3 Classification of turbulence modulation

The velocity fluctuations of the continuous phase, induced by the presence of a dispersed phase (turbulence modulation), are usually decomposed into two separate parts, i.e. shear-induced turbulence and bubble-induced turbulence [36], [32]. The two phenomena may, however, be difficult to distinguish if they interact. The first part is assumed to be independent of the relative motion of bubbles and liquid, and the second part has been addressed by considering the following contributions [27]:

- velocity changes caused by the displacement of the liquid moving around individual bubbles (often simulated by potential flow), leading to strong velocity fluctuations and giving to this part the highest importance;
- velocity changes induced by bubble wakes;
- velocity changes produced by vortex shedding behind bubbles;
- velocity changes induced by unsteady deformation of bubbles;
- velocity changes generated by the discrete distribution of buoyancy forces in the flow field which drag lumps of fluid along with the bubbles, especially in case of high fluid viscosity. These changes can occur even if there is no relative velocity between bubbles and surrounding liquid.

The above-classified interactions between dispersed and continuous phase should be in a way included in the turbulence models and necessarily checked and validated against experiments. There are strong reasons that so-called constants appearing in the turbulence models in reality depend on bubble size and shape as well as on the void fraction, and therefore checking of the models against experiments cannot be avoided. This, of course, creates the very difficult task of designing an experiment that fulfils important conditions of the theoretical modelling and, at the same time, provides a variety of controllable input parameters.

2.3 Survey of experimental investigations

To improve physical insight and to support numerical analyses, a number of basic experiments in bubbly flows have been carried out. In relation to free shear flows, research has been performed on bubbly jets and plane bubbly mixing layers. In these tests, effects of bubble size and concentration on turbulence, velocity and void distributions, shear-layer spreading rates, mixing, characteristic length scales and velocity correlations have been studied. However, these measurements mainly provide results for statistical properties and the spatial distribution of local stochastic variables and do not investigate spatial coherence and the effects of large structures (vortices), which are very important in shear layers and have been extensively analyzed in single-phase flows.

Only few experimental studies have been performed with bubbly jet flows, and most of them for fully-developed steady-state flows. Even though some of the studies were performed in the bubbly plume zone where buoyancy dominates the flow, the authors refer to them as bubbly jets.

Details of experiments on coherent flow structures in bubble column reactors, with flows driven by a bubbly plume, are presented in the review paper of Joshi [26].

Similarly, experiments with single-phase jets summarized in [50], mainly describe the steady-state fully-developed field of the jet.

Some of the most interesting experiments will be commented on in the following sections.

2.3.1 Experimental investigations of bubbly jets

The following recent publications relate to experiments with bubbly jets:

Extensive experiments have been carried out by Sun and Faeth [59], [60] with a bubbly jet issuing from a 5 mm nozzle. It contained bubbles with about 1 mm mean diameter at void fractions up to 9% and was characterized by a Jet Reynolds number (Re_{jet}) of about 9000 and Jet Richardson numbers (Ri_0) up to $1.6 \cdot 10^{-3}$. The values of the Froude number (Fr_0) ranged between 50 and 65 and those of the Trapping parameter (Γ) between 8 and 10. The authors measured mean and fluctuating velocities of the liquid and of the bubbles in the developing and asymptotic region of the jet, using Laser Doppler Anemometry (LDA), and compared these with numerical results. No measurements were made in the jet-to-plume transition region.

Kumar et al. [29] investigated in particular the effect of bubbles with mean diameters between 0.6 and 2 mm on liquid turbulence in the developing region of a 12.5 mm jet using two-component LDA. They applied void fractions of up to 20%, Jet Reynolds numbers of 5000 to 10000, Jet Richardson numbers up to 0.2 - reaching thus also the transition region - and Froude numbers between 1 and 4. The effect of these parameters on jet spreading was not investigated. A particular feature of their tests was the long straight jet inlet tube ('nozzle').

Stanley and Nikitopoulos [57] used Phase Doppler Velocimetry (PDV) to simultaneously measure bubble size and streamwise velocity in a bubbly jet with 12.7 mm nozzle diameter at Jet Reynolds numbers of about 11500, void fractions about 0.5% and mean bubble diameters of 1.5 to 2.4 mm. Their standard deviation of 20 to 25% of the mean bubble diameters was fairly small. The Fr_0 number of the tests was about 6, Γ about 3 and Ri_0 about $8 \cdot 10^{-4}$. The authors observed an effect of the bubbles on turbulence and noticed that, close to the jet exit, lift forces ejected bubbles laterally out of the jet. No measurements were made in the transition region.

Iguchi et al. [23], [24] investigated two different types of flows, which were formed either by injecting water-gas mixtures or just gas. The latter case is however disregarded, here. They produced bubbles with mean diameter of 2 mm and a void range between 0 and 50% in a jet with a 5 mm diameter nozzle and $Re_{jet} = 11000$. Fr_0 was about 90 and Γ about 7. The Ri_0 numbers ranged between 0 and $5.5 \cdot 10^{-3}$, and the experiments were thus, in part, also performed in the jet-to-plume transition region. They used resistivity probes and photographic techniques for bubble detection and two-component LDA for liquid-velocity measurement.

In the work mentioned, no systematic investigation of the dependence of bubble motion and jet development on the above-mentioned parameters, as well as on bubble size and void fraction has been undertaken. The Re_{jet} number was about the same in all experiments, and bubble sizes were relatively large compared to the nozzle diameter and the large eddies formed in the developing region. The tests were performed only for high values of Fr_0 and Γ , apart from the experiments of Kumar et al. [29] where the number of investigated cases, however, was relatively small. In all the tests, only local measurements of velocities, void and bubble properties were made without considering effects of large-scale or coherent structures. The bubble size was not closely controlled in many experiments.

2.3.2 Experiments on jet instabilities and buoyant jets and plumes

Since one of the objectives of the project is to analyze coherent structures of liquid and bubbles in bubbly jets, especially also by making use of triggering techniques for producing periodically developing vortex structures in the jet, a short survey of pertinent work on the subject is given. Most research is of course conducted with single-phase jets. To the best of the author's knowledge, no data related to excited bubbly jets are available in the literature.

There are two types of jet instabilities, the shear-layer mode and the jet-column mode [66], [20].

These two distinct modes characterize the conditions for vortex development in the near field of circular jets.

The first mode is attributed to the instability of the shear layer forming at the jet exit. The exit shear layer momentum thickness appears as scaling factor in the Strouhal number. This mode may be convective or absolute [19], where absolute instabilities can be important for jets with void fractions above 30%. For the present experiments, only the convective mode is of interest.

The second mode, called jet-column mode, is characterized by a Strouhal number scaled by the jet diameter. The preferred mode leads to the formation of large vortices with Strouhal numbers $St = \frac{f \cdot D}{V_{jet}} \approx 0.3$ in the downstream region of y/D between 2 and 6 [20], [6]. This mode is called preferred because the first maximum of the center-line vertical velocity fluctuation occurring at 4 jet diameters from the jet exit corresponds to this mode. Periodical triggering of this or any other mode allows one to produce large coherent structures in the jet. By phase-locking the measuring equipment to the triggering mechanism, it is possible to analyze coherent structures with constant, but variable phase [22], [66], [21].

Experiments with buoyant, turbulent single-phase jets were performed in [46], and the effect of periodic forcing on mixing in neutral and buoyant jets was analyzed in [39]. It was found that higher levels of forcing (triggering intensity) were required for turbulent jets than for laminar ones and that a maximum enhancement of jet mixing with ambient fluid resulted for $St = 0.6$, which might have been the consequence of pairing induced by triggering a harmonic together with the basic mode.

2.3.3 Experimental results for bubble effects on turbulence and spreading of mixing layers

In the past decades, a few bubbly-flow experiments and DNS calculations were carried out in order to quantify and to separate the two turbulence components mentioned above. Part of the work applies to particles as well as to bubbles and will also be referred to in the following.

The presence of bubbles in turbulent flows causes an increase of the turbulence level, as found by Lance and Bataille [32] in homogeneous grid turbulence. They distinguish two regions of void fraction, i.e. $\varepsilon < 1\%$, where turbulence increases linearly with ε , and $\varepsilon > 1\%$, where a non-linear increase can be detected and effects of bubble interactions come into play.

The role of the length scale ratio $\beta = d/L$ (defined and explained in more details in Chapter 5) and of the Stokes number (ratio between particle time scale and integral time scale) that is evident for the trapping and dispersion of particles in mixing layers [17], [18], [7] is somewhat unclear in the case of bubbles [58].

The question of how shear-induced and bubble-induced turbulence, the energies of which usually are superimposed [36], interact is also not resolved. Whereas Roig [52] measured a larger spreading of mixing layers for bubbly flow, Loth [37] did not detect a significant difference from single-phase conditions. The authors of a survey on results from different experiments state that linear superposition is appropriate only for weak shear flows [33].

Recent results of experiments performed in naturally-developing or triggered, horizontal bubbly mixing layers for dilute concentrations of very small bubbles ($50 \mu m$) were presented in [49], [38].

2.4 Conclusions

In order to understand the complexity and physics of phenomena that occur in two-phase flow, it is necessary to use a variety of approaches, methods, problems and solutions.

The above-presented review of various aspects of two-phase flow phenomena reveals the problems that occur in multifluid systems and, in particular, in two-phase bubbly flows. It also shows that a variety of computational and experimental methods have been applied in order to explain different phenomena.

Although during the last decades progress has been made in the analysis of simple two-phase systems like dilute particle-laden flows, dispersed drops or bubbles, additional complications arise due to the changing of the interface between phases. Phenomena such as deformation, break-up and coalescence, which are most probably controlled by the microphysics, are not completely understood. The study of controlling mechanisms at the microlevel, the formation of large-scale structures, understanding of interaction mechanisms between large structures and individual bubbles and evaluation of interfacial configurations are the top priorities to be addressed in future theoretical and experimental investigations.

Obviously, the performance of experiments for providing information to be used by computational methods is not the only objective. Carefully coupled computations and simple experiments can improve theoretical approaches and bring in new ideas, improve numerical calculations and validate models. Quantities such as liquid-phase velocity distributions and turbulence, distribution of the bubble density and velocity, gas-liquid interfacial properties can be calculated by numerical methods as well as obtained experimentally. In addition, some specific experiments, which can provide fundamental empirical correlations, must be carefully planned and carried out in parallel with numerical simulations.

Therefore, it would be very useful to create experimental conditions which can form a good basis for establishing new ideas and theories and provide clear conditions for observing and simulating complex two-phase phenomena. Naturally-developing and triggered bubbly jet flows with controllable inlet parameters, such as liquid phase flow rate, bubble size and void fraction represent an excellent scientific basis that should be better explored by advanced measurement techniques and simulating tools in the future.

From the overview of performed analytical and experimental work on bubbly flows, a number of subjects suggest themselves to be investigated more thoroughly. More experimental information is required, in particular, for an improved understanding of the following issues:

- The detailed understanding of how to model the forces acting on *deformable bubbles*, of the feedback and of bubble interactions, of shear-layer and bubble-induced turbulence interactions etc.
- Simultaneous measurements of stress terms, phase velocities and void fraction in the inertial, transitional and buoyancy-dominated regions, of bubbly flows may provide interesting results to be used for improving simulations.
- Bubble motion inside large eddies controlled by different forces acting on bubbles together with void fraction should be investigated in more detail.
- Experiments which can provide variable conditions affecting the relative ranges of forces acting on bubbles, bubble and eddy size, void fraction, etc. can be used for improving existing models for forces acting on bubbles as well as momentum exchange due to these forces and understanding of the physics behind complex bubble-liquid and bubble-bubble interactions.

In regard of turbulence modulation, there are still some unsolved problems and open questions like:

- How do shear-induced and bubble-induced turbulence interact? Because of these interactions it is impossible to distinguish the shear-induced component in two-phase flow. Pseudo turbulence (bubble-induced kinetic energy of turbulent fluctuations of liquid) cannot be simply obtained by subtracting the shear-induced component of single-phase flow from the total, measured quantity in two-phase flow. Obviously, the open questions especially in relation with turbulence modulation by the bubbles and interactions between large eddies and bubbles cannot be easily separated and answered. Suggestions and new ideas for future work can be found in Chapter 11.
- What is the role of the length-scale ratio (bubble size versus size of large-scale eddy structures) in bubbly shear flows?
- How is the Kolmogorov scale affected by bubbles?
- What are the effects of bubble size (bubble Reynolds number), bubble density and variations of bubble size and shape on turbulence modulation in two-phase flows? Is it possible to design and conduct experiments in order to investigate individual effects of all the above-mentioned quantities? What are the flow conditions to be investigated, such as the Reynolds numbers and void fractions?

It is to be expected that many of these questions will not be answered for a long time to come, but an attempt is made here to make a contribution in this direction.

3 Experimental techniques and links to simulations

Experimental techniques such as Particle Image Velocimetry (PIV), Laser-Induced Fluorescence (LIF) and Photographic Techniques have been applied besides local void-fraction and bubble-velocity measurements using Double Optical Sensors (DOS).

3.1 Particle Image Velocimetry (PIV)

The standard, commercial PIV system used consists of dual cavity lasers and two CCD (charge-coupled device) cameras that work in a two-frame double exposure mode. The laser light sheet illuminates the mid plane of the axisymmetric jet, while the two cameras behind the beam splitter look perpendicularly to the laser light sheet. The first camera with a green filter captures bubble reflections, while the second camera with a red filter acquires the images of light emitted from fluorescent seeding particles added to the flow. A special dosing system (barrel, dosing pump and mixer) is used for feeding the flow with seeding particles.

The PIV system consisted of components from Dantec and TSI. More details about the PIV system, its components, the experimental technique in general, main principles and measurement accuracy can be found in [9], [63] and [48]. Therefore, in this section, only the basic principles of this standard measurement technique are briefly explained.

Basic principle of PIV

Two consecutive images that contain light emitted from the fluorescent particles or reflected laser light from the bubbles are acquired with the CCD camera. The main idea is to estimate the average particle displacements $(\Delta x, \Delta y)$ in small areas of the images called interrogation areas (IA) by cross-correlation techniques. Since the time shift between images corresponds to the time between two laser shots (Δt_{las}) , the two velocity components can be calculated as:

$$U = \frac{\Delta x}{\Delta t_{las}}; V = \frac{\Delta y}{\Delta t_{las}} \quad (3.1)$$

Therefore, after dividing both images into small interrogation areas, the following PIV analyzing algorithm is applied:

- 1) Filters called window functions manipulate the image gray-scale values and therefore act as input filters to the FFT (Fast Fourier Transform) algorithm. The window functions are suitable weighting functions (Top-hat, Gaussian and etc.). Depending on the pixel position in the IA, the recorded intensity is multiplied with a factor between 0 and 1. Application of these filters allows one to suppress so-called phantom particles and phantom correlations near the edges of the IA,
- 2) In order to efficiently compute cross-correlations for each IA, the gray-scale image intensity fields are transformed by the FFT algorithm into the frequency spectrum of the gray-intensity distribution,
- 3) In order to estimate the average particle displacement, the cross-correlation function is calculated for each IA. This function statistically measures the degree of match between two corre-

sponding IA pictures for a given shift. The position of the highest value in the correlation plane is used as the final estimate of the average particle displacement. The space-averaged horizontal and vertical velocity components are obtained by dividing the horizontal and vertical average particle displacement by the time between two laser shots. In general, these results represent time- and space-filtered quantities.

For the experiments conducted with periodically excited jets, it must be possible to obtain velocity and vorticity fields at various phases within the triggering period, i.e., positions of the vortices in the flow field. For this a data acquisition scheme has been devised that is synchronized with the excitation (more details can be found in Appendix D). PIV acquisition is started by a periodic external signal from an encoder attached to the periodic excitation device, which covers two excitation periods. The PIV recordings are acquired with higher frequency (usually with $12Hz$ and $15Hz$) than the excitation frequency. Thus several shots per excitation period are captured, allowing phase-averaging at different times within the excitation period to be performed. The data acquired this way yield information on deformations, size modifications and velocity of the vortex rings. This acquisition method, called here vortex tracking method, is a very useful tool for tracking large vortices in a flow field.

3.2 Double Optical Sensors (DOS)

A standard instrument, often used in bubbly flows, is the Double Optical Sensor (DOS). Void fraction (ε), number of bubbles (N), bubble chord length distribution, as well as bubble vertical velocity (V_B) can be measured with a double optical sensor. The two tips of the DOS used in the tests were horizontally oriented for technical reasons, i.e. the sensor was perpendicular to the mean flow direction of the bubbles [28]. The measurements have been conducted with two different sensors. The distance between the two sapphire tips of the first sensor was $0.75mm$ and that of the second one $0.91mm$. The diameter of a tip was $0.08mm$. A photo of the second sensor is shown in Figure (3.1).

Light is guided from a source to the tips by a glass fibre. If the tips are surrounded by water, light leaves them. When air bubbles touch the tips, the light is reflected and then routed by the optical fibre to the optical amplifier. This light increases the detected voltage. Therefore, high voltage indicates the presence of air bubbles on the sensor tips, while low voltage corresponds to water.

The mean void fraction $\varepsilon(x, y)$ at a position in the flow field $P(x, y)$ is defined as the ratio between the time when air is present at the sensor tip and the total measuring time. Therefore, the mean void fraction is estimated by averaging of the void signal over a long-time period.

The bubble velocity V_B , which corresponds to the vertical bubble velocity component, is defined as the ratio between the tip separation distance and the measured time of flight. The bubble velocity is obtained by averaging over a suitably long time, that must be properly chosen in order to obtain statistically secured results. It can vary between 300 and 600s depending on bubble concentration. So, the vertical bubble velocity measured by DOS represents a long-time average.

More details about signal phase discrimination, thresholding, void fraction and bubble rise velocity measurements are presented in [28]. Experimental results on method testing and selection of the relevant parameters are given in Appendix C.

In order to perform phase averaging of experimental results for void fraction and bubble velocity in case of triggered jets, the data acquisition was started by the external encoder signal and was stopped after an integer number of periods. Each excitation period was divided into M equal

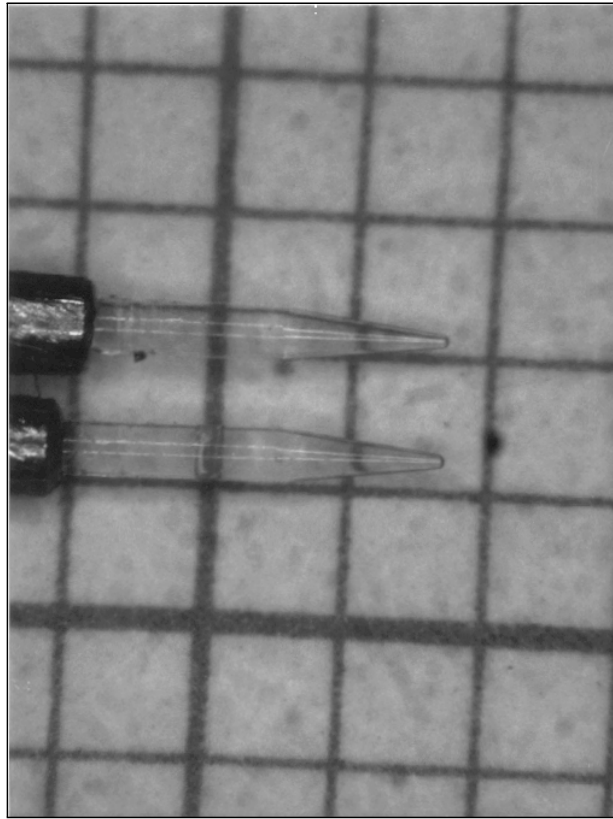


Figure (3.1): *DOS tips.*

intervals. Bubble number, void fraction and bubble velocity data were averaged for each of these intervals.

More details about synchronization of the DOS data acquisition and external triggering of large eddy structures is given in Appendix A.

3.3 Photographic recordings and image analysis

Photographic Recordings

In order to illustrate bubble trapping and clustering in shear-layer vortices, the PIV and the shadowgraphy technique were simultaneously used to acquire pictures that can be analyzed in order to obtain velocity fields and photographs of the bubbles, especially in cases when a bubble ring is formed. In addition, the images with bubble reflections can be phase-averaged and compared with the phase-averaged liquid vorticity field. Since the laser light sheet illuminates 2D intersections of the 3D jet, only bubbles trapped in the shear-layer that are illuminated by the laser sheet can be detected. In these images, bubble shapes cannot be distinguished any more. A photo obtained by superimposing several shots synchronized with vortex triggering and filtered with the *Max Pixel Operator* technique (see Chapter 9 for more details) is presented in Figure (3.2).

If every or every second frame captured with the camera that is used for obtaining the liquid velocity field is illuminated with uniform backlight, the projection of a bubble ring on the image plane can be visualized. In order to simultaneously observe bubble ring movement and to be able to analyze PIV images, it is preferable to use uniform, medium light intensity of the

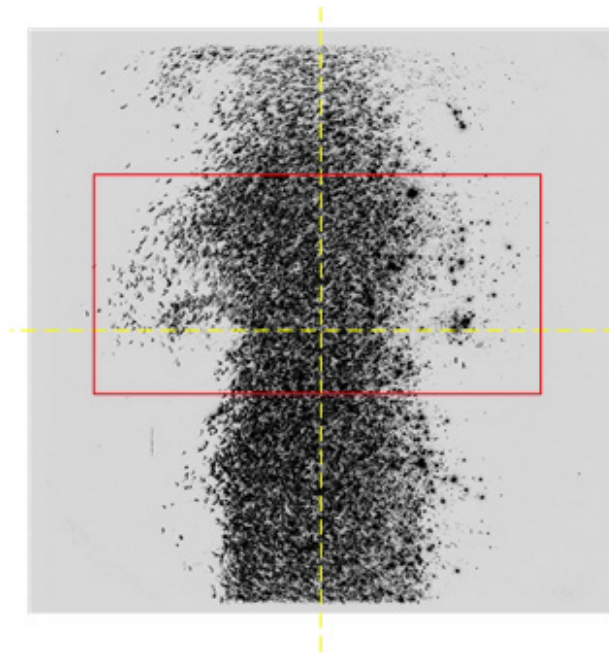


Figure (3.2): *Laser light reflections from the bubbles.*

backlight. The intensity of the backlight must be smaller than that of the laser, so that the backlight does not disturb the pictures with reflected laser light from the bubbles. If the same method is applied to vortex tracking, it is possible to observe the movement of the bubble ring and to estimate its velocity.

In order to illustrate the above-mentioned method, the flow field was simultaneously illuminated with both laser and backlight. This photograph is presented in Figure (3.3). Single bubble ring can be observed as well as back-light source and seeding particles. Since the back-light intensity in this case was neither negligible nor uniform, the light emitted by the seeding particles cannot be distinguished at some places from the backlight. Therefore, this picture can not be analyzed by the PIV algorithm.

The images of the fluorescent particles should be pre-processed before applying the PIV analyzing algorithm. The histogram plot of these images reveals which gray levels belong to the background including bubbles and which belong to the light emitted by seeding particles. After thresholding, i.e., dividing an image into two pictures (seeding-particle image and a background image), the PIV analysis and cross-correlation algorithm can be applied to obtain the liquid velocity field. Results that illustrate this method are presented in Appendix D.

To avoid the risk of adding noise to the PIV pictures, the experimental data can be split into two parts: the first contains standard PIV images and the second the PIV images with back-light illumination. The first set of images is used for usual PIV analysis, while the second one is used to observe phase-averaged positions of bubble rings.

Image Analysis

The objective of image analysis is to detect and analyze distinct two-dimensional shapes within a region of an image, which can provide measurements of different parameters characterizing presence or absence, number, location, shape, area, perimeter, and orientation of particles or bubbles in bubbly two-phase fluid flow.

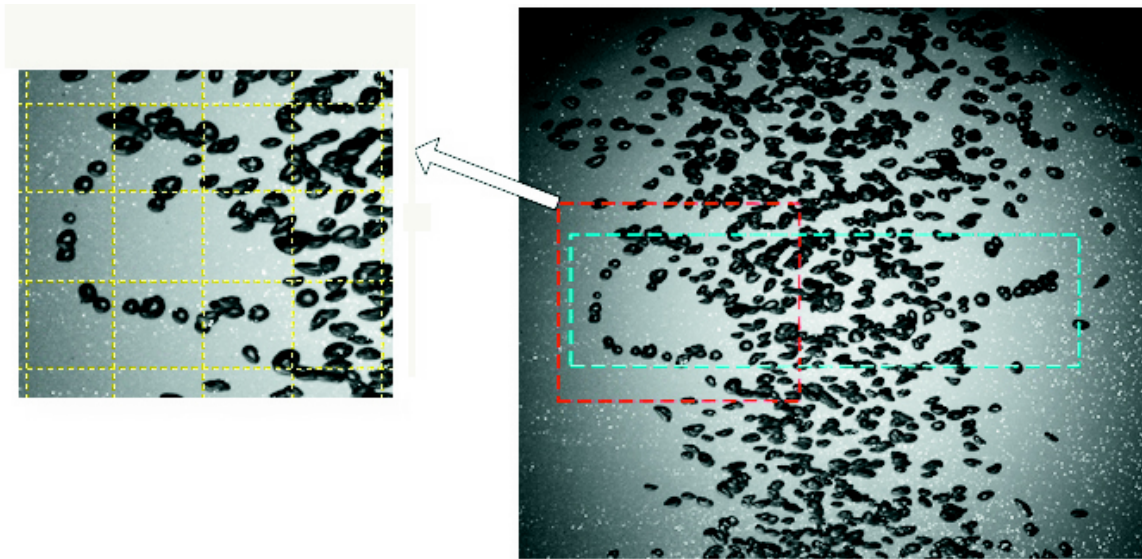


Figure (3.3): Photograph of bubble rings illuminated simultaneously by the laser and back light.

In image analysis, a particle is identified if a group of connected pixels that have similar intensity is found. In our case we consider *a bubble as a particle*. Image processing operates on these objects to calculate the area and perimeter or to count the number of distinguishable bubbles. Before applying bubble analysis, pre-processing of the image must be performed by converting a grey scale image (an image with 256 levels) to an image with only two grey scales – zeros and ones. The objective is to separate the important objects, bubbles, from the unimportant information, such as background, noise and shadows. Before applying a technique called thresholding that appropriately separates the objects from the background, a histogramming is needed to identify the threshold values. The result of the thresholding process is a binary image, which is an image of pixel values of only ones and zeros. The objects are represented by the connected pixels of ones, and the zeros represent the background. It is clear that thresholding of the image is a subjective process, depending also on the image quality.

By binarizing the image into ones and zeros, the task of writing image processing algorithms for object analysis is made easier. For example, to find the area of an object, one simply needs to count the pixels with value one that are connected. Another benefit of binarizing the image for object analysis is that the calculations are fast.

In summary, here are the basic steps for counting and measuring size and position of objects:

1. Acquiring the image
2. Calibration
3. Histogramming, to identify the threshold values
4. Thresholding, to create a binary image
5. Filtering, to remove noise, false objects and particles on the border of the image
6. Particle analysis, to estimate particle diameter, position, number etc.

After Thresholding and Filtering, as seen in Figure (3.4), only single bubbles, as well as coalesced or overlapped bubbles are left. By manual insertion of a white line between overlapped bubbles, two bubbles are separated in the final image.

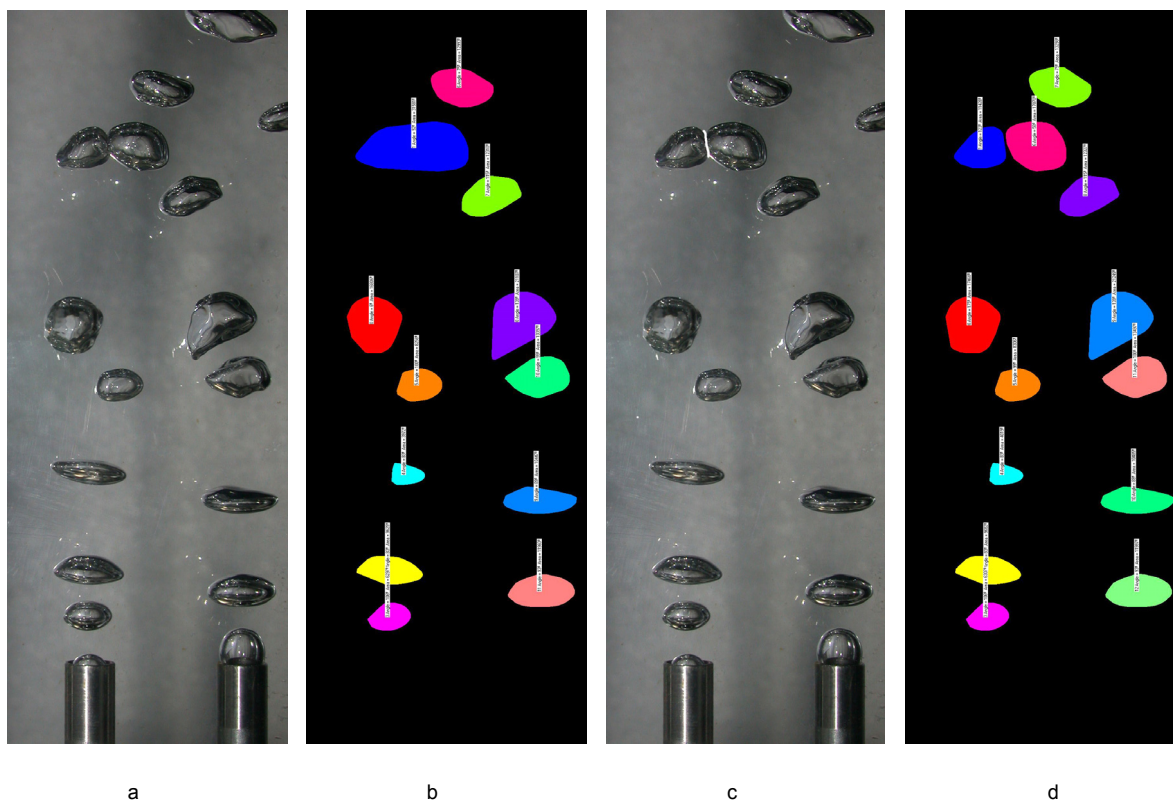


Figure (3.4): *Bubbles after Thresholding and Processing: a) Input Image, b) Resulting output image with overlapped bubble, c) Input image with inserted white line that separates overlapping bubbles, d) Inserting white line helped to separate overlapping bubbles.*

3.4 Laser-Induced Fluorescence (LIF)

Flow visualization is very often the best method of getting insight into mixing processes. In case of turbulent bubbly jet flows, the simultaneous visualization of liquid flow structures and bubbles is a very powerful and effective method of exploring complicate interaction phenomena that occur in two-phase flows.

Laser-Induced Fluorescence (LIF) has been primarily used as a method for obtaining visualization of the concentration field of a passive scalar in naturally-developing and periodically-excited shear layers. In general, the flow is illuminated by using a laser light source. Fluorescent dye, which is injected into the flow or into the shear layers, absorbs the laser energy and re-emits light at a longer wavelength. Having used an appropriate filter installed in front of the camera, images with the emitted light are recorded and can be later processed and analyzed (Figure 3.5). Phenomena that include:

- development and spreading of the shear layer in case of naturally-developing and triggered single-phase turbulent jets, as well as corresponding cases of turbulent bubbly jets,
- creation, development, dynamics and disappearance of large eddy structures, as well as interaction with bubbles,

can be quantified by converting the local fluorescence intensity into the scalar concentration field of the dye, since the fluorescence intensity level is a function of the laser light intensity and of dye concentration. This function can be estimated by a calibration procedure. However, it is also possible to deduce information about the above-mentioned phenomena directly from the distribution of the detected light intensity without performing a complicated calibration.

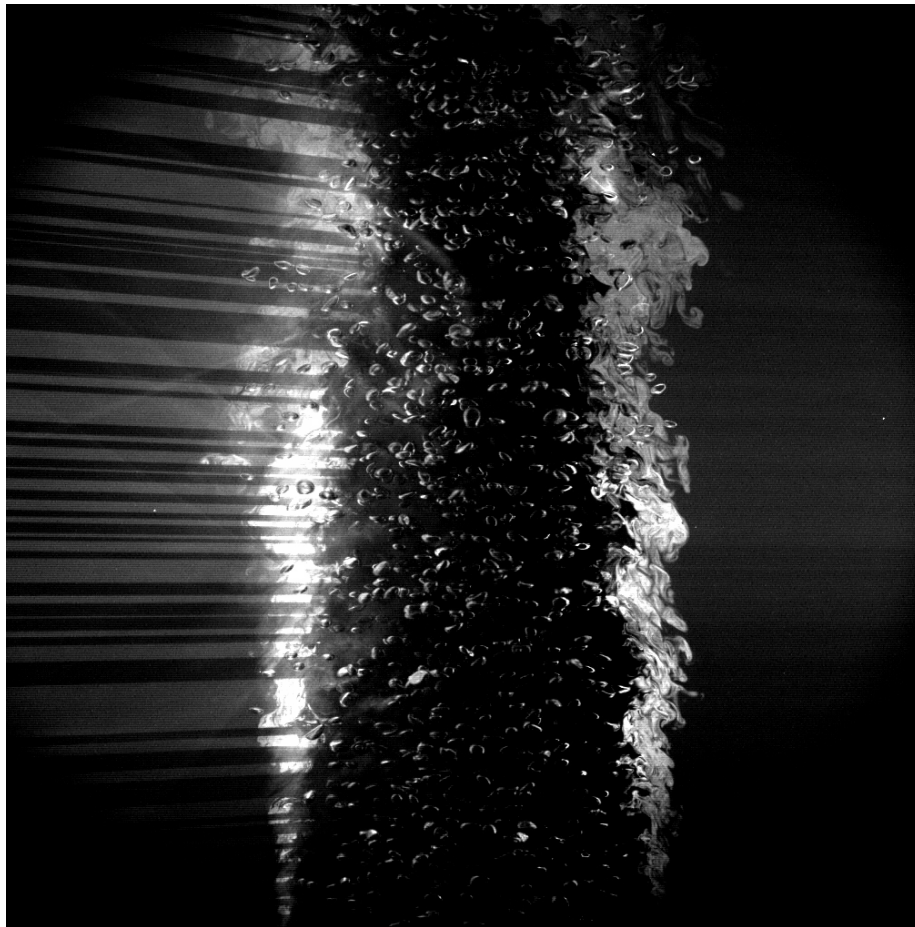


Figure (3.5): *LIF image of turbulent naturally-developing bubbly jet.*

For the LIF visualization test, the same equipment, including optical filters and cameras, was used as for the PIV experiments. The fluorescent dye was only injected into the shear layer in order to visualize large vortices and bubble rings.

3.5 Discussion on relationship between bubbly flow modelling and experiments

3.5.1 Signal decomposition and filtering

Neither CFD methods nor experimental techniques like PIV produce results with infinitesimal resolution in space or time. For a thorough discussion of experimental results obtained by PIV and their comparison with CFD results, it is therefore necessary to properly define and distinguish different filtered quantities. The complete signals can then be decomposed into sums of filtered and fluctuating components. *Filtering* means that a time- and space- dependent quantity is multiplied with a weight function and integrated over an interval in time or space. In general, the space and time filter functions defined here as $G_x(x, x')$ and $G_t(t, t')$ may have Gaussian, box (top hat) or any other suitable shape.

3.5.1.1 Mathematical signal decomposition and filtering

Time filtering

A signal can be decomposed into a time-filtered value $\widehat{F}(t, x)$ and a fluctuating component $f_t(t, x)$.

$$F(t, x) = \widehat{F}(t, x) + f_t(t, x) \quad (3.2)$$

Time filtering is defined by:

$$\widehat{F}(t, x) = \int_{t'} G_t(t, t') \cdot F(t', x) \cdot dt' \quad \text{with} \quad \int_{t'} G_t(t, t') \cdot dt' = 1 \quad (3.3)$$

where $G_t(t, t')$ is the time filtering function. $f_t(t, x)$ represents the fluctuating part of the signal with $\widehat{f}_t(t, x) = 0$.

This decomposition can be considered as a generalized form of the Reynolds decomposition that is obtained with the filtering function

$$G_t(t, t') = \frac{H[t' - (t - \frac{T}{2})] \cdot \{1 - H[t' - (t + \frac{T}{2})]\}}{T} \quad (3.4)$$

where $H(t)$ is the Heavyside function.

A *long-term time-averaged* quantity is obtained from:

$$\overline{F}(t, x) = \frac{1}{T} \cdot \int_{t - \frac{T}{2}}^{t + \frac{T}{2}} F(t', x) \cdot dt' \quad (3.5)$$

if the total averaging time T is much longer than the characteristic time of large eddies. For non-stationary flow conditions \overline{F} can still be time-dependent.

Since in experiments and time-dependent CFD one obtains short-term time-filtered values, these quantities must be distinguished from long-term averages. The superscript (\widehat{F}) is here used for the short-term time filtering operation, whereas (\overline{F}) denotes long-term time averaging.

Space filtering

Signal decomposition into a space-filtered quantity and a fluctuating component can be described by

$$F(t, x) = \widetilde{F}(t, x) + f_x(t, x) \quad (3.6)$$

where $f_x(t, x)$ is the part of the signal that fluctuates about the space-filtered value $\widetilde{F}(t, x)$.

Space filtering can be described by:

$$\widetilde{F}(t, x) = \int_{x'} G_x(x, x') \cdot F(t, x') \cdot dx' \quad \text{with} \quad \int_{x'} G_x(x, x') \cdot dx' = 1 \quad (3.7)$$

where $G_x(x, x')$ is the space filtering function. Obviously, the filtered fluctuating part of the signal $\widetilde{f}_x(t, x) = 0$. The superscript (\widetilde{F}) is used here for the space filtering operation.

Combined filtering

Finally, *signal decomposition* into a combined-filtered value and a fluctuating component can be described as:

$$F(t, x) = \widehat{F}(t, x) + f_{tx}(t, x) \quad (3.8)$$

where

$$\widehat{F}(t, x) = \int_{t', x'} G_{tx}(t, t', x, x') \cdot F(t', x') \cdot dt' \cdot dx' \quad (3.9)$$

If the kernel G_{tx} of this integral can be decomposed into time- and space-dependent functions, the two filtering operations commute:

$$\widehat{F}(t, x) = \int_{t', x'} G_{tx}(t, t', x, x') \cdot F(t', x') \cdot dt' \cdot dx' = \int_{x'} G_x(x, x') \cdot dx' \cdot \int_{t'} G_t(t, t') \cdot F(t', x') \cdot dt' = \quad (3.10)$$

$$= \int_{t'} G_t(t, t') \cdot dt' \cdot \int_{x'} G_x(x, x') \cdot F(t', x') \cdot dx'$$

$$\widehat{F}(t, x) = \widetilde{F}(t, x) \quad (3.11)$$

Thus the different filtered and fluctuating quantities are related in the following way:

$$\widehat{F} = \widehat{F} + \widehat{f}_x \quad (3.12)$$

$$\widetilde{F} = \widetilde{F} + \widetilde{f}_t \quad (3.13)$$

$$F = \widetilde{F} + f_{tx} \quad (3.14)$$

Therefore

$$\widehat{F} = \widetilde{F} = \widehat{F} - \widehat{f}_x = \widetilde{F} - \widetilde{f}_t = F - f_{tx} \quad (3.15)$$

and

$$f_{tx} = F - \widehat{F} + \widehat{f}_x = f_t + \widehat{f}_x = F - \widetilde{F} + \widetilde{f}_t = f_x + \widetilde{f}_t \quad (3.16)$$

A common characteristic of time- and space-dependent PIV and LES results is that both are filtered in space as well as in time. Space filtering in PIV is applied over the interrogation volume (area \times laser light thickness) and in LES over the mesh boxes. Whereas in PIV the size of the interrogation volume is roughly constant, which means that a constant size of the interrogation mesh is chosen for processing the images, the box size in LES may be spatially variable. Time filtering in PIV occurs because velocities are obtained by integrating displacements between two laser flashes and, in LES, because of the integration time step. The two time steps have the same order of magnitude, although the criteria for their selection are, of course, different. Thus, decomposition (3.8) applies in both cases. With PIV, the fluctuations f_{tx} cannot be measured, and in LES they are simulated by the SGS model. An important difference between LES and

PIV results is, however, that PIV data can only be scanned at relatively low frequencies of up to $15Hz$, whereas, with LES, 1000 time steps per second or more are typical.

In stationary experiments in turbulent flows, one usually attempts to obtain statistical long-term averages such as \overline{F}_i , \overline{F}_j and $\overline{f_i \cdot f_j}$, which appear in the normal Reynolds decomposition:

$$F_i = \overline{F}_i + f_i \quad (3.17)$$

$$F_j = \overline{F}_j + f_j \quad (3.18)$$

PIV results now yield only signals filtered in space and time. With the commutation assumption, it follows from ((3.17) and (3.18)):

$$\widehat{F} = \widehat{\overline{F}} + \widehat{f} = \widetilde{\overline{F}} + \widehat{f} \quad (3.19)$$

where

$$\widetilde{\overline{F}} = \frac{1}{T} \cdot \int_{-\frac{T}{2}}^{+\frac{T}{2}} \widehat{F}(t') \cdot dt' \quad (3.20)$$

With PIV (or LES) the integral (3.20) is, in reality, a sum over a number of discrete, scanned values of \widehat{F} . The fluctuating part \widehat{f} and moments thereof can be related to f by making use of (3.8), (3.9), (3.17) and (3.18):

$$\widehat{f} = \widehat{F} - \widetilde{\overline{F}} = F - f_{tx} - \widetilde{\overline{F}} = f - f_{tx} + \overline{F} - \widetilde{\overline{F}} \quad (3.21)$$

Assuming that $\widetilde{\overline{F}} \approx \overline{F}$ yields:

$$\widehat{f} \approx f - f_{tx} \quad (3.22)$$

Since f_{tx} is positively correlated with f , the filtered signal \widehat{f} is, in general, smaller than f . Thus, the variance obtained with PIV is:

$$\overline{\widehat{f}^2} \approx \overline{f^2} + \overline{f_{tx}^2} - 2 \cdot \overline{f \cdot f_{tx}} < \overline{f^2} \quad (3.23)$$

Of course, the measured \widehat{f} in reality also contains noise contributions which have not been taken into account in these considerations. Using these results, the turbulent shear stress resolved by PIV and the sub-grid stress modelled in LES can be represented as:

$$\overline{\tau_{ij,PIV}} = \rho \cdot \overline{\widehat{u}_i \cdot \widehat{u}_j} \quad (3.24)$$

and

$$\tau_{ij,SG} = \rho \cdot \overline{\widehat{\widehat{u}_{i,tx} \cdot u_{j,tx}}} \quad (3.25)$$

In the following, the superscript ($\widehat{\quad}$) for short-term time filtering will be dropped because, in PIV and LES, space and time filtering are always combined.

Besides single-point correlations, PIV data could also yield two- or multi-point correlation functions, and they can be applied in conditional sampling. In this work, a phase-averaging technique for periodically triggered flows will be used in order to obtain information on large-scale, coherent structures.

3.5.1.2 Filtering in DOS

Although the detection of bubbles by DOS is highly localized in space and time, spacial filtering is applied because of the finite sizes of the probe tips and bubbles and time filtering because of the limited scanning frequency. What is more important, however, filtering operations are required for calculating bubble velocities and void fractions from DOS signals. The instantaneous bubble velocity, calculated from the time delay between the two sensor signals, corresponds to an averaging time equal to the time delay and void fractions can only be calculated by averaging over relatively long time periods.

3.5.1.3 Physical signal decomposition, phase averaging and filtering

In order to distinguish between coherent, i.e. relatively regular, large-scale structures, and incoherent stochastic turbulence, the fluctuating part of flow quantities can be decomposed. This method is particularly useful if flows are periodically modulated. The Reynolds decomposition (3.17) then can be represented as:

$$F = \overline{F} + f_{coh} + f_{incoh} \quad (3.26)$$

f_{coh} contains that part of the fluctuating signal that essentially consists of large-scale coherent structures and has the same period as the excitation function. This part is defined as the space-time function that is obtained by averaging a field variable F that is scanned over a large number of periods at a phase delay φ with respect to a periodic trigger signal, which is synchronized with the flow modulation function. The phase-averaged quantity, which is symbolically denoted here by $\{F\}_\varphi$, can be decomposed into a time-averaged component and a coherent fluctuating part of the signal

$$\{F\}_\varphi = \overline{F} + f_{coh}(\varphi) \quad (3.27)$$

By this operation, the incoherent part is filtered out. If this operator is applied on the product of f_{coh} and f_{incoh} , it has the effect that incoherent and coherent parts are not correlated, i.e.

$$\{f_{coh} \cdot f_{incoh}\}_\varphi = \{f_{incoh}\}_\varphi \cdot f_{coh}(\varphi) = 0 \quad (3.28)$$

because $\{f_{incoh}\}_\varphi = 0$ and $f_{coh}(\varphi) = const.$

However, if subharmonics of the basic modulation mode, which are also coherent in the physical sense, were also excited by the triggering, they would be eliminated by this phase-averaging. Subharmonics of this kind occur for instance in case of vortex pairing.

If one applies a space filtering operation as in PIV and LES, disregarding again the short-term time filter as mentioned above, one obtains:

$$\tilde{F} = \overline{F} + \tilde{f}_{coh} + \tilde{f}_{incoh} \quad (3.29)$$

One may expect that the filtering operation only weakly attenuates the coherent part, that contains mainly large-scale fluctuations, whereas f_{incoh} is more strongly suppressed, similarly to SGS turbulence.

Applying the phase averaging operation to \tilde{F} obviously yields:

$$\{\tilde{F}\}_\varphi = \overline{F} + \tilde{f}_{coh}(\varphi) \quad (3.30)$$

The variance of the incoherent part thus is

$$\{\tilde{f}_{incoh}^2\}_\varphi = \left\{ \left(\tilde{F} - \overline{F} - \tilde{f}_{coh}(\varphi) \right)^2 \right\}_\varphi \quad (3.31)$$

Phase averaging and filtering do not strictly commute for PIV results (i.e. $\{\tilde{F}\}_\varphi \neq \overline{\{\tilde{F}\}_\varphi}$) because space filtering includes averaging over a short time interval.

For the phase-averaged Reynolds stress one obtains:

$$\{u_i \cdot u_j\}_\varphi = \{u_{i,coh} \cdot u_{j,coh}\}_\varphi + \{u_{i,incoh} \cdot u_{j,incoh}\}_\varphi \quad (3.32)$$

The second part does not vanish, but there is no mixed term. For the filtered or resolved part of the Reynolds stress, a corresponding similar relation holds:

$$\{\tilde{u}_i \cdot \tilde{u}_j\}_\varphi = \{\tilde{u}_{i,coh} \cdot \tilde{u}_{j,coh}\}_\varphi + \{\tilde{u}_{i,incoh} \cdot \tilde{u}_{j,incoh}\}_\varphi \quad (3.33)$$

In the simulation of a periodically modulated experiment obtained by LES, F_{LES} may also consist of both coherent and incoherent parts

$$F_{LES} = \overline{F}_{LES} + \tilde{f}_{LES,coh} + \tilde{f}_{LES,incoh} \quad (3.34)$$

Whether the incoherent part exists or not depends on modelling of SGS turbulence and on the mathematical properties of the LES equations. Again, subharmonics could be contained in the incoherent part.

Differences between LES and PIV

Despite the similarity of LES and PIV, the filtering procedure in PIV is, in reality, a more complicated operation than a simple convolution of filter functions in space and time with the velocity field.

Firstly, only the particle field can be observed and the time filter consists in the integration of the particle velocities for finding the final positions of the particles from the initial ones.

Secondly, the displacement vectors of the particles in the IA are averaged by finding the peak of the cross-correlation function of the particle image patterns obtained at the beginning and the end of the time step. Filter functions can be used to give less weight to particles near the boundary of the IA in order to avoid spurious effects caused by reflections.

Thirdly, the spatial resolution of the particle images is limited by the pixel size of the cameras.

Thus, the filtering operation in space and time, Equation (3.10), applied in LES to the liquid velocity field yields a result that differs from that of the PIV method. The correlation procedure does not yield the arithmetic average displacement of all particles in the IA, but it results in a mean value obtained by a weight function which contains information on intensity of the particle images but cannot really identify individual particles.

It is, therefore, somewhat misleading to consider PIV measurements of the fluid velocity as a well-defined mathematical filtering operation on its velocity field. PIV results contain an appreciable contribution of noise resulting from the stochastic distribution of the particles and their image intensities in the IAs.

These considerations should show the importance of carefully distinguishing the various averaged and filtered quantities used in numerical and experimental analysis. They also illustrate the difficulty of quantifying the difference between LES and PIV.

3.6 Filtering and scanning characteristics of LES and PIV

In the following section, some filtering and scanning characteristics of LES and PIV will be emphasized and compared.

Space filtering

In the case of two-phase flow, considering jointly PIV as an experimental method and LES as an appropriate simulation method, a new fundamental problem arises. The selection of the LES mesh size (filter width) and the size of the PIV interrogation area depends on what bubble diameters and turbulent length scales have to be resolved. Since, with LES, large scales of fluid motion are directly resolved and small scales are modeled, the PIV method should reach the same aim: resolving the large eddy structures.

On the other hand, the LES mesh size should not be smaller than the characteristic length-scale of the dispersed phase, i.e. the bubble diameter. In PIV, the issue is the same: the size of the interrogation area should be large enough to contain enough reflections from the bubbles in order to achieve sufficient statistical accuracy for estimating the cross-correlation function. However, this only plays a role in the case when the bubble velocity is needed in each interrogation volume at all measuring times, because in regions with low bubble concentration this is not possible to achieve. Another open question is, whether the measured bubble velocity is correct if bubble size is comparable to the IA size. In any case, the size of the chosen LES cut-off filter will be suitable also for PIV measurements.

At the other extreme, the size of the large structures that are resolved by LES and visualized experimentally by PIV or LIF must be large enough in order that interaction effects between large vortices and bubbles can be investigated. For instance, if the bubble trapping phenomenon is investigated, the size of the large vortices should obviously be larger than the size of the bubbles to be tracked inside them.

The schematics of Figure (3.6) illustrate the effect of the bubble size on the size of the cut-off filter and of the IA. The rectangle represents the resolution in LES and the Interrogation Area in PIV. If the bubble diameter is considerably smaller than the size of the filter (Figure (3.6a)), the effects of statistical fluctuations will be smaller, than in the case of medium-sized and large bubbles (Figures (3.6b) and (3.6c)). The more bubbles are contained in the IA, the more successful is the application of the cross-correlation algorithm because of the higher signal-to-noise ratio. Furthermore, in order to suppress the effect of random correlations between initial positions of some bubbles and final positions of other ones, which leads to noise or spurious results, it is preferable to have many bubbles inside the IA. If only one big bubble occupies the complete IA (Figure (3.6c)), it may be that only part of the bubble surface reflects laser light. Therefore, the number of matched reflections can be very small, which means that the measured signal-to-noise peak ratio will be also smaller and the velocity measurement may be biased.

For successful application of the cross-correlation algorithm in case of liquid velocity measurements, the number of particles per IA should be at least 5 [9].

In the second and third case (Figures (3.6b and c)) the following problems appear in LES:

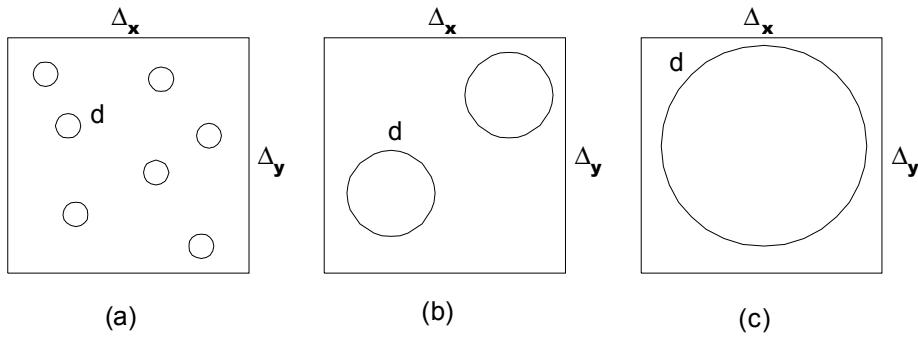


Figure (3.6): Size of the spatial filter (a-small bubbles, b-medium-sized bubbles, c-large bubbles).

With a two-fluid model the real fluctuations of the void fraction in time and space cannot be captured. In case of Lagrangian-tracking of the bubbles and two-way coupling, strong fluctuations of void fraction would result and cause numerical problems.

Time filtering

In LES, time filtering results from the use of a time step for numerical integration, while in PIV a small time interval is necessary for velocity measurement, i.e. the time between two consecutive laser shots which is determined by resolution requirements for velocity measurement. Since the laser pulse duration is more than an order of magnitude smaller than the time interval between two laser shots, the time filter in PIV can be represented by an averaging operation over the time between two consecutive laser shots.

Size of time filter

PIV

The size of the time filter is determined by the maximum velocity in the dominant flow direction and the size of the interrogation area. The following criteria should be taken into account:

- The size of the interrogation area (IA) and the image magnification are balanced against the size of the flow structures to be resolved. One way of expressing this is to require the velocity change to be small within the IA.
- For a given window side of length Δ , a maximum particle displacement (calculated for the dominant flow direction with the maximum velocity component) of $\Delta/4$ is recommended [9] to ensure a reasonable signal-to-noise ratio. In the case when, for instance, a Gaussian or any other window function is applied in order to suppress particles on the boundaries of the IA, the recommended particle displacement can be even smaller.

The time between the two subsequent laser pulses depends on liquid and bubble velocities, concentration of bubbles and seeding particles etc. The value usually used in our PIV experiments was between $1ms$ and $3ms$, depending on the main flow parameters such as jet velocity and void fraction. An inadequate selection of this time can significantly increase the measurement errors (see some experimental results presented in Appendix D).

LES

The IA corresponds to the filter size used in LES. A schematic of a bubble transit trajectory across a LES mesh is shown in Figure (3.7). If effects of large bubbles are to be represented in LES, the integration time step has to be smaller than the transit time. For instance, Milelli [43] used in his calculations a time step of $1ms$ and a grid size greater than the bubble diameter.

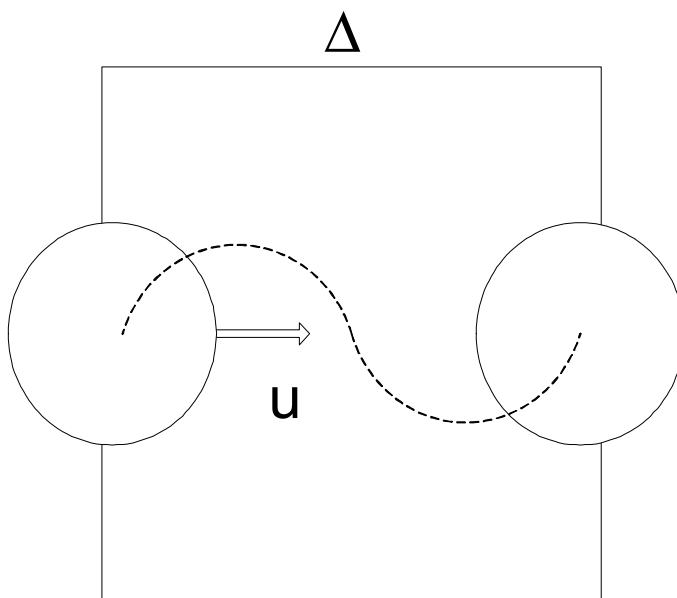


Figure (3.7): Transit time (T) through mesh, including effects of oscillatory movement and fluid displacement. $T \approx \frac{\Delta}{u} = \frac{\text{Mean mesh size}}{\text{Mean velocity (in the shear layer region)}} \Rightarrow \text{Example } \left(\frac{4\text{mm}}{0.5\text{m/s}} = 8\text{ms} \right)$.

If the dispersed phase is represented by a quasi-continuum, Figure (3.7) does not apply, but the time step limitations, which are given by numerical conditions, remain essentially the same.

Time filtering in LES may require additional modeling to account, e.g., for turbulent diffusion of bubbles in the void conservation equation and the turbulent stress in the Reynolds equations.

Scanning frequency

Depending on the kind of flow or phenomenon to be studied, the scanning frequency of the PIV system has to be carefully chosen. The maximum scanning frequency is the maximum laser shooting frequency of 15Hz , which corresponds to the minimum PIV scanning period of 66.7ms . A few choices will be discussed in this section, whereas more details on characterization of flow conditions can be found in Chapter 5.

The frequency f of the most unstable jet oscillations in case of naturally-developing flows, for the range of jet diameters and Reynolds jet numbers considered in Section 5.1.1, allows the condition $f < 15\text{Hz}$ to be satisfied if $Re_{jet} < 80000$ for the smallest nozzle diameter. For example, the shedding frequency f of the most unstable vortices given by the Strouhal number $St = 0.3$ yields for the 90mm nozzle the frequency range of 0.2 to 1.9Hz for $Re_{jet} = 5000 - 50000$.

For phase averaging in case of the triggered jet, the scanning frequency should also be preferably higher than the excitation frequency but, in principle, experiments could also be performed for scanning frequencies that are an integer fraction of the excitation frequency. The excitation frequency, which can be selected based on the corresponding Strouhal number, falls into the range $0.5 - 4\text{Hz}$.

3.7 Summary and some examples

Two main approaches used in two-phase-flow modelling are LES and RANS. In LES, the basic decomposition of instantaneous velocities is done in a way that large structures are resolved and small structures are cut off by applying a space filter (resulting in a wave number cut-off in the Fourier space). Thus, velocities can be decomposed into filtered values and fluctuations about filtered values. The size of spatial filters in the flow domain is chosen with respect to the flow structures that have to be resolved. (The same approach is actually done in PIV, the size of the filter being defined by the size of the interrogation area and laser-sheet thickness). The next step is the modification of the Navier-Stokes equations, which produces a so-called sub-grid-scale tensor or Reynolds stress due to the SGS (Sub-Grid-Scale) turbulence. This tensor is different from the Reynolds stress term which results from Reynolds averaging of the Navier-Stokes equations, because it does not contain contributions from large-scale phenomena. Thus, in the RANS model, the Reynolds stress tensor must be modelled and, in LES, the sub-grid-scale tensor.

The PIV experimental technique is principally based on the same spatial filtering as LES, so that the two methods should lead to comparable results.

One of the goals of this thesis is to provide experimental data, especially on large structures. Since PIV is the main experimental technique used to produce *time and space-filtered quantities*, including also *phase-averaged, periodic, simultaneous two-phase velocity components*, the following discussion contains hints on choosing appropriate filters in both experimental and simulation methods. Descriptions of both space and time filtering as well as mathematical and physical decomposition are presented in Section 3.5.1.

In detail, the following points have to be considered when comparing RANS and LES with LDA, HFA and PIV:

- In LES, the filtered velocity field is calculated and velocity fluctuations about filtered values are estimated by an SGS turbulence model. The resulting SG stress term, mistakenly often called Reynolds stress, is actually completely different from the one that appears in the RANS model and should be called Reynolds stress due to the SG turbulence. The basic difficulty of LES is to model this term and one of the important questions regarding the comparison with PIV is whether this term can be measured.
- In PIV, one can experimentally determine instantaneous, filtered velocity fields and also fluctuations of filtered quantities about time-averaged values. For bubbly flows, one must also take into account that the characteristic length scale of the dispersed phase, which is approximately equal to the bubble diameter, should be smaller than that of the interrogation area. In practice, the same spatial resolution can be used in PIV and LES and filtering conditions can be chosen for both approaches so that the results of the two methods are comparable. However, space and time-filtered quantities which are obtained experimentally by means of PIV must be distinguished from those measured by HFA and LDA, because they contain only fluctuations of the filtered velocities.
- It is also not possible to measure the time-dependent SG stress terms appearing in the LES equations because the PIV method produces only *filtered velocities* ($\tilde{f} \cdot \tilde{g}$), but not *filtered products* of different quantities ($\widetilde{f \cdot g}$) and the resolved quantities do not contain the whole spectrum of fluctuation energy.
- If one decreases the size of the interrogation area in PIV, the fluctuating energy obtained by PIV increases, but the signal-to-noise ratio decreases.
- With triggered PIV, one can determine phase-averaged, time-dependent quantities that can be compared with the time-dependent LES solution of an equivalent numerical problem.

The fluctuations about the phase averages contain the filtered incoherent part of the signals. These are, however, not related to the SGS fluctuations.

- In order to illustrate the discussion presented in this chapter, some examples regarding flow conditions and phenomena as well as scanning and filtering characteristics of experimental techniques such as PIV and DOS are presented below.

PIV

Considering, for example, a single-phase or bubbly two-phase jet with a Reynolds number of 100000, one obtains, for a jet diameter of $0.05m$ and a maximum velocity of $2m/s$, a Kolmogorov length scale of $9\mu m$, a maximum frequency of the velocity fluctuation of about $0.2MHz$, integral time scales of $0.025s$, a maximum wave number of turbulent fluctuations of $0.7 \cdot 10^6 m^{-1}$ and a required sampling rate of about $0.5MHz$. If one would like to measure *the spectral distribution* of second moments appearing in RANS models, the sampling rate should therefore be about $3.33 \cdot 10^4$ times greater than the available PIV sampling resolution ($15Hz$).

To compare these numbers with the PIV spatial and temporal resolution let us assume the following parameters:

- Field of view: $200 \times 200mm$.
- Camera resolution: $1000 \times 1000pixels$.
- Bubble size: $3mm$.
- Interrogation area size: 32×32 pixels, i.e. $6.4 \times 6.4mm$. This means that the size of the PIV cut-off filter is greater than the bubble size. Also, the size of this filter is three orders of magnitude larger than the Kolmogorov length scale.
- Sampling frequency: $15Hz$ (i.e. a period of $66.7ms$) is much smaller than the maximum frequency of velocity fluctuations for the above-considered jet flow.
- The total integration time for acquiring one sequence of 2000 samples is $133s$. Of course, one can perform averaging over longer times by acquiring several sequences for the same stationary conditions. If the jet is triggered in phase with the sampling, one obtains phase-averaged quantities instead of pure time averages of stochastic variables.

DOS

- Bubble velocity measurements with a Double Optical Sensor (DOS) can be also considered as some kind of space- and time-filtered data, because two probe tips are used for measuring the vertical velocity component. They are staggered in space, which can be considered as space filtering, and bubbles must travel for a certain time from the first to the second tip, which results in a time delay between two measurements (time filtering). Furthermore, a double optical probe occupies a 3D fluid volume in the flow field.
- The next questions related to DOS are the minimum time intervals required for counting bubbles, determining void fraction and measuring velocity. These times depend on the bubble residence and transit times, which are determined by probe-tip size and distance, bubble size and bubble velocity. Assuming a bubble of $2mm$ diameter with a velocity of $1m/s$, $0.75mm$ tip distance and negligible tip size, results in a residence time of $2ms$ and a transit time of $0.75ms$. The total minimum time interval for analyzing the whole signal is thus $2.75ms$. Since the probe signal must be completely contained in the time windows selected for analysis, the bubble chord length cannot be measured if a probe signal overlaps a window boundary. For the determination of average chord lengths and void fractions, much larger time windows, which contain a representative number of bubble signals, are required. In periodically triggered experiments, the total length of this time window given by the sum of

the selected time intervals inside the excitation periods (see results presented in Chapter 7 and 8) is long enough to obtain adequate statistical results.

- If the sampling frequency of acquiring the DOS data is $100.000s^{-1}$, one can acquire 200 points during the residence time and 75 points within the transit time. This means that the chord length can be obtained with 0.5% and the velocity with 1.33% resolution, respectively.

Comparison of LES with PIV and DOS for different flow conditions

In the case of *naturally-developing flows*, the following quantities calculated by LES and measured by PIV or DOS can be compared:

- Time-averaged, space-filtered phase velocities and bubble densities (void fraction, bubble concentration);
- Fluctuations of the filtered velocity components;
- Standard deviation and variance of the filtered velocity components;
- Correlations of space-filtered quantities $\overline{\tilde{f}_i \cdot \tilde{f}_j}$ that represent e.g. large-scale contributions to measured stresses.

In the case of *periodically triggered flows*, the following quantities can be compared:

- Phase-averaged quantities:

$$\{F\}_\varphi = \frac{1}{K} \cdot \sum_{k=0}^{K-1} F(t_o + k \cdot \Delta T + \tau) = \overline{F} + f_{coh}(\varphi); \quad \varphi = 2 \cdot \pi \cdot \frac{\tau}{\Delta T}$$

- Standard deviation and variance of incoherent, filtered parts;
- Correlations of phase-averaged, space-filtered quantities $\left\{ \tilde{f}_i \cdot \tilde{f}_j \right\}_\varphi$ that, in general, represent filtered, coherent and incoherent contributions to time-dependent measured stresses.

General conclusion on comparability of DOS, PIV and LES results

It is recommended to select equal time windows (time steps) and IAs (mesh sizes) in experiments and numerical analyses, respectively, to generate comparable results. The details of the techniques used in experiments and of the numerical and modelling methods of LES will, however, always give rise to differences between experimental and numerical results, disregarding effects of imperfect knowledge of simulation of experimental conditions.

4 Bubbly jet flow conditions

4.1 Working principle of the injector

The gas/liquid injector presented in Figure (4.2) was developed by running a series of experiments to determine the optimal configuration of tubes and capillaries for forming bubbles with uniform size in the range between 1 and 4mm in co-currently upward-flowing liquid [42]. In order to produce the bubbly jet with uniform but variable bubble sizes, injectors with one and four capillaries were developed and tested in a small experimental set-up presented in Appendix A.

Bubbles are formed by continuously injecting air (AF) through the capillaries into the co-currently flowing water (i.e. the internal liquid flow-ILF). The jet flow is formed afterwards by adding the second liquid flow (i.e. the external liquid flow -ELF). This configuration enables controlling and adjusting the flow characteristics which include liquid-phase velocity and turbulence as well as bubble size and void fraction.

A schematic of the bubbly jet production is presented in Figure (4.1).

4.2 Design and geometrical characteristics of the gas/liquid injector

As shown in Figure (4.2), the injector contains three chambers for air injection through the capillaries, water injection into the tubes and water injection into the space outside the tubes constrained by a cylindrical or conical shroud called jet nozzle. The main dimensions and compositions are:

- Inlet diameter of the jet nozzle: $D_1 = 90mm$,
- Exit diameter of the jet nozzle: $D = 40mm; 60mm; 90mm$,
- Contraction ratios: $CR = \frac{D_1^2}{D^2} = 5.06; 2.25; 1$,
- Diameter of water tubes: $d_{to}/d_{ti} = 4.0/3.4mm$,
- Diameter of capillaries: length of the first part 79mm and $d_{nio}/d_{nii} = 0.4/0.2mm$; length of the exit part 51mm and $d_{neo}/d_{nei} = 1.0/0.6mm$ (Figure (4.3)),
- Number of tubes and capillaries: 39 (Figure (4.4)).

The effects of dimensions, such as diameter of tube and capillary, length of tube and capillary, together with liquid velocity inside the tube (internal liquid flow), air flow rate and external liquid flow rate, on bubble diameters and shapes were experimentally investigated. Finally, a tube-capillary configuration (Figure (4.3)) was chosen that avoids unstable bubble formation.

4.3 Parameters and flow conditions in the injector

- *Liquid flow rate inside the tubes (Q_{Lin}):*

The liquid velocity inside the tubes (V_{Lin}) affects the bubble size, i.e. with increasing liquid velocity bubbles become smaller. The velocity range in which uniform bubbles could be

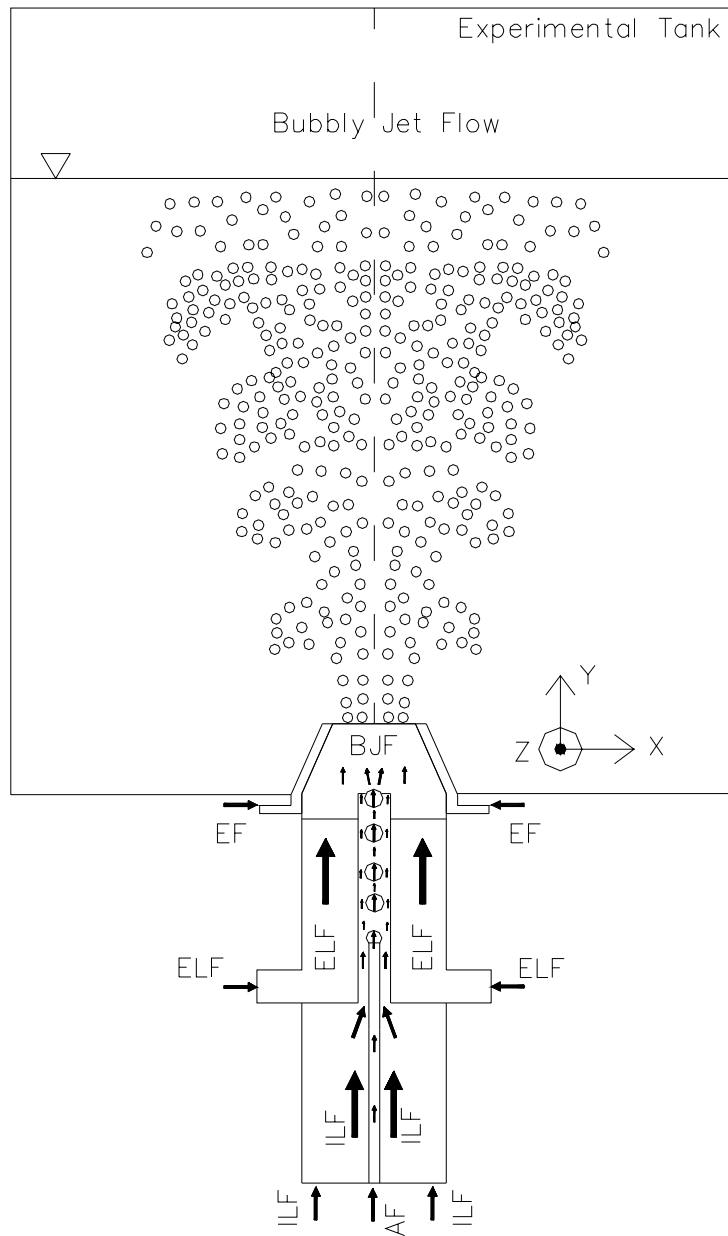


Figure (4.1): Schematic of bubbly jet production. The injector shown at the bottom at a much larger scale has 39 injection capillaries (only one is shown).

produced in the experiments with one- and four-capillary injectors extended from about 0.01 up to 1m/s, which corresponds to a water flow rate range in the 39 tubes of $Q_{Lin} = 0.3$ to $Q_{Lin} = 21.24l/min$. The experiments with the four-capillary injector showed that zero liquid velocity inside the tubes leads to a nonsymmetric condition with air backflow in one of the tubes. Bubbles then go down into the inlet chamber of the liquid, where they can be trapped. In order to avoid this, a minimum internal liquid flow inside the tubes is used in all tests.

● *External liquid flow rate (Q_{Lea}):*

This parameter mainly controls the jet liquid velocity and void fraction. It must be large enough to avoid bubble trapping as well as coalescence downstream of the tube exits. It does not affect the bubble size.

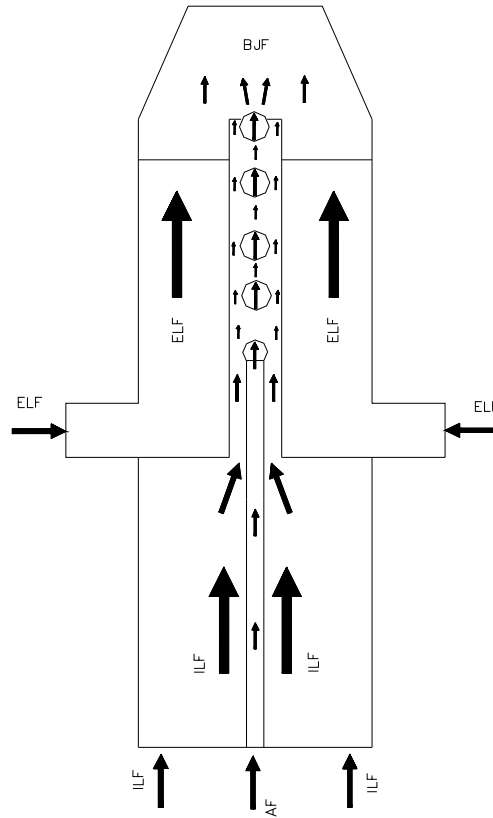


Figure (4.2): Working principle of injector (ELF-External Liquid Flow, ILF-Internal Liquid Flow, AF- Air Flow, BJF- Bubbly Jet Flow).

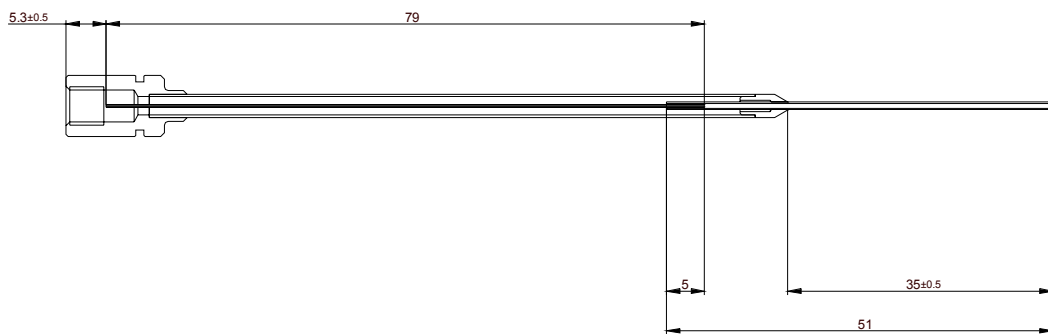


Figure (4.3): Capillary.

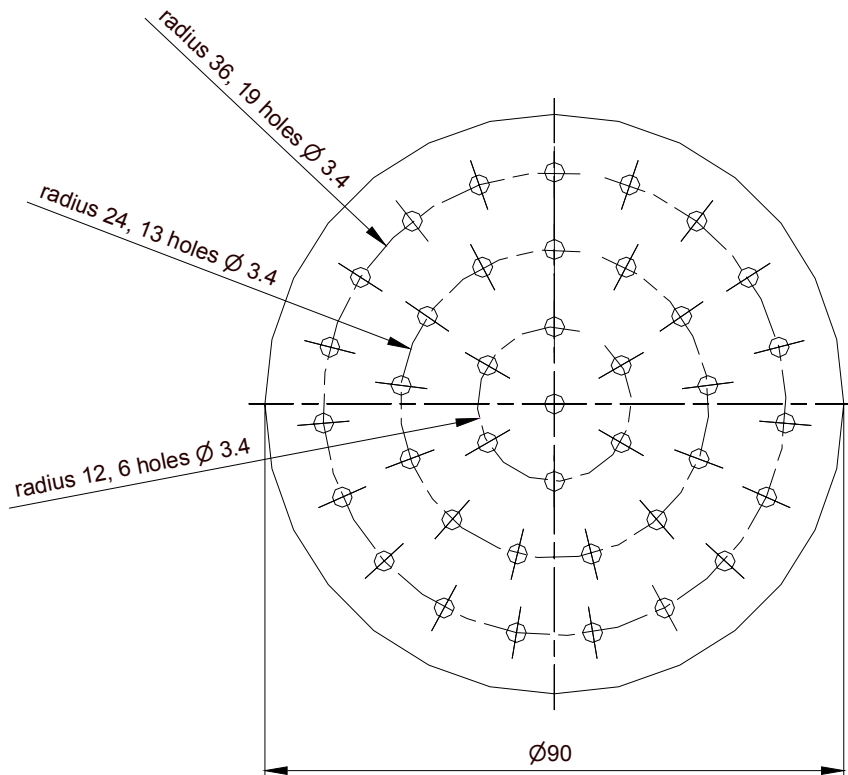


Figure (4.4): Distribution of the tubes for bubble generation in the jet nozzle.

• **Total liquid flow rate at the exit of the jet (Q_{Ltot}):**

The superficial liquid velocity at the exit of the jet (V_{jet}) should be adjustable in a sufficiently wide range. With the proposed design, it extends from a minimum value of about $0.01m/s$, corresponding to a Jet Reynolds number of about 500, to a maximum value of about $2m/s$, leading to a Jet Reynolds number of approximately 100000. The minimum liquid velocity at the jet exit is achieved with zero outside liquid flow rate and the minimum liquid flow rate inside the tubes mentioned above. The maximum liquid velocity at the jet exit can be achieved within a range of combinations of inside and outside liquid flow rates in the injector. Since the inside flow rate is determined by the desired bubble size and its maximum is rather small, most of the flow will go outside. The maximum flow rate for the largest D amounts to $7l/s$ at $Re_{jet} = 105000$.

• **Gas flow rate (Q_G):**

Together with the liquid flows, this parameter also controls bubble size and void fraction. It is an important parameter that has to be carefully adjusted in the experiments.

The gas velocities inside the capillaries (V_{Gin}) can be varied between about 0.5 and $33m/s$, corresponding to total gas flow rates between 0.3 and $20Nl/min$. Increasing the gas flow rate beyond certain limits leads to unstable conditions in the injection tubes, i.e. to non-uniform bubble sizes and bubble coalescence.

•*Bubble size (d):*

The bubbles that were produced in the above-mentioned four-capillary injector tests had diameters between about 1 to 6mm, i.e. they belong to the wobbly regime. Bubbles can be distinguished according to the flow regime for single bubbles rising in quiescent water, i.e.

1. laminar flow conditions for $d < 1.5mm$,
2. unsteady (wobbly) flow conditions for $1.5 < d < 6mm$.

•*Void fraction:*

The void fraction of the jet is determined by the gas flow rate and the total liquid flow rate. Since the bubble size is determined by the liquid flow rate in the tubes together with the gas flow rate, a desired combination of bubble size and void fraction is obtained by adjusting the outer flow for a selected gas flow rate. Calculations of the homogenous void fraction (ϵ_h) for operating flow conditions show that, for stable bubbly-flow conditions, a range between very low void fractions of about 0.1% up to 20% and more can be covered. The achievable values are, however, strongly correlated to bubble size and to the liquid velocity at the jet exit.

•*Other parameters:*

The system temperature is kept constant during the experiments in order to control the physical conditions for bubble formation. The possible experimental temperature range lies between about 20 and 25°C.

The absolute pressure of the gas at the exit of the pressure reducer is adjusted to 6bar as recommended to be the working pressure of the gas flow meter.

Measurements can be done in the development and the fully-developed region of the jet, i.e. up to about 1m downstream of the jet exit.

The considerations made above show that the basic adjustable parameters are jet diameter, internal and external liquid flow rate and gas flow rate.

4.4 Flow conditions in the test tank

The experiments have been carried out in single-phase, liquid and bubbly jet flows generated by the injector. Single-phase liquid jet flows consisted of either only external liquid flow or both external and internal liquid flows. Bubbly jet flows are formed by a vertical water jet containing bubbles of variable well-controlled size and volume fraction. The jet is injected into a water volume contained in a large Plexiglas tank to minimize wall effects. Such flows, with constant inlet flow rate of liquid and gas are here called naturally-developing jets. If the jet flow is periodically excited with controllable frequency and amplitude, it is then called triggered jet. The excitation is achieved by periodically modulating the jet shear layer by means of a coaxial water layer (EF) injected close to the jet exit through a separate nozzle (Figure (4.1)). The excitation frequency was limited so that the flow meter could measure the flow variations and should not exceed about 5Hz. In the tests the frequency was varied between 0.5 and 3Hz. Additional details about the experimental installation can be found in Appendix A.

5 Turbulent bubbly jets

In order to improve physical insight into turbulent bubbly jet flows, the experimental investigations are separated into two different approaches.

The first approach is related with experiments that reveal the spatial coherence and interactions between large eddy structures (vortices) that play a very important role in shear or mixing layers and the bubbles that interfere with these structures.

The second approach, which is used here to *explain the physics* of naturally-developing turbulent bubbly jet flow, has been very extensively applied during past decades for the analysis of mostly single-phase flows. This approach considers the statistical properties and the spatial distribution of local stochastic parameters.

5.1 Bubble movement and trapping in large eddy structures and the relevant non-dimensional parameters

The equation of motion for a bubble with neglected Basset and Faxen terms [53], [1], shows that four forces, Buoyancy, Drag, Inertia, and Lift, determine bubble movement.

$$C_m \frac{d\mathbf{V}_B}{dt} = -\mathbf{g} - \frac{3}{4} \cdot \frac{C_d}{d} \cdot |\mathbf{W}| \cdot \mathbf{W} + (1 + C_m) \cdot \frac{D_L \mathbf{V}_L}{Dt} - C_l \cdot [\mathbf{W} \times (\nabla \times \mathbf{V}_L)] \quad (5.1)$$

with

$$\frac{D_L}{Dt} = \frac{\partial ()}{\partial t} + \mathbf{V}_L \cdot \nabla () \quad (5.2)$$

$$\mathbf{W} = \mathbf{V}_B - \mathbf{V}_L \quad (5.3)$$

where \mathbf{V}_L is the liquid velocity, \mathbf{V}_B is the bubble velocity and \mathbf{W} is the relative velocity.

Equation (5.1) contains the added mass coefficient C_m and the lift coefficient C_l . Coefficient C_d is the drag coefficient and d is the bubble diameter. In order to discuss the relative importance of the four forces, Equation (5.1) is made non-dimensional. Thus, \mathbf{V}_B and \mathbf{V}_L are divided by the superficial liquid velocity V_{jet} and W by the terminal bubble velocity V_T in quiescent fluid

$$V_T = \sqrt{\frac{4 \cdot g \cdot d}{3 \cdot C_{dT}}} \quad (5.4)$$

Time is made dimensionless by R/V_{jet} and length by $R = D/2$, where D is the jet diameter. The different normalization of \mathbf{V}_L and \mathbf{W} makes sense because the order of magnitude of these velocities is determined by V_{jet} and V_T , respectively. The normalization of \mathbf{V}_B by V_{jet} is arbitrary.

In this way, the following dimensionless equation is obtained from Equation (5.1):

$$C_m \cdot \frac{d\hat{\mathbf{V}}_B}{d\hat{t}} = -\frac{1}{2 \cdot Fr_{jet}} \cdot \frac{\mathbf{g}}{g} - \frac{1}{Fr_{jet}} \cdot \frac{C_d(Re_B)}{2 \cdot C_{dT}} \cdot \left| \hat{\mathbf{W}} \right| \cdot \hat{\mathbf{W}} + (1 + C_m) \cdot \frac{D_L \hat{\mathbf{V}}_L}{D \hat{t}} - C_l \cdot \frac{1}{\Gamma} \cdot \left[\hat{\mathbf{W}} \times \left(\hat{\nabla} \times \hat{\mathbf{V}}_L \right) \right] \quad (5.5)$$

with

$$\hat{\mathbf{V}}_B = \frac{\mathbf{V}_B}{V_{jet}}; \hat{\mathbf{V}}_L = \frac{\mathbf{V}_L}{V_{jet}}; \hat{\mathbf{W}} = \frac{\mathbf{W}}{V_T}; \hat{t} = \frac{t \cdot V_{jet}}{R} \text{ and } \hat{\nabla} = R \cdot \nabla \quad (5.6)$$

The instantaneous drag coefficient (C_d) can strongly differ from the drag coefficient that corresponds to the terminal rise velocity (C_{dT}) if $|\mathbf{W}|$ is not close to V_T . Instead of C_{dT} one could also use the Bubble Froude number (Fr_b):

$$C_{dT} = \frac{4 \cdot g \cdot d}{3 \cdot V_T^2} = \frac{2}{3} \cdot \frac{2 \cdot g \cdot d}{V_T^2} = \frac{2}{3} \cdot \frac{1}{Fr_b} \quad (5.7)$$

$$\Gamma = \frac{V_{jet}}{V_T} \quad (5.8)$$

denotes the Trapping parameter of the jet shear layer and

$$Fr_{jet} = \frac{V_{jet}^2}{2 \cdot g \cdot R} \quad (5.9)$$

the Jet Froude number with characteristic dimension (R).

The Jet Froude number equals the Froude number of the large vortices, Fr_v , with characteristic diameter δ , downstream at a distance of $4 \cdot D$ from the nozzle exit, where $\delta \approx R$ [6].

$$Fr_v = \frac{V_{jet}^2}{2 \cdot g \cdot \delta} \quad (5.10)$$

Fr_v depends on the distance from the jet exit because of the growth of δ with the downstream distance.

Besides being a function of the Bubble Reynolds number

$$Re_b = \frac{W \cdot d}{\nu} \quad (5.11)$$

C_d and C_{dT} also depend on the physical properties of the fluid (Morton number), the dimensionless bubble diameter (Eötvös number) and on shear-induced bubble deformation [15], [37]. In the range of bubble sizes considered, in the unsteady (wobbly) flow regime, C_{dT} lies between 0.2 and 3 [41].

In general, the terminal bubble velocity in still fluid is a function of the bubble diameter and thermophysical properties of the fluid, as it was presented in [41]. The relevant thermophysical properties of the fluid and the bubble dimension lead to two independent non-dimensional groups, e.g. defined as the Morton number:

$$Mo = \frac{g \cdot \nu^4 \cdot \rho^3}{\sigma^3} \quad (5.12)$$

and the Eötvös or Bond number:

$$Eo = \frac{\rho \cdot d^2 \cdot g}{\sigma} \quad (5.13)$$

The terminal rise velocity or the Bubble Reynolds number Re_T and the corresponding drag coefficient C_{dT} can be expressed as functions of these dimensionless numbers ([41], [5]).

Experimental data on bubble terminal velocities in pure water at $20^\circ C$ ($Mo = 2.722 \cdot 10^{-11}$) have been fitted for two regions:

- the first covers bubble diameters in the range $d = 1.5 - 4mm$ and corresponds to the unsteady flow region ($Re_T > 500$).

The fitting function is given by

$$V_T = 0.6552 - 316.62 \cdot d + 87169.25 \cdot d^2 - 8.506 \cdot 10^6 \cdot d^3 \quad (5.14)$$

where $V_T [m/s]$ and $d[mm]$.

- the second covers bubble diameters in the range $d = 0.1 - 1.5mm$ and lies in the laminar flow region ($Re_T < 500$). Since the experiments have not been performed in this range, the fitting function is not given here.

For a bubble of given size, the remaining parameters Γ , Fr_v and the Jet Reynolds number

$$Re_{jet} = \frac{V_{jet} \cdot D}{\nu} \quad (5.15)$$

determine its movement together with inlet, boundary and geometric conditions. The latter group includes also the ratio between bubble and vortex size

$$\beta = \frac{d}{\delta} \quad (5.16)$$

and triggering conditions for producing coherent vortices.

From Equation (5.5) it can be qualitatively deduced that bubbles can be trapped in the large vortices of the jet if $\Gamma > O(1)$, i.e. inertial forces are larger than lift forces, and for $Fr_v > O(1)$, meaning that buoyancy forces can be balanced by inertial forces. Vortex Froude number and Trapping parameter actually depend on one another by:

$$Fr_v = \frac{V_{jet}^2}{2 \cdot g \cdot \delta} = \frac{V_{jet}^2}{V_T^2} \cdot \frac{V_T^2}{2 \cdot g \cdot d} \cdot \frac{d}{\delta} = \Gamma^2 \cdot Fr_b \cdot \beta \quad (5.17)$$

In a vertical shear layer, the lift forces can drive bubbles to either side of the layer, the direction depending on whether they are strongly deformed or remain spherical [37], which affects the value and sign of C_l , and buoyancy may cause them to leave the large vortices in the vertical direction if $Fr_v \leq O(1)$. The equations, of course, do not contain effects of bubble interactions such as those discussed in [12], and the effect of the void fraction is not considered.

The Stokes number of the bubbles in the large vortices of the jet, defined as the ratio between bubble acceleration time and eddy turnover time,

$$St_T = \frac{\frac{V_{jet}}{\delta}}{\frac{3}{2} \cdot C_{dT} \cdot \frac{V_T}{d}} = \frac{Fr_v}{\Gamma} \quad (5.18)$$

turns out to be given by the Trapping parameter Γ and the Froude number of large vortices Fr_v . Instead of Γ and Fr_v , one could also use St_T and Γ as determining parameters. According to

Equation (5.5) St_T also gives the ratio between lift and buoyancy forces in the large eddies with $\delta \approx R$ and expresses the effect of lift forces on bubble movement in buoyancy-dominated shear layers.

5.1.1 The range of characteristic non-dimensional parameters

The experimental parameters are chosen in such a way that the relative size of the different forces acting on the bubbles and the related non-dimensional groups can be varied in order to investigate their importance. One of the main objectives of this work is to determine the influence and the role of the coherent large structures on the distribution of bubbles in shear layers.

The ranges of the dimensionless groups Fr_{jet} , Γ and St_T are calculated as functions of Re_{jet} and are shown in the subsequent figures for three jet sizes and for a bubble of $2mm$ in diameter, belonging to the unsteady flow regime. The dependency of the parameters on bubble diameter is not very pronounced in the size range considered, because of the moderate change of the terminal rise velocity.

The Jet Reynolds number is varied in a range covering the laminar, transition and turbulent regions. As mentioned before, the range $500 < Re_{jet} < 100000$ can be achieved.

Variation of the parameter Γ also changes the ratio between shear-induced and bubble-induced turbulence in the jet.

Different jet sizes should be used for the following reasons:

- the relative size of the bubbles $\beta = d/\delta$ is an important geometrical parameter for bubble movement in vortices and also plays a role in visualization and application of PIV for bubble velocity measurements,
- the parameters Fr_{jet} and Γ , both of which grow with V_{jet} , should be varied as independently as possible,
- for the injector considered, different jet diameters also mean different inlet conditions (velocity profile, turbulence level).

Fr_{jet} , Γ and St_T ($\delta \approx R$) can be expressed as functions of the Jet Reynolds number as follows:

$$Fr_{jet} = C_{Fr} \cdot Re_{jet}^2 \quad \text{with } C_{Fr} = \frac{\nu^2}{g \cdot D^3} \quad (5.19)$$

$$\Gamma = C_{\Gamma} \cdot Re_{jet} \quad \text{with } C_{\Gamma} = \frac{\nu}{V_T \cdot D} \quad (5.20)$$

$$St_T = C_{St} \cdot Re_{jet} \quad \text{with } C_{St} = \frac{\nu \cdot V_T}{g \cdot D^2} = \frac{\nu}{D \cdot V_T} \cdot \frac{V_T^2}{g \cdot D} \quad (5.21)$$

C_{Fr} , C_{Γ} and C_{St} are also dimensionless and can be expressed in terms of the Bubble Reynolds number for $W = V_T$, the Bubble Froude number $Fr_b = \frac{V_T^2}{2 \cdot g \cdot d}$ and $\beta(\delta = R)$.

Considering the expressions for St_T and Γ , one can easily conclude that an increase of the bubble diameter, which causes a decrease of the terminal velocity, leads to a slight increase of the Trapping parameter and Stokes number, as it is shown in the following diagrams given for a fixed jet diameter.

In the second bubble-size range, the effect of d on V_T , and correspondingly, on Γ and St_T is much greater; these quantities vary by an order of magnitude between $d = 0.1mm$ and $d = 1.5mm$. Finally, the total liquid flow rate Q_L and the shedding frequency f are also related

to the Re_{jet} number. For simplicity, V_{jet} is assumed to be the superficial liquid velocity. It follows for the flow rate that:

$$Q_{Ltot} = C_Q \cdot Re_{jet} \text{ with } C_Q = \frac{\pi \cdot D \cdot \nu}{4} \quad (5.22)$$

The shedding frequency f of the most unstable jet oscillations corresponds to a Strouhal number [6]:

$$St = \frac{D \cdot f}{V_{jet}} \approx 0.3 \quad (5.23)$$

and therefore:

$$f = C_f \cdot Re_{jet} \text{ with } C_f = 0.3 \cdot \frac{\nu}{D^2} \quad (5.24)$$

The range of jet diameters and Reynolds numbers considered allows the condition $f < 15Hz$ imposed by the maximum scanning frequency of the PIV system to be satisfied if $Re_{jet} < 80000$ for the smallest nozzle diameter.

The coefficients of Equations (5.19)-(5.24) and the length scale ratio $\beta(\delta = R)$ are displayed in Table (5.1) for three different nozzle diameters and a fixed bubble size, $d = 2mm$ ($V_T = 0.29m/s$). These coefficients can be used for a quick estimation of dimensionless and controlling parameters during adjustments of flow conditions needed for bubble trapping inside large vortices in cases of naturally-developing jets.

$D[mm]$	C_{Fr}	C_Γ	C_{St}	$C_Q[l/s]$	$C_f[Hz]$	β
40	$1.59 \cdot 10^{-9}$	$8.62 \cdot 10^{-5}$	$1.85 \cdot 10^{-5}$	$3.14 \cdot 10^{-5}$	$1.875 \cdot 10^{-4}$	$1.00 \cdot 10^{-1}$
60	$4.72 \cdot 10^{-10}$	$5.75 \cdot 10^{-5}$	$8.21 \cdot 10^{-6}$	$4.71 \cdot 10^{-5}$	$8.333 \cdot 10^{-5}$	$0.67 \cdot 10^{-1}$
90	$1.40 \cdot 10^{-10}$	$3.83 \cdot 10^{-5}$	$3.65 \cdot 10^{-6}$	$7.07 \cdot 10^{-5}$	$3.704 \cdot 10^{-5}$	$0.44 \cdot 10^{-1}$

Table 5.1: Coefficients used for estimation of main nondimensional parameters.

In order to vary the importance of Fr_{jet} and Γ within a sufficiently wide domain (see Figures 5.1 and 5.2), it would be desirable to select their ranges such that they extend from about 0.1 to 10. In order to fulfil the conditions for bubble trapping inside the large vortices of the most unstable mode, Fr_{jet} and Γ must be greater than about 1. More details on bubble trapping conditions are given in Section 5.1.2.

In the considerations made above, the (homogeneous) void fraction $\varepsilon_h = Q_G/(Q_{Ltot} + Q_G)$ has not been mentioned, since it is not contained in Equation (5.5), although it is an important parameter of the experiments. It determines void feedback and, together with the bubble size, also bubble interaction. Equation (5.5) has to be modified together with the equation for the liquid to include this effect.

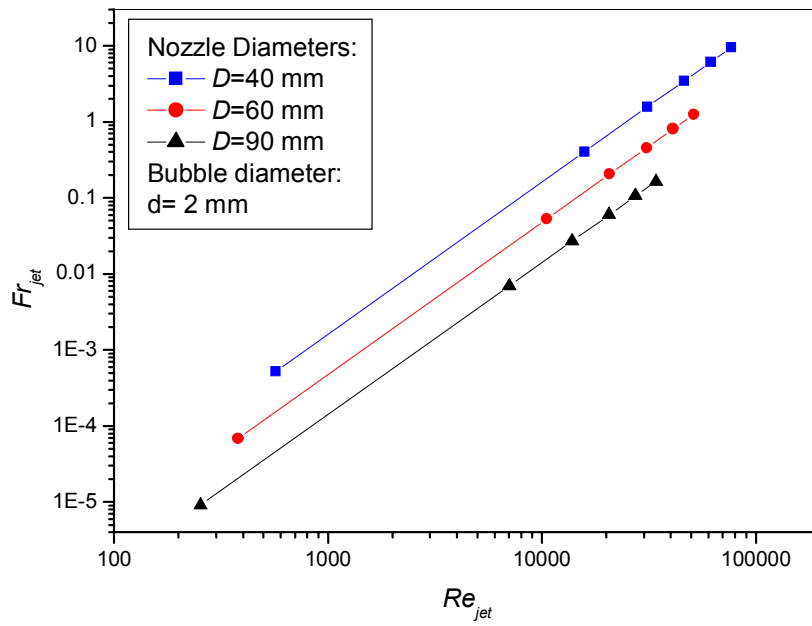


Figure (5.1): Jet Froude number as function of Re_{jet} for three different nozzle diameters.

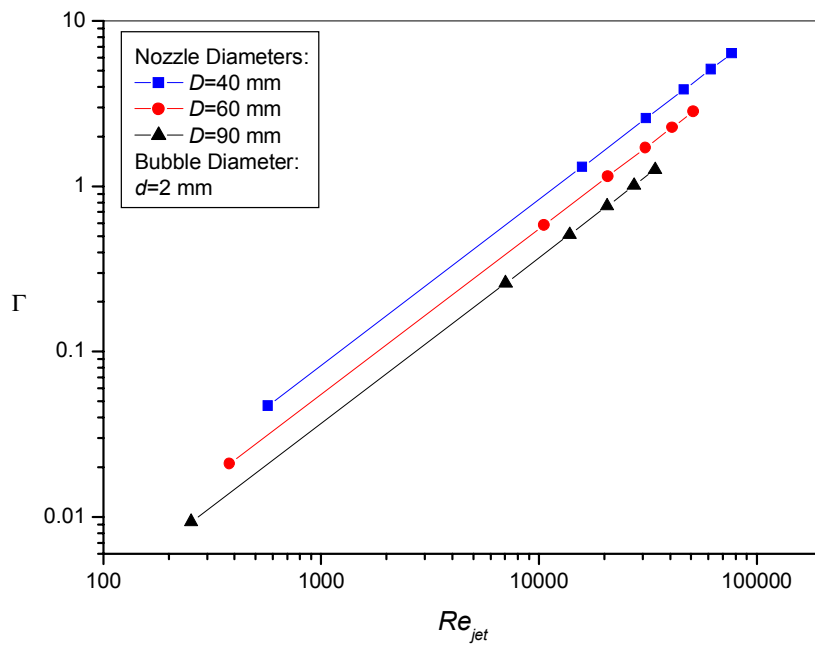


Figure (5.2): Trapping parameter as function of Re_{jet} for three different nozzle diameters.

The void fraction range (see Figure 5.3) that can be covered in the experiments strongly increases with bubble size, so that high void fractions can only be attained for large bubbles, which result from the high gas flow rates. The gas velocity in the needles must be limited in order to avoid non-uniform bubble sizes, and therefore only small void fractions can be produced for small bubble diameters.

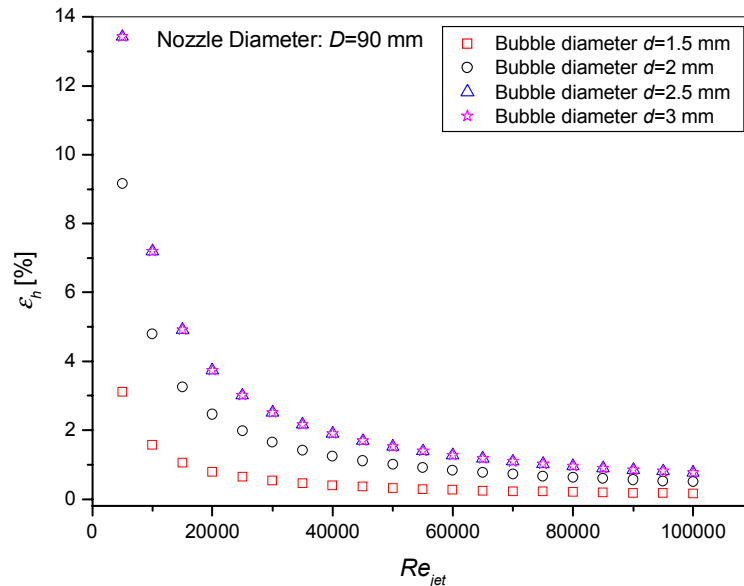


Figure (5.3): Maximum homogeneous void fraction for a nozzle diameter of 90 mm and four different bubble sizes as function of Re_{jet} .

If nonuniform bubble sizes are acceptable, higher void fractions can also be obtained for large Re_{jet} numbers by further increasing the gas flow rate. Even then, the mean bubble size can also be changed by varying the internal liquid flow rate. Taking into account that the terminal bubble velocity for the given bubble size range varies only between $0.25 - 0.35 m/s$, which leads to small changes of the Trapping parameter and Stokes number, effects of different forces acting on bubbles can also be investigated for higher void-fraction jets containing a wider range of bubble sizes.

Conclusions:

- 1) For the laminar and transition range where $Re_{jet} < 10^4$, Fr_{jet} and Γ are small and bubble trapping should not occur. Only for very small bubbles ($< 0.7 mm$) with $V_T < 0.1 m/s$ trapping may become important. For $Re_{jet} > 10^4$, the vortex Froude number and trapping parameter become large enough for trapping, but with $D = 90 mm$ only at about $Re_{jet} = 10^5$ (see Figures 5.1 and 5.2).
- 2) Using a smaller minimum nozzle diameter in order to obtain larger Γ at small Re_{jet} numbers is not recommended because the length scale ratio β becomes rather large. This possibility, can be considered if bubbles with smaller diameters, i.e. $d < 1 mm$, are used during the experimental investigation.
- 3) Reasonable shedding frequencies f and liquid flow rates Q_L are obtained for the range $10^4 < Re_{jet} < 10^5$.
- 4) The range of attainable void fractions strongly increases with bubble size and decreases with

Re_{jet} . The maximum void fractions are rather small for Re_{jet} numbers above 20000. If bubbles are not required to have uniform size, homogeneous void fractions of up to 10% can also be obtained with higher Re_{jet} numbers (see Figure 5.3).

More details about the test matrix for studying naturally-developing jets can be found in Chapter 6.

5.1.2 Bubble trapping condition for "Gaussian" vortex

In order to study interactions between bubbles and large eddies formed in the shear layer and especially bubble trapping phenomena, it is necessary to formulate a simplified condition that should be fulfilled for bubble trapping and to predict the corresponding flow parameters. Obviously, despite the fact that flow conditions for bubble trapping will vary in the flow field, the presented approach can be used to check if the conditions for bubbles reaching an equilibrium position in large vortices are fulfilled.

In this section, a simplified cylindrical vortex with axis normal to the buoyancy direction is considered and the forces acting on a single bubble are formulated. Trapping of the bubble is then defined as the existence of an equilibrium position of the bubble inside the vortex. A more general form of trapping is that of a bubble moving inside a vortex [53], [15].

The large, coherent, toroidal vortices surrounding the jet travel vertically with about half of the mean jet velocity (V_{jet}) [6]. For simplicity these toroidal objects are replaced by cylindrical vortices with axis normal to the $x - y$ plane in Figure (5.4).

Their vorticity ω_z has approximately Gaussian shape, i.e.:

$$\omega_z = \omega_o \cdot e^{-\frac{r^2}{R_v^2}} \quad (5.25)$$

With

$$\omega_z = \frac{1}{r} \cdot \frac{\partial}{\partial r} (r \cdot U_\varphi) \quad (5.26)$$

results

$$U_\varphi = \frac{1}{r} \int_0^r \omega_z \cdot r' \cdot dr' = \frac{\omega_o \cdot R_v^2}{2 \cdot r} \cdot \left(1 - e^{-\frac{r^2}{R_v^2}}\right) \quad (5.27)$$

where $R_v = \frac{D_v}{2}$ is the effective radius of the vortex shown in Figure (5.4). This Gaussian vortex satisfies the Navier Stokes equations for temporally increasing R_v^2 and decreasing ω_o .

As mentioned before, the four forces, Buoyancy (**B**), Drag (**D**), Inertia (**I**), and Lift (**L**), determine bubble movement in the flow field (see Figure (5.4)).

The radial components of **L**, **I**, **B** are

$$L_r = C_l \cdot U_\varphi \cdot \omega_z = C_l \cdot \frac{\omega_o \cdot R_v^2}{2 \cdot r} \cdot \left(1 - e^{-\frac{r^2}{R_v^2}}\right) \cdot \omega_o \cdot e^{-\frac{r^2}{R_v^2}} \quad (5.28)$$

$$I_r = -(1 + C_m) \cdot \frac{U_\varphi^2}{r} = -(1 + C_m) \cdot \frac{\omega_o^2 \cdot R_v^4}{4 \cdot r^3} \cdot \left(1 - e^{-\frac{r^2}{R_v^2}}\right)^2 \quad (5.29)$$

$$B_r = g \cdot \cos\left(\varphi - \frac{\pi}{2}\right) = g \cdot \sin \varphi \quad (5.30)$$

Neglecting the time dependence of the vortex shape, the following condition must be fulfilled at an equilibrium position of the bubble inside the vortex,

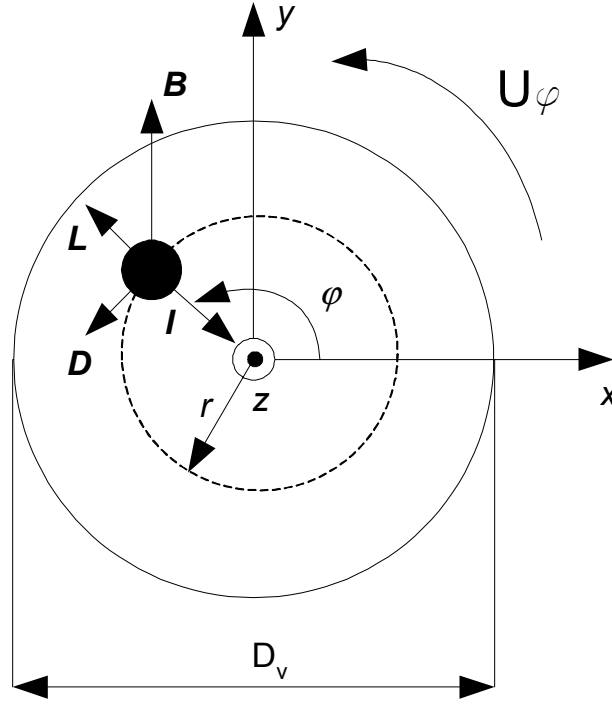


Figure (5.4): Forces acting on a single bubble in a vortex.

$$L_r + I_r + B_r = 0 \quad (5.31)$$

which results in

$$\sin \varphi = (1 + C_m) \cdot \frac{\omega_o^2 \cdot R_v^4}{4 \cdot r^3 \cdot g} \cdot \left(1 - e^{-\frac{r^2}{R_v^2}}\right)^2 - C_l \cdot \frac{\omega_o^2 \cdot R_v^2}{2 \cdot g \cdot r} \cdot \left(1 - e^{-\frac{r^2}{R_v^2}}\right) \cdot e^{-\frac{r^2}{R_v^2}} \quad (5.32)$$

Similarly, the azimuthal components are

$$B_\varphi = g \cdot \cos \varphi \quad (5.33)$$

$$D_\varphi = \frac{3}{4} \cdot \frac{C_d}{d} \cdot U_\varphi^2 = \frac{3}{4} \cdot \frac{C_d}{d} \cdot \frac{\omega_o^2 \cdot R_v^4}{4 \cdot r^2} \cdot \left(1 - e^{-\frac{r^2}{R_v^2}}\right)^2 \quad (5.34)$$

and with $\frac{3}{4} \cdot \frac{C_d}{d} = \frac{g}{V_T^2}$:

$$D_\varphi = \frac{g}{V_T^2} \cdot \frac{\omega_o^2 \cdot R_v^4}{4 \cdot r^2} \cdot \left(1 - e^{-\frac{r^2}{R_v^2}}\right)^2 \quad (5.35)$$

For equilibrium

$$B_\varphi + D_\varphi = 0 \quad (5.36)$$

and therefore

$$\cos \varphi = -\frac{\omega_o^2 \cdot R_v^4}{4 \cdot V_T^2 \cdot r^2} \cdot \left(1 - e^{-\frac{r^2}{R_v^2}}\right)^2 \quad (5.37)$$

Rearrangement of Equations (5.32) and (5.37) gives

$$\sin \varphi = \frac{\omega_o^2 \cdot R_v}{4 \cdot g} \cdot f_1\left(\frac{r}{R_v}\right) \quad (5.38)$$

$$-\cos \varphi = \frac{\omega_o^2 \cdot R_v^2}{V_T^2} \cdot f_2\left(\frac{r}{R_v}\right) \quad (5.39)$$

with

$$f_1\left(\frac{r}{R_v}\right) = \frac{R_v}{r} \cdot \left(1 - e^{-\frac{r^2}{R_v^2}}\right) \left[(1 + C_m) \cdot \frac{R_v^2}{r^2} \cdot \left(1 - e^{-\frac{r^2}{R_v^2}}\right) - 2 \cdot C_l \cdot e^{-\frac{r^2}{R_v^2}} \right] \quad (5.40)$$

$$f_2\left(\frac{r}{R_v}\right) = \frac{R_v^2}{4 \cdot r^2} \left(1 - e^{-\frac{r^2}{R_v^2}}\right)^2 \quad (5.41)$$

Equilibrium points must lie at $\frac{r}{R_v} < \frac{r_1}{R_v}$ where the function $f_1\left(\frac{r}{R_v}\right)$ has its maximum.

The general trapping criterion can be obtained by noting that

$$\sin^2 \varphi + \cos^2 \varphi = 1 \quad (5.42)$$

i.e.

$$\frac{\omega_o^4 \cdot R_v^2}{16 \cdot g^2} \cdot f_1^2\left(\frac{r}{R_v}\right) + \frac{\omega_o^4 \cdot R_v^4}{V_T^4} \cdot f_2^2\left(\frac{r}{R_v}\right) = 1 \quad (5.43)$$

The parameters

$$Fr_\omega = \frac{\omega_o^2 \cdot R_v}{4 \cdot g} \text{ and } \Gamma_\omega = \frac{\omega_o \cdot R_v}{V_T} \quad (5.44)$$

are again related by:

$$Fr_\omega = \frac{\omega_o^2 \cdot R_v^2}{4 \cdot R_v \cdot g} = \Gamma_\omega^2 \cdot Fr_b \cdot \beta \quad (5.45)$$

where $Fr_b = \frac{V_T^2}{2 \cdot g \cdot d}$ is the Bubble Froude number and $\beta = \frac{d}{2 \cdot R_v}$ the length scale ratio. Fr_b can be replaced with $\frac{3}{2 \cdot C_{dT}}$.

The suffix used for the quantities Fr_ω and Γ_ω implies that these quantities are not equal to the quantities Fr_v and Γ presented in Section 5.1.

From Equations (5.43) to (5.45):

$$\Gamma_\omega = \left(\frac{1}{Fr_b^2 \cdot \beta^2 \cdot f_1^2\left(\frac{r}{R_v}\right) + f_2^2\left(\frac{r}{R_v}\right)} \right)^{1/4} \quad (5.46)$$

$$Fr_\omega = \frac{Fr_b \cdot \beta}{\left(Fr_b^2 \cdot \beta^2 \cdot f_1^2\left(\frac{r}{R_v}\right) + f_2^2\left(\frac{r}{R_v}\right) \right)^{1/2}} \quad (5.47)$$

The minimum values for Γ_ω and Fr_ω are obtained if the allowable maximum value for $\frac{r}{R_v}$ is used because, for $C_l = C_m = 0.5$, the functions f_1 and f_2 have their maxima at $\frac{r_1}{R_v} = 1.027$ and $\frac{r_2}{R_v} = 1.121$, respectively. For simplicity, $f_1\left(\frac{r}{R_v} = 1\right)$ and $f_2\left(\frac{r}{R_v} = 1\right)$ are now used to calculate the minima of Γ_ω and Fr_ω that are required for trapping. The results are plotted in

Figure (5.5) as functions of $Fr_b \cdot \beta$. These results are used for quantifying the bubble trapping condition inside large vortices at different locations in the flow field. Experimental results are presented in Chapter 8.

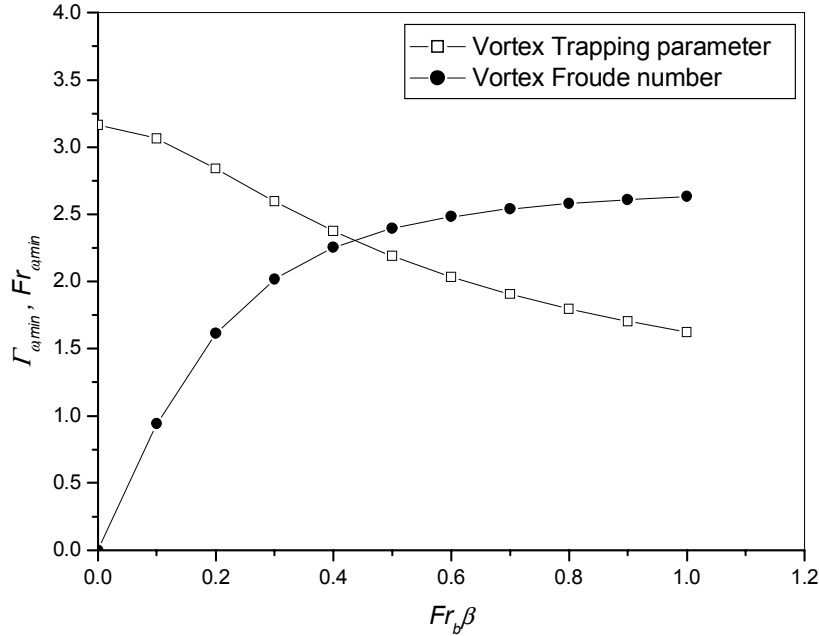


Figure (5.5): Minimum Vortex Trapping parameter and Vortex Froude number as functions of $Fr_b \cdot \beta$ for $C_l = C_m = 0.5$.

The trapping condition $\Gamma_{\omega} > 2$ [53] simplifies the exact bubble-trapping requirement, which depends on bubble and vortex size. The condition can be expressed in terms of both numbers, Γ_{ω} or Fr_{ω} .

With the definition of Γ_{ω} (5.44) follows for the minimum value of $\omega_{o, \min}$ required for trapping a bubble inside a Gaussian vortex:

$$\omega_{o, \min} = \Gamma_{\omega, \min} \cdot \frac{V_T}{R_v} \quad (5.48)$$

Figure (5.6) shows $\omega_{o, \min}$ as a function of the bubble diameter and the vortex radius for water at 20°C and bubbles in the wobbly regime.

Since the vorticity of the liquid phase for different positions of the vortex structures in the flow field can be directly estimated from PIV measurements, the data presented in Figure (5.6) for given bubble and vortex size can be used for quickly estimating whether the conditions for bubble trapping are fulfilled or not.

It was mentioned in Chapter 5 that C_d and C_l depend on shear and bubble deformation, so that the trapping condition ((5.46)-(5.47)) could become quite different.

Furthermore, because the real velocity field is more complicated than that used for deriving the trapping criterion, the results obtained in this section can only be approximately applied. In order to discuss the effect of changing C_l , the approximate range within which C_l may vary has to be estimated. According to [15] C_l lies between about 0.2 and 0.35 inside a vortex.

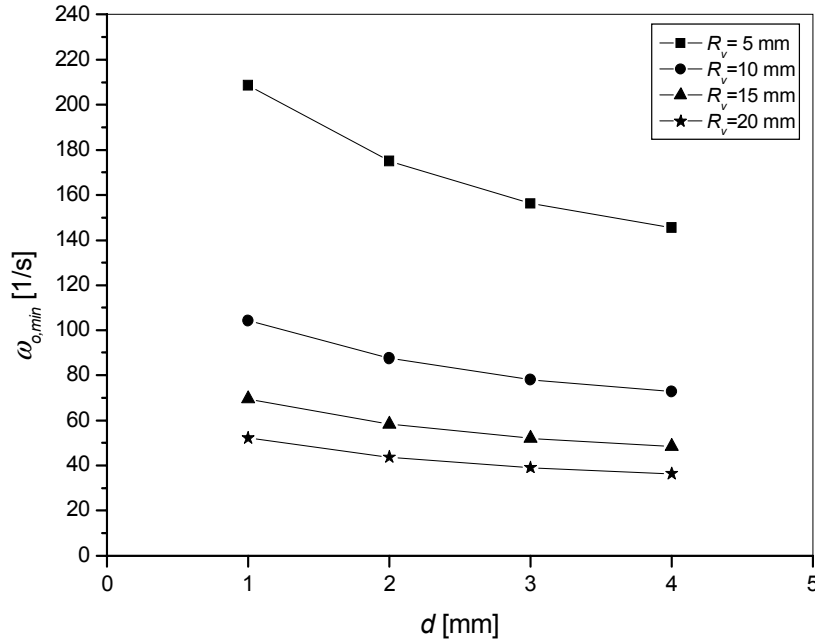


Figure (5.6): The minimum value of ω_o required for trapping a single bubble with diameter d inside a Gaussian vortex.

Experimental data obtained in simple shear air-water systems [61] show that the lift coefficient of small bubbles ($0 < d < 5\text{mm}$) takes values ranging from 0 to 0.3, whereas for big bubbles ($d > 6\text{mm}$) the lift coefficient range is from 0 to -0.3 . In order to illustrate the effect of different values of C_l on the Trapping parameter and the Vortex Froude number a range of $-0.25 \leq C_l \leq 0.5$ is chosen.

To obtain the results presented in Figure (5.7) it has been taken into account that the radius r_1 where the function f_1 reaches its maximum decreases with diminishing C_l . The diagram shows that for the negative ($C_l = -0.25$) or vanishing ($C_l = 0$) lift force, bubbles can be more easily trapped than in the case of $C_l = +0.5$.

The effect of shear on C_d can be determined based on results in [35], where it is stated that the drag coefficient increases with shear, i.e.

$$C_d(Re_b, S) = C_d(Re_b, 0) \cdot (1 + 0.55 \cdot S^2) \quad (5.49)$$

where S is the nondimensional shear rate in case of plane shear

$$S = \frac{\partial V_L}{\partial x} \cdot \frac{d}{|W|} \quad (5.50)$$

At an equilibrium position inside a Gaussian vortex, the following results in cylindrical geometry are obtained [56]:

$$S = r \cdot \frac{\partial}{\partial r} \left(\frac{U_\varphi}{r} \right) \cdot \frac{d}{U_\varphi} \quad (5.51)$$

i.e. with (5.27)

$$S = \frac{d}{2 \cdot R_v} \cdot \frac{4 \cdot R_v}{r} \cdot \left[\frac{r^2}{R_v^2} \cdot \frac{e^{-\frac{r^2}{R_v^2}}}{\left(1 - e^{-\frac{r^2}{R_v^2}}\right)} - 1 \right] \quad (5.52)$$

The absolute value of S increases almost linearly with $\frac{r}{R_v}$ and reaches a value of $1.672 \cdot \beta$ at $\frac{r}{R_v} = 1$. Thus, the maximum value of the correction factor for C_d is:

$$1 + 1.54 \cdot \beta^2$$

For a bubble with $d = 2mm$ inside a vortex $R_v = 10mm$ (i.e. $\beta = 0.1$) one obtains

$$(1 + 0.55 \cdot S^2) < 1.0154$$

and for a bubble with $d = 6mm$ (i.e. $\beta = 0.3$)

$$(1 + 0.55 \cdot S^2) < 1.138$$

The correction factor thus does not significantly change the trapping condition, but it facilitates trapping in all cases.

The discussion of flow-induced change of C_l and C_d thus shows that bubble deformation and shear tend to support trapping, although the vortex region where force equilibrium can exist decreases if C_l is reduced.

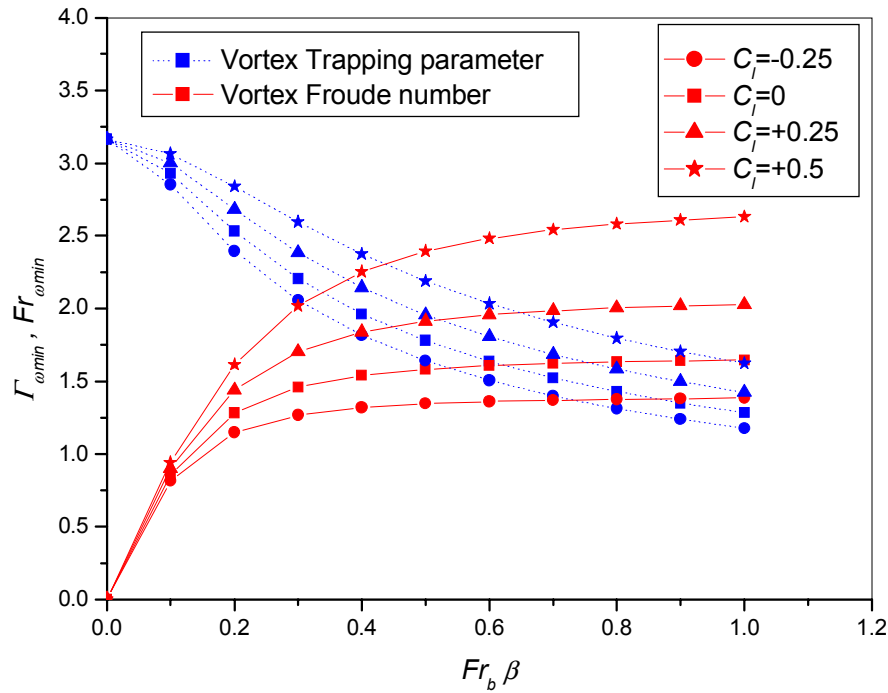


Figure (5.7): Effect of lift coefficient on the Vortex Trapping parameter and the Vortex Froude number.

5.2 Development of turbulent bubbly jets, relevant non-dimensional parameters and characteristic regions

The bubbly jet formed in the bubble injector is directed upward and injected into stagnant water. The flow can be classified as a turbulent two-phase jet, which means that both an initial momentum and a buoyancy flux are present at the nozzle exit. These quantities can be systematically varied in order to achieve more plume-like or jet-like flow conditions. Obviously, the bubbly jet, by its nature, has also an initial volume flux.

In any kind of bubbly jet flow, the momentum flux increases downstream because of buoyancy and the bubbly jet ultimately behaves like a bubbly plume. This means that a transition region that separates the region of inertia-dominated flow from the region where buoyancy dominates, i.e. the jet-like and plume-like regions in jet flow, occurs within a certain vertical range downstream of the jet exit. The boundaries of the range can be defined by means of a Richardson number, initially introduced by Morton [50]. This dimensionless number has been widely used in case of turbulent single-phase buoyant jets, and it can be applied to turbulent bubbly jets. The Richardson number (Ri) and the densimetric Froude number (Fr), that is also used to characterize jets, are defined at the jet exit as follows [50] :

$$Ri_0 = \frac{Q_0 \cdot B_0^{1/2}}{M_0^{5/4}} \quad (5.53)$$

$$Fr_0 = \frac{M_0 \cdot V_{jet}}{B_0 \cdot D} \quad (5.54)$$

where Q_0 is the initial volume flux, B_0 is the initial buoyancy flux, M_0 is the initial momentum flux, D the size of the nozzle and V_{jet} the superficial water velocity.

The Richardson number and the densimetric Froude number characterize the degree of jet-like or plume-like behavior of the initial flow, since they represent the relative importance of inertial and buoyancy forces at the inlet.

The initial buoyancy flux B_0 is defined as:

$$B_0 = g \cdot \frac{\Delta\rho_0}{\rho_{ref}} \cdot Q_0 \quad (5.55)$$

According to references [50] and [16], the density deficiency must be scaled with the density (ρ_{ref}) of the source fluid. For the bubbly jet considered here as a mixture of air and water, $\rho_{ref} = \rho_{BJ} = (1 - \varepsilon) \cdot \rho_L + \varepsilon \cdot \rho_G$, where ρ_{BJ} is the mixture density. In other references [46], [60], the scaling density is the density of the ambient fluid, which is in our case the water density ρ_L .

Here, the second definition is preferred because the quantities Q , M and B must also be formulated as integrals over the radial coordinate r at any downstream position, where the mixture density is a function of r . Because of the small values of ε , the difference between the two approaches is not important; indeed:

$$\frac{\Delta\rho}{\rho_L} = \frac{\rho_L - \rho_{BJ}}{\rho_L} = \frac{\rho_L - [(1 - \varepsilon) \cdot \rho_L + \varepsilon \cdot \rho_G]}{\rho_L} = \frac{\varepsilon \cdot (\rho_L - \rho_G)}{\rho_L} \approx \varepsilon \quad (5.56)$$

as $\rho_G \ll \rho_L$, and

5.2 Development of turbulent bubbly jets, relevant non-dimensional parameters and characteristic regions

$$\frac{\Delta\rho}{\rho_{BJ}} = \frac{\rho_L - \rho_{BJ}}{\rho_{BJ}} = \frac{\rho_L - [(1-\varepsilon) \cdot \rho_L + \varepsilon \cdot \rho_G]}{(1-\varepsilon) \cdot \rho_L + \varepsilon \cdot \rho_G} = \frac{\varepsilon \cdot (\rho_L - \rho_G)}{(1-\varepsilon) \cdot \rho_L} \approx \varepsilon \quad (5.57)$$

for $\varepsilon \ll 1$.

The fluxes are given as

$$Q_0 = \frac{\pi}{4} \cdot D^2 \cdot V_{jet} \quad (5.58)$$

$$M_0 = \frac{\pi}{4} \cdot D^2 \cdot \frac{V_{jet}^2}{(1-\varepsilon)} \quad (5.59)$$

$$B_0 = \frac{\pi}{4} \cdot D^2 \cdot \varepsilon \cdot g \cdot V_{jet} \quad (5.60)$$

The Richardson and the densimetric Froude number can then be written as:

$$\begin{aligned} Ri_0 &= \frac{\frac{\pi}{4} \cdot D^2 \cdot V_{jet} \cdot \left(\frac{\pi}{4} \cdot D^2 \cdot \varepsilon \cdot g \cdot V_{jet}\right)^{1/2}}{\left(\frac{\pi}{4} \cdot D^2 \cdot \frac{V_{jet}^2}{(1-\varepsilon)}\right)^{5/4}} = \\ &= \left(\frac{\pi}{4}\right)^{1/4} \cdot D^{1/2} \cdot V_{jet}^{-1} \cdot g^{1/2} \cdot \varepsilon^{1/2} \cdot (1-\varepsilon)^{5/4} \end{aligned} \quad (5.61)$$

$$\begin{aligned} Fr_0 &= \frac{\frac{\pi}{4} \cdot D^2 \cdot \frac{V_{jet}^2}{(1-\varepsilon)} \cdot \frac{V_{jet}}{1-\varepsilon}}{\frac{\pi}{4} \cdot D^2 \cdot \varepsilon \cdot g \cdot V_{jet} \cdot D} = \\ &= \frac{V_{jet}^2}{\varepsilon \cdot (1-\varepsilon)^2 \cdot g \cdot D} \end{aligned} \quad (5.62)$$

$$Fr_0^{-1/2} = \frac{\varepsilon^{1/2} \cdot (1-\varepsilon) \cdot g^{1/2} \cdot D^{1/2}}{V_{jet}} \quad (5.63)$$

Then

$$Ri_0 = \left(\frac{\pi}{4}\right)^{1/4} \cdot Fr_0^{-1/2} \cdot (1-\varepsilon)^{5/4} \quad (5.64)$$

The Richardson number is also related to the previously defined Jet Froude number because:

$$Fr_0 = \frac{V_{jet}^2}{g \cdot D \cdot \varepsilon \cdot (1-\varepsilon)^2} = \frac{Fr_{jet}}{\varepsilon \cdot (1-\varepsilon)^2} \quad (5.65)$$

and thus:

$$Ri_0 = \left(\frac{\pi}{4}\right)^{1/4} \cdot \varepsilon^{1/2} \cdot (1-\varepsilon)^{5/4} \cdot Fr_{jet}^{-1/2} \quad (5.66)$$

Since the two quantities are closely related and the Richardson number can also be directly defined at any downstream level, only the Richardson number will be used in the following.

For the distinction between jet, transition and plume region, the length scale ratio l_M is used [50]:

$$\begin{aligned} l_M &= \frac{M_0^{3/4}}{B_0^{1/2}} = \frac{\left(\frac{\pi}{4} \cdot D^2 \cdot \frac{V_{jet}^2}{1-\varepsilon}\right)^{3/4}}{\left(\frac{\pi}{4} \cdot D^2 \cdot \varepsilon \cdot g \cdot V_{jet}\right)^{1/2}} = \\ &= \left(\frac{\pi}{4}\right)^{1/2} \cdot Ri_0^{-1} \cdot D \cdot \frac{1}{(1-\varepsilon)^{1/2}} \end{aligned} \quad (5.67)$$

Reference [46] presents criteria for the limits of the regions for *turbulent single-phase jets*; no such criteria were found for *turbulent bubbly jets* but possibly the same criteria apply:

$$0 < \frac{y}{D} \cdot Ri_0 < 1, \text{ jet region} \quad (5.68)$$

$$1 < \frac{y}{D} \cdot Ri_0 < 5, \text{ transition region} \quad (5.69)$$

$$5 < \frac{y}{D} \cdot Ri_0 < \infty, \text{ plume region} \quad (5.70)$$

For $Ri_0 < 0.2$, the buoyancy forces begin to influence the jet only downstream of the developing region ($\frac{y}{D} > 5$). However, with $Ri_0 > 1$, the transition from jet to plume already starts at $\frac{y}{D} < 1$. At such values of Ri_0 , buoyancy has a strong influence on the development of the large vortices.

For simplicity, the homogeneous void fraction (ε_h) could be used instead of the void fraction (ε), but a better approximation of the void fraction (marked here as ε_2) is:

$$\varepsilon_2 = \varepsilon_h \cdot \frac{V_{jet}}{V_{jet} + V_T} = \varepsilon_h \cdot \frac{V_{jet}/V_T}{V_{jet}/V_T + 1} = \varepsilon_h \cdot \frac{\Gamma}{\Gamma + 1} = \varepsilon_h \cdot \frac{C_\Gamma \cdot Re_{jet}}{C_\Gamma \cdot Re_{jet} + 1} \quad (5.71)$$

where the parameters Γ , C_Γ and Re_{jet} are defined in the previous section.

With $Fr_{jet} = C_{Fr} \cdot Re_{jet}^2$ (defined in Section 5.1), the Jet Richardson number can be expressed as a function of the Jet Reynolds number:

$$Ri_0 = \varepsilon_h^{1/2} \cdot \left(\frac{C_\Gamma \cdot Re_{jet}}{C_\Gamma \cdot Re_{jet} + 1}\right)^{1/2} \cdot \left(\frac{\pi}{4}\right)^{1/2} \cdot (1 - \varepsilon_2)^{5/4} \cdot \frac{1}{C_{Fr}^{1/2} \cdot Re_{jet}} \quad (5.72)$$

In order to provide an estimate of the local degree of plume-like or jet-like behavior for the flow, the local Richardson number is used [46]:

$$Ri(y) = \frac{Q(y) \cdot B(y)^{1/2}}{M(y)^{5/4}} \quad (5.73)$$

where $M(y)$, $B(y)$ and $Q(y)$ are the estimates of the momentum, buoyancy and volume flux of the mean flow at a distance y from the jet origin.

Assuming axisymmetric flow, the estimates of the mean local fluxes can be obtained by integration of the void fraction and liquid velocity profiles as follows:

$$Q(y) = \int_0^\infty V_L(y, r) \cdot [1 - \varepsilon(r)] \cdot 2\pi r \cdot dr \quad (5.74)$$

5.2 Development of turbulent bubbly jets, relevant non-dimensional parameters and characteristic regions

$$B(y) = \int_0^{\infty} g \cdot V_L(y, r) \cdot \varepsilon(r) \cdot 2\pi r \cdot dr \quad (5.75)$$

$$M(y) = \int_0^{\infty} V_L^2(y, r) \cdot [1 - \varepsilon(r)] \cdot 2\pi r \cdot dr \quad (5.76)$$

Since the void fraction profiles $\varepsilon(r)$ obtained by DOS represent time-averaged quantities, integration should be done using the time-averaged velocity profiles $V_L(y, r)$, as well.

In [46] it is shown that in the three regions defined in Equations (5.68)-(5.70), $Ri(y)$ and $M(y)$ depend very differently on y/l_M . $Ri(y)$, for instance, varies linearly with y/l_M up to $y/l_M \approx 1.5$ and is constant for $y/l_M > 5$.

6 Experimental results for naturally-developing turbulent bubbly jets

In order to improve physical insight and to support numerical analysis, a number of basic experiments in single-phase as well as bubbly flows have been carried out during the past decades. In case of free shear flows, research has been performed on bubbly jets and plane bubbly mixing layers (see Chapter 2). In these tests, the effects of bubble size and concentration on turbulence, velocity and void distributions, shear-layer spreading rates, mixing, characteristic length scales and velocity correlations have been studied. However, these measurements only provide results for statistical properties and the spatial distribution of local stochastic variables.

Single-phase flow

The experiments in single-phase jet flows (for instance presented in [50]) have been mostly conducted in the fully developed regions using mainly experimental techniques such as LDA, HFA and HWA. In the near field of axisymmetric jets, there is a lack of data. Also, no publications could be found in which PIV measurements were compared with LDA or other data in the developing region of single-phase jets. Therefore, one of the objectives of this study was to provide PIV data for the developing region of single-phase jets that could be compared with corresponding data obtained by HWA for an air jet [6]. The main reason for performing experiments in single-phase jet flows was, however, to obtain reference data that could be compared with results for bubbly jets obtained with the same liquid flow rates. In this way the effects of parameters such as void fraction and Jet Reynolds number can be studied.

Range of void fraction and Jet Reynolds number

In order to study the effects of void fraction and Jet Reynolds number, experiments were conducted with two different void fractions of about 1.8 and 3.6%, and essentially three different Jet Reynolds numbers of 17661, 30275 and 42890. This parameter range has been selected based on the considerations in Chapter 5. The two selected void fraction belong to the domains of *weakly dilute* and *dense* bubbly flows, which are of special interest because feedback and bubble-bubble interactions play a significant role.

Effect of bubble size

For the chosen range of void fractions between 1 and 4%, a preliminary examination showed no effect of bubble size (in the range between 2 and 4mm) on turbulent properties of the liquid phase, and therefore no further effort was made to use PIV for this purpose. It will be easier to perform these experiments with dilute bubbly flows ($\varepsilon < 1\%$) using PIV for velocity measurement and simultaneously a visualization technique for bubble concentration determination. Such measurements, however, require advance image analysis for automatic data evaluation. During this study no attempt was made to develop such a sophisticated method because of lack of time. If simultaneous measurements of the stress terms, of the bubble and liquid velocity fields (that appear for instance in the LES model) as well as of the void fraction or bubble concentration fields could be performed by a special experimental technique, it would be possible to correlate data and to validate empirical closure models. An in-depth discussion on classification of turbulence modulation and the effects of the bubble size in two-phase flows was presented in Chapter 2.

6.1 Test matrix

The test matrix presented in Tables 6.1, 6.3 and 6.2 has been prepared after performing a series of preliminary experiments with different injection configurations. The test matrix covers flow regimes that were investigated for naturally-developing and triggered single-phase as well as bubbly jets. Inlet parameters have been varied in order to change the Jet Reynolds number and the void fraction. All parameters were calculated using the equations presented in Chapter 5. The description of the main operational parameters such as Q_{Lin} , Q_{Lex} , Q_G and Q_{Ltot} is presented in Chapter 4.

The following identification letters and numbers in the test matrix indicate different jet flow conditions:

- The letter F is associated with the total liquid flow rate in the nozzle;
- The letter V means "void fraction" and characterizes the chosen void fraction of the bubbly jet flow;
- The abbreviation SP means "Single-phase Jet";
- $SPIWF$ means "Single-phase Jet with Internal Water (Liquid) Flow in the Tubes";
- BJ means "Bubbly Jet".

This nomenclature will be used, for simplification of the further discussions. For example:

- Flow conditions $F3$ include cases $TSPIWF3$, $TSPF3$, $TF3V1$ and $TF3V2$.

The water level in the tank was $1200mm$ and the nozzle diameter $90mm$. Thermophysical properties for water and air are taken at $23^\circ C$. The bubble diameter was in the range between 3 and $4mm$. Other dimensions and configurations of the system are presented in Chapter 4.

Test Name	TF1V1	TF1V2	TF2V1	TF2V2	TF3V1	TF3V2
Q_{Lin} [L/ min]	20	20	20	20	20	20
Q_{Lex} [L/ min]	50	50	100	100	150	150
Q_G [NL/ min]	3	6	3.85	7.6	4.7	9.25
Q_{Ltot} [L/ min]	70	70	120	120	170	170
Re_{jet}	17661	17661	30275	30275	42890	42890
Fr_{jet}	0.04	0.04	0.11	0.11	0.23	0.23
Γ	0.71	0.71	1.21	1.21	1.72	1.72
St_T	0.054	0.054	0.093	0.093	0.132	0.132
ε_h [%]	4.49	8.6	3.4	6.49	2.94	5.63
ε_2 [%]	1.86	3.56	1.86	3.56	1.86	3.56
V_{Lin} [m/s]	0.94	0.94	0.94	0.94	0.94	0.94
V_{Gin} [m/s]	4.99	9.97	6.4	12.63	7.81	15.37
V_{jet} [m/s]	0.18	0.18	0.32	0.32	0.45	0.45
Ri_0	0.7	0.96	0.41	0.56	0.29	0.4
Fr_0	1.97	1.03	6.24	3.24	12.33	6.41
$\frac{y}{D} \cdot Ri_0; \frac{y}{D} = 1.12$	0.78	1.07	0.46	0.63	0.32	0.45
$\frac{y}{D} \cdot Ri_0; \frac{y}{D} = 3.9$	2.73	3.7	1.6	2.2	1.13	1.56

Table 6.1: Test matrix for experimental investigation of bubbly jets.

Test Name	TSPIWF1	TSPIWF2	TSPIWF3
Q_{Lin} [L/ min]	20	20	20
Q_{Lex} [L/ min]	50	100	150
Q_{Ltot} [L/ min]	70	120	170
Re_{jet}	17661	30275	42890
V_{Lin} [m/s]	0.94	0.94	0.94
V_{jet} [m/s]	0.18	0.32	0.45

Table 6.2: Test matrix for experimental investigation of single-phase jets with internal flow rate.

Test Name	TSPF1	TSPF2	TSPF3	TSPF4
Q_{Lin} [L/ min]	0	0	0	0
Q_{Lex} [L/ min]	70	120	170	220
Q_{Ltot} [L/ min]	70	120	170	220
Re_{jet}	17661	30275	42890	55055
V_{jet} [m/s]	0.18	0.32	0.45	0.58

Table 6.3: Test matrix for experimental investigation of single-phase jets without internal flow.

In order to simplify the symbols used for the presentation of experimental results in diagrams and figures, the following nomenclature is used and relate to the symbols used in the text (symbols which come after $\xrightarrow{\text{text}}$) in the next sections and chapters.

PIV experimental results:

- $U_L \xrightarrow{\text{text}} \overline{U}_L$ time-averaged horizontal velocity component of the liquid,
- $V_L \xrightarrow{\text{text}} \overline{V}_L$ time-averaged vertical velocity component of the liquid,
- $Stdev V_L \xrightarrow{\text{text}} (\overline{v_L^2})^{1/2}$ – standard deviation of vertical velocity component of the liquid,
- $Var U_L \xrightarrow{\text{text}} \overline{u_L^2}$ – variance of horizontal velocity component of the liquid,
- $Var V_L \xrightarrow{\text{text}} \overline{v_L^2}$ – variance of vertical velocity component of the liquid,
- k_L – time-averaged kinetic energy of the liquid ($k_L \approx \frac{1}{2} \cdot (Var V_L + 2 \cdot Var U_L)$),
- $V_B \xrightarrow{\text{text}} \overline{V}_B$ time-averaged vertical velocity component of the bubbles,
- ω_z – time-averaged azimuthal vorticity component of the liquid,
- $\langle u \cdot v \rangle_L \xrightarrow{\text{text}} \overline{u_L \cdot v_L}$ – turbulent shear stress component resolved by PIV.

DOS experimental results:

- ε – void fraction,
- N – total number of counted bubbles.

If a quantity represents a phase-averaged value (mostly for results presented in Chapter 8), this will be indicated.

6.2 Single-phase jets

The mean velocities and turbulent quantities for single-phase jets ($V_{jet} = 0.18, 0.32, 0.45, 0.58\text{m/s}$) at $y/D = 1.12$ ($y = 100\text{mm}$), generated without water flow inside the injector tubes, are presented in Figures (6.1 a), (6.1 b), (6.1 c) and (6.1 d). Comparison of the results with data obtained with hot-wire anemometry by Crow [6] for a naturally-developing air jet at $Re_{jet} = 100000$ gives reasonable agreement for V_L (Figure (6.1 a)) and $StdevV_L$ (Figure 6.1 b). Despite the filtering effect of the PIV method, the measured standard deviations are slightly higher, mainly caused by the higher turbulence level at the jet exit (less than 1% in measurements of Crow). The profiles are normalized with the centerline vertical liquid velocity of the single-phase jet ($V_{L,0}$) as used in [6].

The measured turbulence properties of single-phase jets will be tested against well-known simple turbulence models. The results are presented in Section 6.5.

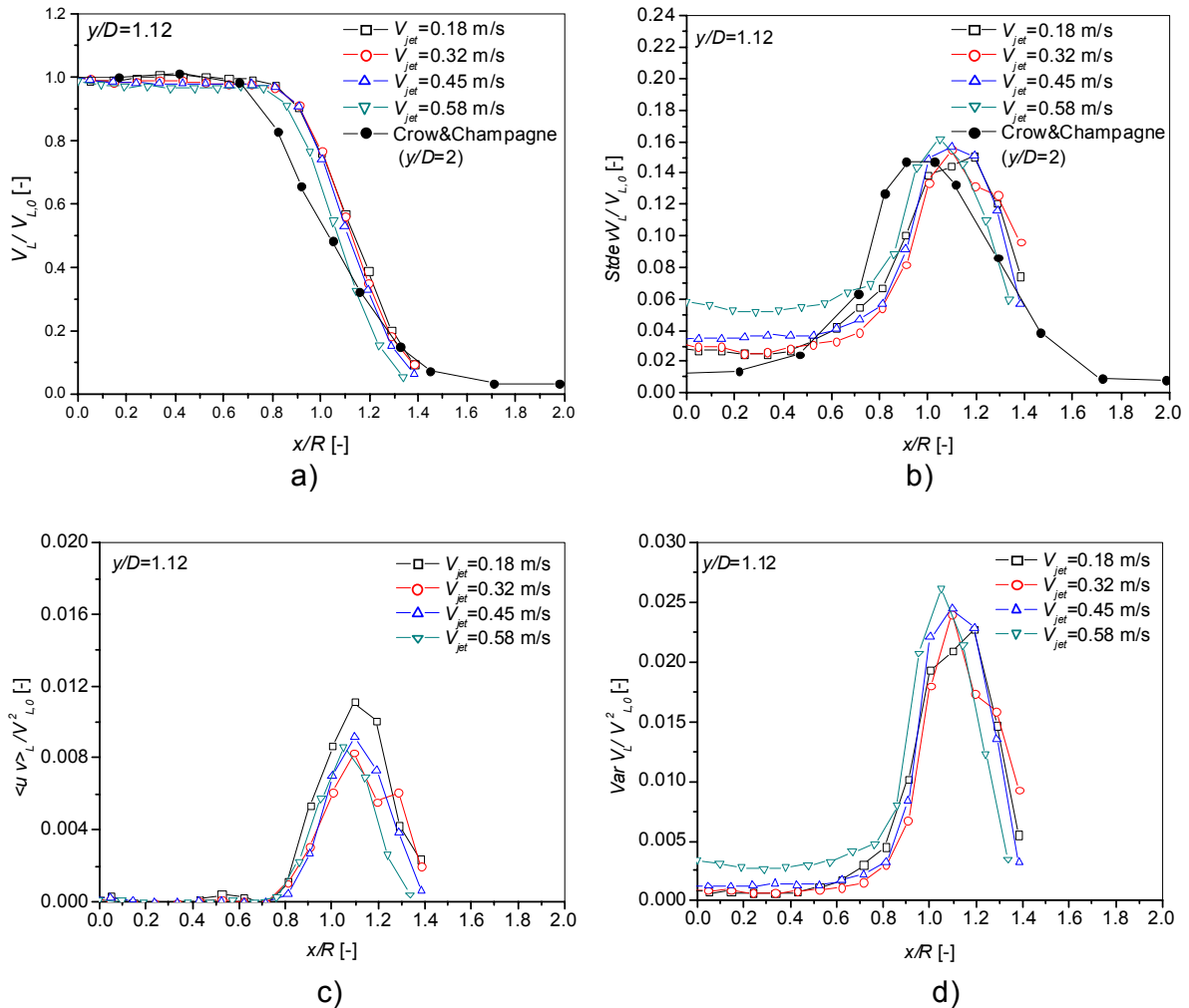


Figure (6.1): Single-phase jets (TSPF1-4): a) Vertical liquid velocity, b) Standard deviation of vertical liquid velocity, c) Turbulent shear stress (PIV) and d) Variance of vertical liquid velocity.

6.3 Effect of bubbles on entrainment and the liquid velocity

The objective of these investigations is to quantify the augmentation of entrainment in the *inertial and transition regions of the bubbly jet* (discussion is given in Chapter 5.2) for the chosen flow regimes. *Most data found in the literature relate to the far field of the flow, where nearly asymptotic conditions prevail.*

Entrainment is defined as:

$$Q_e(y) = Q(y) - Q_{FM} \quad (6.1)$$

where

- the volume flow $Q(y)$ is defined by an area integral over the axial component of the mean liquid velocity at the axial elevation y .

For a single-phase jet

$$Q(y) = \int_0^{\infty} V_L(y, r) \cdot 2\pi r \cdot dr \quad (6.2)$$

For a two-phase jet

$$Q(y) = \int_0^{\infty} V_L(y, r) \cdot [(1 - \varepsilon(r))] \cdot 2\pi r \cdot dr \quad (6.3)$$

- Q_{FM} is the inlet volume flow rate measured by flow meters installed in the water loop.

Normalized flow profiles ($Q_e(y)/Q_{FM}$) for single-phase cases and a bubbly jet (flow conditions *TF3V1* and *TF3V2*) (Figure (6.2)) show that entrainment is indeed enhanced due to the presence of bubbles. In the region of inertia-dominated flow ($y/D = 1.12$), the effect of the bubbles on entrainment is much less pronounced than in the transition region. Nevertheless, the results of the integrals (see Equations (6.2) and (6.3)) presented in Figure (6.2) show that bubbles affect entrainment also in the inertial region of the jet. This effect is, however, obvious close to the nozzle exit only for the highest void fraction (case *TF3V2*). The enhancement is about 40% in the transition region of the bubbly jet at $y/D = 3.9$, where the buoyancy forces start to dominate in the flow.

The velocity profiles are presented in Figures (6.3), (6.4) and (6.5). Obviously, even at $y/D = 1.12$, the vertical liquid velocity profiles in the case of bubbly jets already have a Gaussian shape, which is characteristic of buoyancy-dominated flows.

For single-phase jets, the vertical-velocity profile is flat. The small jets, which are generated by the flow inside the tubes, strongly affect the profiles of the vertical liquid velocity in case of single-phase flow even after one diameter above the nozzle exit (see Figures (6.3) and (6.4)).

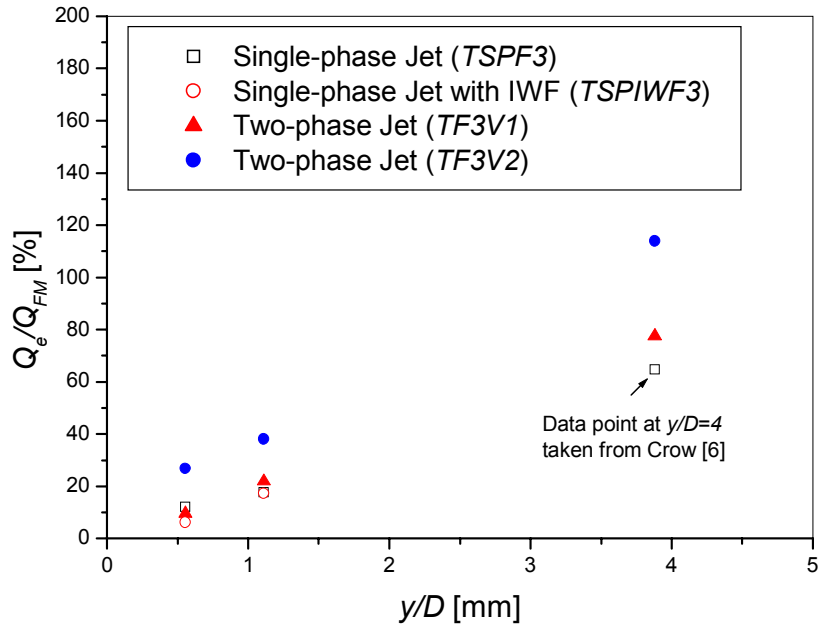


Figure (6.2): Entrainment for tests TF3V1 and TF3V2 ($D=90\text{mm}$).

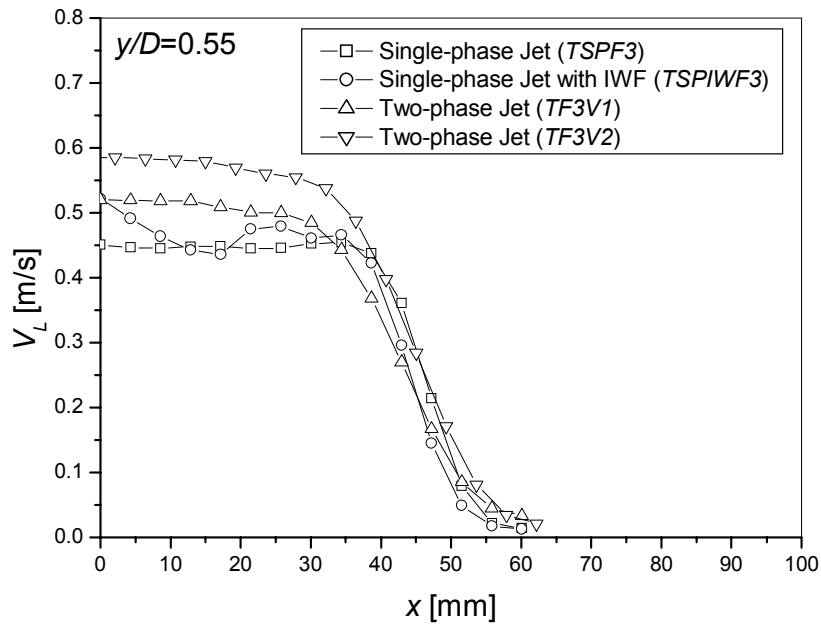


Figure (6.3): Vertical liquid velocity profiles at $y/D=0.55$ ($D=90\text{mm}$).

6.3 Effect of bubbles on entrainment and the liquid velocity

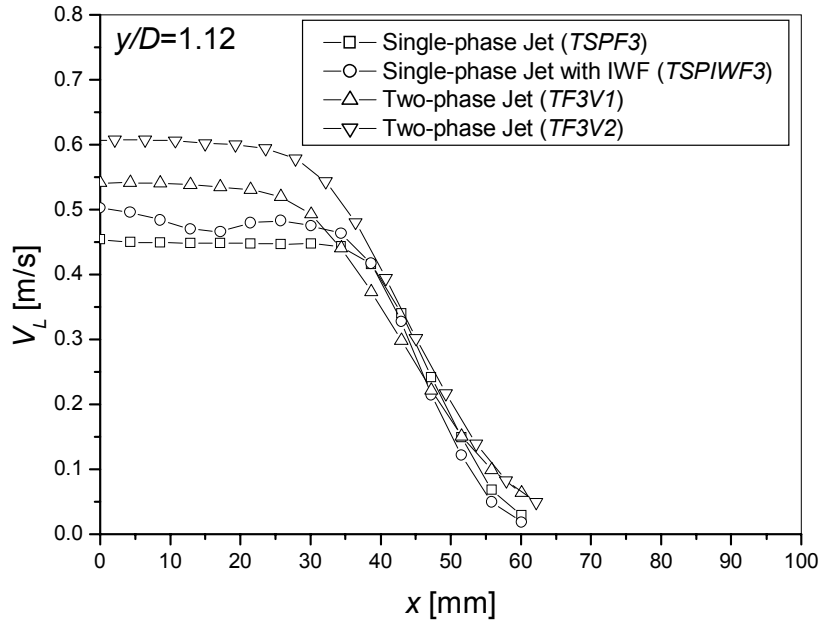


Figure (6.4): Vertical liquid velocity profiles at $y/D=1.12$ ($D=90\text{mm}$).

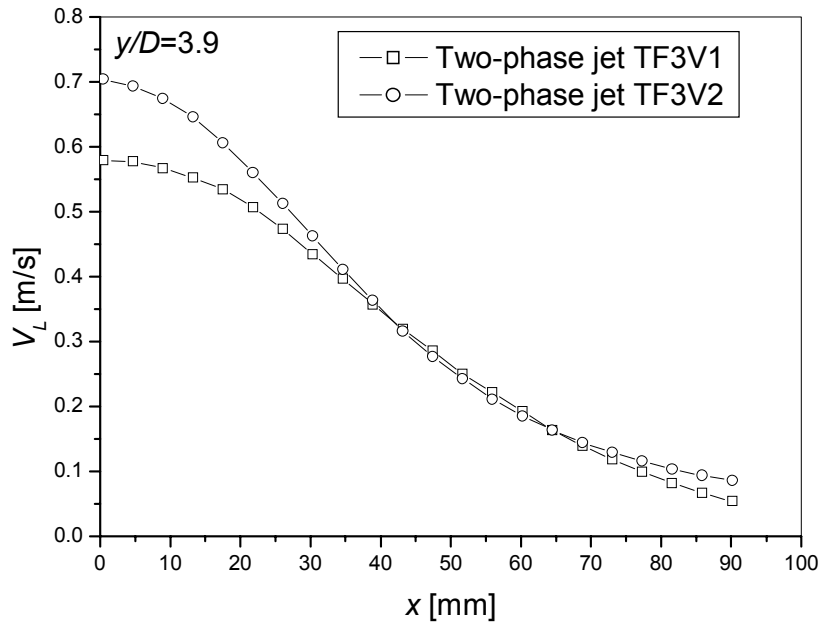


Figure (6.5): Vertical liquid velocity profiles at $y/D=3.9$ ($D=90\text{mm}$).

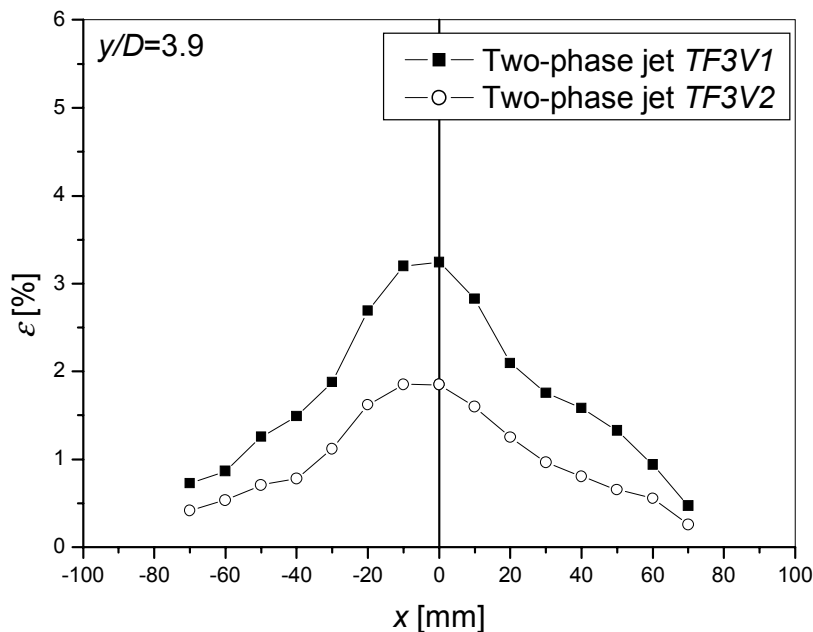


Figure (6.6): Void profiles for tests *TF3V1* and *TF3V2* at $y/D=3.9$ ($D=90\text{mm}$).

Void fraction profiles at $y/D = 3.9$ for cases *TF3V1* and *TF3V2* are compared in Figure (6.6). A discussion of the void fraction peak at the jet centre line and other results on void fraction profiles for test *TF3.V1* are presented in Chapter 7.

Main conclusions and recommendations for future work

In general, the entrainment is obviously affected by the bubbles. The void fraction effect on entrainment varies in different regions of the jet. In order to provide an extensive data base on these effects, the velocity and void fraction profiles for various flow regimes of bubbly as well as single-phase jets for the same inlet liquid flow rate must be measured and integrated for a variety of flow conditions and at a large number of axial levels. At first, local volume, buoyancy and momentum flow can be estimated and, afterwards, the local Richardson number ($Ri(y)$) and length scale ratio (l_M) defined in Chapter 5.2 calculated. Experimental data can be presented in the form that was used by Papanicolaou [46] in case of vertical buoyant single-phase jets. Namely, the local Richardson number ($Ri(y)$) can be plotted versus the local nondimensional quantity (y/l_M). This kind of information for two-phase jets does not yet exist in the literature. In addition, it will be especially interesting to compare entrainment rates and spreading in the plume region of the bubbly jet with analytical, experimental and computational data for the far field of purely buoyancy-induced bubbly plumes, that exist in the pertinent literature (more information could be found in [54] and [28]). Because of time limitations, the required number of measurements and data analyses could not be carried out during this project and only a few exemplary results will be presented in Section 6.4.3.

6.4 Effects of void and Jet Reynolds number on mean and turbulent properties of the liquid

In industrial applications, it is important to design apparatuses and to control flow characteristics in such a way that processes perform optimally. The flow characteristics include liquid-phase velocity distribution and turbulence and gas-liquid interfacial properties for mass, momentum and heat exchange. The results presented here can be helpful for the qualitative understanding of the involved physical processes and the validation of computational tools that are needed in design.

The experiments discussed here have been performed in order to investigate the basic properties of free turbulent bubbly shear flows using a vertical bubbly jet with variable flow parameters such as the Jet Reynolds number and the void fraction. As shown in Section 5.2, the Jet Richardson number and the densimetric Froude number depend on these flow quantities and therefore they influence the degree of jet-like or plume-like behavior.

In order to estimate the effect of the void-fraction on the main flow properties such as: *mean liquid velocity, standard deviation of the liquid velocity, variance of the liquid velocity, kinetic energy and turbulent stress*, experiments have been carried out at constant Jet Reynolds number (i.e. superficial liquid jet velocity), while the void fraction was varied. Also, the turbulent properties at constant void fraction but variable Jet Reynolds number were compared. Furthermore, an attempt was made to keep the bubble diameter constant, as well as possible, while varying the void fraction. This task was very difficult to achieve, because a variation of the gas flow rate affects not only the void fraction but also the bubble size. So, in order to keep the bubble diameter constant at high gas flow rates, the liquid flow rate inside the tubes had to be increased.

Flow conditions

A basic description of the flow conditions in the test tank can be found in Chapter 4. Since very complex phenomena take place during bubble and jet formation in the injector, it is necessary to discuss the effects of the different flows which mix in the injector. First, the flow conditions in the injector as well as in the zone close to the jet exit must be analyzed before the additional effects of bubbles on liquid turbulent properties can be discussed.

The liquid volume flow at the nozzle exit (Q_{FM}), i.e. the superficial averaged liquid velocity at the nozzle exit (V_{jet}) was kept constant for different internal flow rates (Q_{Lin}) (compare test conditions presented in Tables 6.3 with 6.1 and 6.2). Since the injection tubes are positioned below the nozzle exit, both single phase and two-phase flow properties are influenced by mixing phenomena which already take place in *the zone of flow establishment* and the boundary layer forming in the injector nozzle (see Chapter 4). Thus, the level of turbulence in the liquid, i.e. the standard deviation of the vertical liquid velocity, is not the same in the different cases investigated. In case of single-phase flow with liquid (water) flow inside the tubes, the small jets generated at the tube exits raise the turbulence level in the jet. In principle, one can compare different single-phase cases in order to estimate the effect of turbulence on the spreading and entrainment characteristics of the single-phase jets.

Further downstream, above the nozzle exit, a *zone of flow development* can be identified. In this zone the jets or wakes formed by the tubes as well as the geometry of the boundary layer at the nozzle exit affect both, flow properties and bubble distribution. Long nozzles, with or without contraction sections, can produce bubble trapping in the boundary layer near the nozzle wall, and thus increase the bubble concentration in the developing shear layer. Some tests performed with contracting nozzles show void peaks in boundaries at the nozzle exit. Furthermore, the jets created by high liquid flow rates inside the tubes can still be observed at a distance of 30–40mm

from the nozzle exit.

In case of two-phase flow, additional turbulence is produced by the bubbles (for more details see classification presented in Chapter 2). Since bubbles are formed by injecting gas into the liquid flow inside the tubes (see Chapter 4 for more details about injector design and bubble formation), it is difficult to separate pseudo turbulence induced by the bubbles from turbulence produced by the liquid jets from the tubes, because these phenomena interact. Therefore, in order to quantitatively estimate the effect of the void fraction on turbulent properties, it is necessary to first perform experiments with single-phase jets produced with and without internal liquid flow inside the tubes. It is also important to compare these data with results of turbulence calculations in the near jet region (see section 6.5). Additional information regarding enhancement of turbulence due to the presence of bubbles in case of inertia-dominated bubbly jet flow can be obtained from CFD calculations. The experimental results on single-phase and bubbly jets can be useful for validating codes and especially the models for pseudo turbulence in the inertial region of the bubbly jet.

The measurements were conducted by the PIV technique in the bubbly jet region as well as in the transition region (more details about the nature of the quantities that are measured by PIV can be found in Chapter 3). The velocity profiles presented in the following sections are normalized by the superficial vertical liquid velocity at the jet exit (V_{jet}) in order to visualize the effect of the void fraction and of the Jet Reynolds number on the properties of the liquid phase. Discussions and the results of the integration of the profiles are presented in section 6.4.3.

Since the chosen size of the field of view of the PIV cameras was about $138 \times 138mm$, the results in the transition region of the jet are only shown in one half of the jet. Measurements in the near jet region were performed over the whole jet diameter and very good symmetry of the profiles was obtained. Some of these profiles are presented in Chapter 8 and in Appendix D. Additional experiments, which were done for triggered jets with another beam splitter for the PIV camera, allowed extension of the field of view to $220 \times 220mm$.

6.4.1 Jet region ($y/D = 1.12$)

Profiles of the mean liquid velocity

In Figure (6.7), the normalized mean velocity profiles of the liquid are compared at $y/D = 1.12$, in the jet region, for three Jet Reynolds numbers. For each Jet Reynolds number data are presented for a single-phase jet (with and without) inertial liquid water flow in the tubes and for the two void fractions given in Table 6.1. The increase of the momentum flow caused by bubble-induced buoyancy enhances entrainment of the surrounding fluid.

Standard deviation of the liquid velocity, stress term and kinetic energy of the liquid

Profiles of these data are compared at $y/D = 1.12$, in the jet region, for the same conditions in Figures (6.7)-(6.8).

6.4 Effects of void and Jet Reynolds number on mean and turbulent properties of the liquid

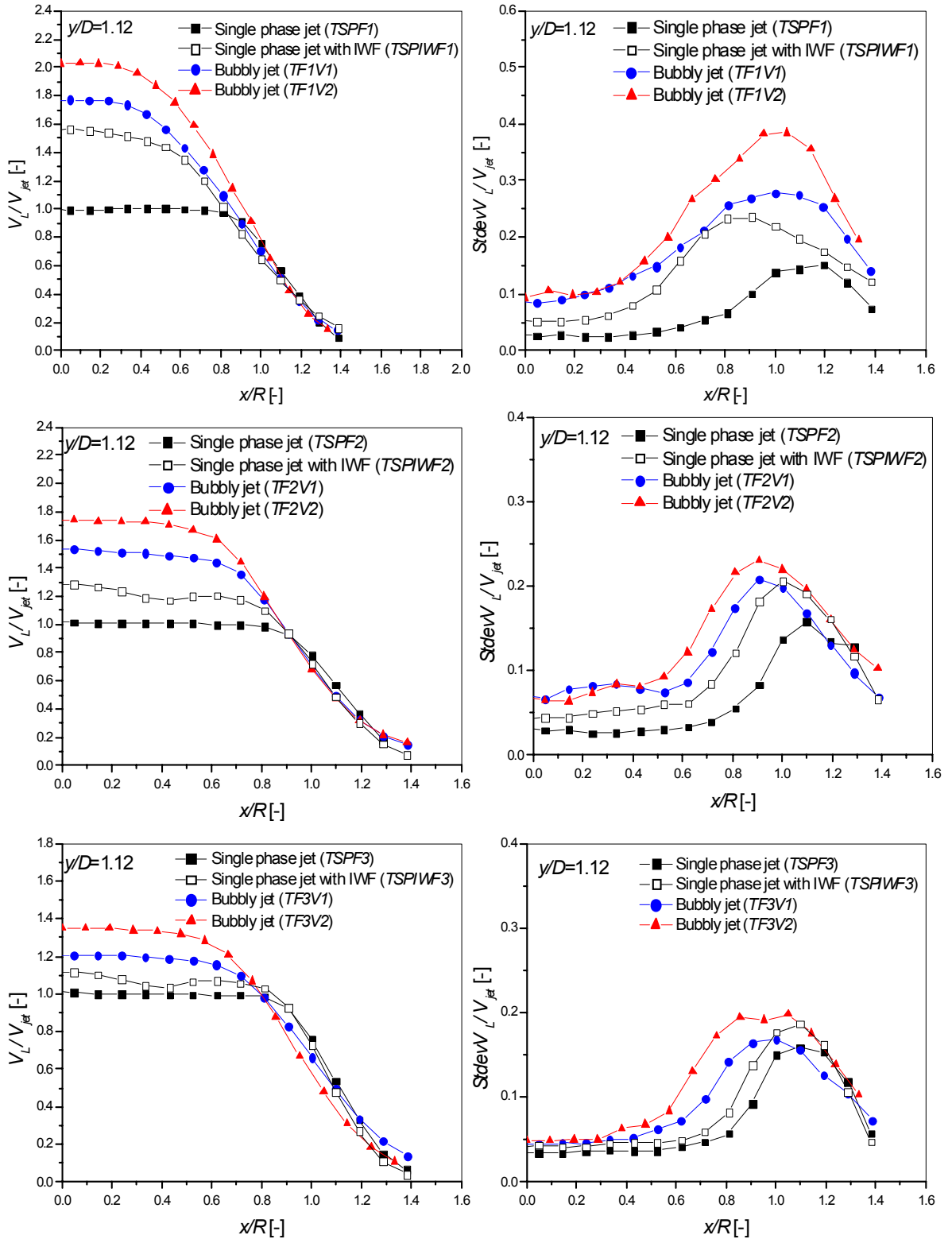


Figure (6.7): Profiles of the normalized mean velocity of the liquid and of the normalized standard deviation of the vertical liquid velocity at $y/D = 1.12$. $V1$ corresponds $\varepsilon_2 = 1.86\%$ and $V2$ to $\varepsilon_2 = 3.56\%$.

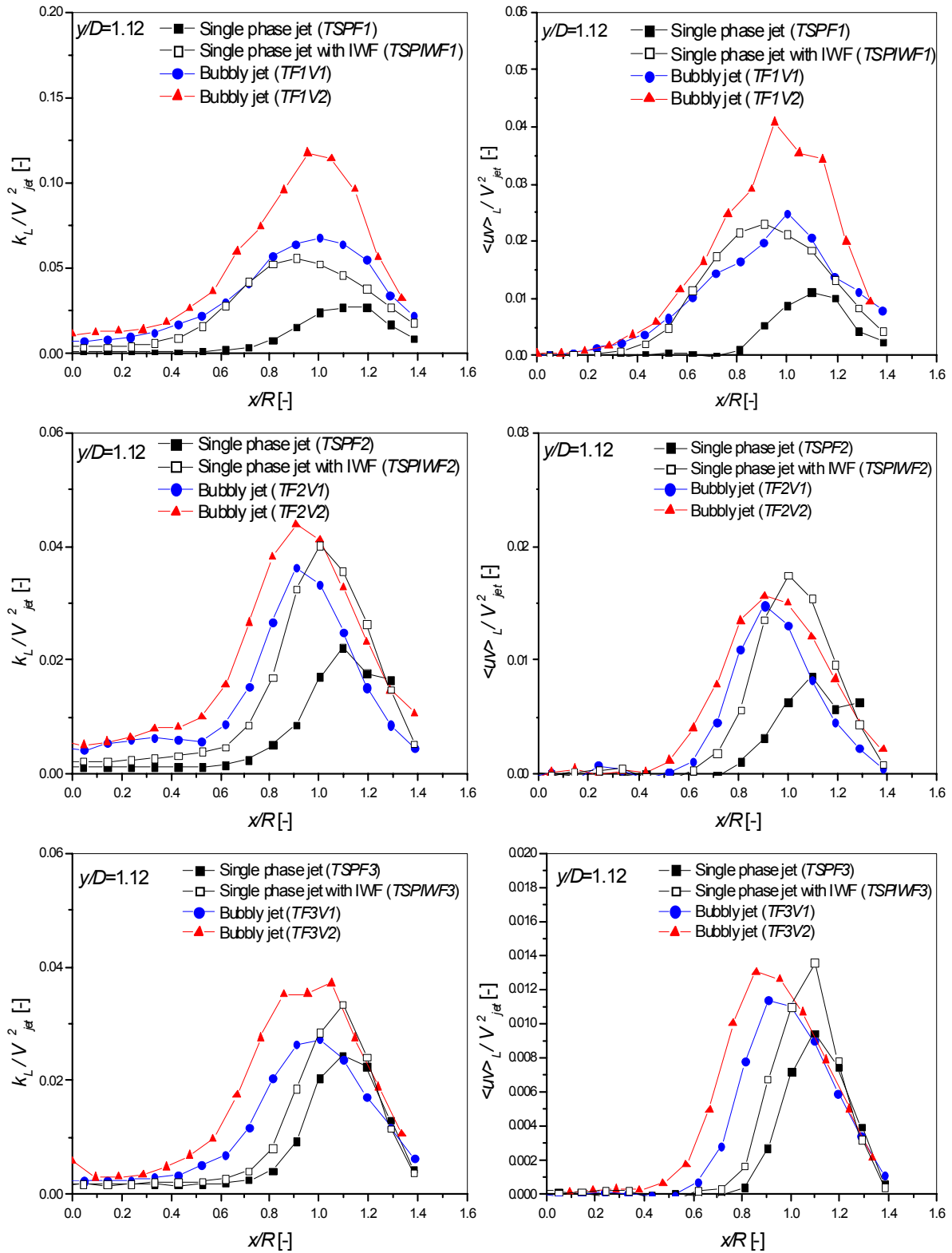


Figure (6.8): Profiles of the normalized kinetic energy of the liquid and of the normalized stress term of the liquid at $y/D = 1.12$. V1 corresponds $\varepsilon_2 = 1.86\%$ and V2 to $\varepsilon_2 = 3.56\%$.

6.4.2 Transition region ($y/D = 3.9$)

Mean liquid velocity

Profiles of the normalized mean velocity of the liquid are compared at $y/D = 3.9$, in the transition region, for two Reynolds jet numbers in Figure (6.9, left). Data are presented for the two different void fractions of Table 6.1.

Standard deviation of the liquid velocity, stress term and kinetic energy of the liquid

Profiles of these normalized data are compared at $y/D = 3.9$ in Figures (6.9, right), (6.10, right) and (6.10, left), respectively.

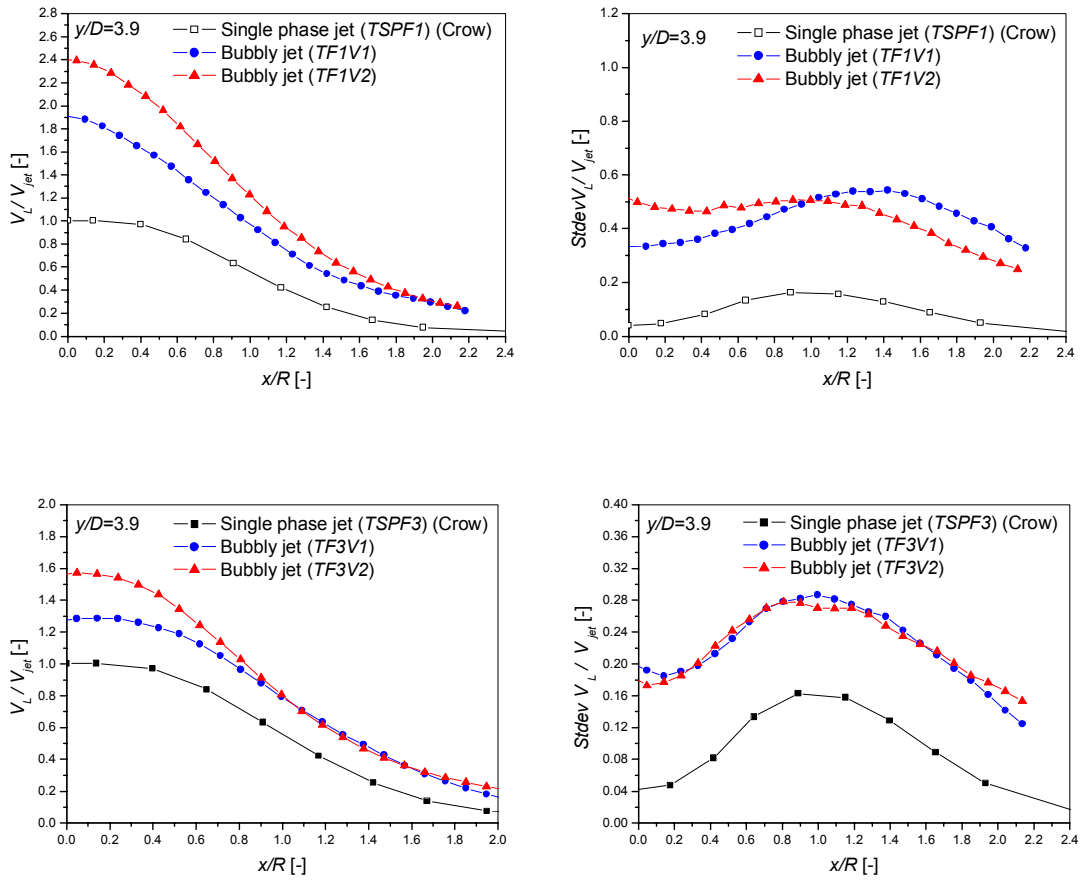


Figure (6.9): Profiles of the normalized mean velocity of the liquid (left) and of the normalized standard deviation of the vertical liquid velocity (right) at $y/D = 3.9$ for two different void fractions. The data of Crow for single-phase jet are also included. V1 corresponds to $\varepsilon_2 = 1.86\%$ and V2 to $\varepsilon_2 = 3.56\%$.

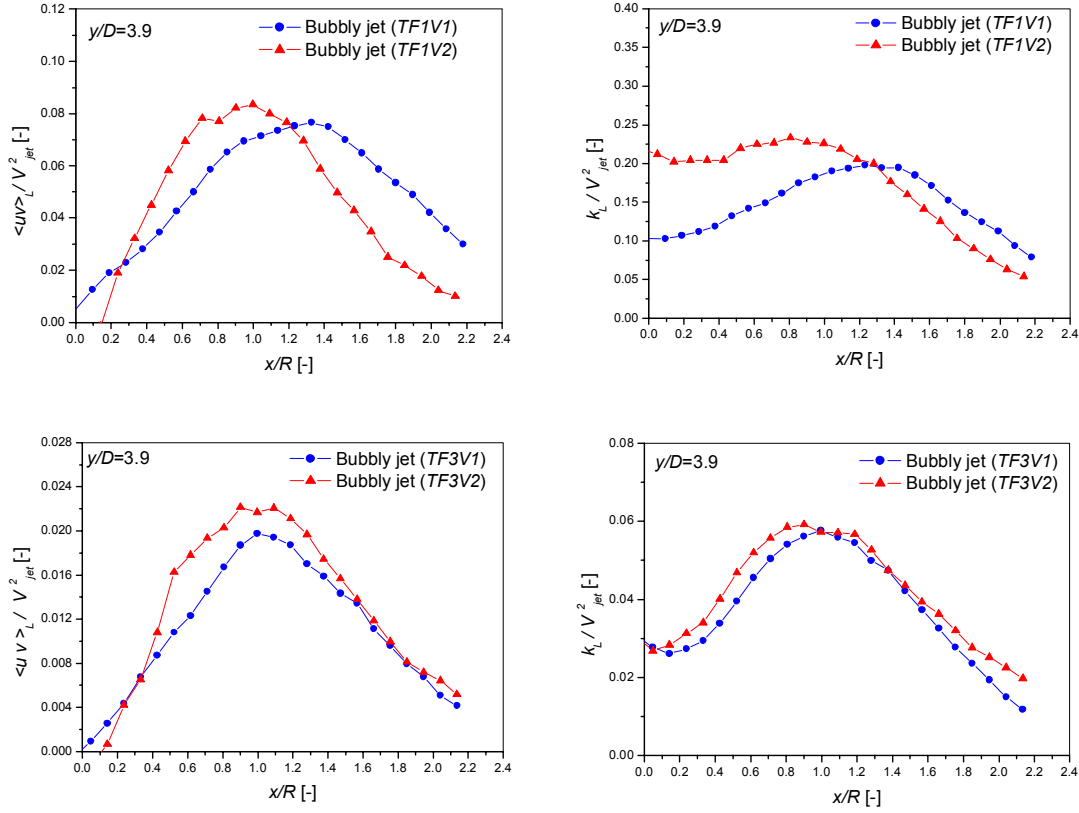


Figure (6.10): Profiles of the normalized stress term of the liquid and profiles of the normalized kinetic energy of the liquid at $y/D = 3.9$ for different flow regimes. *V1* corresponds to $\varepsilon_2 = 1.86\%$ and *V2* to $\varepsilon_2 = 3.56\%$.

6.4.3 Discussion

In order to distinguish inertia- and buoyancy-dominated regions of the jet, it is necessary to determine the local Jet Richardson number defined in Section 5.2.2. Therefore, the total momentum and buoyancy flow must be calculated from the profiles presented in the previous section.

The total turbulent momentum flow can be obtained by integration of the profiles of the mean vertical velocity of the liquid and of the standard deviation of the vertical liquid velocity (see Figures presented in Sections 6.4.1 and 6.4.2).

In general, the mean total momentum flow of a jet can be decomposed into the momentum of the mean and turbulent components

$$M_{tot} = \overline{M} + m \quad (6.4)$$

where, for axisymmetric flow:

$$\overline{M} = \int_0^{\infty} \overline{V}^2(y, r) \cdot \frac{\overline{\rho}(y, r)}{\rho_L} \cdot 2\pi r dr \quad (6.5)$$

$$m = \int_0^{\infty} \overline{v^2}(y, r) \cdot \frac{\overline{\rho}(y, r)}{\rho_L} \cdot 2\pi r dr \quad (6.6)$$

In (6.5) and (6.6), \overline{V} represents the long-term time average of the space-filtered vertical velocity of the liquid obtained by PIV (see Chapter 3 for more details) and $\overline{v^2}$ is the variance of the liquid velocity. Index L for liquid phase is dropped.

In order to determine the effect of the bubbles on jet characteristics (see discussions Section 5.2), it is necessary to compare results for single-phase jets with and without internal liquid flow inside the tubes with results of bubbly jets formed by using the same internal liquid flow inside the tubes (see Chapter 4 for details about injector and Section 6.1 for details about test conditions).

Single-phase jets

For single-phase jets, the total momentum flow at elevation y is

$$M_{tot,SP}(y) = \int_0^{\infty} \left[\overline{V^2}(y, r) + \overline{v^2}(y, r) \right] \cdot 2\pi r dr \quad (6.7)$$

At the nozzle exit ($y = 0$) the following relations hold for the tests with and without internal liquid flow:

$$\int_0^R \overline{V}_{SP} \cdot 2\pi r dr = \int_0^R \overline{V}_{SPIWF} \cdot 2\pi r dr \quad (6.8)$$

$$\int_0^R \overline{v^2}_{SP} \cdot 2\pi r dr \neq \int_0^R \overline{v^2}_{SPIWF} \cdot 2\pi r dr \quad (6.9)$$

Bubbly jets

For bubbly jets, when both gas and liquid are injected through the capillaries and tubes, respectively, the total momentum flow at elevation y is

$$M_{tot,BJ}(y) = \int_0^{\infty} \left[\overline{V}_L^2(y, r) + \overline{v}_L^2(y, r) \right] \cdot [1 - \varepsilon(y, r)] \cdot 2\pi r dr \quad (6.10)$$

The buoyant flow is

$$\overline{B}(y) = \int_0^{\infty} g \cdot \overline{V}_L(y, r) \cdot \varepsilon(y, r) \cdot 2\pi r dr \quad (6.11)$$

It is important to emphasize that in the tests discussed here, the average superficial jet velocities (V_{jet}) at the nozzle exit for, different void fractions are equal.

The integration results for the mean momentum flow of the jet (\overline{M}), the turbulent component of the momentum flow (m) of the jet, as well as the local Richardson number ($Ri(y)$) and the nondimensional coordinate ($\frac{y}{D} \cdot Ri_0$), which characterize jet-like and plume-like behavior of the bubbly jet, are presented in Tables (6.4), (6.5), (6.6) and (6.7).

<i>TSPF3</i>	$\bar{M} \cdot 10^3 [m^4/s^2]$	$m \cdot 10^5 [m^4/s^2]$
$y/D = 0.555$	1.26	2.1
$y/D = 1.12$	1.26	2.6

 Table 6.4: Results of the integration for test *TSPF3*.

<i>TSPIWF3</i>	$\bar{M} \cdot 10^3 [m^4/s^2]$	$m \cdot 10^5 [m^4/s^2]$
$y/D = 0.555$	1.2	2.25
$y/D = 1.12$	1.3	3.46

 Table 6.5: Results of the integration for test *TSPIWF3*.

These results show the following:

- The values of m in Table 6.5 (case *TSPIWF3*) are higher than those in Table 6.4 (case *TSPF3*) because of the small jets formed downstream of tubes in the zone of flow establishment (in the injector nozzle).
- In the transition region of the jet, m increases with the void fraction. The enhancement of turbulent momentum flow is caused by buoyancy.
- In case of *turbulent bubbly jets*, the nondimensional elevation at $y/D = 1.12$ falls into the inertial region, because $\frac{y}{D} \cdot Ri_0 < 1$, whereas $y/D = 3.9$ falls into the transition region ($\frac{y}{D} \cdot Ri_0 > 1$) (Section 5.2). The results for $Ri(y)$, however, do not show the linear increase with y/l_M that was presented in [46] for buoyant jets in the range $y/l_M \lesssim 1.5$.

The integrals (6.7) and (6.10) can be compared with the momentum flow prevailing at the tube exit and with that of the nozzle exit. All the quantities that appear below and details on injector design are presented in Chapter 4.

The total turbulent momentum flow in the jet nozzle prevailing at the tube exit level (M_{tot}) is given by:

$$M_{tot} = Q_{Lin} \cdot V_{Lin} \cdot \frac{Q_{Lin} + Q_G}{Q_{Lin}} + Q_{Lex} \cdot V_{Lex} \cdot \left[1 + \left(\frac{v_{Lex}^2}{V_{Lex}^2} \right) \right] \quad (6.12)$$

where the first part of the equation represents the momentum flow at the exit of the tubes corrected with the homogeneous void fraction in the tubes, and the second part is the contribution by the outer flow. The turbulent contribution $\left(\frac{v_{Lex}^2}{V_{Lex}^2} \right)$ is the same as that of the single-phase case without internal liquid flow.

<i>TF3V1</i>	$\frac{y}{D} \cdot Ri_0$	$\bar{M} \cdot 10^3 [m^4/s^2]$	$m \cdot 10^5 [m^4/s^2]$	$Ri(y)$
$y/D = 0.555$	0.16	1.23	2.87	0.3
$y/D = 1.12$	0.32	1.38	3.3	0.28
$y/D = 3.9$	1.13	1.66	23.3	0.29

 Table 6.6: Results of the integration for test *TF3V1*.

<i>TF3V2</i>	$\frac{y}{D} \cdot Ri_0$	$\bar{M} \cdot 10^3 [m^4/s^2]$	$m \cdot 10^5 [m^4/s^2]$	$Ri(y)$
$y/D = 0.555$	0.22	1.64	3.6	0.34
$y/D = 1.12$	0.45	1.8	5.3	0.27
$y/D = 3.9$	1.56	2.4	22.9	0.33

 Table 6.7: Results of the integration for test *TF3V2*.

6.4 Effects of void and Jet Reynolds number on mean and turbulent properties of the liquid

The liquid velocity (V_{Lex}) is defined by

$$V_{Lex} = \frac{Q_{Ltot}}{(D^2 - N \cdot d_{to}^2) \cdot \frac{\pi}{4}} \quad (6.13)$$

The momentum of the mean flow at the jet nozzle exit is given by

$$\overline{M} = Q_{Ltot} \cdot \frac{V_{jet}}{1 - \varepsilon_2} \quad (6.14)$$

where ε_2 is the approximate average void fraction at the nozzle exit defined in Section 5.2.

ΔM is the difference between M_{tot} and \overline{M} . It is larger than the turbulent portion at the nozzle exit (m) because only part of ΔM is transformed into turbulent momentum flow, the rest going into pressure increase (compare m given in Tables (6.4), (6.5), (6.6) and (6.7) with ΔM given in Table (6.8)).

The calculated values of the momentum for cases *TSPIWF3*, *TF3V1* and *TF3V2* are presented in Table (6.8).

Test Name	$M_{tot} \cdot 10^3 [m^4/s^2]$	$\overline{M} \cdot 10^3 [m^4/s^2]$	$\Delta M \cdot 10^4 [m^4/s^2]$	ε_2 (%)
<i>TSPIWF3</i>	1.38	1.26	1.16	0
<i>TF3V1</i>	1.45	1.29	1.6	1.86
<i>TF3V2</i>	1.52	1.31	2.1	3.56

Table 6.8: Total momentum in the nozzle at the tube exit and momentum of mean flow at the nozzle exit.

Conclusions on flow conditions in the injector

The analysis presented above is performed in order to explain how single- and two-phase flow properties for different flow conditions should be compared in order to estimate the effects of the bubbles.

Since, in case of bubble production, the liquid slugs ejected from the tubes have higher velocity than in single-phase flows with equal internal liquid flow (Q_{Lin}) (see Chapter 4), the momentum flows of bubble-laden fluids in the developing region of the jet are different from those of the corresponding single-phase case. On the other side, it is possible to compare two-phase flow cases with different void fraction in order to quantify concomitant effects of its variation, and the single-phase case with internal flow is just the limiting case with $\varepsilon = 0\%$. Thus, *there is about the same difference of additional momentum flow produced by the internal liquid flow between the case $\varepsilon = 1.86\%$ and $\varepsilon = 3.6\%$ as between single-phase and $\varepsilon = 1.86\%$* (see data in Table 6.8).

Main conclusions from experimental results:

Based on the experimental results of mean and turbulent properties of the liquid presented above, the following conclusions can be drawn:

- Turbulent fluctuations of the single-phase jet produced with internal liquid flow are stronger than those of the jet produced without flow in the tubes due to the higher turbulence level at the nozzle exit, which is induced by the liquid jets from the tubes. This effect is especially pronounced in case of small Jet Reynolds numbers. For higher Jet Reynolds numbers, the enhancement of turbulence due to the effects of the small jets is weak. The cause of this is the same internal flow (Q_{Lin}) for all three Jet Reynolds numbers (see plots of the normalized standard deviation of the vertical velocity of the liquid presented in Figure (6.7)).

- The kinetic energy of liquid in case of the bubbly jets increases with increasing void fraction in both the inertial and transition regions (see Figure (6.8)).
- The joint effects of bubbles and inlet turbulence are more pronounced in case of low Jet Reynolds number. This can be concluded by comparing vertical-velocity profiles. In the inertial region of the jet, the velocity profiles already have a Gaussian shape. In case of higher Jet Reynolds number, the profiles are still flat in the inertial region (see Figure (6.7)).
- The effect of the bubbles on entrainment is less intense in the case of higher Jet Reynolds number.
- In the inertial region of the bubbly jet, the shear layer is shifted toward the jet centerline, which means contracting, i.e. shrinking of the jet due to acceleration. This effect is more pronounced in case of higher Jet Reynolds number (see Figure (6.8)).
- In the transition region of the bubbly jet, where the vertical velocity profiles have Gaussian shape, the entrainment mechanism is much more efficient due to the buoyancy effect (see Figure (6.2)) and shear layer turbulence decays (see Figures (6.9) and (6.10)).
- The evaluated results for $Ri(y)$ do not show the expected linear dependency on y/l_M in the inertial region. More analysis is required for clarification (see data in Tables 6.6 and 6.7).
- In general, bubbles affect turbulent properties in the jet center as well as in the shear layer and significantly affect entrainment in the transition region of the bubbly jet (see Figures (6.7) and (6.8)).
- The PIV measurements presented in this chapter provide mainly results for statistical properties of bubbly jets similar to results produced by LDA or HWA. Nevertheless, they can be very useful for validating CMFD codes, especially because they cover the inertial and transition regions of bubbly jets, which have not been yet explored in detail.

6.5 Modeling of the turbulent shear stress in the liquid and turbulence modulation by the bubbles

During the past decades many turbulence models have been developed and extensively used in single-phase flows. A variety of calculations and experiments have been carried out in order to study the mechanics of turbulent flows as well as large-scale structures. An excellent summary of these works can be found in [50] and [4]. Among them maybe the greatest attention was given to turbulent buoyant jets and plumes. The discovery of apparent large-scale structures especially in the developing region of turbulent jet flows brought a great development of a variety of visualization techniques. On the other side, mathematical modelling and numerical simulation of turbulent flows enabled by fast progress in computer power provided a wide research field for both experimentalists and mathematicians.

In turbulent bubbly flows, where liquid and gas represent the continuous and dispersed phase, respectively, the modelling methods of single phase flows can be used as building blocks, taking into account the effect of the void fraction. Some of the basic concepts such as the mixing-length model of Prandtl, the $k - L$ model and two-equation models like $k - \varepsilon$ have been tested. *In experimental work on bubbly jets and plumes, most data found in the literature relate to the far field of the flow, where nearly asymptotic conditions prevail.* One objective of this work is, however, to experimentally analyze the developing part of bubbly jets. In this context, it is interesting to learn if algebraic Reynolds stress expressions that are based on the turbulence models mentioned above are applicable for the investigated flow conditions. In the following sections some of these models are applied to own experimental results, first in relation to the

single-phase jets and then subsequently to the bubbly jets. In addition, the modelling of pseudo-turbulence in the bubbly flows is also discussed.

6.5.1 Single-phase jets

- Prandtl mixing length hypothesis

The first model to describe the distribution of the eddy viscosity suggested by Prandtl in 1925 (see [51]) has the following form:

$$\nu_t = l_m^2 \cdot \left| \frac{\partial V_L}{\partial x} \right| \quad (6.15)$$

The eddy viscosity (ν_t) is related to the local mean velocity gradient and also involves an unknown parameter called the mixing length (l_m). This hypothesis has been applied with great success to relatively simple flows, where the mixing length can be expressed by a simple empirical formula. The definition and values of the length scale that appears in this quantity for single-phase free shear layers are summarized in [51]. Since the turbulence is assumed to be in local equilibrium, this model fails for rapidly developing flows, as shown in [51].

The mixing length (l_m) of a jet is defined as

$$l_m = C \cdot \delta \quad (6.16)$$

$$\delta = \frac{V_{L,0}}{\left| \frac{\partial V}{\partial x} \right|_{\max}} \quad (6.17)$$

where $V_{L,0}$ is the velocity of the liquid phase at centerline of the jet and δ is the gradient thickness of the shear layer. The Reynolds stress term for single phase jets (flow conditions are presented Table (6.3))

$$-\overline{\tilde{u}_L \cdot \tilde{v}_L} = \nu_t \cdot \left(\frac{\partial V_L}{\partial x} \right) \quad (6.18)$$

is compared here with the measured stress term (symbol used in Figures $\langle u \cdot v \rangle_L$) obtained by PIV at $y/D = 1.12$. The velocity gradient is also found from PIV liquid velocity data. The results are presented in Figure (6.11) for four different jet velocities.

Comparison between the calculated Reynolds stress term based on the Prandtl mixing length hypothesis for single-phase jets and the one measured by PIV shows very good agreement, although slightly different values of the constant C were used for fitting the data. It is also interesting to emphasize that this model, which is actually applicable in RANS modelling, here very well fits the PIV data despite the filtering involved (see Chapter 3).

- $k - L$ model

In comparison to the Prandtl hypothesis, an improvement was introduced by the $k - L$ model (see [51]). The eddy viscosity can be expressed by the velocity scale ($\sqrt{k_L}$) and a turbulent length scale (L), resulting from the mean velocity gradient, as follows

$$\nu_t = C_\mu'' \cdot \sqrt{k_L} \cdot L \quad (6.19)$$

where k_L is the kinetic energy of the turbulent motion and L is here defined as the above-mentioned scale (δ). The kinetic energy can be calculated by

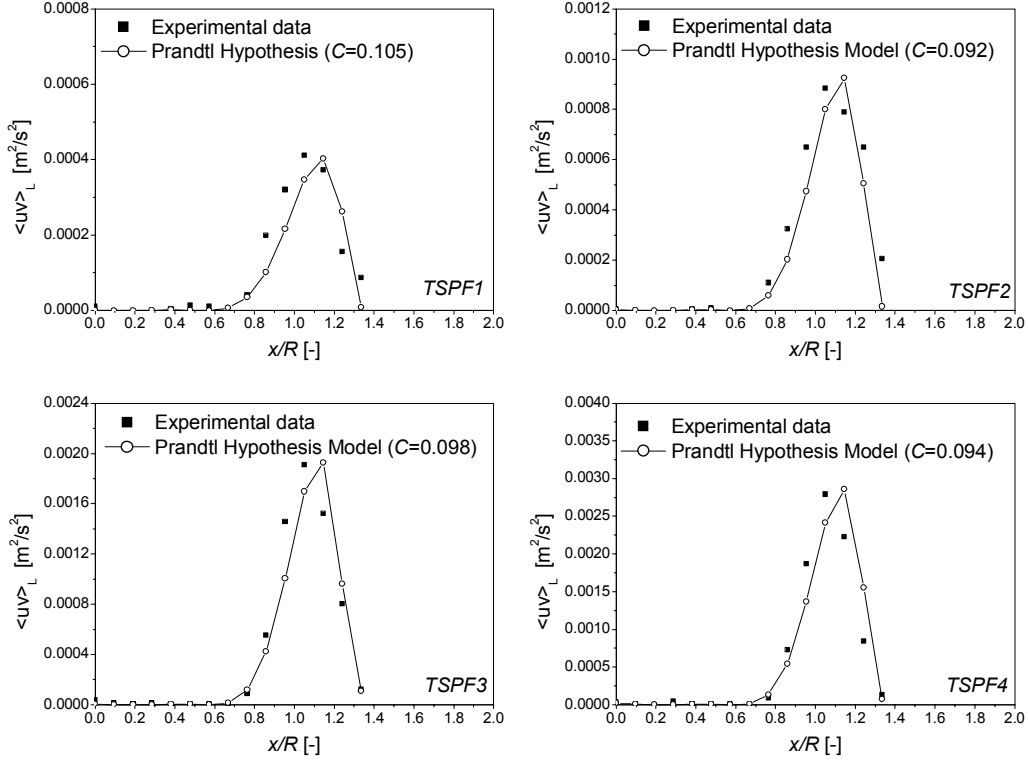


Figure (6.11): Comparison between the calculated Reynolds stress term based on Prandtl mixing length hypothesis for single-phase jets and the one measured by PIV.

$$k_L = \frac{1}{2} \cdot \left(\overline{v_L^2} + \overline{u_L^2} + \overline{w_L^2} \right) \approx \frac{1}{2} \cdot \left(\overline{v_L^2} + 2 \cdot \overline{u_L^2} \right) \quad (6.20)$$

It should be emphasized that the definition of L chosen here as the representative length scale differs from the original one presented in [51]. This is the reason why the original constant named C'_μ is replaced with C''_μ . The results are presented in Figure (6.12) for four different single-phase jet velocities at $y/D = 1.12$. The value for the constant C''_μ used to fit the experimental data was 0.06.

This model also fits the PIV data in the near jet region very well (see comparison presented in Figure (6.12)).

- $k - \varepsilon$ model

In this model, one of the most popular, the eddy viscosity is represented by [see [51]]

$$\nu_t = C_\mu \frac{k_L^2}{\varepsilon_D} \quad (6.21)$$

For shear layers in local equilibrium where production of the kinetic energy is equal to the dissipation, experiments have shown that

6.5 Modeling of the turbulent shear stress in the liquid and turbulence modulation by the bubbles

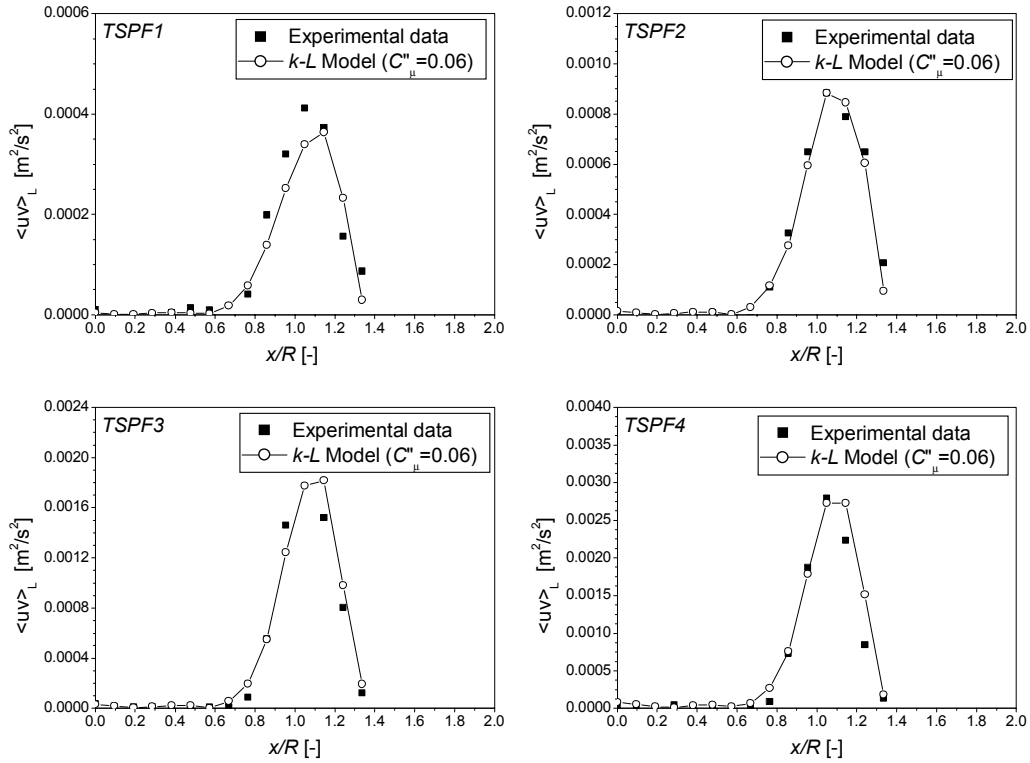


Figure (6.12): Comparison between the calculated Reynolds stress term based on the $k - L$ model for single-phase jets and the measured one by PIV.

$$C_\mu = \left(\frac{\overline{u \cdot v}}{k} \right)^2 \approx 0.09 \quad (6.22)$$

i.e.

$$\frac{\overline{\tilde{u}_L \cdot \tilde{v}_L}}{k_L} \approx 0.3 \quad (6.23)$$

Experimentally determined values for the constant C_μ , that relates the measured stress term ($\langle u \cdot v \rangle_L$) and the kinetic energy (k_L) in the near field region of the single-phase jet, are presented in Figure (6.13) for four different jet velocities. Using Equation (6.23) with $C_\mu = 0.09$, very good agreement between calculated (presented as $C_\mu^{0.5} \cdot k_L$ in Figure (6.13)) and measured stress is achieved for all cases. The data are scaled with the centerline single-phase superficial velocity at the nozzle exit ($V_{LSP,0}$).

The stress term obtained by the PIV technique and simplified models for the turbulent stress that are usually used in RANS modelling agree very well in the near jet region of the single-phase jets generated by the injector without internal liquid flow inside the tubes. Therefore, despite the fact that these data were obtained by PIV, they can be very useful for code validation and for comparing with data obtained with the LDA or HWA techniques.

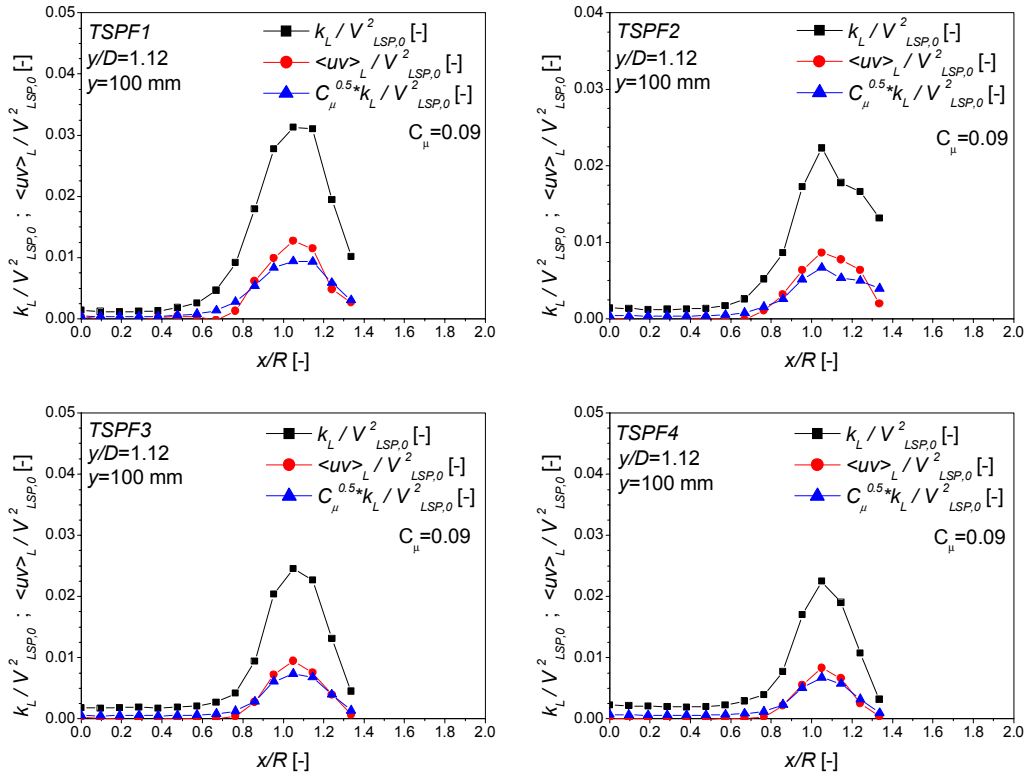


Figure (6.13): Comparison of experimentally determined normalized values of measured and calculated stress term ($\langle u \cdot v \rangle_L$) from measured kinetic energy (k_L) and constant $C_\mu = 0.09$.

6.5.2 Bubbly jet

Jet region

- Prandtl mixing length hypothesis model and $k - L$ model

In the inertia-dominated region of the bubbly jet ($y/D = 1.12$), the above-mentioned Prandtl mixing length and $k - L$ models were tested for four flow regimes. Namely, experiments were done for two different Jet Reynolds numbers, while the void fraction was also varied in order to examine the bubble effects on jet turbulence. Since the effect of buoyancy in this region is relatively small compared to inertial forces, it is realistic to assume that existing single-phase models work well, as shown in [43]. This is reasonable to expect, since the liquid-phase turbulence is mainly driven by shear in the near jet region. In the case of a bubbly jet with void fraction of about 2%, the situation will not be dramatically changed.

The diagrams presented in Figures (6.14) and (6.15) show a comparison between experimental data and predictions of the turbulent shear stress calculated with the Prandtl mixing length and $k - L$ turbulence models, respectively. Very good agreement was found between calculated Reynolds stress term and measured PIV stress term in the inertial region of bubbly jets.

In the case of the bubbly jet, no data on the jet development region have been found in the literature.

6.5 Modeling of the turbulent shear stress in the liquid and turbulence modulation by the bubbles

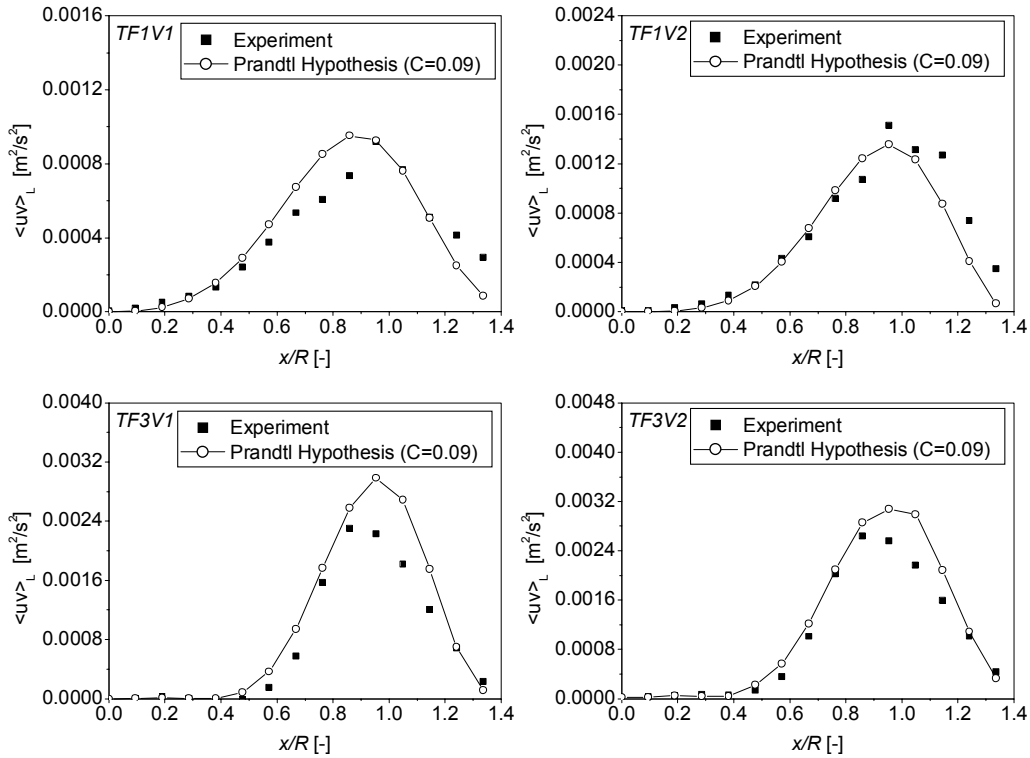


Figure (6.14): Comparison between the measured PIV term and the calculated Reynolds stress term based on the Prandtl mixing length model in the inertial region of bubbly jets.

Transition region

- Prandtl mixing length hypothesis model and $k - L$ model

Further downstream, where the effect of the buoyancy forces starts to dominate the flow, bubbles can significantly influence the turbulence of the liquid phase and also affect the shear-induced turbulence in the mixing layer. Results presented in Figures (6.16) and (6.17) show that turbulence fluctuations in the transitional and, further downstream, in the plume regions cannot be predicted by using single-phase Reynolds stress models. Therefore these data can be used for testing new models that are to be developed.

- Modelling of pseudo turbulence

The variance of the vertical velocity fluctuations ($\overline{\tilde{v}_{L,pt}^2}$) of the liquid that accounts for the pseudo turbulence in the liquid produced by the bubbles for low-void bubbly flows can be expressed as [32]:

$$\overline{\tilde{v}_{L,pt}^2} \approx \varepsilon \cdot \overline{W}^2 \quad (6.24)$$

where \overline{W} is the relative velocity. In our case, the void fraction is higher than 1.5%, and therefore the chosen model may not be applicable. Anyway, the variance of the residual vertical velocity fluctuation ($\overline{\tilde{v}_{L,res}^2}$) calculated as

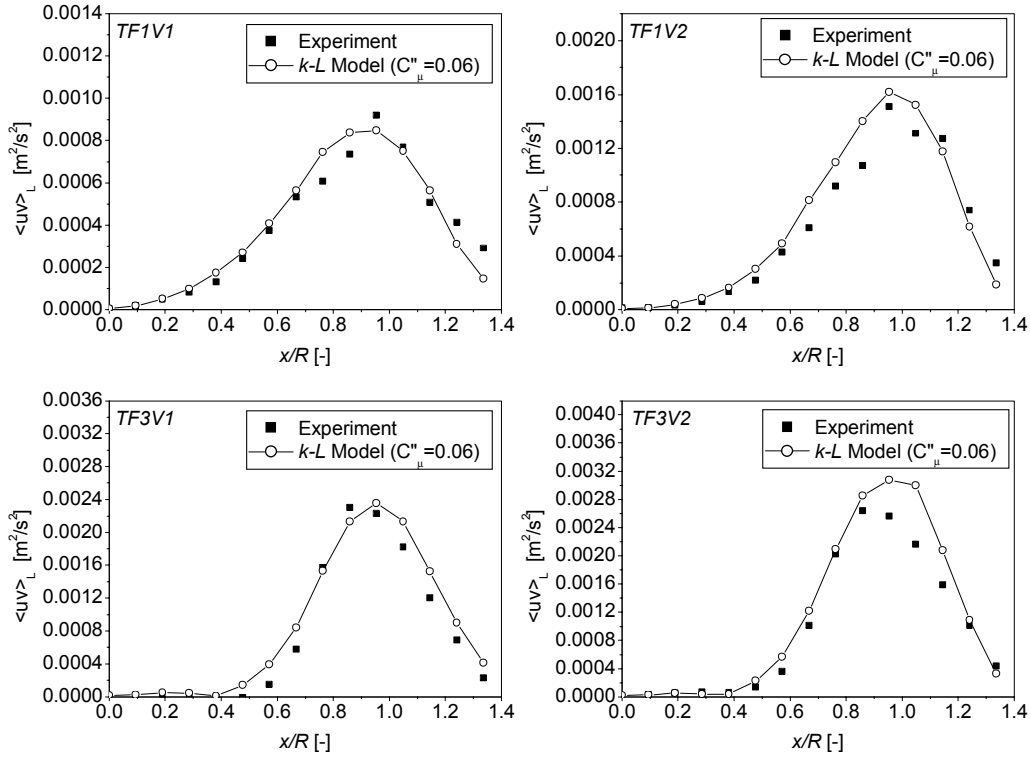


Figure (6.15): Comparison between measured PIV term and the calculated Reynolds stress term based on the *k-L* model in the inertial region of bubbly jets.

$$\overline{\tilde{v}_{L,res}^2} = \overline{\tilde{v}_L^2} - \overline{\tilde{v}_{L,pt}^2} \quad (6.25)$$

is presented in Figures (6.18 a) and (6.18 b) for two Jet Reynolds numbers and the highest void fraction cases.

Since shear-induced and bubble-induced turbulence interact in the transition and plume regions of bubbly jets, it is not easily possible to separate their effects. On the other hand, one can compare the variance of the residual velocity fluctuations with that of essentially shear-induced velocity fluctuations of the corresponding single-phase flow case, which, however, have not been measured at $y/D = 3.9$. Nevertheless, it is to be expected that the two quantities are distinctly different, since the Reynolds stress models discussed previously did not perform well in the transition region of bubbly jets.

The presented experimental data can be very useful for:

- Testing the pseudo turbulence model proposed by Lance (Equation (6.24)) in case of bubbly flows with higher void fractions than those investigated by Roig [52], who found good agreement between these two quantities in case of a bubbly mixing layer with void fraction 1.9%.
- Testing different turbulence models, first in the transition region of bubbly jets, where inertial forces are still dominant, and subsequently in the purely buoyancy-dominated region which can also be called bubbly plume. Obviously, additional extensive experimental work

6.5 Modeling of the turbulent shear stress in the liquid and turbulence modulation by the bubbles

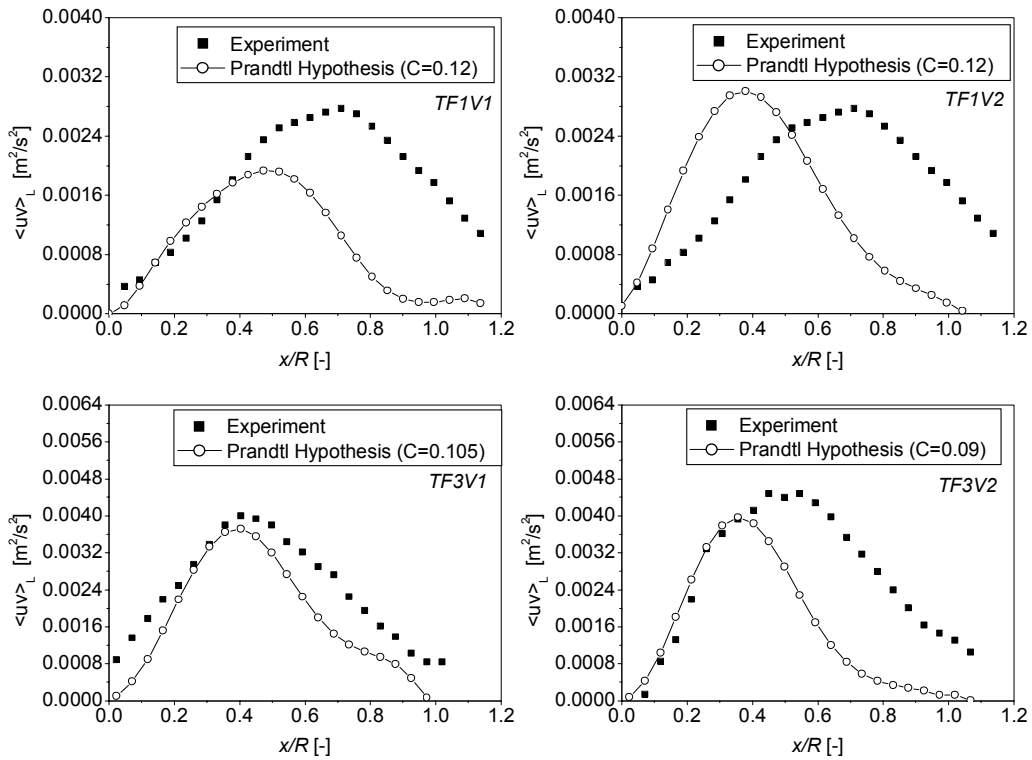


Figure (6.16): Comparison between the measured PIV term and the calculated Reynolds stress term based on the Prandtl mixing length model in the transition region of bubbly jets.

is needed for generating an adequate database for CFD simulations. Furthermore, it is recommended to develop new experimental techniques that enable simultaneous measurement of the relative velocity and of the void fraction. This information can play an important role in turbulence modelling of bubbly flows.

Summary:

- Reynolds stress models work well in the single-phase cases, also in the developing region. It may be assumed that they are also suitable in the transitional or fully-developed region of the single-phase jets.
- In bubbly jets, Reynolds stress models such as the Prandtl mixing-length model and $k - L$ turbulence model work well in the jet region, whereas in the transitional region where buoyancy dominates, a wrong prediction of the turbulent shear stress can be obtained.

Recommendations for future work:

- Testing of the Reynolds stress models in the transitional or fully-developed region of the single-phase jets.
- Testing of the Reynolds stress models for single-phase jets with liquid flow inside the tubes. It will be very interesting to compare those data with corresponding data for single-phase jets without internal liquid flow and with data for bubbly jets.

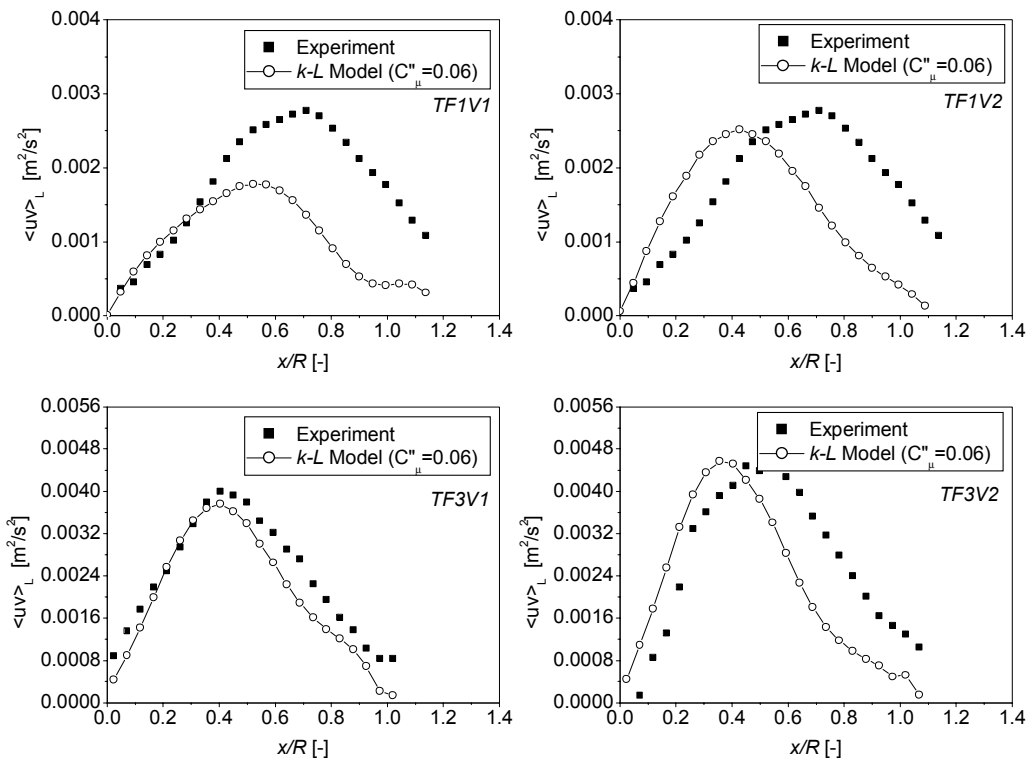


Figure (6.17): Comparison between the measured PIV term and the calculated Reynolds stress term based on the k-L model in the transitional region of bubbly jets.

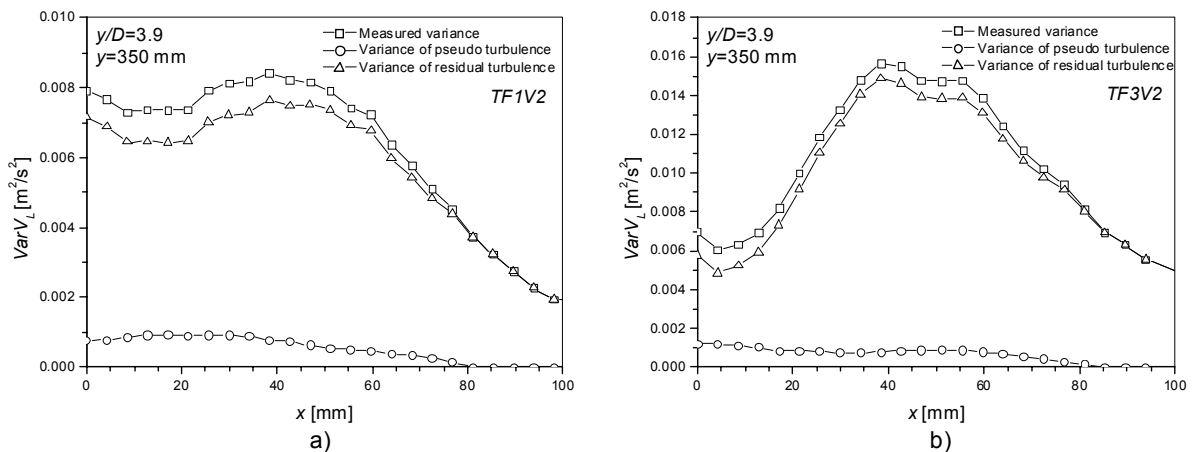


Figure (6.18): Kinetic energy of the liquid for case TF1V2 (a) and for case TF3V2 (b).

- Extensive testing of other Reynolds stress models in the jet, transition and plume region of a bubbly jet by CFD codes.
- Testing of the model for pseudo-turbulence presented in [32] in the jet, transition and plume regions of bubbly jets at higher void fractions.

7 Bubble clustering and trapping in large vortices: naturally developing vs. triggered jets

In this Chapter, an attempt is made to show whether bubble clustering or trapping can be demonstrated in case of naturally-developing jets by DOS and PIV. If these techniques are applied in a standard way, only the spatial distribution of local statistical quantities can be measured. Since bubble clustering and trapping in case of naturally-developing jets are stochastic processes, it is very difficult to deduce important information regarding size of the structures, azimuthal vorticity distribution and bubble/liquid velocities across these structures from distributions of statistical properties. Therefore, it was decided to externally and periodically excite the bubbly jet as discussed below. Preliminary results are presented in this chapter in order to understand the advantage of triggering the jet and to compare data for naturally-developing and triggered jets. These results also show what happens if the trapping conditions are not fulfilled and therefore represent a basis for further study of triggered jets.

The test condition *TF3V1* ($V_{jet} = 0.45m/s$; $\varepsilon_2 = 1.86\%$) was initially chosen to create an inertia-dominated flow with highest possible values of the non-dimensional parameters that can be achieved with the existing water pump and the installed jet nozzle ($D = 90mm$). Despite the fact that the trapping conditions defined in [53] were not fulfilled because the Froude number (Fr_v) was less than 1 and the Trapping parameter (Γ) only about 1.7, both, the naturally-developing and the triggered case with $St = 0.3$ were investigated. The results that are presented in the following sections indeed prove that significant bubble trapping cannot be found in both cases.

In order to fulfill the trapping condition, jet flow conditions with higher values of Froude number and Trapping parameter must be reached. Therefore, two possibilities were considered:

1. The Jet Reynolds number could be increased either by installing a more powerful pump or a smaller jet nozzle. In general, the size of the large eddy structures generated in the shear layer is affected by the size of the nozzle. If smaller nozzles are used, smaller structures will be produced. It is however preferable to achieve a high ratio of the size of large vortices to that of bubbles in order to study the interaction between bubbles and large vortices. Further, appropriate PIV settings such as dimension of the field of view and camera resolution, as well as size of the interrogation area must be carefully chosen in order to optimally resolve flow structures. In addition, experiments presented in this chapter show that it is very difficult to systematically study interactions between bubbles and large-eddy structures, even in case of naturally-developing jets with systematically controlled inlet conditions, because the trapping phenomenon is stochastic. This avenue was not pursued.
2. The second possibility was to trigger the jet by a periodical surging flow imposed at the nozzle exit in order to achieve a concentration of the shear layer vorticity in coherent large-scale ring structures. Obviously, this method is more convenient because the trapping conditions can be controlled and varied just by modification of the amplitude and of the frequency of the surging flow. Variation of these parameters affects the maximum vorticity in the vortex center and therefore both, the Vortex Froude number and the Trapping parameter. This second option was

chosen.

In the following sections, results obtained with both naturally-developing and triggered jets, are presented and discussed. More results on triggered-jet cases are presented in Chapter 8. For these experiments the triggering flow conditions were adjusted in a way that the trapping conditions were fulfilled while the effects of the excitation frequency were investigated.

7.1 Naturally-developing bubbly jet

For the case of a naturally-developing jet, the following PIV and DOS experimental results are presented:

- void fraction and bubble velocity profiles obtained by DOS,
- horizontal profiles of liquid and bubble velocities measured by PIV.

7.1.1 Void fraction and bubble velocity measurement with DOS

Void fraction and bubble velocity measurements have been done with DOS at selected distances from the exit of the nozzle with $D = 90mm$. Experimental vertical elevations were: $y = 25, 50, 100, 200, 350, 500$ and $600mm$. The horizontal step for point measurements was $10mm$. The development of the profiles is presented in Figure (7.1).

In the transition region ($y/D \geq 3.9$), a void peak can be detected in the jet center (see Figure (7.1)). The reason for this is not quite clear, but it may be the consequence of jet contraction produced by buoyancy. If the bubble would behave like a passive contaminant, only a broadening of the initial top-hat profile would occur. The void fraction profiles also show the existence of a peak in the shear layer at $y/D = 1.12$. In order to provide more detailed experimental results on this effect, additional, more detailed measurements in the inertial region have been conducted by DOS. These measurements are presented in Figures (7.2 a) and (7.2 b).

The void peak in the shear layer indicates displacement of bubbles from inside the mixing layer to its outer part due to the lift force. The zone where this force is important is located in the jet region and in the developing part of the transition region.

In general, information about trapping of bubbles and their interaction with large eddy structures cannot be obtained from mean flow properties measured by DOS. On the other side, information on jet spreading, average distribution of the bubbles in the jet and some effects of forces acting on bubbles can be deduced from this kind of data. In order to obtain a more detailed picture of the flow field, PIV velocity profiles are presented in the next section.

7.1.2 PIV experimental results

Profiles of the mean vertical velocity of bubbles and liquid obtained by PIV are presented in Figure (7.3 a). Bubbles have higher velocity than the liquid at all downstream positions in the shear layer, which appears to indicate that they are not trapped inside large structures formed in the mixing layer. One has to add, however, that only a fraction of the bubbles that would be detected at radial positions of the jet where large vortices occur could be trapped inside such vortices.

The azimuthal vorticity presented in Figure (7.3 b) is produced by the mean shear. Its maximum in the shear layer at $y = 100mm$ ($y/D = 1.12$) from the nozzle exit is about $25s^{-1}$.

The thickness of the shear layer is about $25mm$. If one assumes that the radius of the large structures in the shear layer corresponds to half of its thickness, the non-dimensional parameters

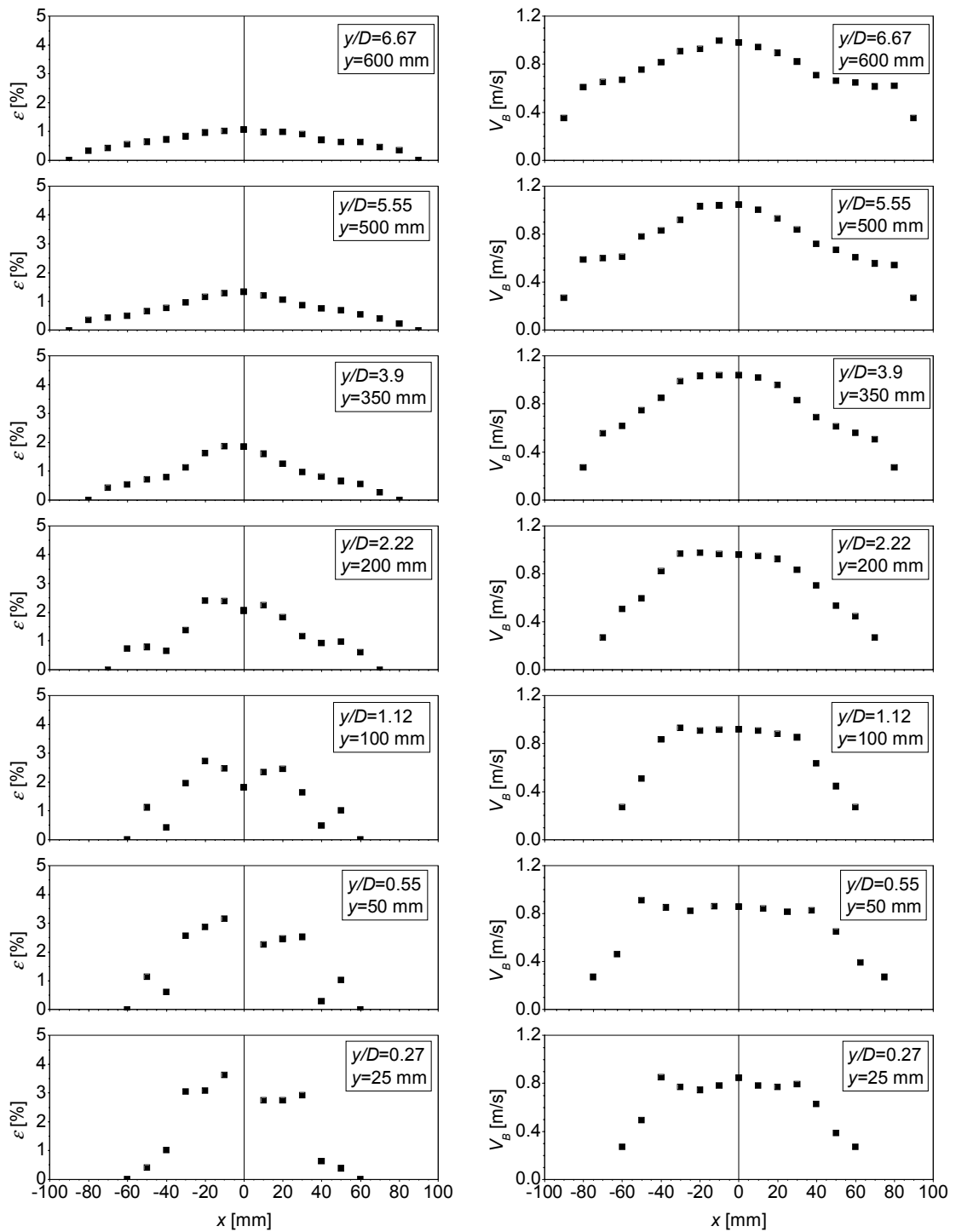


Figure (7.1): Void fraction profiles and bubble velocity profiles obtained by DOS for TF3V1.

presented in Chapter 5 can be calculated in order to check trapping conditions. The terminal bubble rise velocity for 3mm bubbles is about 0.26m/s . Based on these values, the Trapping parameter is 1.2, while the vortex Froude number is 0.2. The minimum values required for trapping bubbles inside a Gaussian vortex with a radius of 12.5mm , calculated based on criteria presented in Chapter 5, are 2.9 for the Trapping parameter and 1.3 for the Vortex Froude number.

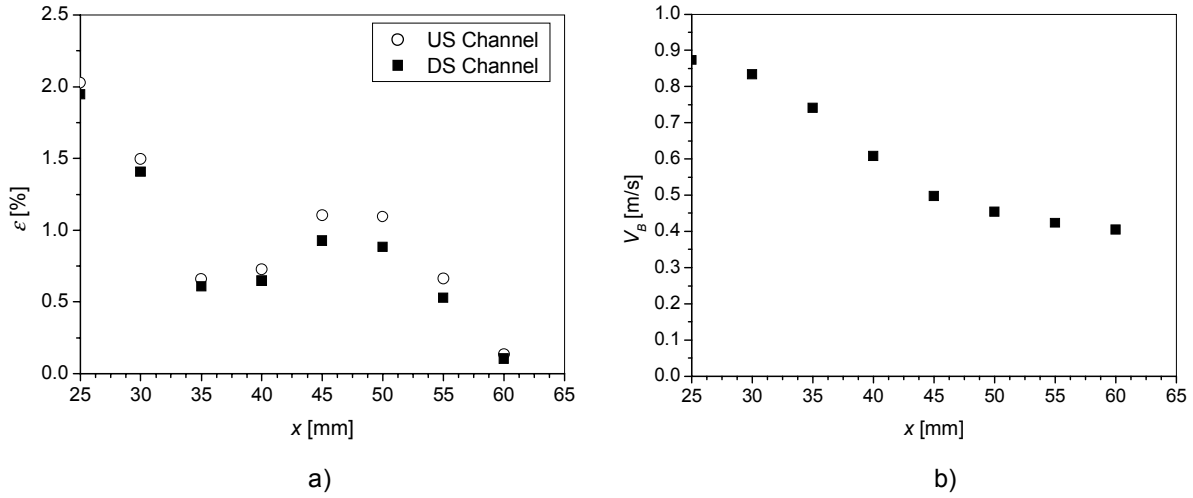


Figure (7.2): Void measurements (a) and bubble velocity in the mixing layer at $y=100mm$.

Basically the trapping conditions are not fulfilled.

However, because of the formation of stochastically distributed large vortices, the peak vorticity inside these structures can be expected to be higher than the mean value. A comparison of bubble velocities measured by DOS and PIV is discussed in Section 7.3.

7.1.3 Statistical analysis of DOS measurements in the transition region

In order to test whether bubble clustering could be detected by the DOS, a statistical analysis was initiated to show whether the number of bubbles hitting the probe per time interval deviates from a probabilistically uniform bubble density distribution. A second goal was to find whether the mean bubble velocity depended on this bubble number or the corresponding void fraction obtained by averaging over small time intervals. Since the void fraction is given by the time fraction during which bubbles contact the sensor, it is obvious that if the measurement-time intervals are small, this "void fraction" fluctuates stochastically between 0 and 1 and no longer has the original physical meaning of void fraction. On the other side, the number of bubbles hitting the sensor per time interval can be precisely counted and statistically analyzed. Furthermore, correlations of the bubble number per time interval and detected "void fractions" with appertaining bubble velocities are presented for different locations in the shear layer.

Experimental data obtained for test *TF3V1* by DOS are presented in Figure (7.4), in which the counted number of bubbles per time interval is correlated with the corresponding vertical bubble velocity. The analysis has been performed for 1500 intervals of $0.2s$ at $y = 100mm$ ($y/D = 1.12$) and $x = 45mm$. This location falls into the inertial region of the jet. Bubble count (N) represents the number of bubbles that are registered by the DOS during a single interval. The results show that there are individual bubbles which have velocity equal and even smaller than the velocity of the liquid measured at the same position in the shear layer. The mean vertical velocity of the liquid obtained by PIV at this position is about $0.3m/s$, while a few bubbles have a velocity of about $0.2m/s$. This result indicates that individual bubbles could be trapped inside large structures and travel with a velocity that corresponds to the velocity of these structures. This process is obviously and clearly stochastic, and therefore, a systematic observation of interactions between bubbles and large eddy structures is difficult in the case

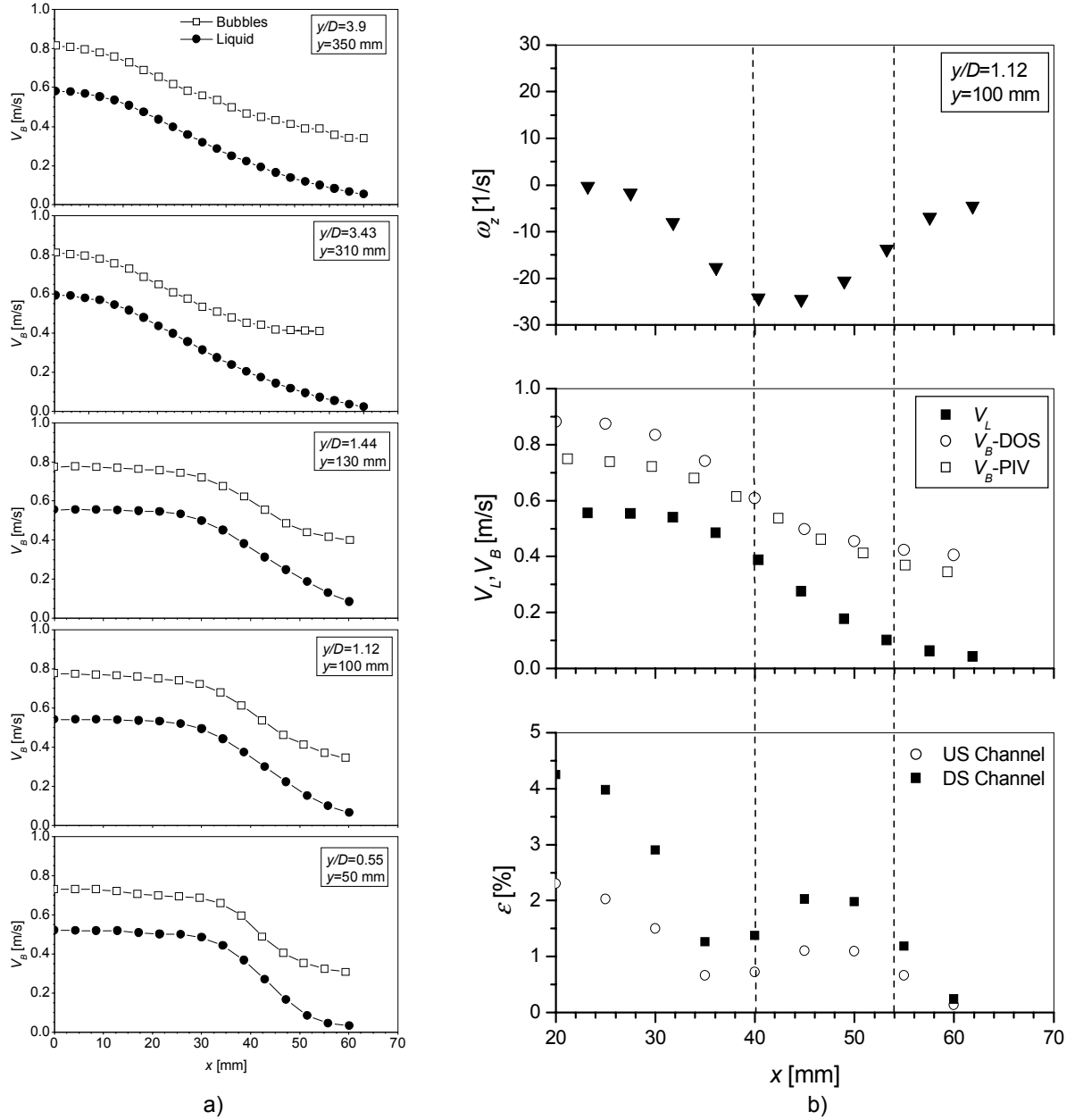


Figure (7.3): Downstream development of the horizontal profiles of the vertical velocity for bubbles and liquid obtained by PIV (a) and vertical-velocity profiles for bubbles and liquid obtained by PIV (middle), void fraction profiles (bottom) and azimuthal vorticity profile (top) at $y=100\text{mm}$ from the nozzle exit (b).

of naturally-developing jets and would require simultaneous detection of bubbles and velocity fields by combining, e.g., photographic techniques with PIV. The red crosses shown in Figure (7.4 a) represent mean bubble velocities for given N . They are not correlated with the number of detected bubbles N .

Long-time-averaged void fraction and bubble velocity profiles for test *TF3V1* at $y = 350\text{mm}$ ($y/D = 3.9$) are presented in Figure (7.4 b).

Additional statistical analyses of DOS data were conducted for the same flow regime at three

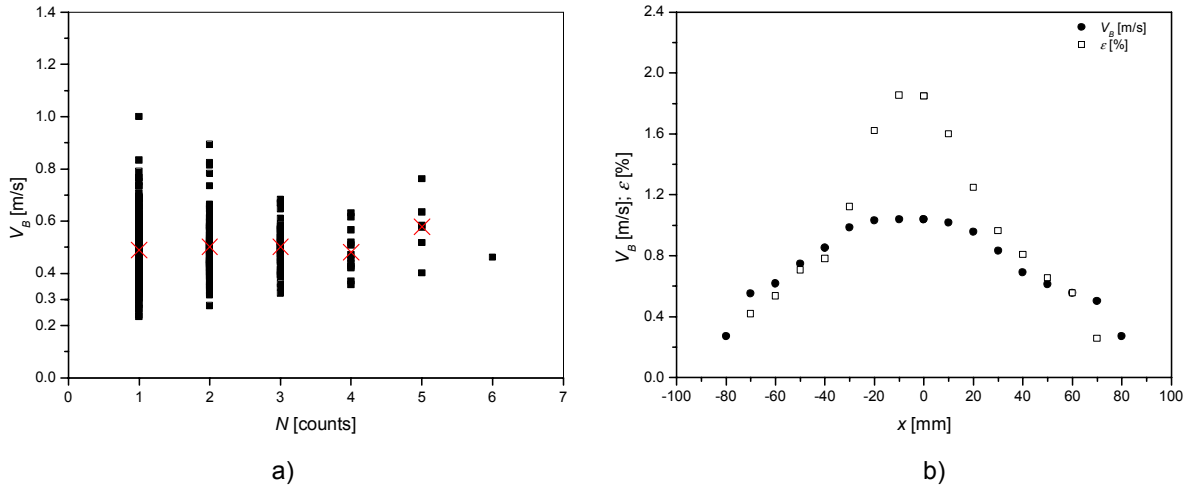


Figure (7.4): Correlation between bubble velocity and bubble number per time interval (of 0.2s) at $y=100\text{mm}$ ($y/D=1.12$, test TF3.V1) (a) and void fraction and bubble velocity profiles for TF3.V1 at $y=350\text{mm}$ ($y/D=3.9$) from the nozzle exit (b).

downstream points at the jet center and in the shear layer at $x = +50\text{mm}$ and $y = 350\text{mm}$ ($y/D = 3.9$), which fall into the transition region of the bubbly jet. Results are presented below in Figures (7.5)-(7.7). In this case, void fraction and bubble velocity data measured by DOS are correlated. A strong correlation between these two quantities indicates a dependency of bubble drag on local bubble density/void fraction.

Statistical analyses of these experimental data have been performed by dividing the total measuring period into smaller intervals of 0.02s or 0.1s . If the mean bubble velocity is about 0.6m/s in the shear layer at the chosen elevation, the DOS data, that are averaged over a time interval of 0.02s , are thus effectively averaged over a vertical distance of 12mm . The time interval of 0.1s corresponds to a vertical distance of 60mm . Assuming that the diameter of the large vortices is about 25mm , the time interval of 0.1s is too large for resolving bubble structures. As mentioned before, a smaller time interval means a smaller number of events for averaging. Therefore, void fractions obtained by integrating the bubble signal over small time intervals vary within a wide range. Since the total number of bubbles in the shear layer is considerably smaller than in the jet center, one should choose longer time intervals in order to increase the probability of hitting more than one bubble per time interval. Anyway, for the point at the jet centerline the data are analyzed by using both time intervals. For the longer time intervals, it is expected that no bubble clustering phenomena can be detected.

The probability of detecting a given number of bubbles per time interval can be compared with the Poisson distribution. This distribution applies in situations where the probability that an event occurs during an infinitesimal time interval does not depend on time, corresponding to a bubbly flow without clustering. The *Poisson probability density function* is a discrete function defined for non-negative integers N , in which λ represents the mean number of events per time interval:

$$P(X = N) = f(N; \lambda) = \frac{\lambda^N e^{-\lambda}}{N!} \quad (7.1)$$

1. Centerline point

a) 15000 intervals of 0.02s

The correlation between bubble velocity and void fraction is presented in Figure (7.5 a) and appears to show a velocity decrease with increasing void fraction. The probability of detecting N bubbles per time interval is presented in Figure (7.5 b). It agrees well with the Poisson distribution, i.e. the difference between experimental and theoretical results is not significant.

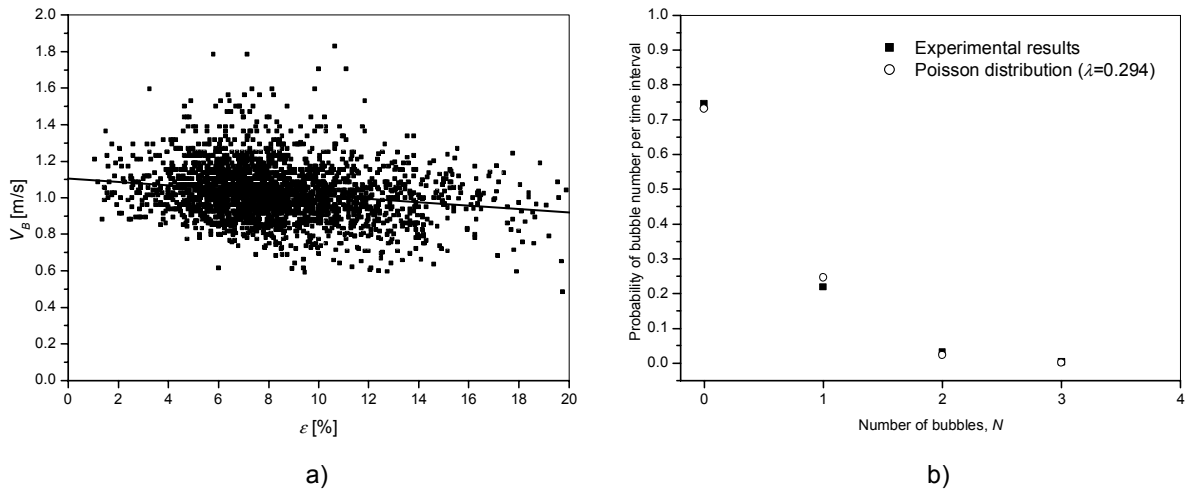


Figure (7.5): Correlation between velocity and void for the centerline point at $y=350\text{mm}$ (interval of 0.02s) (a) and probability of detecting N bubbles per time interval of 0.02s for point at centerline (b).

b) 3000 intervals of 0.1s

The correlation between bubble velocity and void fraction is presented in Figure (7.6 a) and shows the same tendency as in Figure (7.6 a). The probability of detecting N bubbles per time interval presented in Figure (7.6 b) illustrates that the experimental probability distribution differs somewhat from a Poisson distribution. A slight clustering could be the reason why $N = 0$ and $N \geq 3$ are more frequent than those from the Poisson prediction. This effect can not be seen in case a) because there the probability of detecting more than one bubble per time interval is comparatively small.

2. Shear layer point at $x=+50\text{mm}$ (3000 intervals of 0.1s)

The correlation between bubble velocity and void fraction is presented in Figure (7.7 a). The corresponding probability of detecting N bubbles per time interval (comparison with Poisson distribution) is presented in Figure (7.7 b). It does not show a deviation from the Poisson distribution, but this may again be caused by the too-small probability of detecting more than one bubble per time interval. Again, one should carry out the analysis for larger intervals in order to find a deviation from the Poisson distribution.

These statistical analyses of DOS measurements thus show that some clustering of bubbles occurs in naturally-developing jets, but its effects are not very pronounced. It is obviously very difficult to obtain information on the size and the development of the large eddy structures in naturally-developing flows, as well as to quantify the interaction between bubbles and the large vortices that are formed in the shear layer. In general, for correlating flow characteristics such as bubble and liquid velocities as well as void fraction, it is necessary to develop new or to

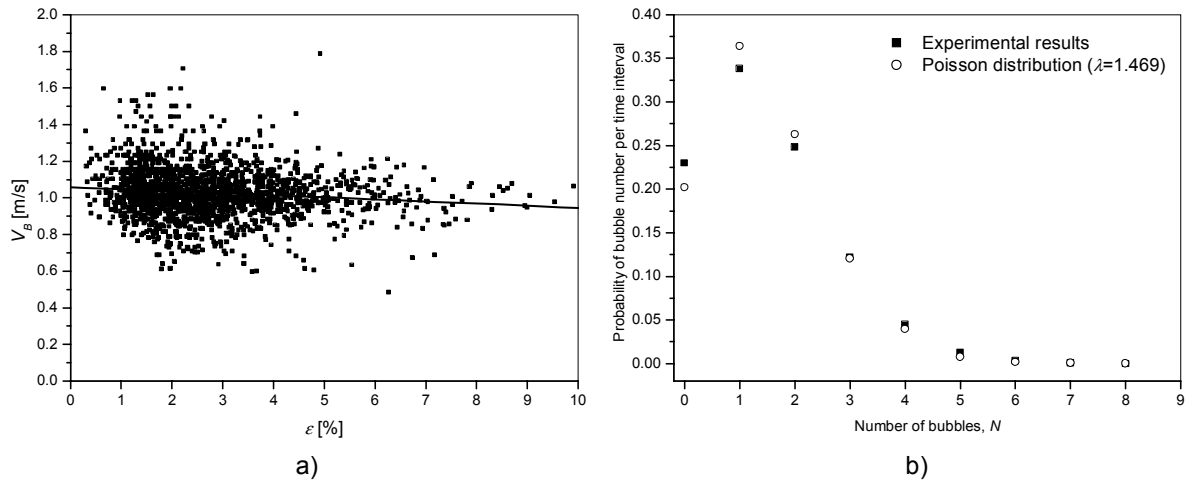


Figure (7.6): Correlation between velocity and void fraction for the centerline point at $y=350\text{mm}$ (interval of 0.1s) (a) and probability of detecting N bubbles per time interval of 0.1s for centerline point at $y=350\text{mm}$ (b).

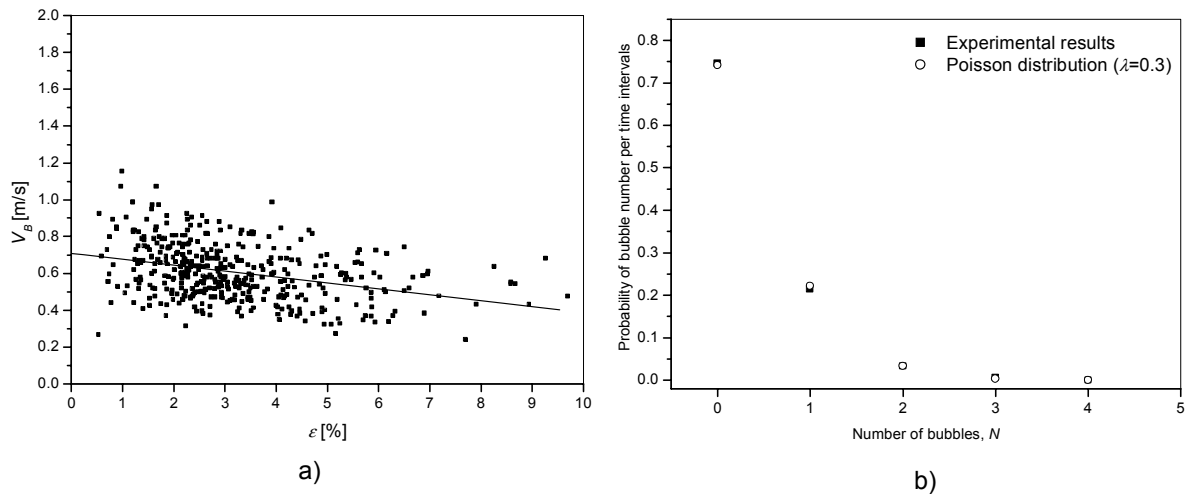


Figure (7.7): Correlation between velocity and void fraction at $x=+50\text{mm}$, $y=350\text{ mm}$ (interval of 0.1s) (a) and probability of detection N bubbles per time interval of 0.1s for the point at $x=+50\text{ mm}$ and $y=350\text{ mm}$ (b).

improve existing experimental techniques for the simultaneous measurement of these quantities. The simultaneous PIV measurements that were performed during this study represent a very first, basic step because they resolve only the velocity fields in two-phase flow. Processing of the images to obtain information on bubble concentration inside the interrogation area could however be a tempting task for future investigations.

If, however, coherent structures are periodically produced, bubble movements inside these structures can be systematically investigated. In order to investigate the possibility of using the DOS technique to obtain phase-averaged void fraction and bubble velocity data, the triggered experiment presented in the next section was conducted.

7.2 Triggered bubbly jet

The second part of the test *TF3VI* was conducted with a triggered bubbly jet. Since the shedding frequency f of the most unstable jet oscillations is given by the Strouhal number $St = 0.3$ (see Chapter 5 for more details), this mode was excited. For the given superficial jet velocity of $V_{jet} = 0.45\text{m/s}$ and the jet diameter of $D = 90\text{mm}$, the excitation frequency is $f = 1.5\text{Hz}$. Triggered DOS measurements were performed for points in the mixing zone at $y = 100\text{mm}$ ($y/D = 1.12$) where the large eddies are located.

The velocity at the exit of the triggering nozzle (see Appendix A) is presented in Figure (7.8 a).

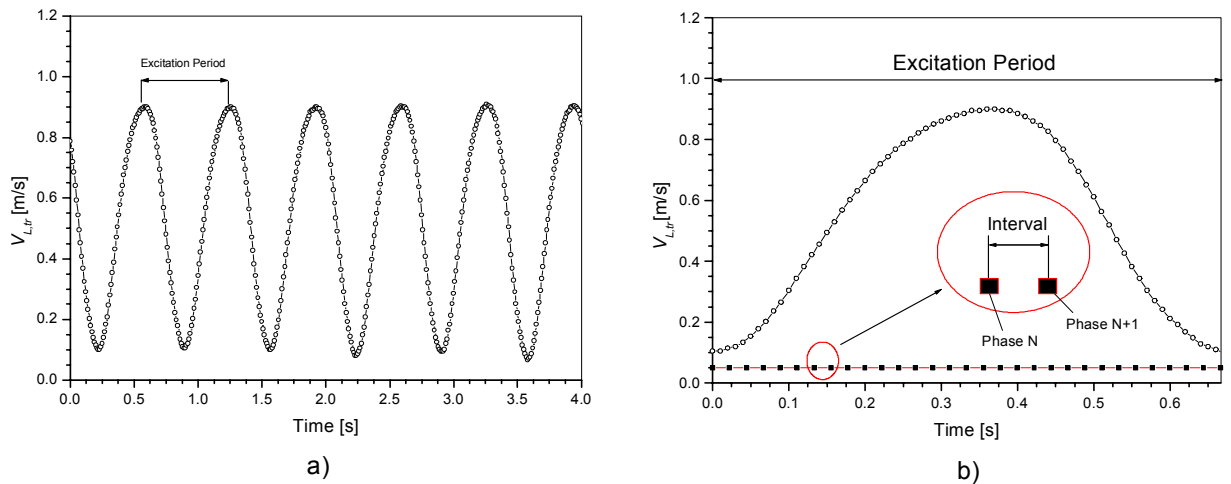


Figure (7.8): Triggering velocity (a) and phase averaging procedure: the triggering period is split into 30 equal intervals corresponding to 30 phases. The data are phase-averaged in each interval (b).

The void fraction and vertical bubble velocity profiles for the naturally-developing and the triggered jets are compared in Figure (7.9). Triggering of the jet obviously increases its spreading and influences the development of the shear layer. The void peak inside the shear layer is diminished. Even though it was not an objective to study the effect of the triggering frequency and amplitude on the mean and turbulent properties of bubbly jets, this kind of data can be easily obtained by PIV and DOS and can be very useful for understanding mixing mechanisms. Whereas for single-phase jets a similar study was conducted by Crow and Champagne (see [6]), for bubbly jets, this kind of data does not exist in the literature.

In order to enable conclusions about bubble trapping, a PIV acquisition that is synchronized with the production of coherent structures must be employed. Thus, an attempt was made to obtain phase-averaged DOS data. Results are presented and discussed below.

Phase-averaged void fraction and vertical bubble velocity

The total measuring time is first divided into intervals that correspond to the triggering period of 0.6666s , and these are further split into 30 intervals of 0.02222s (see Figure (7.8 b)). The data are acquired during 900 excitation periods. The data collected in each of the 30 intervals of the excitation period are phase-averaged.

Data for point $x = 62\text{mm}$ and $y = 100\text{mm}$ (Figure (7.10)), which corresponds to the void peak in the mixing layer, have been analyzed.

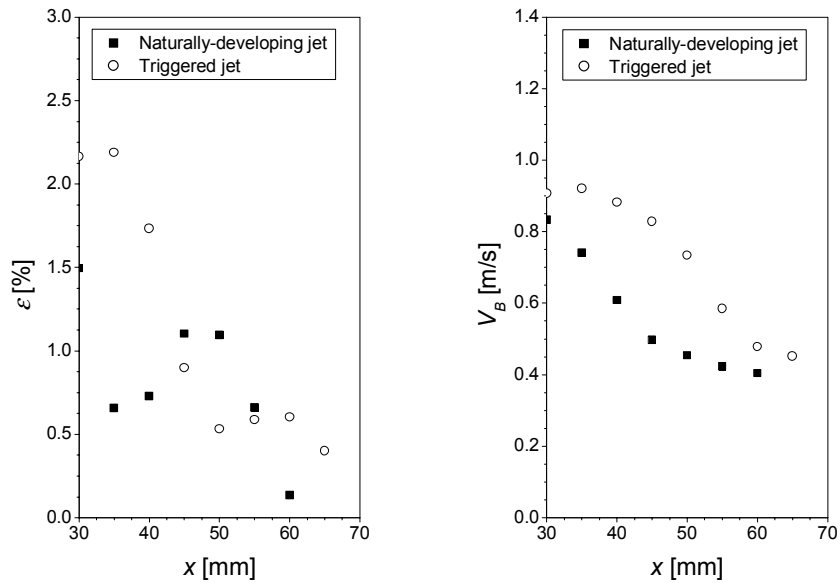


Figure (7.9): Void fraction and bubble rise velocity at $y=100\text{mm}$ for naturally-developing and triggered jet.

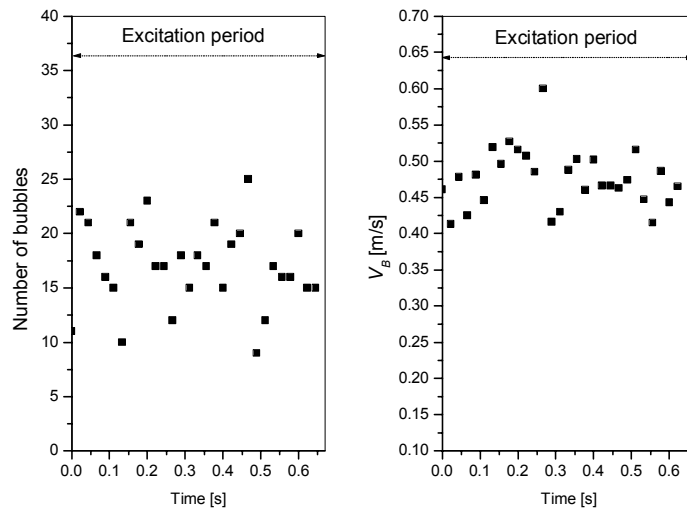


Figure (7.10): Bubble number and velocity within the excitation period (point at $x=62\text{mm}$ and $y=100\text{mm}$).

The numbers of counted bubbles and velocities obtained by DOS do not show significant bubble clustering, although a certain pattern can be recognized. The measurements, however, showed the importance of choosing a sufficiently long total measurement time in order to obtain statistically adequate numbers of bubbles per interval. Therefore the duration of the experiment had to be increased to about 60min in order to obtain statistically significant results.

These preliminary experiments brought forth a new idea, which is fully explored in Chapter

8. Since the test matrix presented in Chapter 6 is more suitable for studying the effects of the Jet Reynolds number and void fraction on the mean and turbulence properties of bubbly jets, new test matrices, that will be presented in Chapter 8, have been set up for investigating flow conditions that enable bubble trapping.

7.3 Comparison of bubble velocity measurements by PIV and DOS

Bubble velocity measurements for most tests were conducted with both PIV and DOS. During this study it was found that the velocities measured by DOS exceed the data obtained by PIV. This phenomenon was studied, e.g., in [34]. Here, only the basic principles and differences of both techniques will be pointed out, accompanied with a comparison of results for typical turbulent flow conditions with high bubble concentration.

DOS measurements

The bubble velocity measured by DOS is computed using the distance between the upstream and downstream sensors and the time of flight measured as the time difference between the bubble arrival times registered by the upstream and downstream sensors. In principle, it is possible to measure very short times of flight with the DOS, while very long-time lags are practically considered to be out of range and are not taken into account.

Another characteristic of the DOS measurements is that the velocity is obtained by long time averaging. In general, the DOS-measured bubble velocities depend on many factors such as sensor response, sensor geometry, bubble shape and bubble velocity fluctuations. More details about the chosen DOS settings can be found in Appendix C.

Corre and Ishii [34] suggested experimental design criteria based on the axial distance of the sensor tips (vertically oriented) if bubbles with given diameters d have to be detected and the overestimation of the velocity measurements is to be minimized, i.e. they recommend to use:

$$0.6 \leq \frac{\Delta y_{tips}}{d} \leq 1$$

for a lateral displacement of the tips of

$$0.05 \leq \frac{\Delta x_{tips}}{d} \leq 0.1$$

The double optical sensor used during this study was horizontally oriented and has $\Delta y_{tips} = 0.75\text{mm}$, without a lateral displacement Δx_{tips} . The recommendation of [34] thus is not strictly applicable. For bubbles between 2 and 4mm, the ratio falls into the range $\frac{\Delta y_{tips}}{d} \in [0.19 - 0.37]$, which is out of the recommended interval.

The main reason for overpredicting the velocity is that bubbles with a relatively large horizontal velocity component lead to a short time delay Δt_{tips} , which is erroneously interpreted as a high axial velocity. Furthermore, for a small ratio $\Delta y_{tips}/d$, the probability of hitting both tips with the front surface of the bubble within a short time interval can be relatively high, which leads to overprediction of the velocity, contrary to the case $\Delta y_{tips}/d > 1$ (shown in Figure (7.11 b and c)).

The results of a numerical evaluation presented by the same authors [34] show an overprediction of up to 15% for the ratio $\frac{\Delta y_{tips}}{d} \in [0.2 - 0.4]$. Furthermore, a very important conclusion was

drawn in relation to the effects of fluctuations of the bubble velocity vector. The model used in [34] is presented in Figure (7.11 a). The authors assumed that the bubble velocity vector can reach any location within a sphere of radius $|v_{B,max}|$, which in their study is called the maximum relative bubble velocity fluctuation. It was shown that the resulting overestimation of the mean velocity can be as high as 30% for a maximum relative bubble velocity fluctuation of $\frac{|v_{B,max}|}{\bar{V}_B} = 1$ with uniform vectorial distribution.

The phenomenon described depends on the flow conditions. The resulting biasing effect on the velocity measurements can be minimized by an optimum choice of the DOS geometry, but it cannot be eliminated.

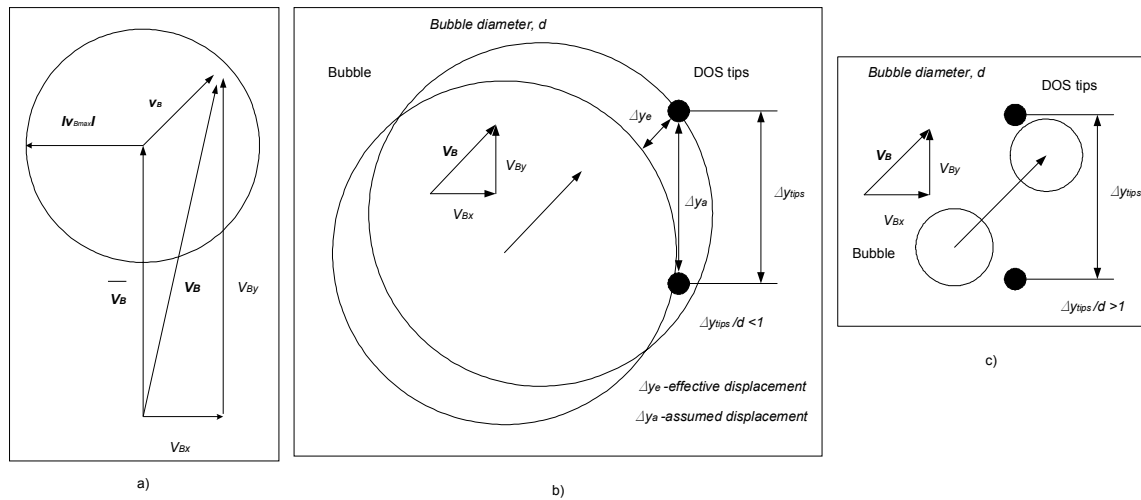


Figure (7.11): Model for bubble velocity vector (a) and possible scenarios of bubble detection by two vertically separated DOS tips. Case b) corresponds to large bubbles, while case c) corresponds to smaller bubbles, where the bubble cannot touch both tips in case of large V_{Bx} .

PIV measurements

The bubble velocity measured by the PIV technique represents a time- and space-filtered value averaged over laser pulse interval and interrogation area. Actually, the cross-correlation function is calculated based on information on the light intensity that is reflected from the bubbles within an interrogation area. Depending on the size of the interrogation area, usually several bubbles contribute to the average bubble velocity measurement (for more details see discussion in Chapter 3).

In the experimental results presented, the velocities obtained by DOS always exceed those obtained by PIV. A comparison for case *TF3V1* is presented in Figure (7.12).

The overestimation reaches maximum values in the regions with very high bubble concentration, while in the region of the shear layer, the differences between PIV and DOS measurements are smaller. A statistical analysis shows that the bubble velocity fluctuations cannot be neglected, and therefore an overestimation of the bubble velocity of up to 30%, as reported in [34], could result.

7.3 Comparison of bubble velocity measurements by PIV and DOS

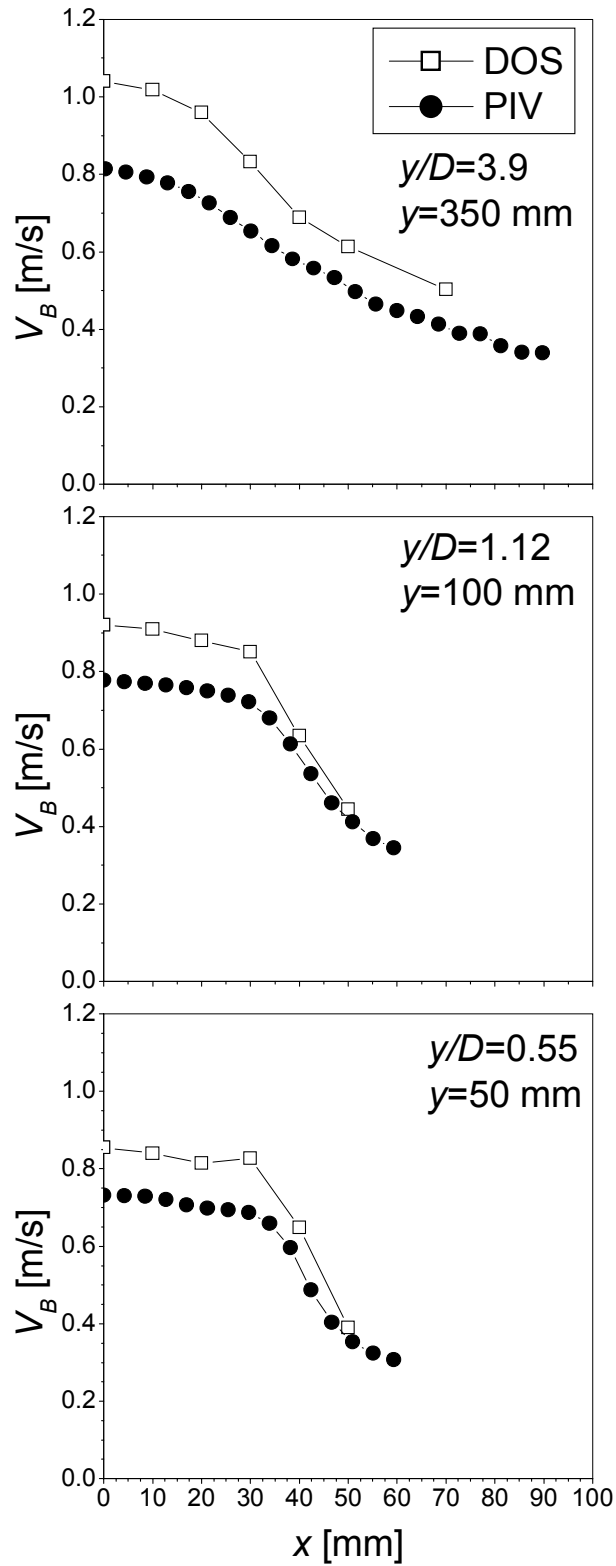


Figure (7.12): Comparison of bubble velocity measurements obtained with DOS and PIV.

8 Velocity and bubble concentration fields for triggered bubbly jets

As shown in the previous chapter, the periodic excitation of bubbly jets was found to be a very useful tool for studying the interactions between large vortices and bubbles. The emphasis is laid here on bubble trapping detection and quantification, but it is also shown that results of these tests could be used to correlate the coherent parts of liquid velocity variations with those of the bubble density or void fraction. Bubble trapping actually means that bubbles reach an equilibrium position within the vortices and travel with them at the same vertical velocity. If sufficient bubbles reach this position in the vortices, a bubble ring is formed. A photo that illustrates this phenomenon is presented in Figure (8.1).

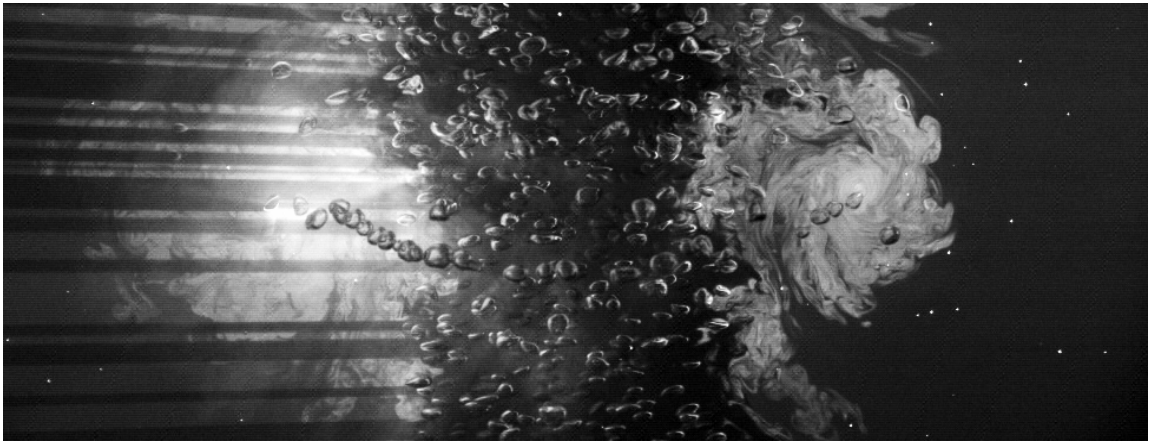


Figure (8.1): *Vortex and bubble ring in a periodically excited bubbly jet visualized by injecting fluorescent dye directly into the modulated shear layer.*

A simplified condition for bubble trapping inside these structures and relevant non-dimensional parameters are presented in Section 5.1. Controlling parameters in these experiments are frequency and amplitude of the surging flow imposed at the nozzle exit. The selected excitation method acts on the shear layer and produces periodic toroidal vortices, which travel downstream at about 50% of the jet exit velocity V_{jet} [6].

Some preliminary tests showed that the variation of the excitation amplitude influences the maximum vorticity at the vortex center and therefore the circumferential velocity. If the amplitude is sufficiently increased, the trapping condition can be reached when the inertial force acting on the bubbles is large enough. If the excitation amplitude is small and the values of the corresponding non-dimensional parameters are below the minima for trapping, the bubbles can escape the vortices. They will be effectively dispersed by large structures in the surrounding fluid. This phenomenon happens in the transition region at $y/l_M \approx 1$ where the buoyancy force starts to dominate the flow, although buoyancy need not be the only cause of bubble escape. In general, the relation between the different forces acting on bubbles is changed, and this affects bubble agglomeration inside large structures and distribution of the bubbles in the shear layer.

The triggering experiments are done with fixed amplitude, adjusted to fulfill trapping conditions,

while different excitation modes that correspond to $St = 0.3$, 0.6 and 0.84 are investigated. The instability corresponding to $St = 0.3$, which is referred to as *preferred mode*, actually is an integral instability (jet column instability) that reaches its peak at $y/D \approx 4$ (see [6]). This mode is called *preferred* because it attains the highest possible amplitude of turbulence intensity. On the other hand, $St = 0.8$ or higher is close to the Strouhal number of the natural shear layer instability of the jet.

The main objectives of the experimental investigations presented in this chapter are to develop an experimental procedure for tracking both liquid and bubbly structures in order to study interactions between them and to obtain quantitative results on bubble trapping inside the large vortices that are formed in the shear layer.

In order to fulfill these tasks the following phase-averaged quantities were simultaneously measured by PIV: the vertical velocity of the liquid and bubbles and the vertical velocity of both vortex ring and bubble ring. The azimuthal liquid vorticity field is then numerically determined based on liquid velocity data. It provides information on size, shape and position of large vortices in the flow field as well as the maximum vorticity at the vortex center. These data can then be used to calculate the Vortex Trapping parameter and the Vortex Froude number and to check if the simplified condition for bubble trapping (see Section 5.1) is fulfilled or not. In addition to the PIV measurements, photographic techniques were used for demonstrating the formation of bubble rings and DOS measurements were performed for obtaining data on the coherent variation of the bubble density and the void fraction.

8.1 Test matrix

Two flow regimes (*TTF2V1.A* and *TTF2V1.B*) were investigated during this study. Both flow regimes are presented in Table (8.1).

Test *TTF2V1.A* was used as a reference test for checking if the trapping conditions presented in Section 5.1 are fulfilled or not for given inlet conditions, as well as to test various data acquisition techniques performed by PIV and DOS in order to check methods for the quantification of bubble trapping. The results of this test are shown here because they demonstrate how experimental techniques such as DOS and PIV can be used for studying periodically excited bubbly jets and how inlet and triggering conditions affect bubble trapping inside large eddies.

Based on the results obtained from test *TTF2V1.A* and the discussion presented in Section 5.1, the new test matrix (*TTF2V1.B*) (see Table (8.1)) was prepared in order to study *the frequency effect* on the development of large eddy structures and bubble trapping inside them. In order to improve test conditions, the following issues have been taken into account:

- The analytical approach (Section 5.1) shows that the largest bubbles can be most easily trapped inside Gaussian vortices because they require the smallest vorticity in the vortex center. This is mainly due to the reduced intensity of the lift force (see discussion on variation of the lift coefficient C_l with bubble diameter in Section 5.1). Therefore, bubbles (with diameter of $4mm$ instead of $2mm$ bubbles as in test *TTF2V1.A*) are used for these tests.
- The liquid flow inside the tubes was minimized in order to reduce the effects of the small jets generated by the tubes (leading to enhancement of jet turbulence and of entrainment, as shown in Chapter 6), whereas the superficial liquid velocity at the nozzle exit was kept the same ($V_{jet} = 0.32m/s$) as for test *TTF2V1.A*. It is important to emphasize that the enhancement of the entrainment due to the increased jet turbulence can significantly affect the liquid velocity field and the azimuthal vorticity field.

- In order to achieve or to augment bubble trapping, the Vortex Trapping parameter and the Vortex Froude number can be increased by adjusting the excitation amplitude. Raising the velocity amplitude at the exit of the triggering nozzle (see Appendix A) increases the maximum azimuthal vorticity of the liquid if the other flow conditions are preserved. The triggering amplitude for test (*TTF2V1.B*) was increased until distinct bubble rings emerged and was then kept constant during the experiments with different excitation frequencies.

Test Name	<i>TTF2V1.A</i>	<i>TTF2V1.B</i>
\dot{Q}_{Lin} [L/ min]	20	4
\dot{Q}_{Lex} [L/ min]	100	116
\dot{Q}_G [NL/ min]	3.85	3.85
\dot{Q}_{Ltot} [L/ min]	120	120
Re_{jet}	30275	30275
Fr_{jet}	0.11	0.11
Γ	1.21	1.21
ε_h [%]	3.4	3.4
ε_2 [%]	1.86	1.86
V_{Lin} [m/s]	0.94	0.94
V_{Gin} [m/s]	6.4	6.4
V_{jet} [m/s]	0.32	0.32
Ri_0	0.4	0.4
d [mm]	~ 2	~ 4
St	0.6	0.3; 0.6; 0.84
f_{ex} [Hz]	2	1; 2; 3
$V_{L,tr,peak}/V_{jet}$	2.3	3.4

Table 8.1: Test conditions for *TTF2V1.A/B*.

8.2 Survey of experimental results for test *TT F2V1.A*

The first triggered experiment was performed for test condition *TTF2V1.A*.

Phase-averaged velocity fields of liquid and bubbles, as well as the azimuthal vorticity of the liquid, were obtained in a frame of $138 \times 138mm$ close to the jet exit (Figure (8.4)).

The DOS point measurements have been conducted at different positions in the shear layer. Phase-averaged results of DOS measurements in the shear layer extending over the full excitation period of $0.5s$ are presented in this section. The vortex ring shown in Figure (8.4) is formed at about $y = 30mm$ from the nozzle exit, which means that a bubble ring can exist at the DOS tips at $y = 50mm$.

The excitation frequency (f) corresponding to the Jet Strouhal number ($St = 0.6$) was $2Hz$. The velocity of the excitation flow corresponding to the modulated flow rate at the exit of the triggering nozzle is shown in Figure (8.2). The peak EF velocity is higher than the liquid velocity in the bubbly jet. The ratio between the peak and the jet velocity is 2.3.

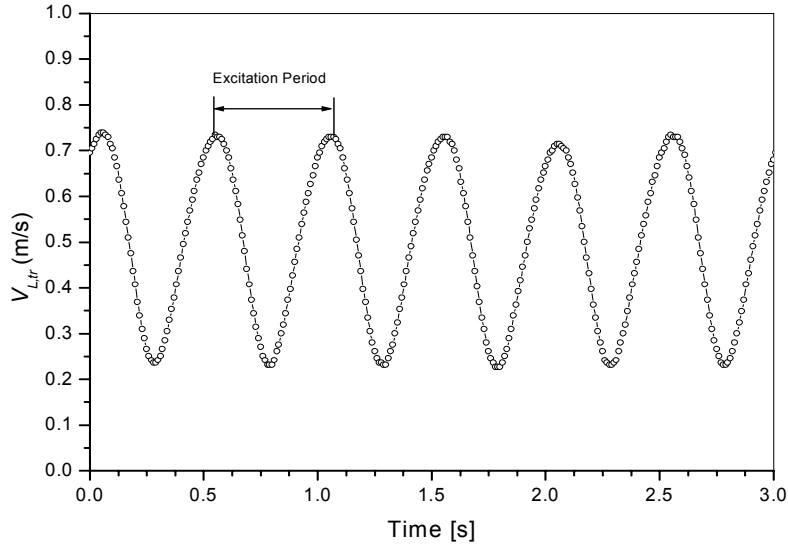


Figure (8.2): Triggering-velocity at the exit of the triggering nozzle.

8.2.1 PIV experimental results

Phase-averaged vorticity field

Figure (8.3) shows the results, namely phase-averaged profiles of the vertical liquid (V_L) and bubble velocity (V_B), standard deviation of vertical liquid velocity ($StdevV_L$) and azimuthal vorticity of the liquid (ω_z) at $y = 50mm$ and $y = 100mm$ downstream of the jet exit.

The first selected level corresponds to the mid-plane of a vortex ring formed in the shear layer around the jet, while the second lies in the middle between the vortices in the shear layer (see Figure (8.4)). Equality of vertical liquid velocity at the vortex center with bubble velocity close to this centre indicates trapping (Figure (8.3), left-top). The phase-averaged value of the standard deviation of the vertical liquid velocity corresponds to the incoherent part of the vertical velocity fluctuations (Figure (8.3), left-bottom). The width of the shear layer at $y = 50mm$ is about $30mm$.

The phase-averaged azimuthal vorticity field presented in (Figure (8.4)) shows the existence of large elliptical Gaussian vortex structures in the shear layer. The peak vorticity at the vortex center is about $60s^{-1}$. The vorticity field actually consists of a localized part, that covers the strong vortex ring, and an extended part, that is produced by the mean shear in between the vortex rings (see Figure (8.4)). The velocity profiles of Figure (8.3) also illustrate that the shear layer is broader in between the vortices.

Horizontal and vertical profiles of the phase-averaged azimuthal vorticity through the centre of the vortex in the shear layer (see Figure (8.5)) are fitted by Gaussian curves:

$$w_z(x, y) = w_0 \cdot e^{-\frac{(x-x_c)^2}{a^2}} \cdot e^{-\frac{(y-y_c)^2}{b^2}} \quad (8.1)$$

The horizontal vortex "radius" (a) estimated from the phase-averaged azimuthal vorticity field at $y = 50mm$ is about $13mm$ (Figure (8.5)). With a terminal bubble rise velocity for $2mm$ -

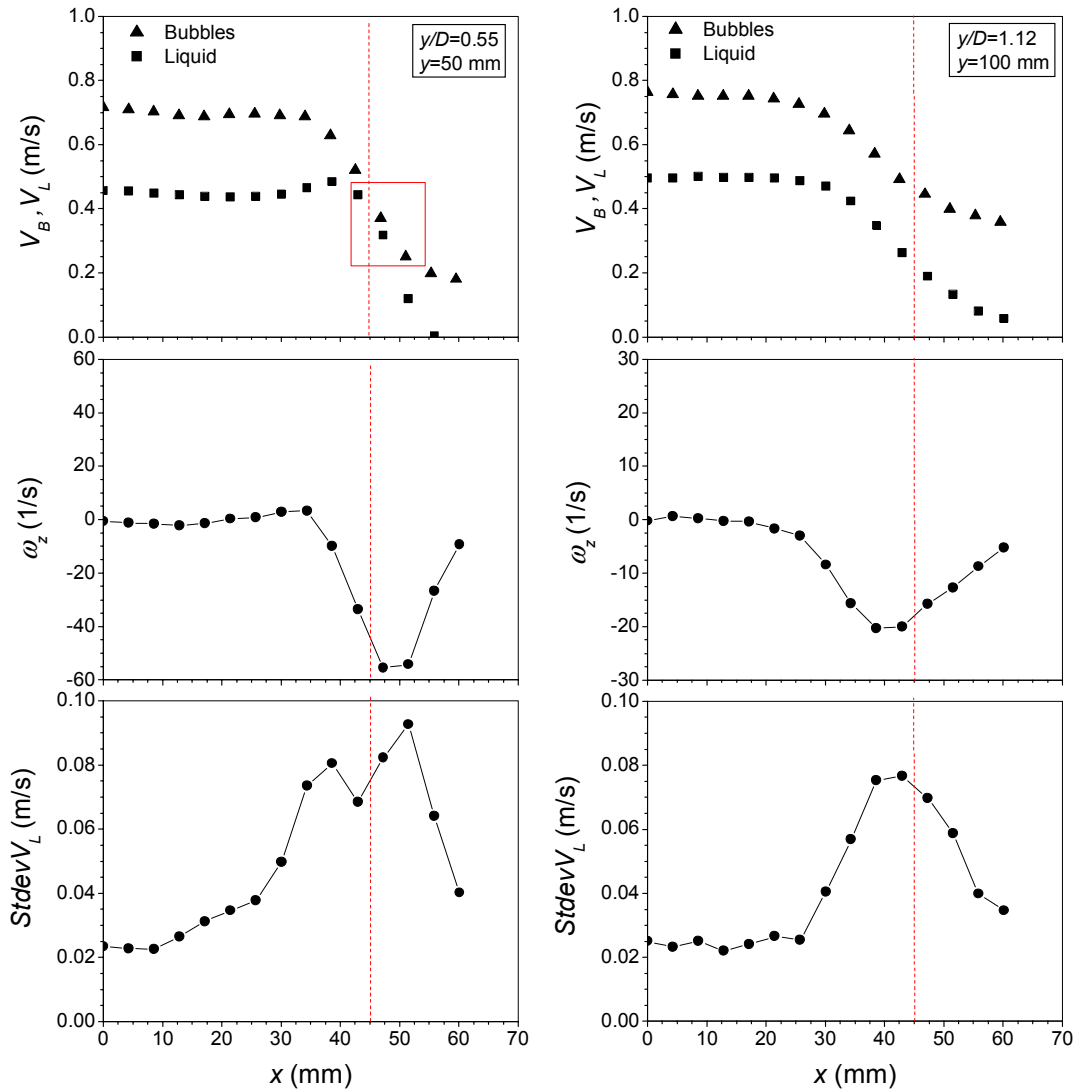


Figure (8.3): Horizontal profiles of phase-averaged vertical velocity (top), standard deviation of vertical velocity (bottom) and azimuthal vorticity (center) of the liquid through the centre of the vortex in the shear layer (right) and between the vortices in the shear layer (left).

bubbles of 0.26m/s a Vortex Trapping parameter of 3 and a Vortex Froude number of 1.2 result. The minimum values of the Vortex Trapping parameter ($\Gamma_\omega = 2.7$) and of the Vortex Froude number ($Fr_\omega = 1.2$) (see Section 5.1) represent the condition for bubble trapping. Even though only one parameter reached the minimum value, the trapping condition is fulfilled. Furthermore, with the vertical vortex "radius" ($b = 16.5\text{mm}$) one obtains the Vortex Trapping parameter ($\Gamma_\omega = 3.81$) and the Vortex Froude number ($Fr_\omega = 1.5$) which are larger and fulfill the trapping condition.

A clear indication of bubble trapping inside the vortex ring is the generation of a bubble ring that travels with the same velocity as the vortex ring. The velocities of both vortex and bubble ring can be estimated from the data acquired by a PIV vortex tracking method (more details are presented in Appendix D) with or/and without illumination of the flow field with backlight. The bubble rings do not remain stably confined in the vortices, because visualization tests show

strong deformations and disintegration of the bubble rings at a y -level of a few jet diameters (this will be shown in following sections).

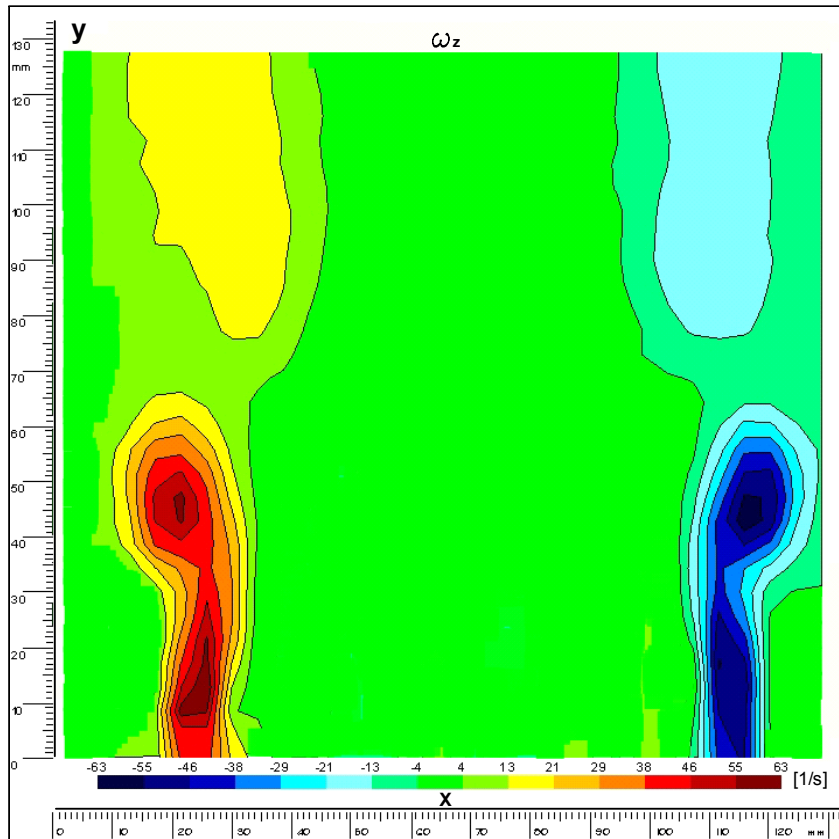


Figure (8.4): Phase-averaged azimuthal vorticity field of the liquid (horizontal coordinate x , vertical coordinate y). The jet center is at about $X=69$ mm.

The phase-averaged image of bubble reflections (Figure (8.6)) obtained by superimposing several shots synchronized with vortex triggering and filtered with the Max Pixel Operator (see Chapter 9) illustrates bubble clustering inside the large vortices. Bubbles that are illuminated by the laser sheet reflect light. The increased bubble concentration inside the large vortices may indicate bubble trapping (see the zone marked with rectangle). The vertical location of this zone corresponds to the position of the vortex ring presented in Figure (8.4).

8.2.2 DOS experimental results

In order to enable phase-averaging of DOS data, the acquisition was started by the external encoder signal and was stopped after a large integer number of periods. Each excitation period of $0.5s$ (corresponding to $St = 0.6$) was divided into 25 intervals of $0.02s$, as already discussed in Section 7.2. The number of detected bubbles, void fraction and vertical bubble velocity data were phase-averaged for each of the 25 intervals. Measurements were done at $y = 50, 60, 100$ and $200mm$, downstream of the jet exit at radial positions $x = 48, 50, 51$ and $52mm$ in the shear layer. The chosen horizontal locations correspond to the position of the vortex ring where bubble trapping occurs (Figure (8.4)).

Figure (8.7) shows phase-averaged results of DOS measurements for points in the shear layer at $y = 50mm$ downstream of the jet exit. The results indicate clustering of the bubbles in shear layer vortex structures, since the void fraction goes through a maximum during the excitation

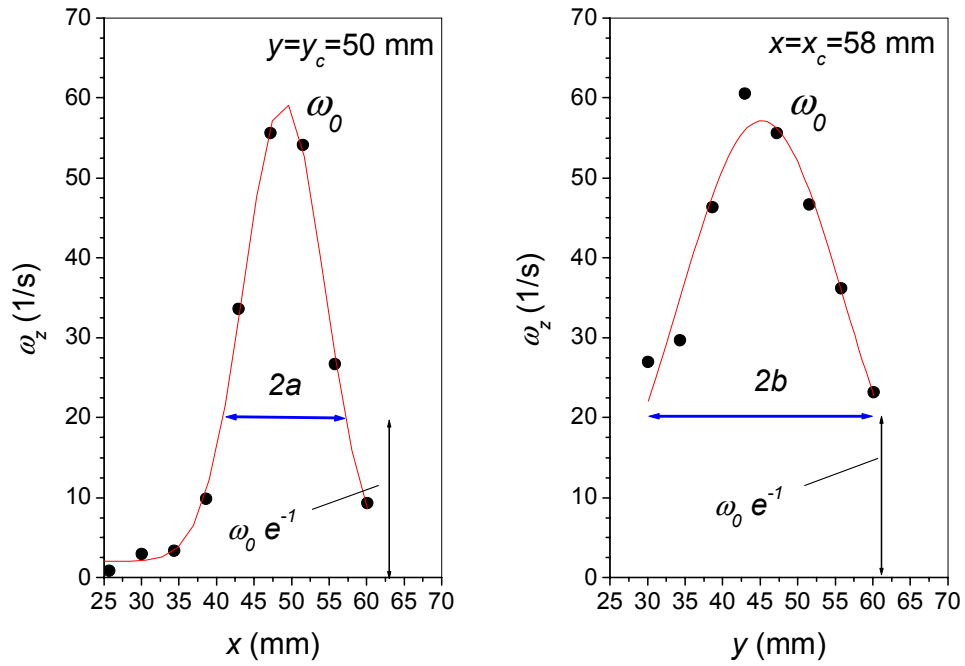


Figure (8.5): Horizontal and vertical profiles of phase-averaged azimuthal vorticity through the centre of the vortex in the shear layer.

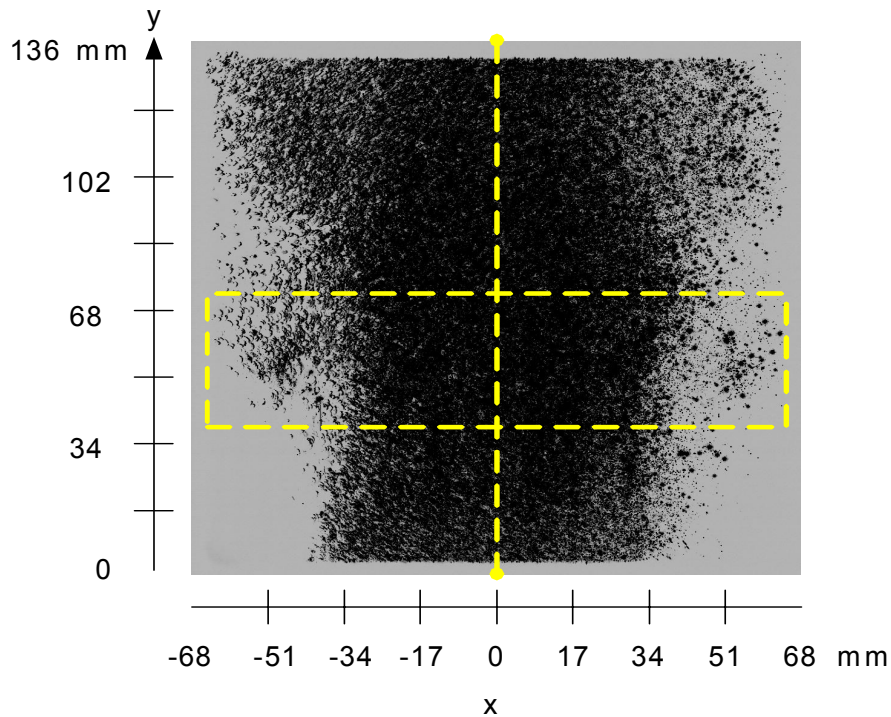


Figure (8.6): Phase-averaged image of bubble reflections in the observation window.

period. Results also show a time-dependence of the vertical bubble velocity during the excitation period. Comparison between vertical bubble velocities measured by means of DOS with data obtained by PIV (see Figures (8.7) and (8.3)) shows strong overprediction of the bubble velocity by DOS (reasons for biasing of DOS data are discussed in Section 7.3). As mentioned earlier, the trapped bubbles have the same velocity as the liquid in the vortex centre. Therefore, it seems that it is not possible to identify trapped bubbles by DOS (i.e. bubbles in the bubble ring) which have the same velocity as the traveling velocity of the vortex ring.

On the other hand, it must also be stressed that void fraction and velocity data are obtained by ensemble-averaging of the DOS signals obtained in the time intervals of $0.02s$ that possess the same phase shift. Since the velocity of the vortex ring obtained by the PIV vortex tracking method is about $0.27m/s$, the time interval of $0.02s$ corresponds to a vertical distance of about $5.5mm$. The void fraction generated by trapped bubbles would then be averaged over $\Delta y = 5.5mm$, which is comparable to the bubble size. Therefore, this resolution should be adequate for distinguishing trapped from non-trapped bubbles in ensemble-averaged void fraction and bubble velocity distributions.

Taking into consideration results from visualization tests that show strong deformations of the bubble ring due to instabilities in the shear layer, it appears that it is very difficult to estimate the vertical velocity of bubbles trapped in shear layer vortices by DOS. Anyway, the periodic variation of the void fraction clearly indicates the existence of coherent bubble structures in the shear layer. This, however, opens another interesting question. If the void fraction peak (i.e. increased bubble concentration) detected during some triggering phases can be connected with the existence of bubble rings, is it possible to estimate their velocity by determining the time shift of the peak between different vertical locations in the flow field? In order to illustrate this, additional DOS results accompanied by information obtained from PIV measurements are presented below.

Figure (8.8) shows void fraction and vertical bubble velocity at downstream position $y = 60mm$ and radial positions in the shear layer at $x = 50$ and $51mm$. If the bubble structure, detected with DOS (see periodic variation of the void fraction), had the same vertical velocity as the vortex ring ($0.27m/s$), it would have traveled across a vertical distance of say $10mm$ within $0.037s$. This time corresponds to the phase shift between the vertical positions $y = 50$ and $60mm$ (Figures (8.7) and (8.8)) in the shear layer and is only twice the chosen time interval ($2 \cdot 0.02s$). Because of the limited temporal resolution of the void fraction distribution, velocity estimates obtained in this way exhibit a large error.

However, additional measurements (Figure (8.9)) performed at higher vertical elevations ($y = 100mm$ and $y = 200mm$) for a point at $x = 48mm$ in the shear layer show clearly the existence of a phase shift of about $0.37s$ (see the time shift between two maxima ε_A and ε_B in Figure (8.9)). This time shift indicates that the bubble structure travels over the vertical distance of $100mm$ at a velocity of $0.27m/s$. Therefore, the detected void fraction peak may correspond to the bubble ring which travels at the same velocity as the vortex ring.

However, since the cluster of trapped bubbles in Figure (8.6) is surrounded by fluid with lower void fraction, rather the smaller peaks shown in Figure (8.8) and (8.9) are caused by the trapped bubbles. The broad void maximum appears to correspond to the big bubble cluster in between the vortices.

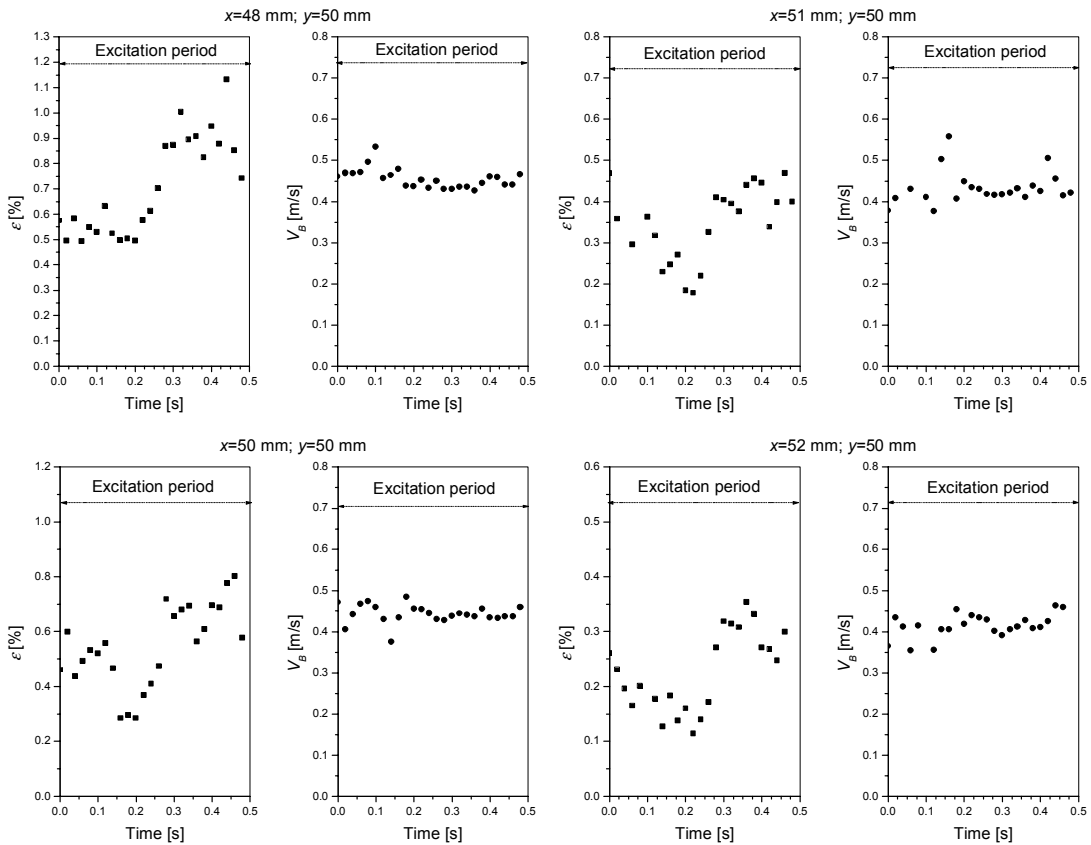


Figure (8.7): Variation of the phase-averaged void fraction and of the vertical bubble velocity measured by DOS during the excitation period at downstream position ($y = 50$ mm) and in the shear layer at radial positions $x = 48, 50, 51$ and 52 mm.

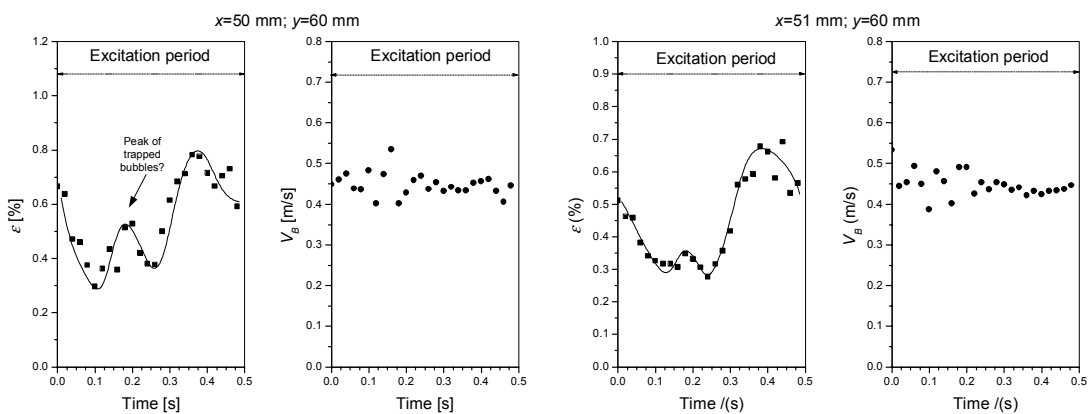


Figure (8.8): Variation of the phase-averaged void fraction and of the vertical bubble velocity measured by DOS during the excitation period at $y = 60$ mm and points in the shear layer at $x = 50$ and 51 mm.

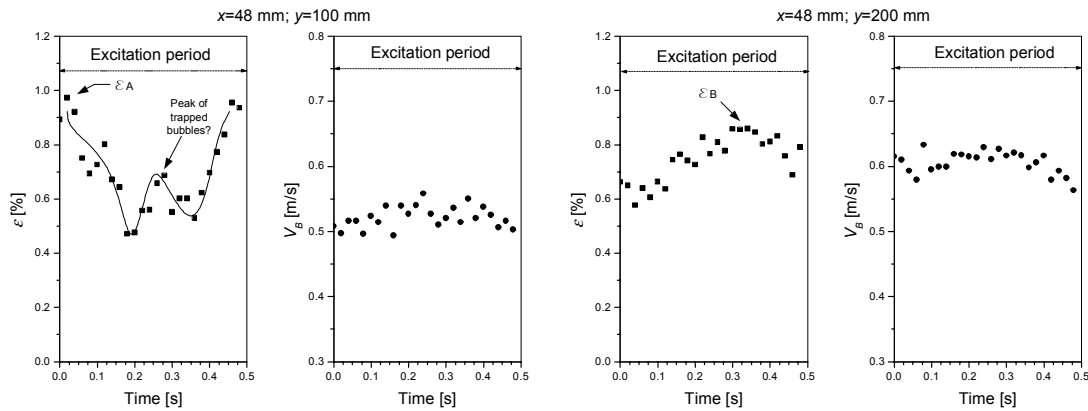


Figure (8.9): Variation of the phase-averaged void fraction and of the vertical bubble velocity measured by DOS during the excitation period at $y = 100$ and 200mm and at $x = 48\text{mm}$.

8.2.3 Correlation of PIV and DOS data

Since only DOS measurements can presently provide quantitative void fraction data, and PIV is required for velocity field measurements, the possibility of correlating data obtained with the two techniques has also been considered.

Since the simultaneous use of PIV and DOS is not feasible for technical reasons (laser light impinging on DOS sensors), only the possibility of correlating the coherent parts of PIV and DOS results can be discussed.

The promising DOS results for the time-dependent void fraction in case of triggered jets could in principle be correlated with synchronized PIV data for velocities and vorticities obtained at the same locations. However, production of PIV data with, e.g., 25 time steps per excitation period of 0.5s cannot be obtained in a single experiment with a maximum available frequency of 15Hz . This would mean that PIV data would have to be produced in series of tests with different phase shifts between vortex excitation and PIV shots. With a PIV frequency of 10Hz , for instance, one would thus have to perform 5 experiments with the phase shifts 0ms , 20ms , 40ms , 60ms and 80ms , respectively. It is obvious that the performance and analysis of such experiments would be very time-consuming and therefore could not be carried out within the time available within this project. They are also delicate because the reproducibility of all relevant experimental conditions has to be ensured.

Evidently, the value of this kind of results is also limited since only the coherent part of the fluctuations can be correlated. For technical and experimental reasons it is thus preferable to develop a photographic technique that enables void (or bubble density) measurements simultaneously with the PIV experiments.

Conclusions:

- The DOS technique alone cannot be used to detect bubble trapping. It can only be shown that the measurements are consistent with PIV results if bubble trapping occurs.
- The greatest profit from phase-averaged DOS measurements (equally from simple void detection sensors) can be drawn if results for space- and time-dependent, coherent bubble densities or void fractions are produced with adequate spatial resolution. The temporal resolution achieved with optical sensors is high enough. The correlation of these results with PIV data

requires, however, that series of PIV experiments with different phase shift between vortex excitation and laser pulsing must be performed, if the same temporal resolution for equal synchronization is to be achieved with both techniques. In order to obtain good, consistent results with PIV and DOS measurements, fairly high demands on reproducibility have to be met.

- The PIV technique, combined with a photographic technique using backlighting, enables one to identify bubble trapping and to verify the required trapping conditions discussed in Chapter 5.

8.3 Survey of experimental results for test *TTF2V1.B*

Improved test conditions (*TTF2V1.B*) (see Section 8.1) were used to study *the frequency effect* on the development of large eddy structures and bubble trapping inside them. The triggering amplitude was increased until distinct bubble rings emerged and was then kept constant during the experiments with different excitation frequencies. In order to study the effects of bubbles on mean and phase-averaged properties of naturally-developing and triggered jets, it was necessary to conduct tests with both, single-phase naturally-developing and single-phase triggered jets.

8.3.1 Single-phase jets

Profiles of mean properties

The downstream development of the mean liquid velocity, of the standard deviation of the vertical liquid velocity and of the azimuthal vorticity for naturally-developing and triggered single-phase jets (cases *f1*, *f2* and *f3*) are presented in this chapter. The data for triggered jets have been continuously acquired at $15Hz$.

Naturally-developing single-phase jets

The mean liquid velocity and the standard deviation of the vertical liquid velocity are presented in Figure (8.10). As it was already found in the previous chapter, the measured *rms* values at the jet exit are about 3% of the mean velocity despite the filtering effect of the PIV method. The measured *rms* peaks show the existence and development of shear layers. The azimuthal vorticity component presented in Figure (8.11) is produced by the mean shear, $(\frac{\partial V_L}{\partial x})$.

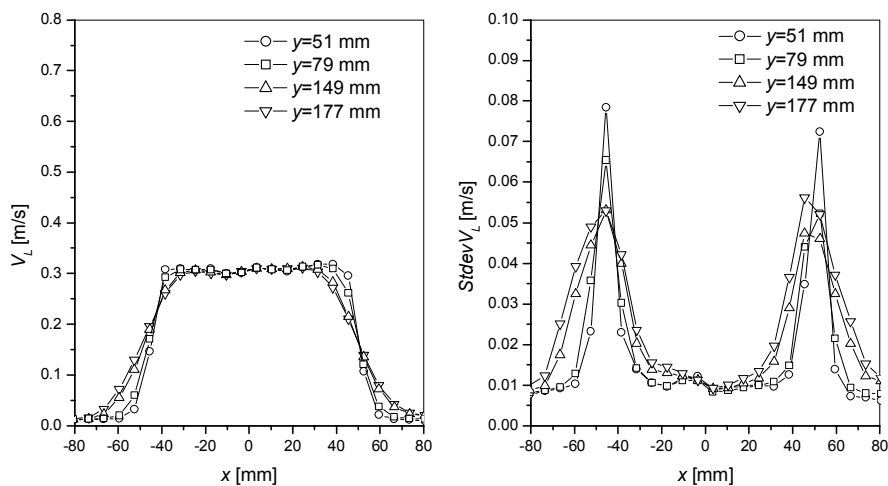


Figure (8.10): Mean liquid velocity field (left) and standard deviation of the vertical liquid velocity field (right) for naturally-developing single-phase jet.

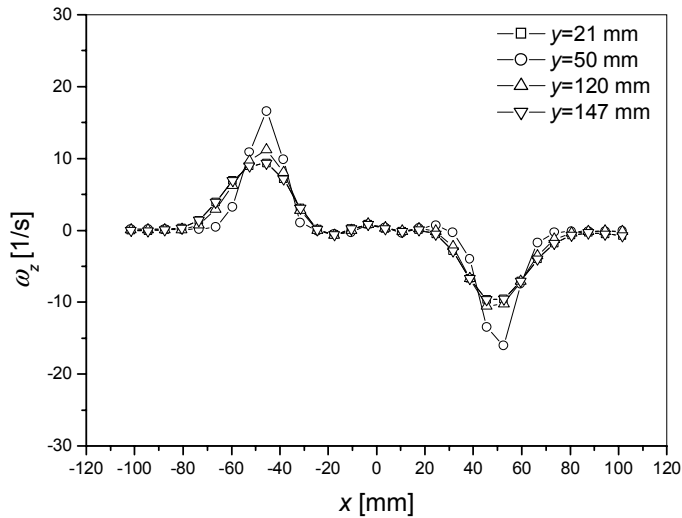


Figure (8.11): Mean azimuthal vorticity component of the liquid velocity for the naturally-developing single-phase jet.

Triggered single-phase jets

Modulating the jet shear layer by means of the coaxial water layer injected close to the jet exit also affects the mean vorticity. Furthermore, phase-averaging of the experimental data is helpful for studying the interaction of bubbles with large-scale liquid structures of a jet (see previous section).

Effects of the excitation frequency can be studied by employing the sophisticated data acquisition procedures discussed and listed in Appendix D. The results for triggered single-phase jets show that the vortices grow more slowly in the y direction if St is increased.

In order to explore the influence of forcing on mean and turbulent properties, experimental results obtained for triggered jets are compared with results obtained for the corresponding naturally-developing single-phase jet (the same superficial liquid velocity and void fraction at the nozzle exit). The results for triggered cases are presented in Figure (8.12), whereas the results for naturally-developing single-phase jets were presented in the preceding section.

Forcing actually does not cause dramatic changes in the mean fields at the different St numbers explored. The mean velocities are just slightly higher than for naturally developing jets. The mean profiles spread faster under forcing and entrainment is enhanced. On the other side, the measured standard deviation of the vertical liquid velocity shows a strong enhancement of the turbulence level inside the jet core, while in the mixing layer this effect is less pronounced. This enhancement is mainly the result of modulation of the velocity i.e. not real turbulence. The fact that it is highest for $St = 0.3$ suggests that it is related to the preferred jet-instability (jet column mode). Variation of the excitation frequency has a measurable effect on the mean velocity and the turbulent fluctuations in the jet center and in the shear layer. The mean azimuthal vorticity fields of the liquid presented in Figure (8.13) also depend on the forcing frequency.

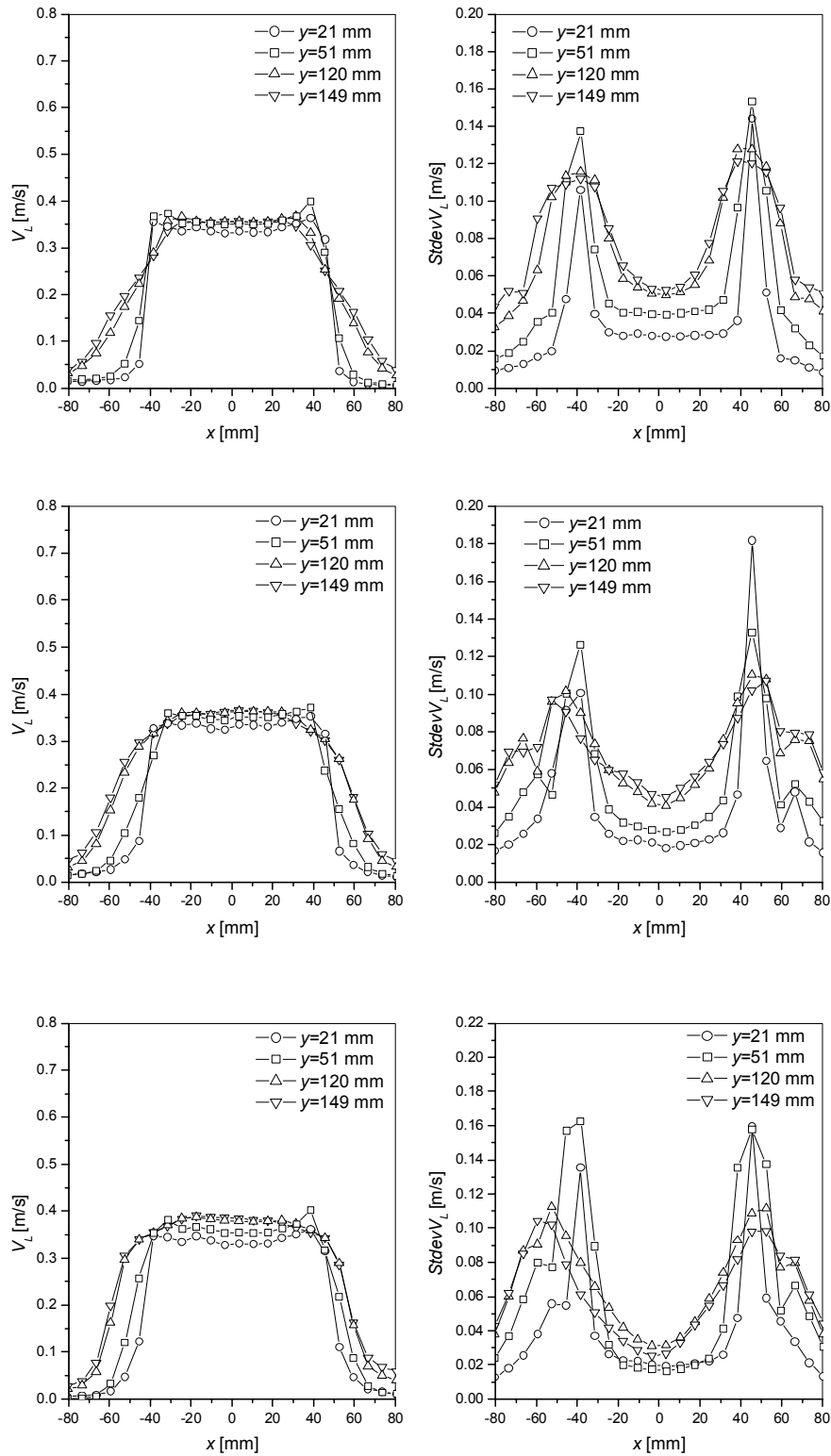


Figure (8.12): Mean liquid velocity field and standard deviation of the vertical liquid velocity field for triggered single-phase jet (case f1-top, case f2-middle, case f3-bottom).

8.3 Survey of experimental results for test TTF2V1.B

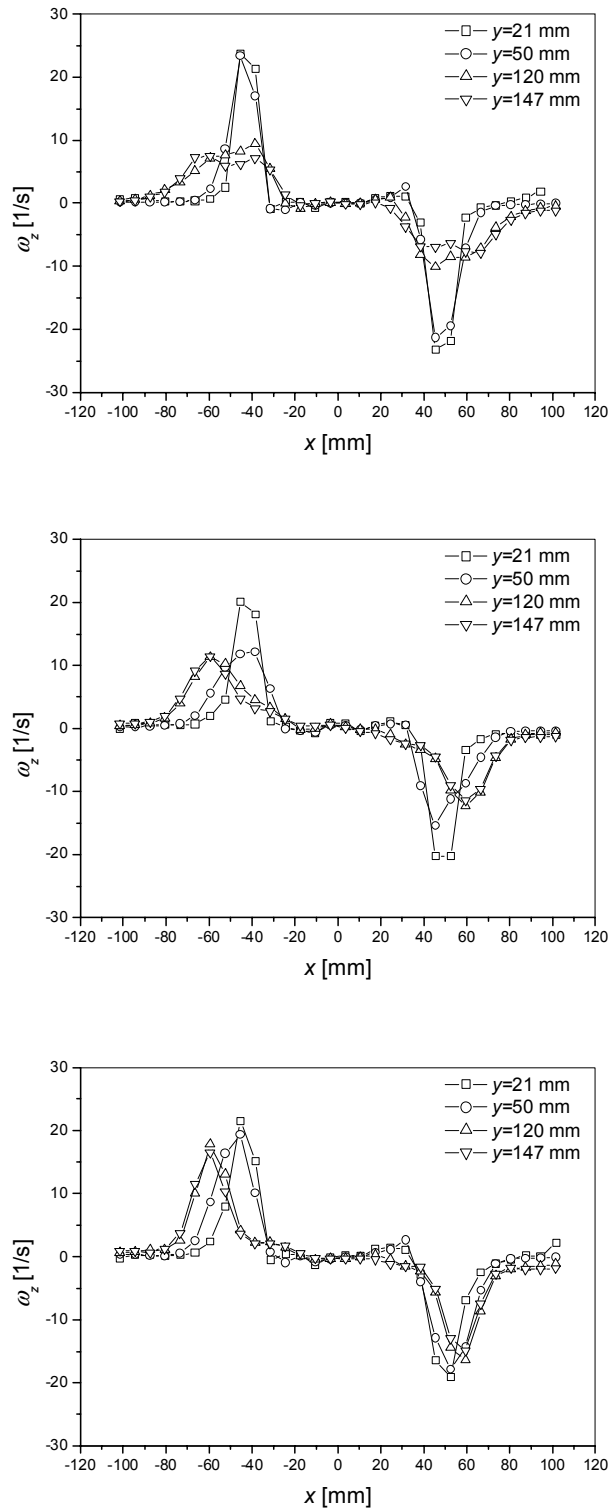


Figure (8.13): Mean azimuthal vorticity component of the liquid velocity for the periodically triggered single-phase jet (case f1-top, case f2-middle, case f3-bottom).

Phase-averaged properties

Scalar maps presented in Figure (8.14) illustrate fields of phase-averaged properties of single-phase jets triggered periodically at frequencies corresponding to $St = 0.3$; 0.6 and 0.84 , respectively (cases $f1$, $f2$ and $f3$).

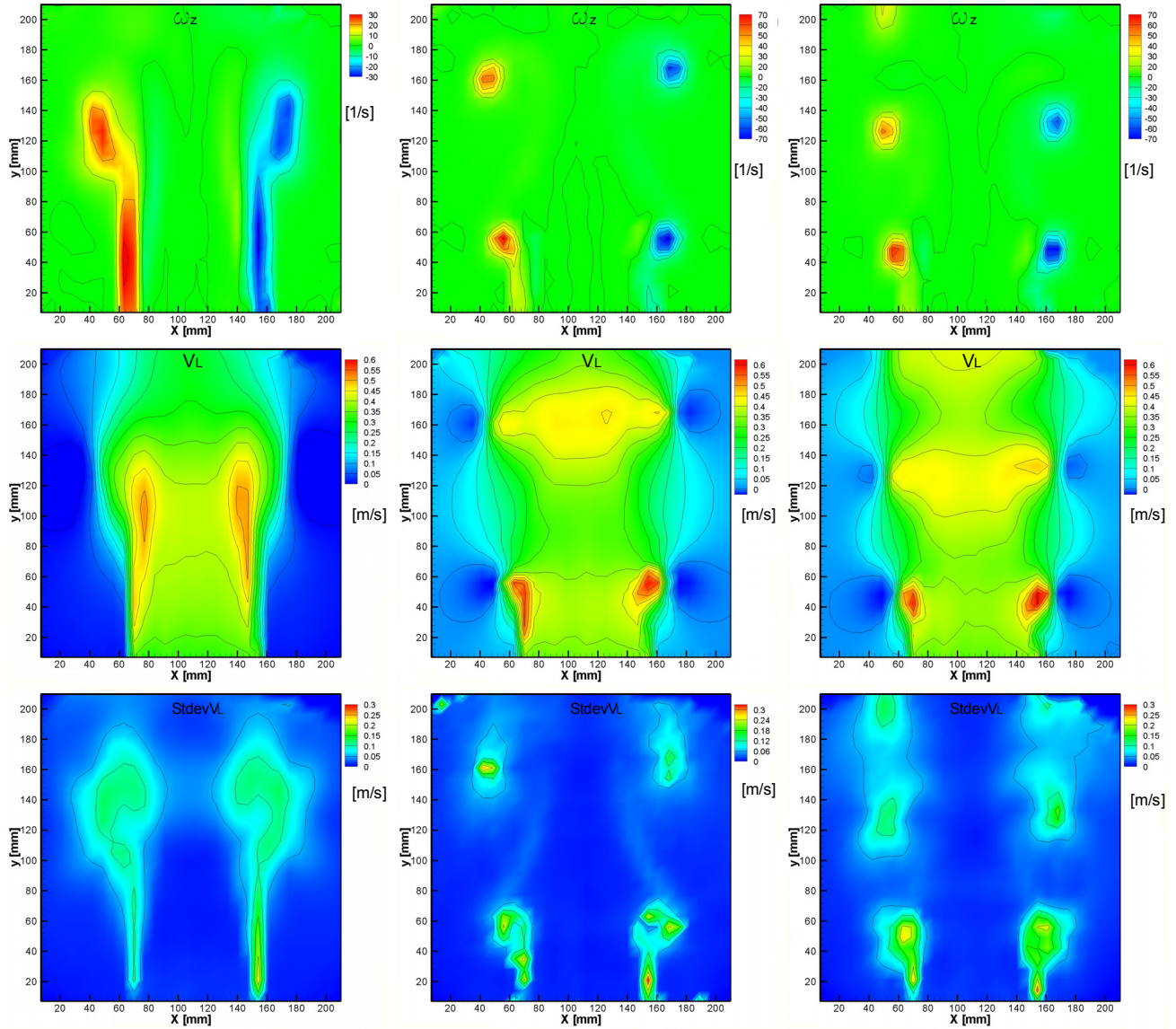


Figure (8.14): Phase-averaged azimuthal vorticity component (first row), vertical velocity component (second row) and standard deviation of the vertical velocity component (third row) for periodically-triggered single-phase jets (first column- $f1$, second column $f2$ and third column $f3$)

The presented contour maps of phase-averaged azimuthal vorticity fields of the liquid show the existence of large coherent structures inside the shear layer. Thanks to the periodic production of the coherent structures as well as to the synchronized data acquisition, some properties such as the velocity, the development and growth of the vortices as well as interactions with bubbles can be systematically studied.

The vorticity is concentrated inside the shear layer, and large coherent elliptical structures can

be observed. In the case of low-frequency triggering, considerable vorticity is also produced by the mean shear in between the vortices (pictures in first column of Figure (8.14)). Forcing at higher Strouhal number raises the peak vorticities and reduces the distance between two consecutive vortex rings. The measured maximum vorticity is about $70s^{-1}$, except in the case *f1* with $St = 0.3$.

In the vortices peaks of the phase-averaged mean values and turbulence properties are found in all cases.

Vortex tracking

The acquisition method called vortex tracking (see acquisition schemes in Appendix D) is applied to observe velocity, positions and deformations of the vortex rings. All presented vorticity fields are phase-averaged. If the excitation of the jet is performed with frequencies that correspond to $St = 0.6$ and 0.84 , two vortex rings can be observed within the field of view, whereas for the case with $St = 0.3$, only one elongated ring is presented (see Figure (8.14)). Therefore excitation frequencies of 2 and $3Hz$ have been chosen to demonstrate the movement of the vortex rings in the field of view.

Case f2 (St=0.6, $f_2 = 2Hz$)

Six consecutive positions of the vortex ring for case *f2* are presented in Figure (8.15). Six phases are captured within an excitation period.

Based on these results the following conclusions can be drawn:

- The measured distance between two consecutive vortex rings is about $110mm$, while the phase shift is $500ms$, which corresponds to the excitation frequency of $2Hz$. The estimated vortex velocity is about $0.22m/s$.
- The positions of the large vortices at positions further downstream are no longer symmetric, because of vortex ring deformations caused by instabilities in the shear layer.

In order to check consistency and reproducibility of the data obtained by the *vortex tracking method*, the scalar maps of the phase-averaged liquid vorticity field for the two phases lying at the beginning of consecutive excitation periods are presented in Figure (8.16). Both vortex rings are located at the same vertical position in the flow field. Furthermore, the same asymmetry of the upper ring can be observed in both cases.

Case f3 (St=0.84, $f_3 = 3Hz$)

An example of results obtained by vortex tracking acquisition for test case *f3* is presented in Figure (8.17). Five consecutive positions of the vortex ring are captured. The measured distance between two consecutive vortex rings is about $80mm$, while the phase shift is $333ms$, which corresponds to the excitation frequency of $3Hz$. The estimated vortex velocity is about $0.24m/s$.

The excitation at higher frequency produces vortex structures that travel with somewhat higher speed. The distance between vortex rings becomes smaller and the instabilities affect coherent structures only further downstream.

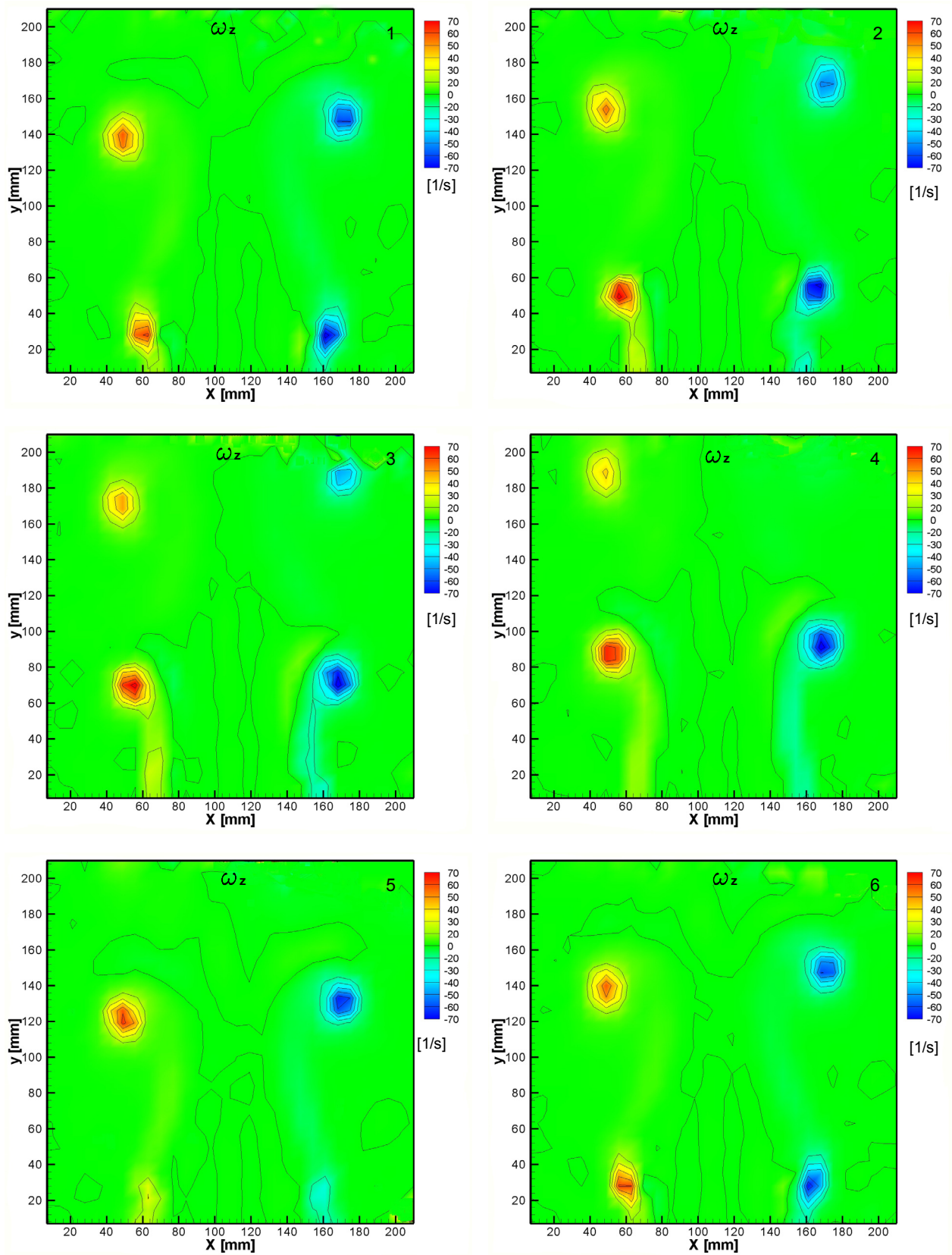


Figure (8.15): Six consecutive phases captured with the vortex tracking acquisition method.

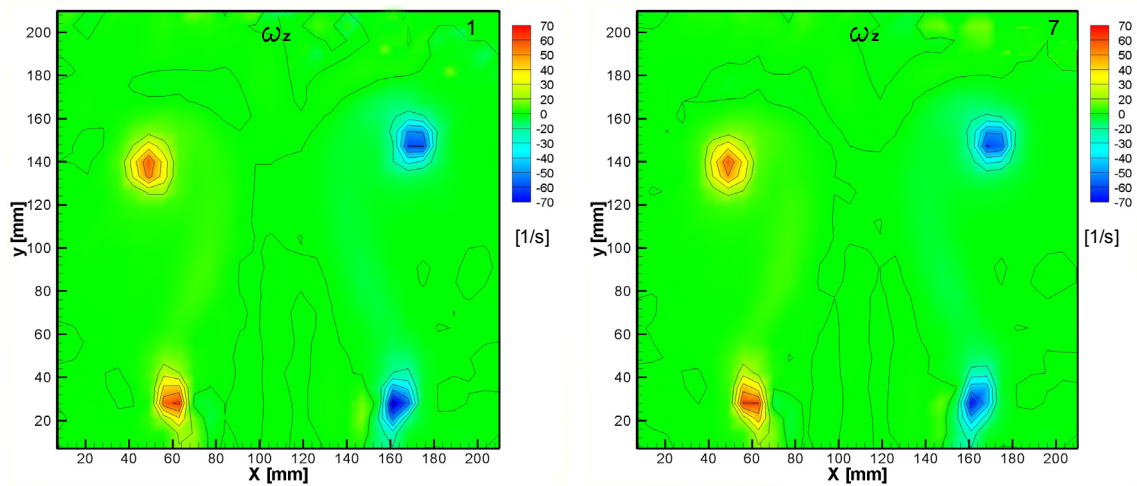


Figure (8.16): Positions of vortex rings at the beginning of the excitation period. Since six recordings are captured within an excitation period, the first (left) and the seventh phase (right) show the same vortex position.

Comparison between mean and phase-averaged properties for a periodically-triggered single-phase jet

A comparison of time-averaged data obtained with normal $15Hz$ PIV acquisition without coordination of excitation and sampling (scalar maps on the left side) and encoder-triggered phase-averaged PIV acquisition (scalar maps on the right side) is presented in Figure (8.18) for case $f2$ and in Figure (8.19) for case $f3$. The images in the first row represent azimuthal liquid vorticity fields, in the second row vertical velocity components and in the third row standard deviations of the vertical velocity component.

Normal acquisition can be used for obtaining mean and fluctuating values, while triggered acquisition is necessary to obtain phase-averaged data. This comparison clearly demonstrates the advantage of the triggered acquisition. Excitation of the jet leads to concentration of the shear layer vortices in coherent ring structures that move in the vertical direction with a certain speed. The coherent parts of size, positions and traveling velocity of these structures can only be obtained by phase-averaging.

These results show that controlled excitation at fixed frequency and with defined amplitude, achieved by producing small flow surges at the jet nozzle, causes large eddy structures to develop at regular intervals. Synchronization between production of the coherent structures and data acquisition combined with phase averaging of the experimental data are found to be useful tools for the systematic study of these structures.

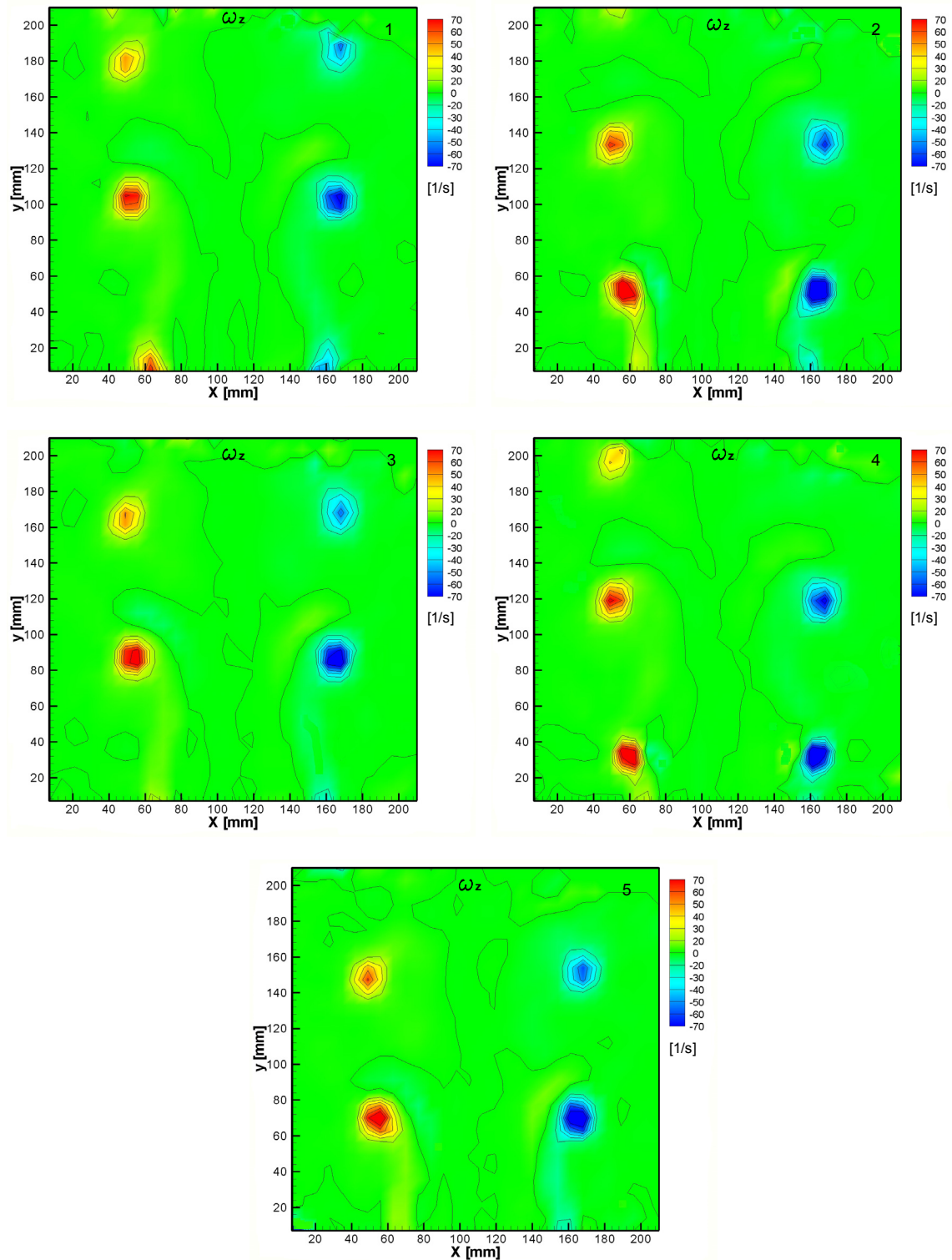


Figure (8.17): Five consecutive phases captured with the vortex tracking method.

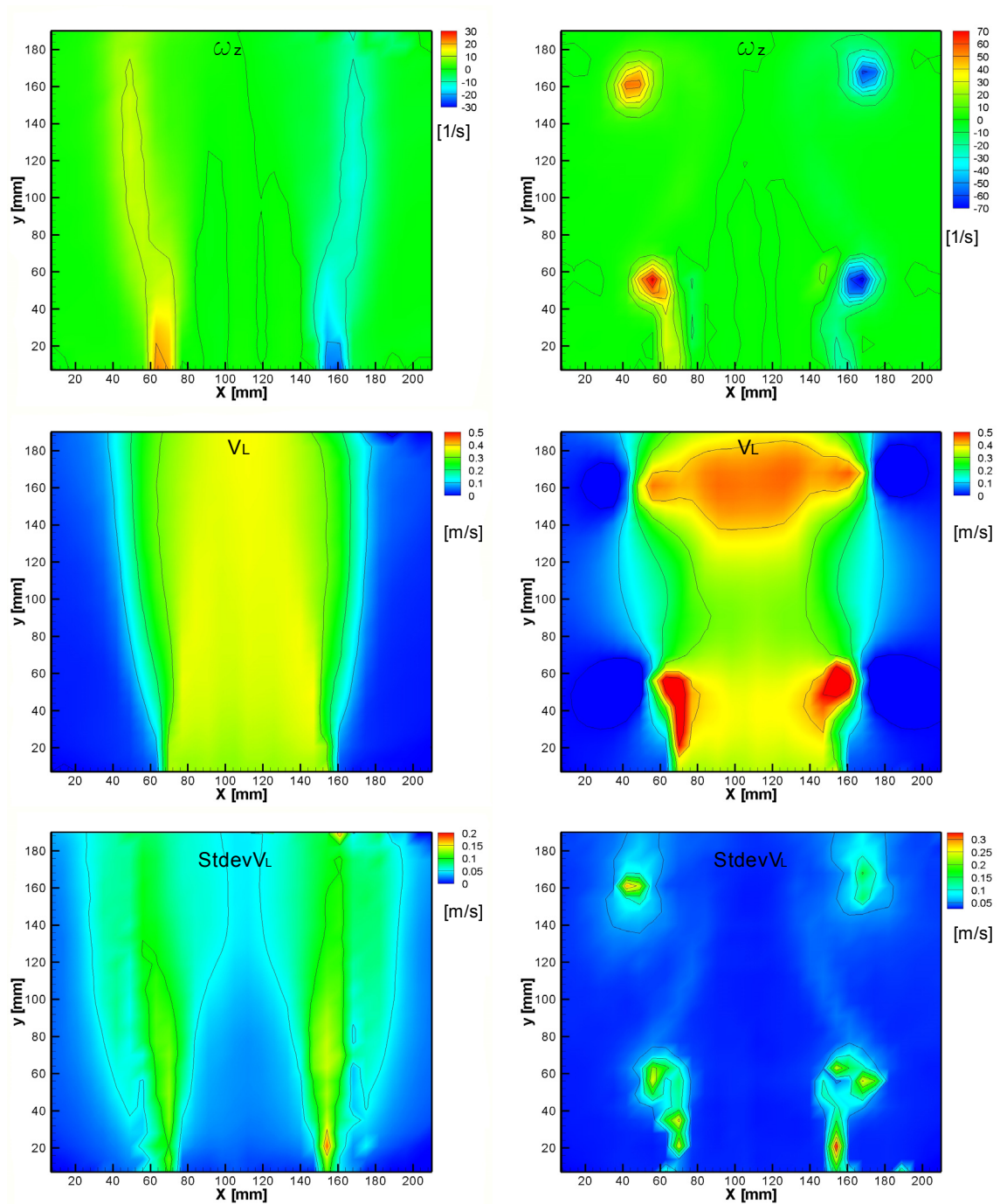


Figure (8.18): Mean azimuthal liquid vorticity field, vertical liquid velocity and standard deviation of the vertical liquid velocity in a triggered jet obtained by normal 15 Hz PIV acquisition (left) and by triggered PIV acquisition (right) for case f2 (2Hz). The fields on the right side are phase-averaged, whereas those on the left are simply time-averaged.

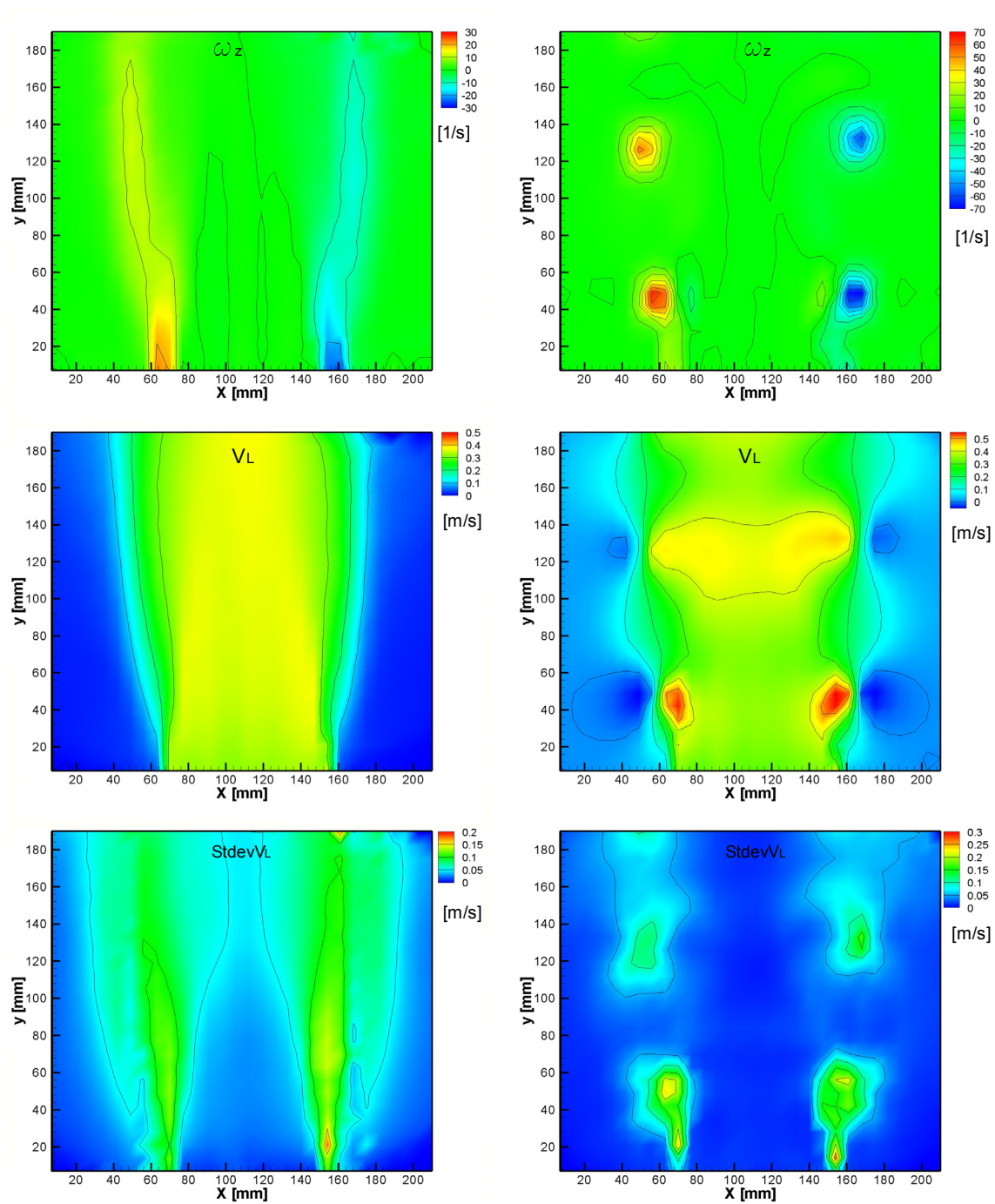


Figure (8.19): Mean azimuthal liquid vorticity field, vertical liquid velocity and standard deviation of the vertical liquid velocity in a triggered jet obtained by normal 15 Hz PIV acquisition (left) and by triggered PIV acquisition (right) for case f3 (3Hz). The fields on the right side are phase-averaged, whereas those on the left are simply time-averaged.

8.4 Effects of excitation frequency

8.4.1 Test f1

The triggering-velocity function for this test is presented in Figure (8.20). It represents the velocity of the excitation flow at the exit of the triggering nozzle that corresponds to the modulated flow rate. The excitation frequency is 1Hz , corresponding to $St = 0.3$.

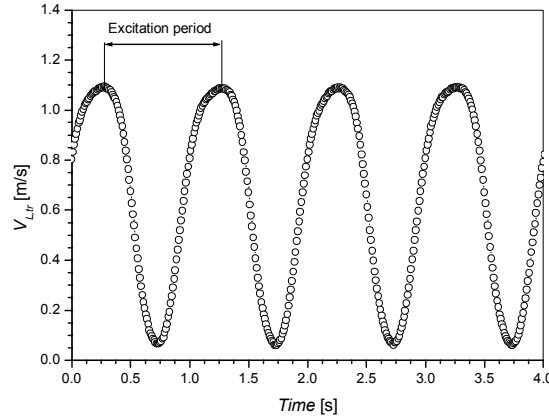


Figure (8.20): Modulated excitation velocity at the exit of the triggering nozzle for case f1 (1Hz).

Phase-averaged azimuthal vorticity fields of the liquid for the single-phase (left) and the bubbly jet (right) are compared in Figure (8.21). Obviously, the bubbles interact very strongly with the large vortices and affect the liquid velocity as well as the vorticity fields. The increased vorticity between the large structures is produced by the mean shear. The contour map of the liquid vorticity for the single-phase case (bottom left image) shows large elliptical structures at about $y = 100\text{mm}$ from the nozzle exit. For the bubbly jet (vorticity contour map at right bottom corner), the captured phase is identified by the position of the vortex ring center at about $y = 150\text{mm}$ above the nozzle exit. Due to an inconsistency in data acquisition, a small time shift may exist between these two experiments. It, however, has no physical importance. The modification of the large structures is most probably caused by the presence of bubbles (compare vorticity fields presented in Figure (8.21)). The color changes (i.e. gray level changes) presented in the contour map of the vertical liquid velocity quantify the acceleration of the liquid caused by the bubbles.

The phase-averaged image of bubble reflections presented in Figure(8.22 b) illustrates bubble clustering inside and above the large vortices.

In order to ascertain whether the trapping conditions presented in Section 5.1.2 are fulfilled or not, profiles of the azimuthal vorticity field of the liquid, as well as the phase-averaged bubble and liquid vertical velocity components are presented in Figure (8.22 a), (8.22 c) and (8.22 d) at levels above the elongated vortex ring formed in the shear layer around the jet (right picture in Figure (8.21)). Measured maximum vorticity at the vortex center is about 20s^{-1} (Figure (8.22 a)). The vortex shape is elliptical. The photographic recordings reveal that bubble trapping appears to happen and that bubbles accumulate on the major axis of the elliptical vortex which has a half-length of $30 - 35\text{mm}$.

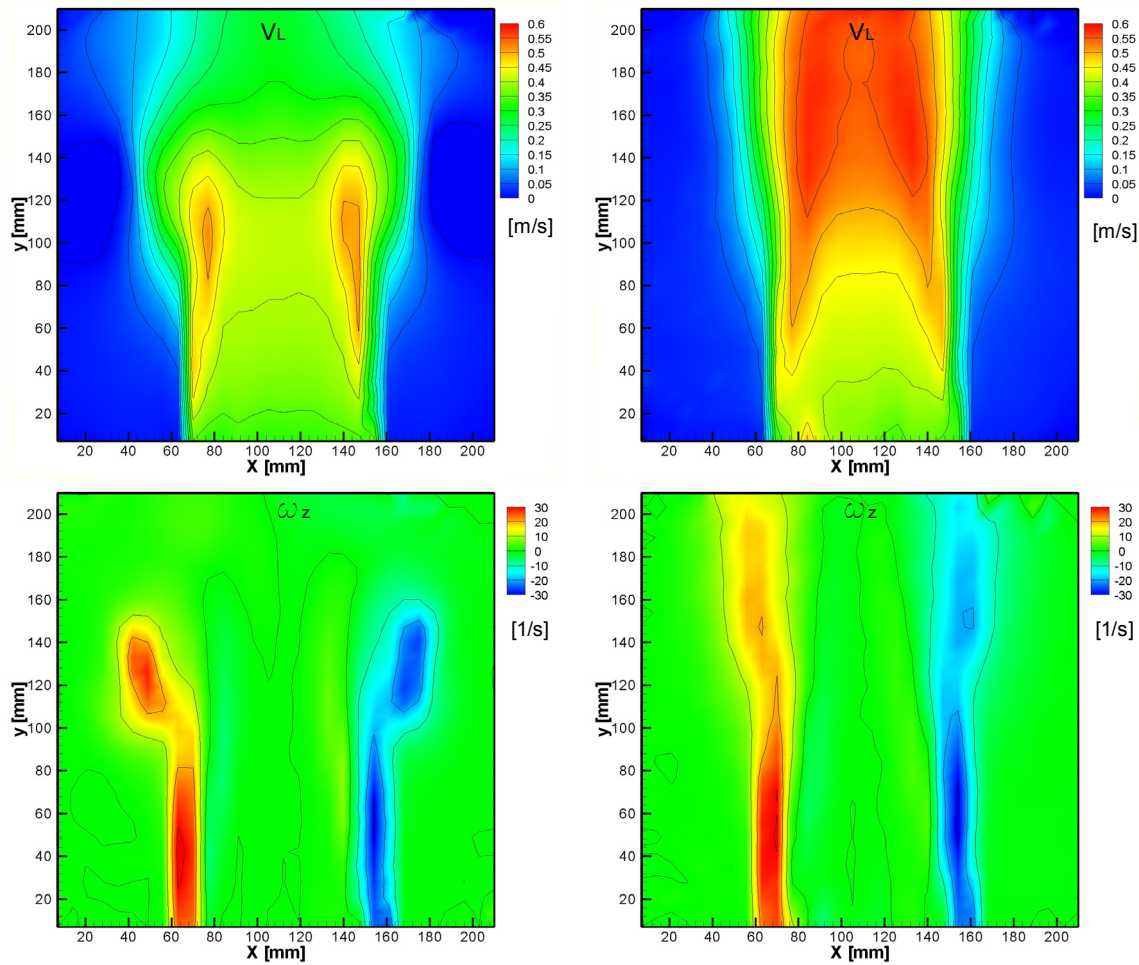


Figure (8.21): Phase-averaged azimuthal vorticity field (bottom) and velocity field (top), of the fluid for single-phase jet (left) and bubbly jet (right). The jet centerline is at $X=108\text{mm}$.

The condition for bubble trapping cannot be calculated by the equations presented in Chapter 5, because the vortex structure is too elongated. If the vortex was circular with a radius of 35mm , the Vortex Froude number of 0.36 and the Vortex Trapping parameter of 2.9 would have indicated that some bubbles have been trapped.

The vertical liquid velocity in the vortex (Figure (8.22 d)) is slightly smaller than the bubble velocity at the same positions (Figure (8.22 c)). At the indicated radius, the bubble velocity is about equal to the liquid velocity in the vortex center. Even though the peak vorticity is not very high, a bubble ring has been formed.

8.4.2 Test f2

The triggering-velocity function for this test, conducted at higher frequency than $f1$, is presented in Figure (8.23). It represents the velocity of the excitation flow at the exit of the triggering nozzle that corresponds to the modulated flow rate. The excitation frequency is 2Hz , corresponding to $St = 0.6$.

Two different phases (called here P_1 and P_2), that correspond to different vertical positions of the vortex ring in the flow field are examined in this section. The time shift between the phases was about 154ms . The results and discussion on bubble trapping are presented in the following

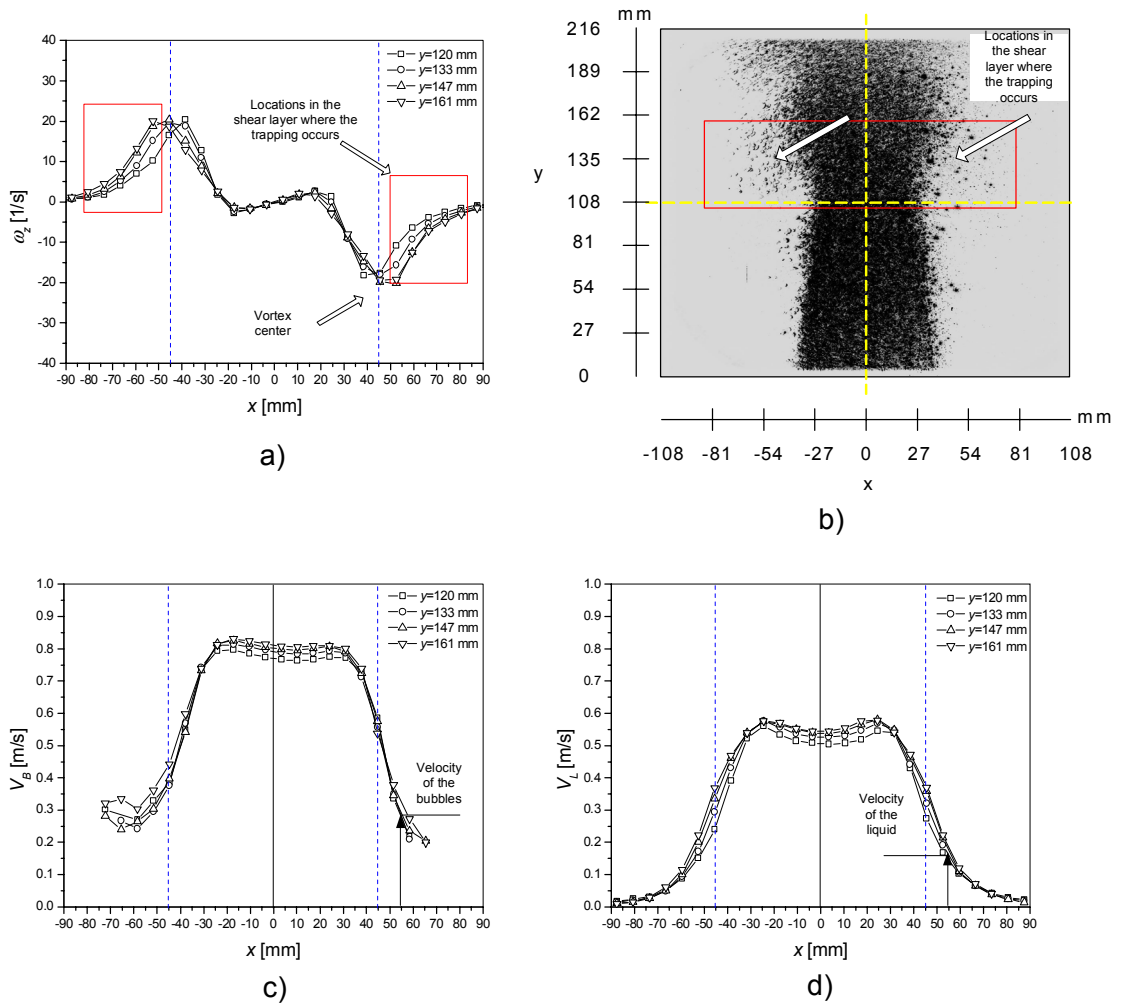


Figure (8.22): Horizontal profiles of phase-averaged azimuthal vorticity of the liquid through the vortex in the shear layer (a), phase-averaged image of bubble reflections in the observation window (b), horizontal profiles of phase-averaged vertical velocity of the bubbles (c) and of the liquid through the vortex in the shear layer (d).

subsections. For phase P_1 , which corresponds to the vortex ring center located at $y = 60$ mm, only PIV data are presented. For phase P_2 , which corresponds to the vortex ring located at $y = 100$ mm, both DOS and PIV data are presented.

8.4.2.1 Phase P_1

Phase-averaged properties obtained by PIV

Phase-averaged vertical velocity components of the bubbles and the liquid, as well as the azimuthal vorticity field of the liquid are presented in Figures (8.24) and (8.25), respectively. The contour maps show the position and the size of the large vortices. The captured phase (phase P_1) shows the position of a vortex ring between 40 and 80 mm from the nozzle exit.

Vortex tracking

The contour map of the phase-averaged azimuthal vorticity of the liquid obtained by the vortex tracking method, presented in Figure (8.26), shows the position of the same vortex ring but

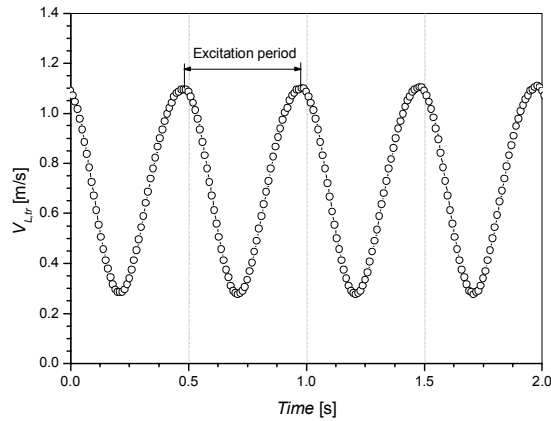


Figure (8.23): Modulated excitation velocity at the exit of the triggering nozzle for case f_2 (2Hz).

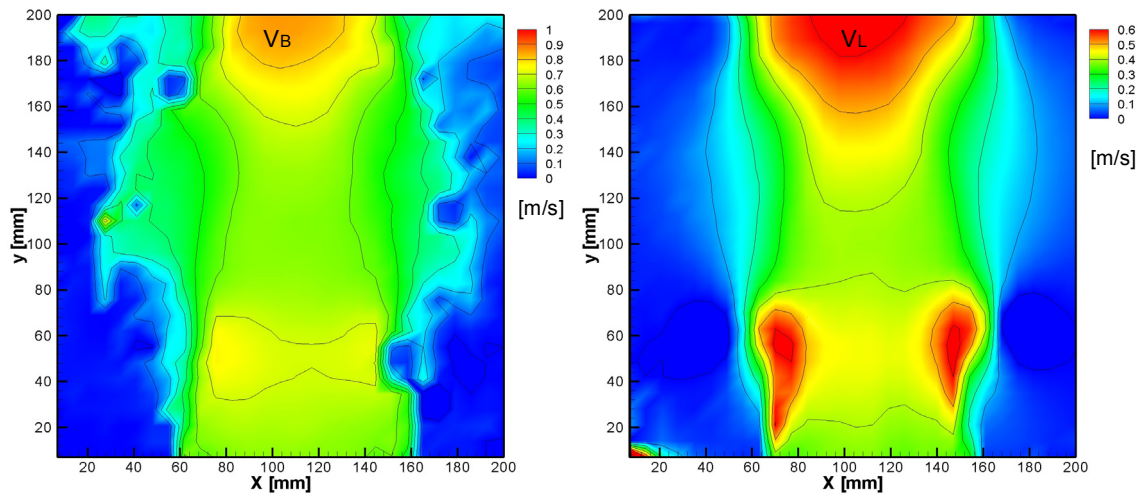


Figure (8.24): Phase-averaged vertical velocity field of the bubbles (left) and of the liquid (right).

shifted downstream by about 65mm for a phase shift of 250ms . The resulting vortex velocity is about 0.26m/s .

Bubble trapping

The liquid velocity peaks (presented in Figure (8.24)) correspond to the position of the vortex ring between 40 and 80mm . The contour map of the vertical bubble velocity shows a structure inside the vortex ring on the right-hand side. In order to further explore this measurement, a comparison between bubble and liquid vertical velocities at $y = 49\text{mm}$, 63 , 70 and 77mm is presented in Figure (8.27). The fact that the bubble velocity is equal to the vortex velocity is an indication that the bubbles are trapped inside the vortex ring. Actually, the bubbles are trapped close to the boundary of the vortex. This phenomenon can cause an absence of bubbles (scalar map in Figure (8.24)) and a bubble velocity peak presented in Figure (8.27 a) at $y = 49\text{mm}$ close to the vortex center (position at $x = 45 - 50\text{mm}$). The bubbles that come from the inner part of the jet and enter the large structures can be imagined to perform a semicircle around the

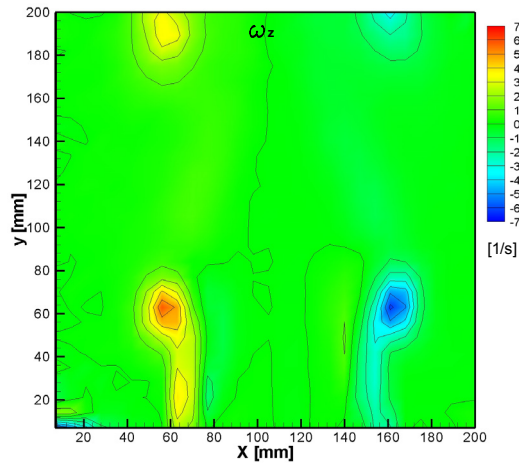


Figure (8.25): Phase-averaged azimuthal vorticity liquid. Center of the jet is at $X=108\text{mm}$.

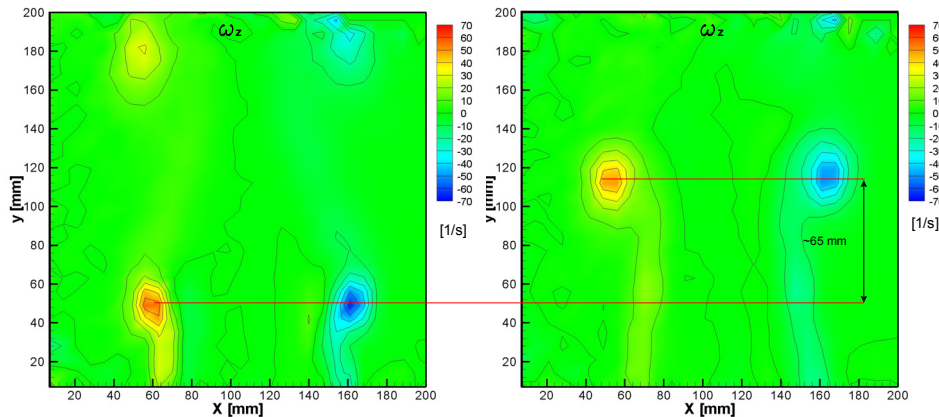


Figure (8.26): Velocity of the vortex structures obtained by vortex tracking tracking method. Center of the jet is at $X=108\text{mm}$.

vortex center. Having arrived at the opposite side of the vortex, bubbles slow down and continue to travel with the same velocity as the vortex ring. Thus, the bubble ring is formed, i.e. bubbles are trapped.

The estimated vortex ring velocity is about 0.26m/s (result obtained by the vortex tracking method presented and discussed above, see Figure (8.26)), which is slightly higher than both, bubble and liquid vertical velocities (0.25m/s).

Due to instabilities of the vortices, the torus shape of the vortices and the bubble rings can be destroyed at some vertical distance from the nozzle exit. These phenomena are explored in more detail in the following sections.

Phase-averaged profiles of the vertical velocity of bubbles and liquid as well as of the azimuthal vorticity below (at $y = 49\text{mm}$), across (at $y = 63\text{mm}$) and above the vortex ring (at $y = 70$ and 77mm) are shown in Figures (8.25), (8.27 a), (8.27 b) and (8.27 c). These data are presented in order to compare bubble and liquid velocities in and above the vortex ring. The velocity of trapped bubbles inside the vortex ring is approximately the same as that of the liquid in the vortex center. The bubbles have higher velocity than the liquid at the same location apart from a spurious minimum shown in Figure (8.27 a). The measured maximum vorticity at the vortex

center is about $55s^{-1}$.

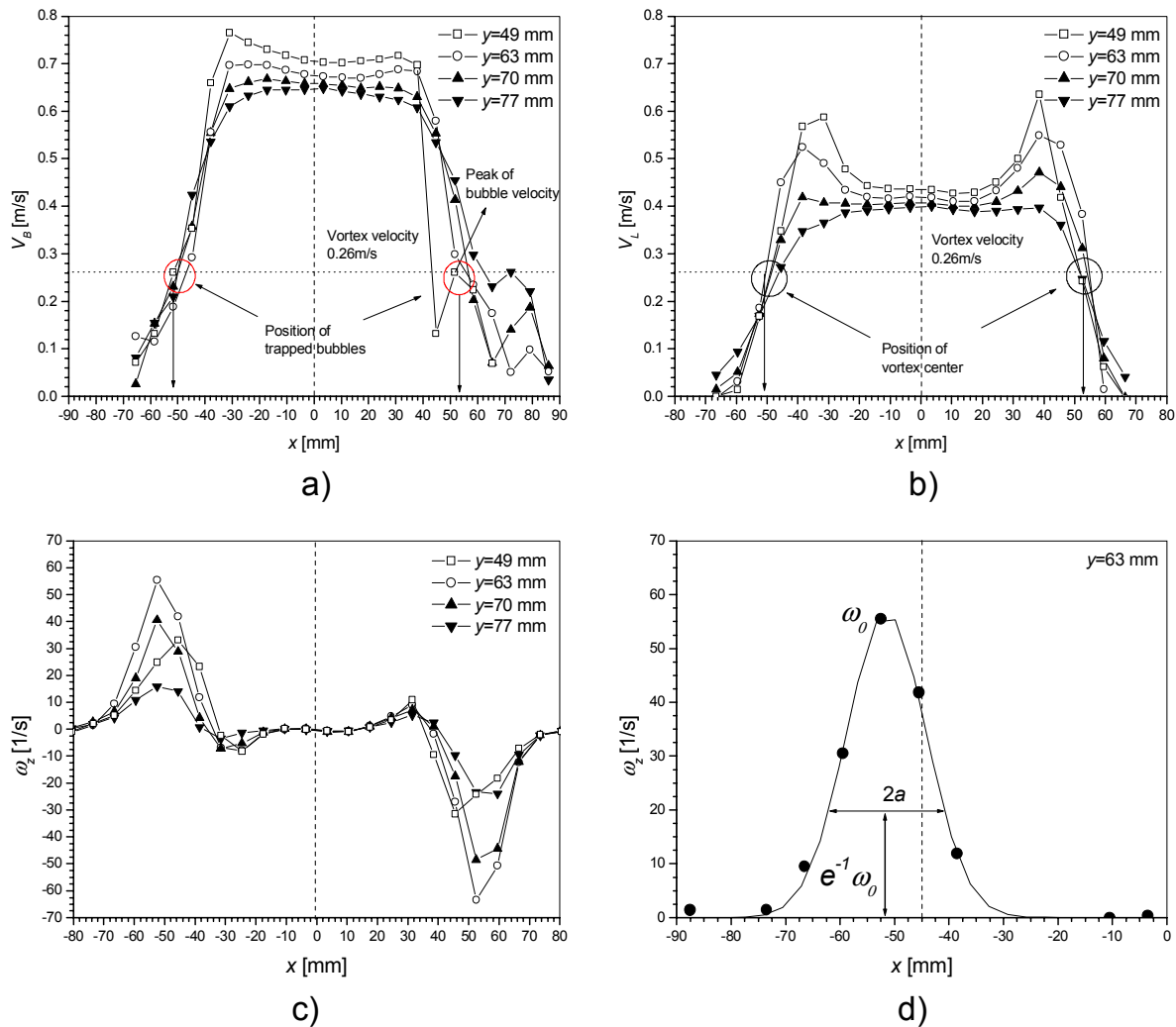


Figure (8.27): Phase-averaged velocity profiles of the bubbles (a), of the liquid (b), and of azimuthal vorticity of the liquid (c) as well as Gaussian fit of the azimuthal vorticity of the liquid across the vortex center (d).

Figure (8.27 d) shows a Gaussian fit of the azimuthal vorticity of the liquid through the vortex center at $y = 63mm$. The vortex radius estimated from this fit is about $11.25mm$. The terminal bubble rise velocity for $4mm$ bubbles is $0.24m/s$. Based on these values, the Vortex Trapping parameter is 2.5, while the Vortex Froude number is 0.85. The minimum values required for trapping of the bubbles inside a Gaussian vortex with radius of $11mm$ calculated with the criteria presented in Section 5.1.2. are the Vortex Trapping parameter of 3 and the Vortex Froude number of 1.2. Basically the trapping conditions are not far for being fulfilled.

Single phase vs. bubbly jet

Phase-averaged azimuthal vorticity fields of the liquid for single-phase (left) and bubbly jets (right) are compared in Figure (8.28). A different time origin of data acquisition (estimated difference of about $85ms$) exists between these two experiments. The measured peak vorticity of the liquid in the bubbly jet is slightly smaller, vortices are more elongated and the liquid

velocity field is affected by the presence of bubbles. The travelling velocity of the vortex rings is also slightly larger for the bubbly jet. The vertical-velocity profile of the liquid in between vortex rings at $y = 110\text{mm}$ in the case of the bubbly jet shows a radial jet contraction of about 30mm . This value is obtained from the distortion of the 0.3m/s isolines. This effect is apparently caused by buoyancy. The contraction shown in the single-phase case is a result of velocity modulation in the shear layer (see Figure (8.28)).

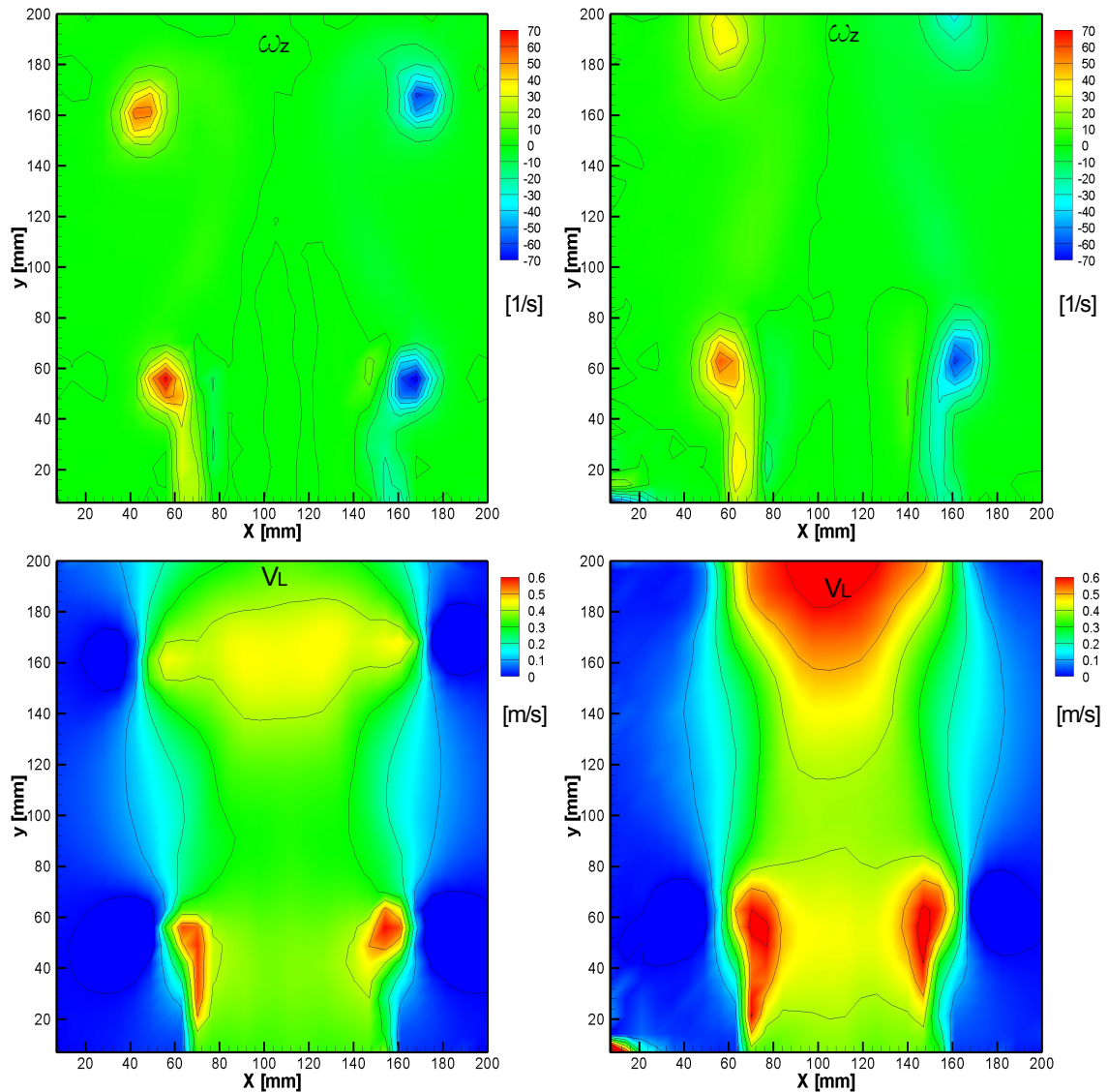


Figure (8.28): Phase-averaged azimuthal vorticity field (top) and vertical velocity (bottom) of the liquid for single-phase (right) and bubbly jet (left). A small time shift exists between these two experiments due to an inconsistency in data acquisition. Center of the jet is at $X=108\text{mm}$.

8.4.2.2 Phase P_2

Phase-averaged properties obtained by PIV

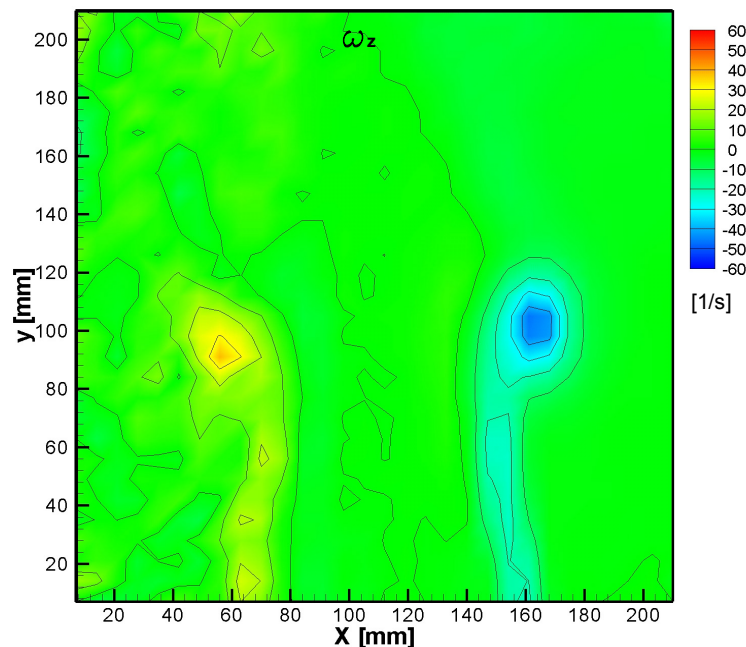


Figure (8.29): Phase-averaged azimuthal vorticity liquid. Jet centerline is at $X=108mm$.

As noted earlier, phase P_2 corresponds to a position of the vortex ring at $y \approx 100 - 105mm$. Both PIV and DOS data were obtained at this position (see Figure (8.29)). Phase-averaged profiles of the vertical velocity of the bubbles and of the liquid as well as of the azimuthal vorticity below and across the vortex ring (at $y = 84, 91, 98$ and $105mm$) are presented in Figures (8.30 a), (8.30 b) and (8.30 c), respectively. The vortex center on the right side is at about $y = 105mm$. These data are presented in order to compare bubble and liquid velocities in and below the vortex ring. The velocity of bubbles inside the vortex ring at $x \approx 60mm$ is in this case higher than the liquid velocity at the same x coordinate and about the same as the vertical velocity of the vortex centre (about $0.26m/s$). Therefore, the bubbles can be trapped at this location and they travel with the same velocity as the vortex ring. In order to check if the trapping conditions are fulfilled, the size of the vortex and the maximum vorticity at the vortex center have to be estimated. Figure (8.30 d) shows a Gaussian fit of the azimuthal vorticity of the liquid through the vortex center at $y = 105mm$. Measured maximum vorticity at the vortex center is about $-48s^{-1}$. The vortex radius estimated from this fit is about $15mm$. The terminal bubble rise velocity for $4mm$ bubbles is $0.24m/s$. Based on these values, the Vortex Trapping parameter is 3 and the Vortex Froude number 0.88. The minimum values required for trapping of bubbles inside a Gaussian vortex with radius of $15mm$ based on the criteria presented in Chapter 5.1.2. are 3.1 for the Vortex Trapping parameter and 0.92 for the Vortex Froude number. Basically the trapping conditions are fulfilled.

Void fraction and vertical bubble velocity measurement by DOS

As noted earlier, the position in the flow field at $y \approx 100 - 105mm$ corresponds to the location of the vortex ring captured during phase P_2 (see Section 8.4.2.2). DOS data have been acquired at

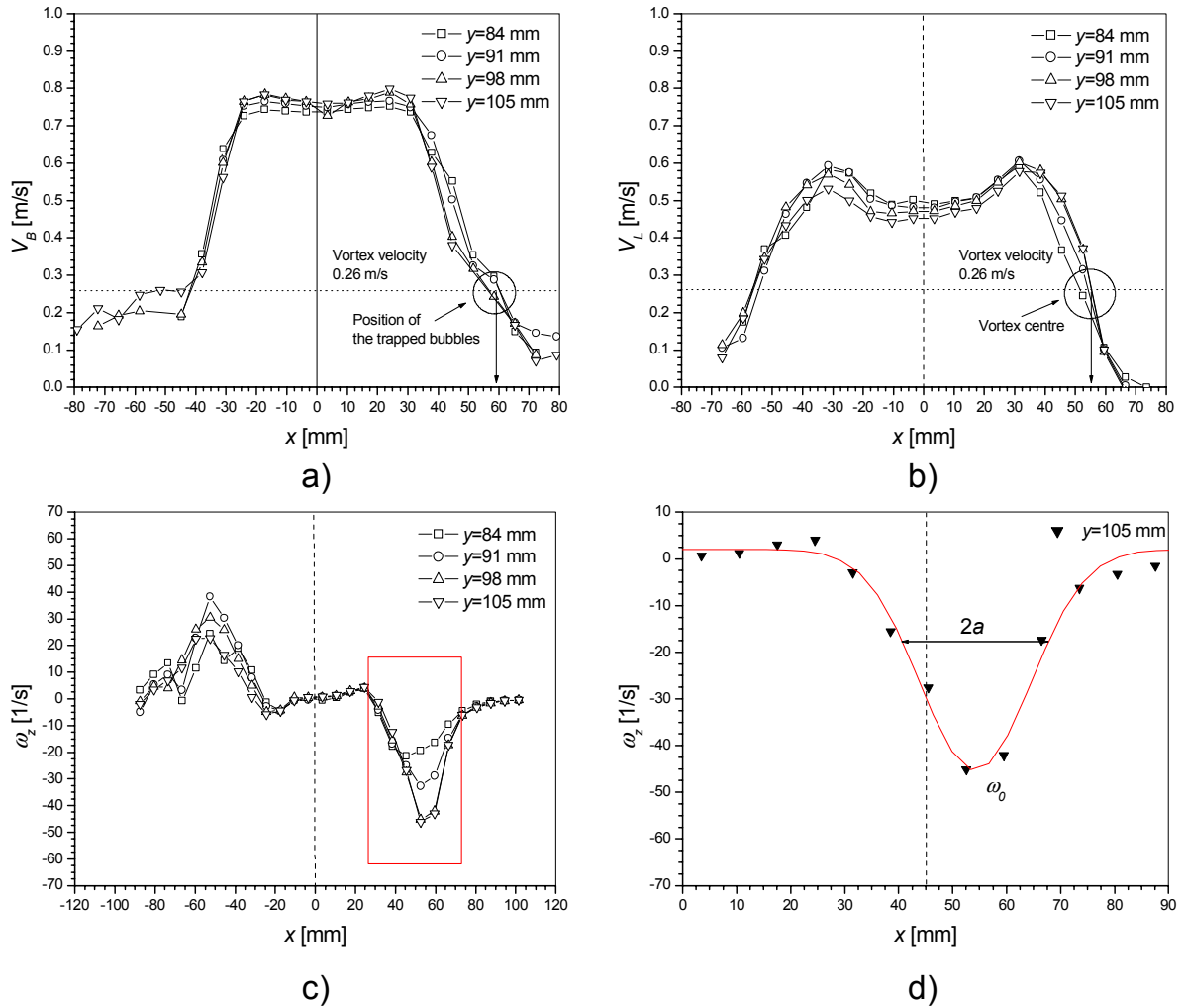


Figure (8.30): Phase-averaged velocity profiles of the bubbles (a), of the liquid (b), and of azimuthal vorticity of the liquid (c) as well as Gaussian fit of the azimuthal vorticity of the liquid across the vortex center (d).

this elevation and in addition at $y = 200\text{mm}$ for the points in the jet center, at the jet boundaries and in the shear layer.

Data acquisition was started by the external encoder signal and was stopped after 6000 excitation periods for points with low bubble concentration and after 3000 excitation for points with higher bubble concentration. Each period of 0.5s was divided into 25 intervals of 0.02s . The bubble number, void fraction and bubble vertical velocity data were phase-averaged for each of the intervals.

DOS results for the centerline point

Experimental results for the centerline point are presented in Figure (8.31). Although there is no possibility for trapping of bubbles due to the absence of large eddy structures, a small clustering effect accompanied by the variation of the bubble velocity can be observed. This periodic effect is caused by the modulation of the jet shape brought about by the periodic surges of the excitation flow, which are slightly inclined towards the jet axis.

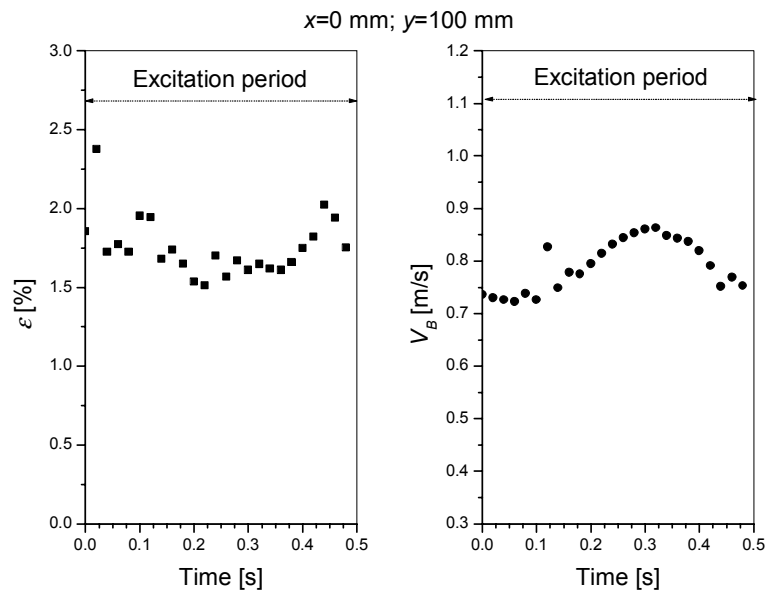


Figure (8.31): Variations of the void fraction and of the vertical bubble velocity during the excitation period (point at $x=0\text{mm}$ and $y=100\text{mm}$).

DOS results for points at the boundary of the shear layer

Experimental results for two points at the boundary of the shear layer ($x = 45\text{mm}$) at $y = 100$ and 200mm are presented in Figure (8.32). At this radius, shear-layer vortices entrain bubbles together with the liquid into the mixing region. As shown in Section 8.2.2, the phase-averaged DOS data indicate bubble clustering in phase with coherent vortex structures. The results show the time-dependence of the bubble velocity and of the void fraction during an excitation period. The velocity peaks ($V_{B,A}$ and $V_{B,B}$) are present at times when a minimum void fraction is measured. The correlation between vertical bubble velocity and void fraction shows the importance of the liquid velocity field around the vortices. The increased bubble concentration during certain phases is mainly caused by a bubble wave driven radially outward ahead of the large vortices, while low concentration indicates phases where the sensor tips are inside the zone behind the bubble wave. The bubbles that arrive at the sensor tip have different mean velocity and direction of flow at different phases of the excitation period. The apparently high bubble velocity prevailing during the low-void phase (see Figure (8.32)) could be caused by the shear layer pulsation but may be affected by the biasing effect discussed in Section 7.3.

The time delay between the void fraction maxima (ϵ_A and ϵ_B) at the two different elevations in Figure (8.32), measured at the same horizontal position in the shear layer ($x = 45\text{mm}$), is about 0.28s for the vertical distance of 100mm . The resulting downstream traveling velocity of the bubble wave of 0.36m/s is distinctly higher than the value for the vortex velocity obtained by PIV. This difference indicates that the bubble density wave appears to drift relative to the coherent liquid vortices.

DOS results for points in the shear layer at $y=100\text{mm}$

Experimental results for points in the shear layer at $x = 45, 53, 54, 57$ and 62mm and $y = 100\text{mm}$ are presented in Figure (8.33). The results show that the void fraction decreases towards the boundaries of the jet, as expected. The void fraction peaks at these locations, especially for

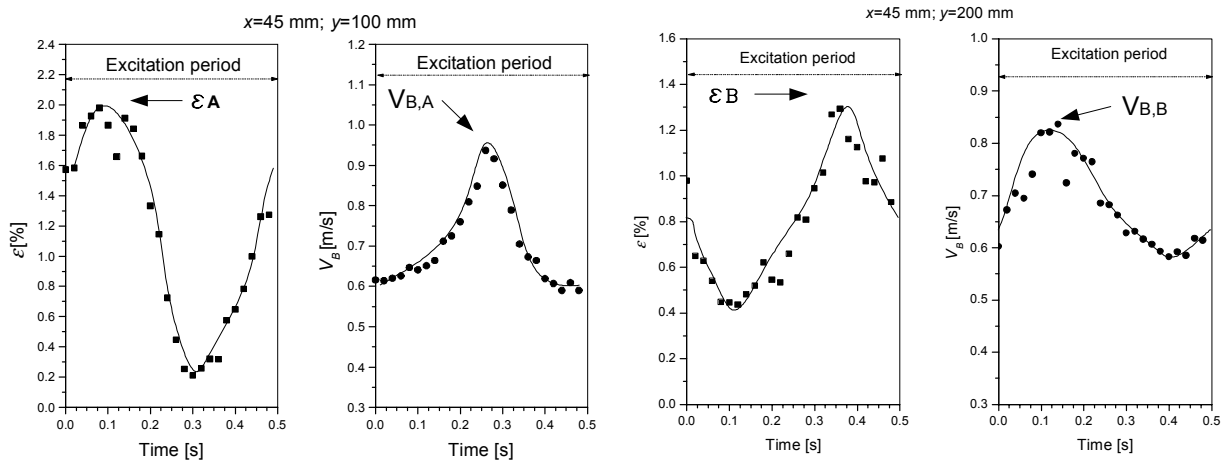


Figure (8.32): Variations of the void fraction and of the vertical bubble velocity during excitation period (for the points in the shear layer at $y=100\text{mm}$ and 200mm).

the points at $x = 62\text{mm}$ and 66mm , may correspond to trapped bubbles, i.e. bubbles which belong to the bubble ring. The PIV data presented in Figure (8.30) show that these points are located close to the vortex center where the bubble trapping occurs.

DOS results for the points at $x = 45, 53, 54$ and 57mm indicate a strong variation of bubble density. These points are located inside the vortex where bubbles are not expected to be trapped. Based on PIV data, the latter three points are very close to the vortex center, where few bubbles can be trapped. The differences between the bubble wave shapes at different axial locations in the shear layer give an indication of its complex space-time distribution and the experimental effort that would be required for obtaining a complete picture.

Obviously, PIV and photographic recordings would be needed to fully record interactions between bubbles and liquid velocity field.

Void fraction and vertical bubble velocity measurement with DOS at $y = 200\text{mm}$

Experimental results for points in the shear layer at $x = 45, 47, 49, 53$ and 55mm at $y = 200\text{mm}$ are presented in Figure (8.34). A strong variation of the bubble density is still visible for all x -coordinates, but the mixing process in the shear layer causes the void fraction to become temporally more uniform than at $y = 100\text{mm}$, especially for $x > 50\text{mm}$.

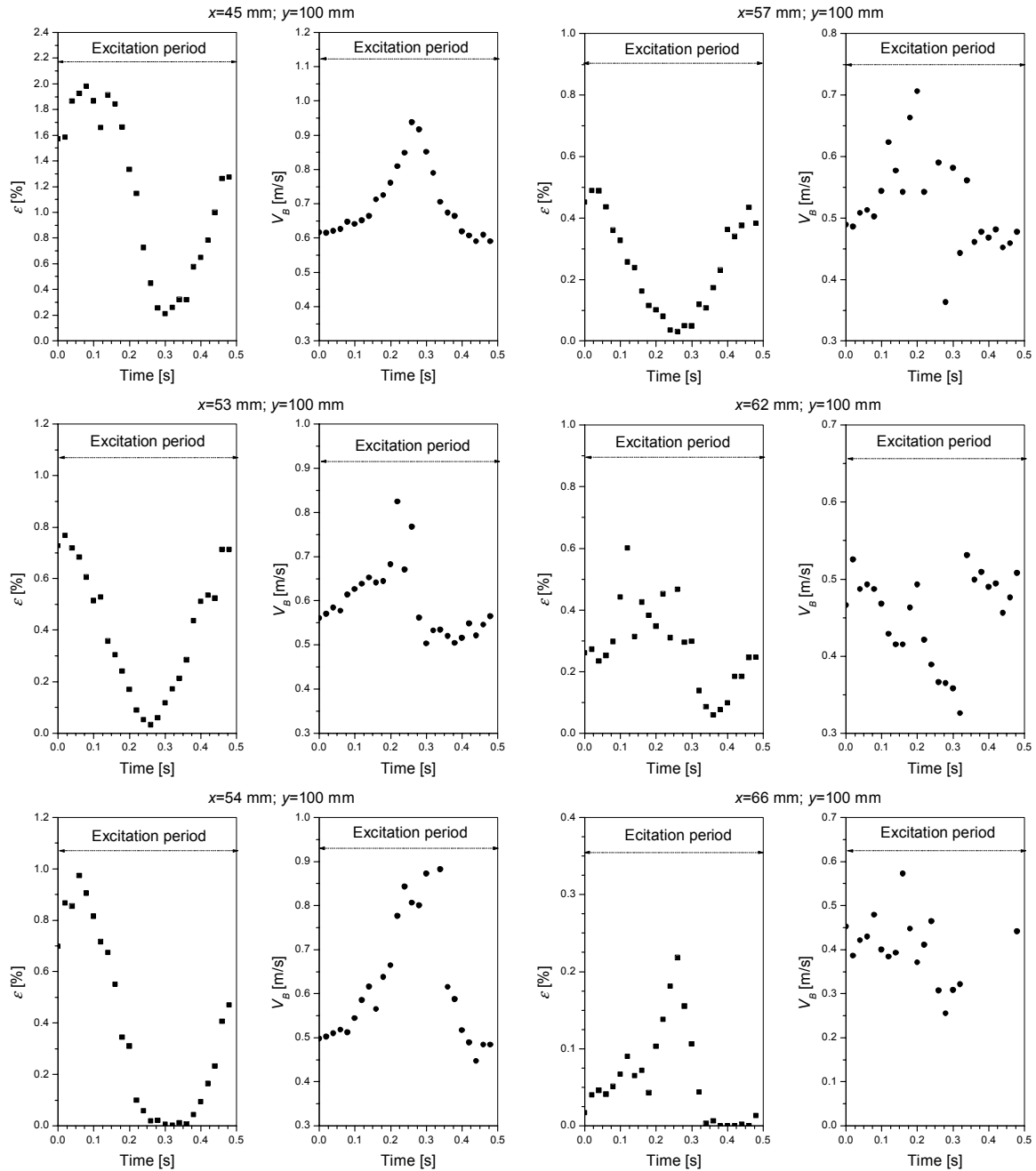


Figure (8.33): Variation of the void fraction and vertical bubble velocity during the excitation period (for the points in the shear layer at $y=100$ mm).

8.4 Effects of excitation frequency

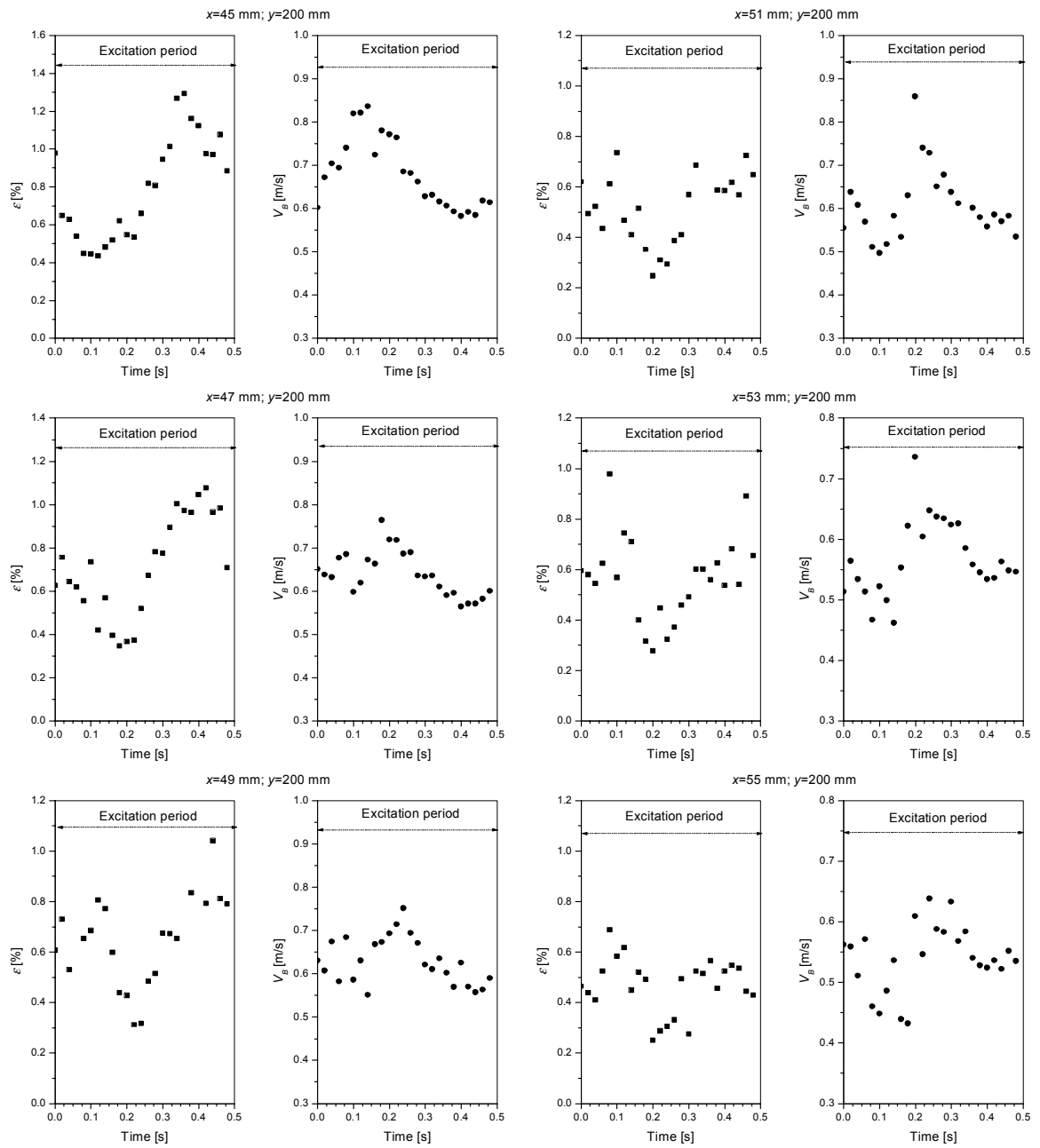


Figure (8.34): Variations of the void fraction and vertical bubble velocity during excitation period (for the points in the shear layer at $y=200\text{mm}$).

Comments on DOS statistics and accuracy of velocity measurements

For the point in the shear layer at $x = 62\text{mm}$ and $y = 100\text{mm}$, the number of detected bubbles during different phases and the vertical bubble velocity are presented in Figure (8.35). The total number of excitation periods was 6000. The relative statistical fluctuation of the bubble number is about $N^{-1/2}$ and the standard deviation of the phase-averaged bubble velocity falls into a range between 15 and 38%. Obviously, in order to obtain a statistically sufficient number of events, especially for points located in the regions with low bubble concentration (in the shear layer), the total number of excitation periods for phase-averaging must be high. This would mean very long measurement times, fairly high demands on DOS signal stability and high-precision hardware. Also, the reasons for the overestimation of the vertical bubble velocity measured by DOS (discussed in Section 7.3) should be carefully considered before generating experimental databases for numerical analysis.

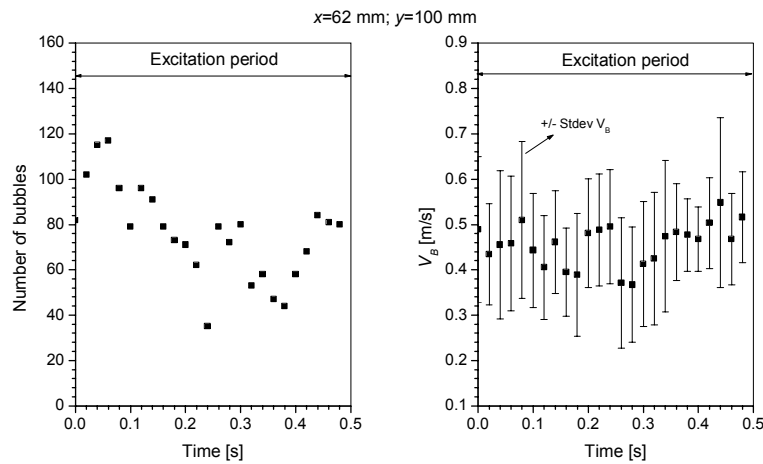


Figure (8.35): Number of bubbles captured during excitation period (left) and standard deviation of vertical bubble velocity (right).

8.4.3 Test f3

The triggering-velocity function at the exit of the triggering nozzle is presented in Figure(8.36). The excitation frequency is $3Hz$, which corresponds to $St = 0.84$. For this excitation condition, two consecutive vortex rings can be observed within the field of view.

Single-phase vs. bubbly jet

Phase-averaged azimuthal vorticity and vertical-velocity fields of the liquid for the single-phase (left) and the bubbly jet (right) are compared in Figure (8.37). Because of an inconsistency in the timing of the data acquisition, a small time shift exists between the two figures. Therefore, somewhat different positions of the vortex rings can be observed between these two experiments. The measured peak vorticity of the liquid in the bubbly jet is slightly smaller, vortices are more elongated and the liquid velocity field is obviously affected by the presence of bubbles. The peak liquid velocity is reached beside the vortex centres. The velocity of the vortex rings is also slightly larger in the case of the bubbly jet.

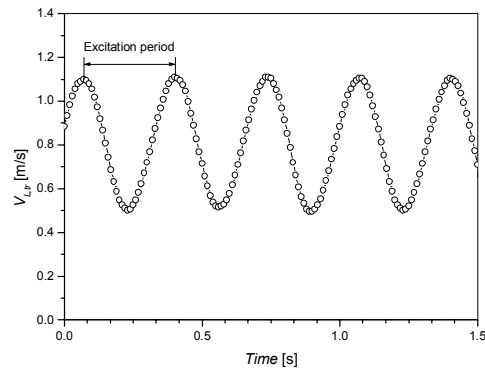


Figure (8.36): Triggering velocity function for test f_3 (3Hz).

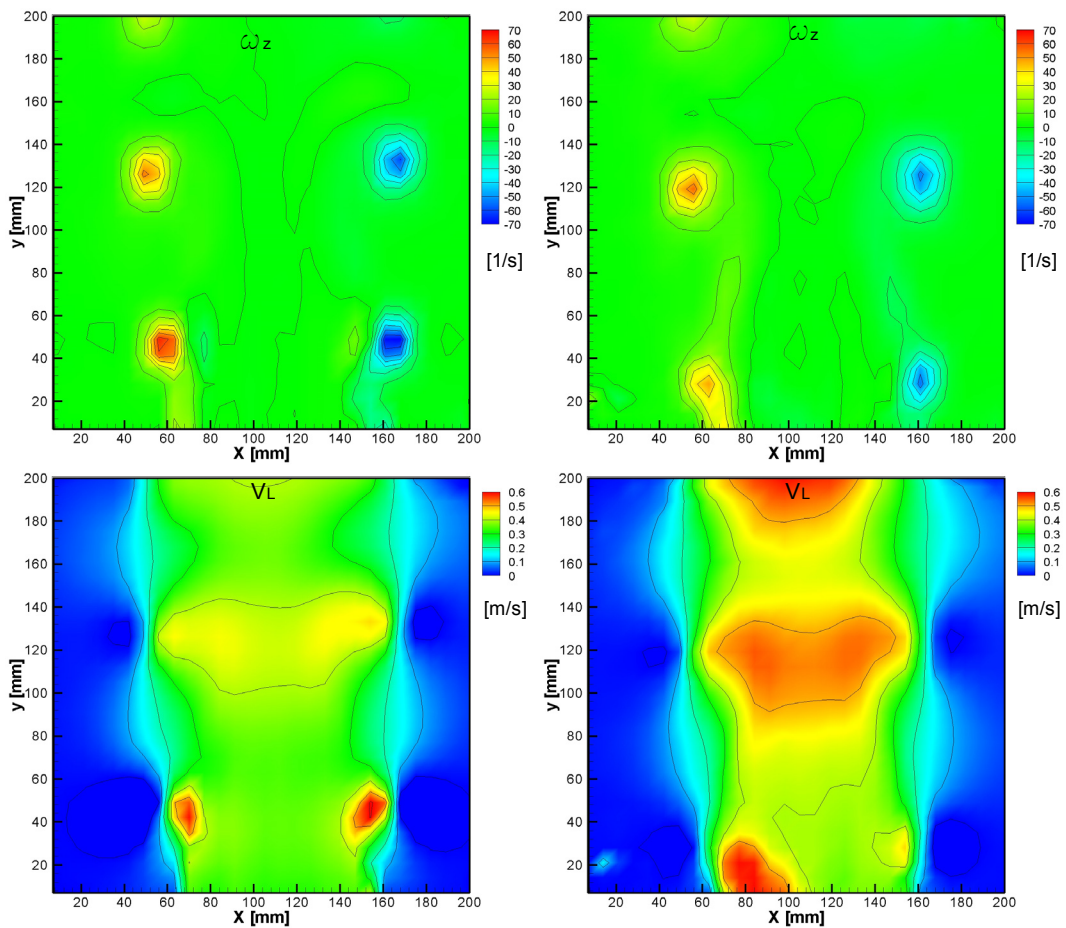


Figure (8.37): Phase-averaged azimuthal vorticity (top) and vertical velocity (bottom) fields of the liquid for the single-phase (left) and the bubbly jet (right).

Bubble velocity field and trapping visualization

Bubble ring tracking accompanied by bubble velocity measurements were performed in order to compare the velocity of vortex rings with phase-averaged bubble velocities in the shear layer as well as with the instantaneous bubble ring velocity.

An attempt was made to measure the velocity of the bubble ring by using the vortex tracking method. Because additional backlight illumination was used, this method is called here *the bubble ring tracking method*. Therefore, the excited bubbly jet was illuminated by the laser light and by the back light (for more details see Appendix D). If bubbles detected in the PIV images belong to a bubble ring, their phase-averaged velocity should be the same as the velocity of the bubble ring or of the vortex ring (in this case about 0.27m/s).

The photos of Figure (8.38) represent two subsequent phases of the jet with shifted bubble ring. The vertical distance that the bubble ring traveled between phases P_1 and P_2 (see rectangles in Figure (8.38)), which are separated by a shift of 266.7ms is about 70mm . The instantaneous velocity of the bubble ring is about 0.26m/s . On the other hand, the vertical distance of 90mm between two bubble rings captured within the same phase (see picture on the right) corresponds to a velocity of 0.27m/s , since the duration of the excitation period was 333.3ms .

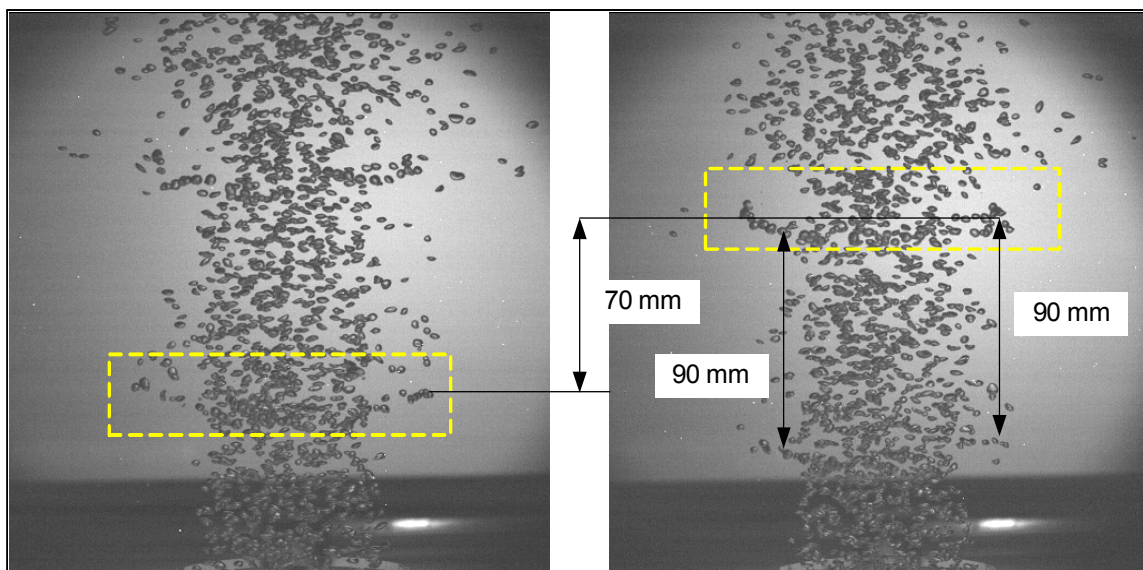


Figure (8.38): Instantaneous images of the bubble ring (Left: starting phase P_1 . Right: phase P_2 266.7ms later).

Phase-averaged photographic recordings of bubble rings are presented in Figure (8.39). This image reveals the overall shape of the excited bubbly jet. Quantitative information cannot easily be obtained from this kind of data. Even though some clusters can be seen, trapped bubbles (i.e. bubble rings) are very difficult to distinguish.

Phase-averaged bubble velocity profiles across the vortex ring ($y = 62 - 83\text{mm}$) obtained by PIV for phase P_1 are presented in Figure (8.40). For phase P_2 experimental PIV results for profiles across the shifted vortex ring ($y = 96 - 117\text{mm}$) are presented in Figures (8.41)-(8.42). These results illustrate that the phase-averaged velocity of the bubbles at some locations in the shear layer is equal to the velocity of the bubble rings, which means that these bubbles can be trapped. In the following sections these results will be compared with results obtained by the vortex tracking method in order to show that trapped bubbles travel with the same vertical velocity as the liquid structures.

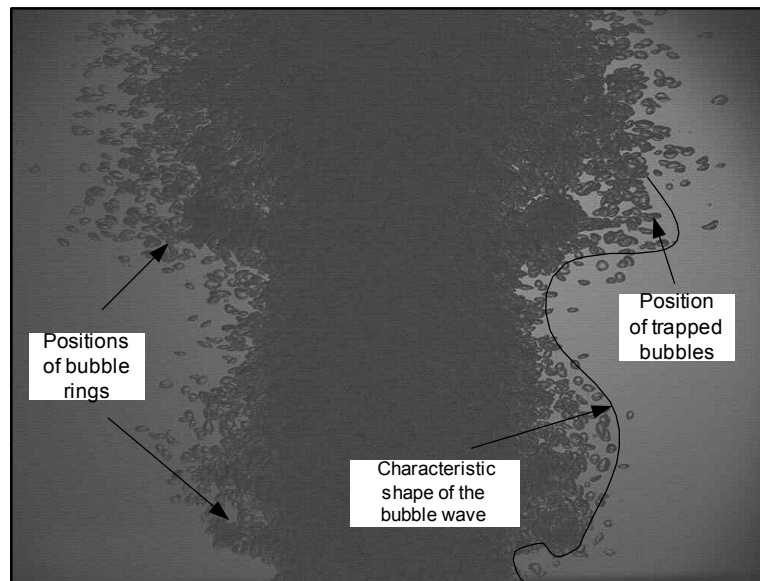


Figure (8.39): Phase-averaged image of trapped bubbles (Phase P_1).

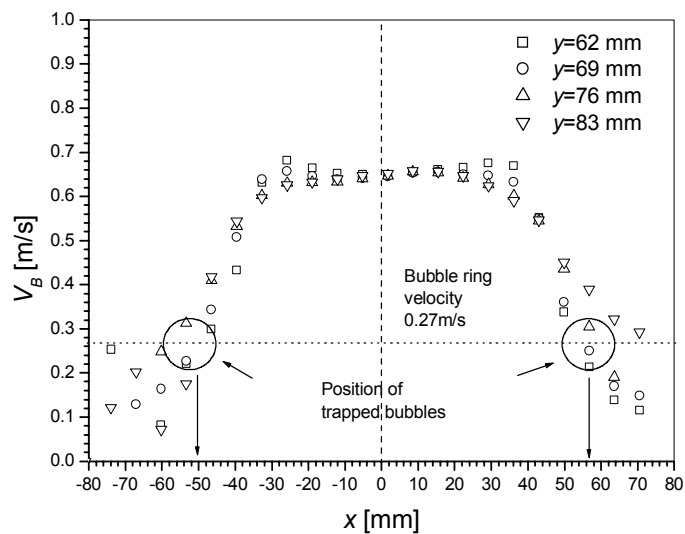


Figure (8.40): Phase-averaged velocity profiles of bubbles for Phase P_1 of Figure (8.38).

Liquid velocity field and bubble trapping

This section contains experimental results obtained by *the vortex tracking method* applied for test condition $f3$. Nine consecutive phases, which show different locations of the vortex rings in the field of view are presented in Figure (8.43). It illustrates the evolution of the jet during one excitation period. The time between consecutive recordings was $66.7ms$ and the duration of the excitation period was $333.3ms$. The sixth contour map of the phase-averaged vorticity of the liquid is identical to the first one (see Figure (8.43)), since both represent the beginning of the excitation period. The data for the second phase presented in Figure (8.43) (marked with number 2-Phase 2), including phase-averaged velocities of bubbles and liquid as well as

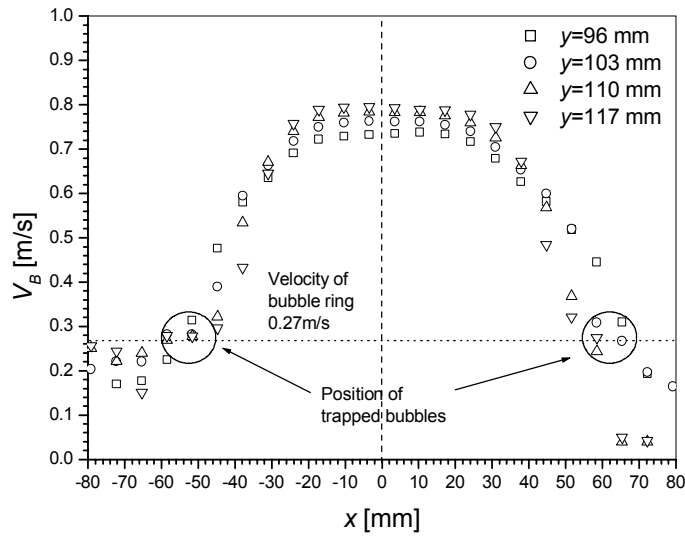


Figure (8.41): Phase-averaged velocity profiles of bubbles $y=96-117\text{mm}$ for phase P_2 of Figure (8.38).

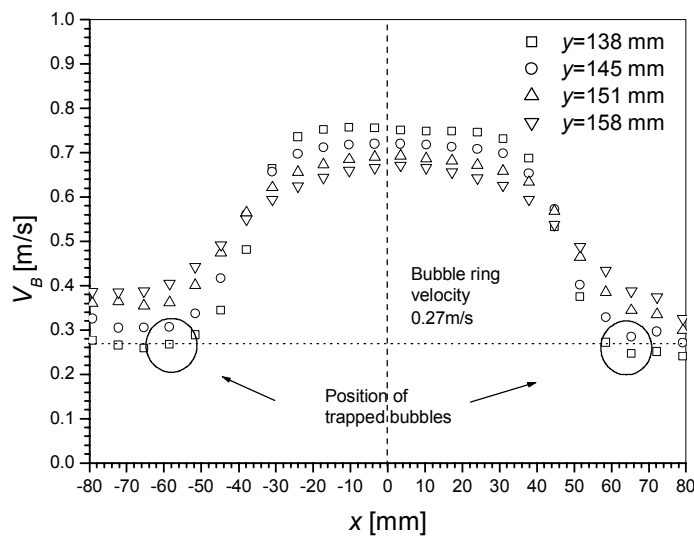


Figure (8.42): Phase-averaged velocity profiles of bubbles at $y=138-158\text{mm}$ for Phase P_2 of Figure (8.38).

azimuthal vorticity of the liquid, are analyzed and results are presented in this section. In order to examine bubble trapping inside large vortices, the location of the instantaneous bubble ring is compared with that of the phase-averaged azimuthal vorticity field of the liquid. Furthermore, as shown above, *vortex tracking* as well as *bubble ring tracking* give consistent information on vortex ring and bubble ring velocities, respectively.

The estimated vortex velocity of about 0.27m/s agrees with the value obtained by the bubble ring tracking method (see previous results). This clearly demonstrates bubble trapping inside large vortices.

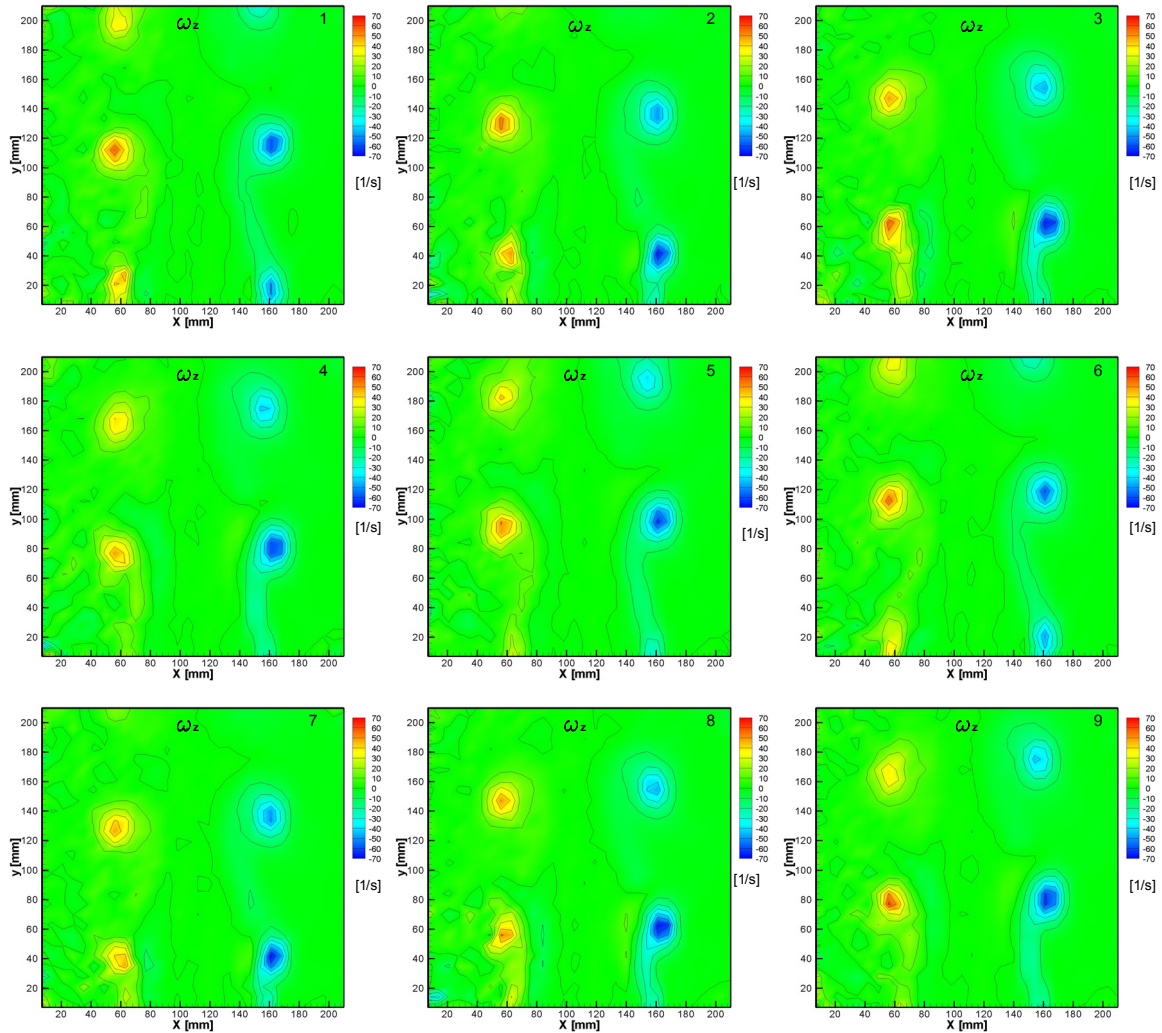


Figure (8.43): Consecutive phases of vortex ring movement obtained with the vortex tracking method. The time shift between the phases was 66.7ms .

Phase-averaged velocity fields

Profiles of vertical bubble and liquid velocity distributions across the vortex rings as well as of the azimuthal vorticity of the liquid for Phase 2 are presented in Figures (8.45). The corresponding vorticity contour map (Figure (8.44)) shows the locations of two vortex rings captured in the field of view.

Therefore, the velocity and azimuthal vorticity profiles are shown across both vortex rings. Also, photographic recordings show the existence of two bubble rings. The vortex rings are

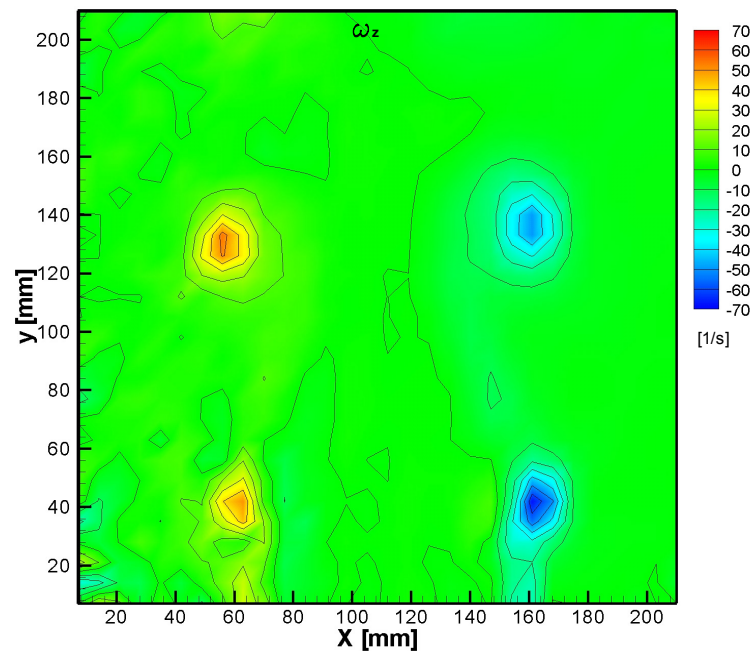


Figure (8.44): Phase-averaged azimuthal vorticity of the liquid (Phase 2).

formed at about 30mm above the nozzle exit, which means that bubble trapping can take place at this location. The phase shift between two exposures and the distance between two consecutive vortex rings determine the vortex velocity. In order to examine the trapping conditions, it is very important to capture the phase, i.e. position of the vortex ring that contains the first trapped bubbles. Thus, the very first phase, when the bubble ring is formed should be acquired. The sizes of the vortex as well as the bubbles and the maximum vorticity at the vortex center during this phase determine whether trapping conditions are fulfilled or not. As it can be seen in Figure (8.43), the second captured phase (marked as phase 2) as well as the seventh one (marked as phase 7) contain the vortex ring at about $y = 30\text{mm}$ from the nozzle exit.

The vertical-velocity profiles of bubbles shown in Figure (8.45, left) across the vortex close to the nozzle exit show the existence of a velocity valley near the vortex center, whereas those of the liquid exhibit a peak. This phenomenon was also observed for case $f2$. The phase-averaged picture of bubble reflections at these locations reveals the existence of a zone where there are only a few bubble reflections. Since bubbles follow a path around the vortex until they are trapped, there is a zone within the vortex structure that is not reachable for most of the bubbles and no realistic velocity measurements are possible in this region. The valley in the bubble velocity distribution, which lies at the side of the vortex close to the jet boundary, therefore is an artifact.

Bubble rings are formed after trapping. The bubbles then continue to travel together with the vortex structures and have the same velocity as the vortex rings. Further downstream, the spreading of the bubbly jet and the secondary instability of the large vortex rings [22], which are also affected by interactions between liquid and bubbles, influence the distribution of the bubbles in the shear layer and their escaping from the coherent structures.

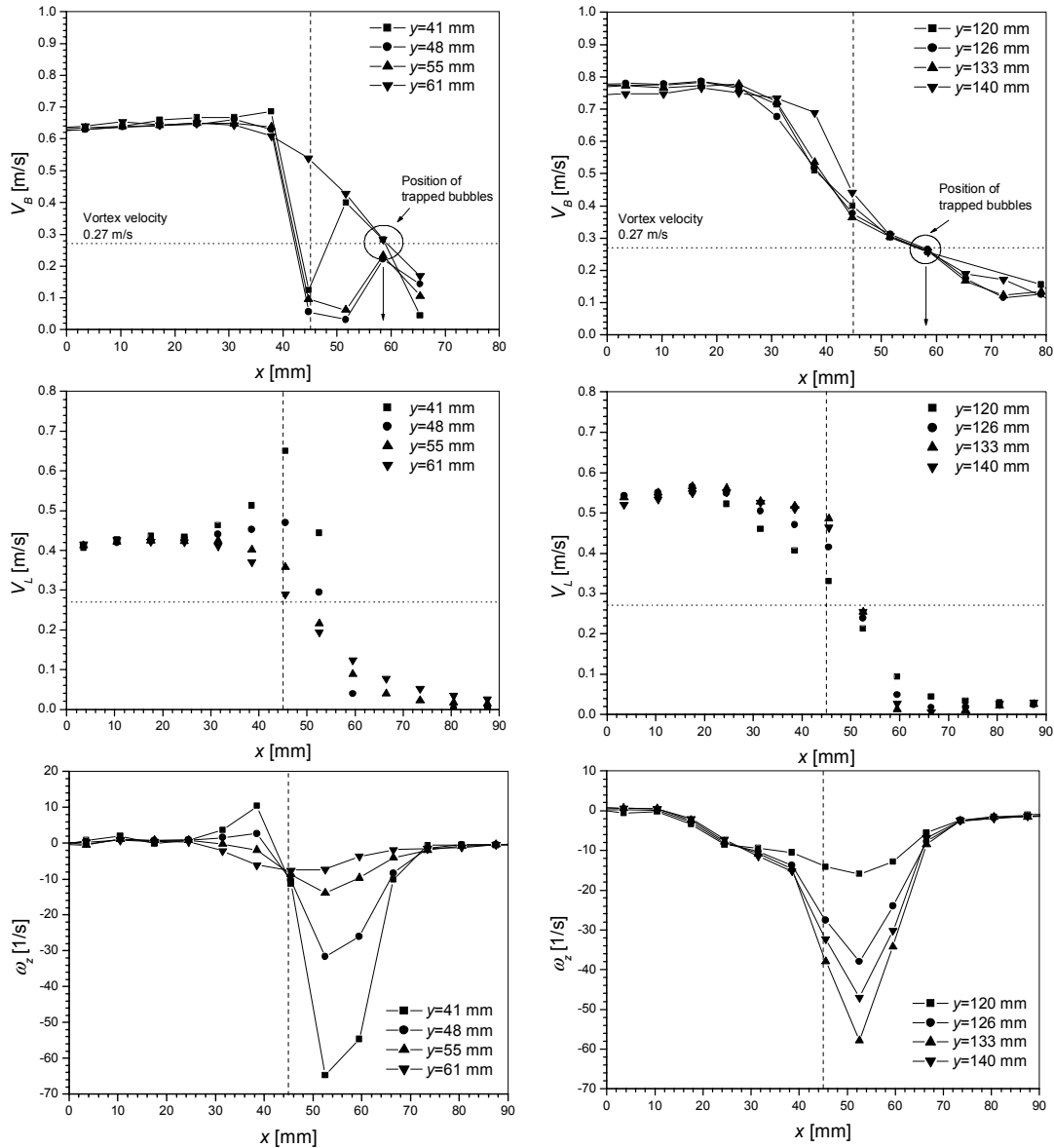


Figure (8.45): Phase-averaged velocity profiles of the bubbles, of the liquid and azimuthal vorticity profiles of the liquid across two vortex rings for phase 2, at various elevations.

Conditions for bubble trapping

The first vortex ring in Figure (8.44) is located near the nozzle exit at about $y = 41\text{mm}$ and the second at about $y = 140\text{mm}$. The measured peak vorticity (-72s^{-1}) of the first ring is higher than that at the center of the second ring (-50s^{-1}) (see Figure (8.46)). For the vortex radius of the first ring of about 9mm and the terminal bubble rise velocity for 4mm bubbles of 0.24m/s , the Vortex Trapping parameter is 2.7, while the vortex Froude number is 1.2. The trapping conditions are fulfilled since a bubble ring is formed, although the required minimum values of these parameters ($\Gamma_\omega = 2.9$ and $Fr_\omega = 1.4$) are not reached. For the second vortex ring which has a radius of about 12mm , the Vortex Trapping parameter is 2.5, while the vortex Froude number is 0.77 (see (Figure (8.46)). In this case, the required minimum value of the

Vortex Trapping parameter is $\Gamma_\omega = 3$ and that of the Vortex Froude number $Fr_\omega = 1.1$.

The maximum vorticity in the vortex center depends on the location of the vortex ring, i.e. its position downstream from the nozzle exit. Close to the nozzle exit, the peak vorticity at the vortex center is higher than further downstream, while the vortex diameter is smaller (Figure (8.46)). The downstream development of these structures, the effects of instabilities in the shear layer on bubble agglomeration and movement in the shear layer and the break up of the bubble ring will be examined in more detail in the next section.

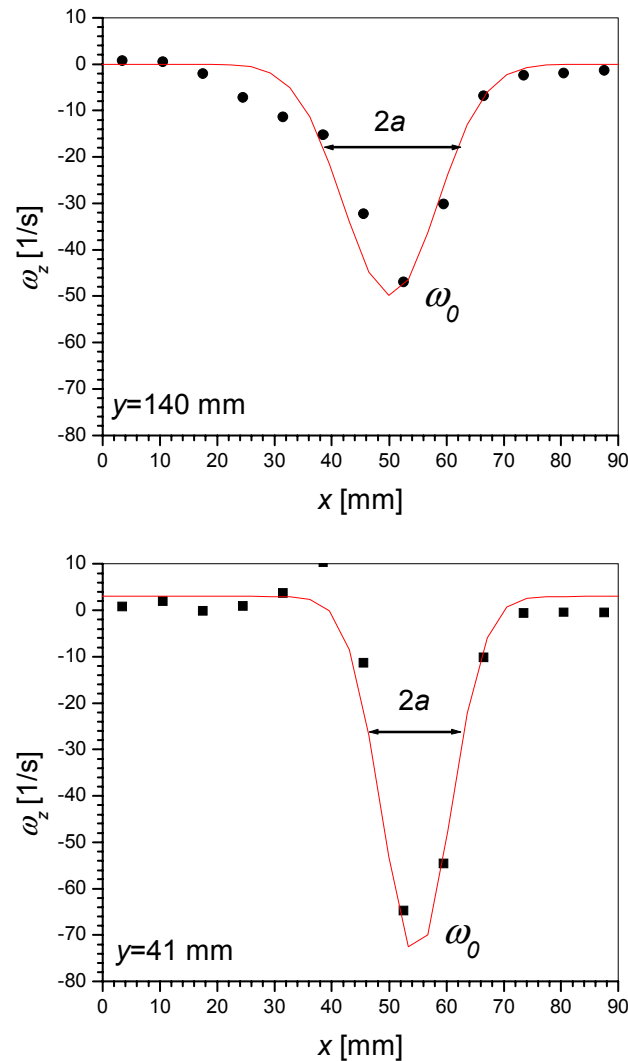


Figure (8.46): Phase-averaged azimuthal vorticity profiles of the liquid at $y=140$ mm (top) and $y=41$ mm (bottom) from the nozzle exit.

Bubble trapping scenario

The sketch of Figure (8.47) illustrates the bubble trapping process inside a large Gaussian vortex. The real situation is visualized by the LIF technique and is presented in Figure ((8.48). The picture shows positions of different bubbles inside the vortex structure. The location of the equilibrium position of the trapped bubbles cannot be determined by the LIF technique, because bubbles cannot be tracked within the structure. According to the equilibrium condition

presented in Chapter 5, the position of stably trapped bubbles lies above the horizontal plane through the vortex centre.

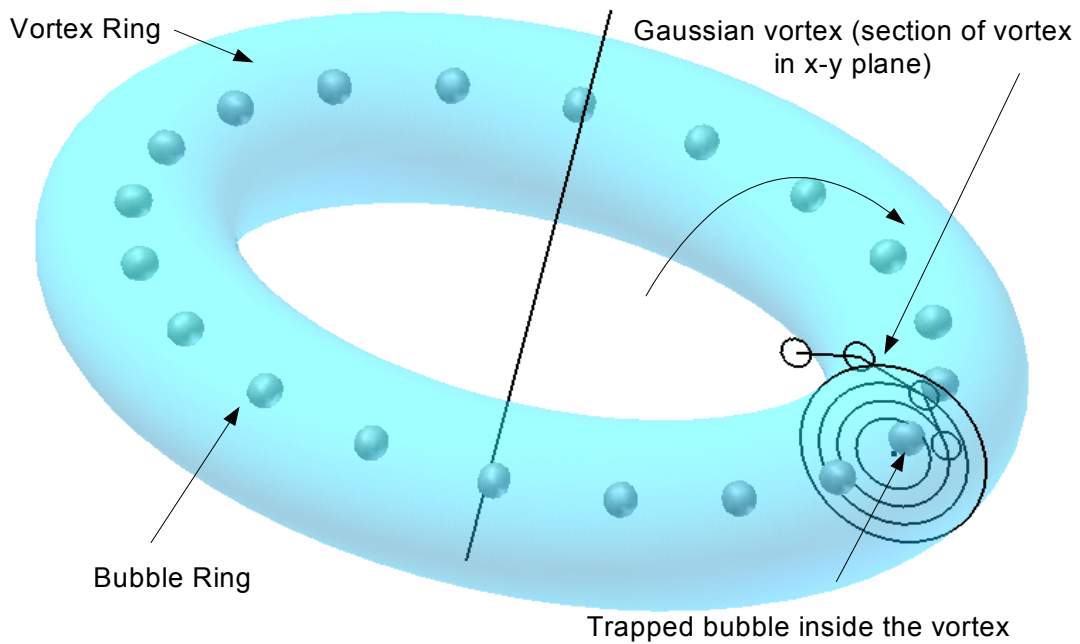


Figure (8.47): *Bubble trapping scenario.*

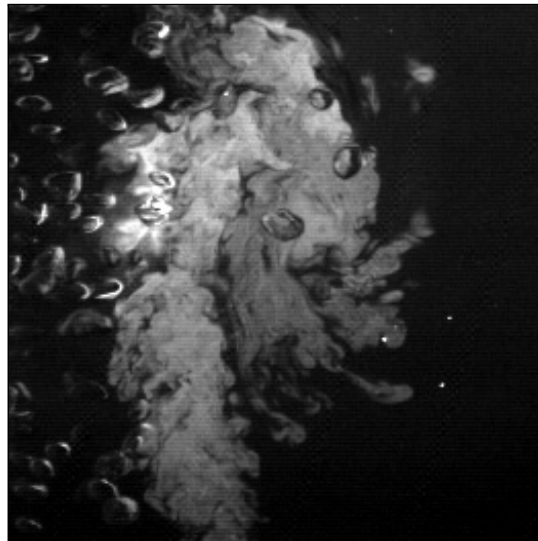


Figure (8.48): *LIF image of bubbles inside a vortex structure visualized by fluorescent dye.*

Figure (8.47) shows that bubbles that are coming from the core of the jet enter the vortex structure, are deflected and move around the vortex center. When they reach an equilibrium position outside the vortex center they continue to move at the same velocity as the vortex ring. Bubbles can be perfectly aligned inside the bubble ring, as it is shown in Figure (8.49).

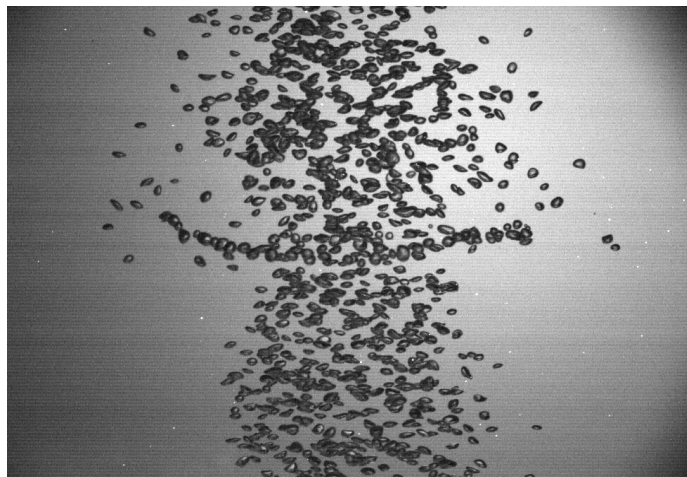


Figure (8.49): *Perfectly aligned bubbles in a bubble ring*

Time-dependent phase-averaged profiles

Profiles of vertical bubble and liquid velocity distributions at $y = 105\text{mm}$, for six different phases (corresponding to the scalar maps of azimuthal vorticity distribution in Figure (8.43)), as well as of the azimuthal vorticity of the liquid are presented in Figure (8.50). In the first as well as the sixth phase, the center of the vortex is located at about $y = 115 - 120\text{mm}$ from the nozzle exit. For these phases, results show that the vertical bubble velocity is slightly larger than the vertical liquid velocity and the vortex velocity. Taking into account that the vortex centre lies already above $y = 105\text{mm}$ for Phases 1 and 6 and that the equilibrium position of the trapped bubbles should be above the vortex centre (see Section 5.1.2), it is not probable that trapped bubbles contribute to the bubble velocity results for Phase 1 and 6 presented in the profiles in Figure (8.50). On the other hand, the vortex centre of Phase 5 lies fairly close to $y = 105\text{mm}$ and trapped bubbles could be expected to mostly contribute to the velocity measurements of this phase. The corresponding values of the vertical bubble velocity and the liquid velocity in the vortex center for Phase 5 are however even higher than for Phases 1 and 6 (see Figure (8.50)).

Conclusions

Phase-averaged profiles of the vertical bubble velocity obtained by PIV may contain contributions from bubbles which move inside the large vortices but do not reach an equilibrium position. If the measured phase-averaged velocity of the bubbles is slightly higher than the vortex or liquid velocity, one may imagine that this is due to a small contribution of faster non-trapped bubbles. An unsolved question is why the measured bubble velocity is closer to the vortex velocity for a point below the vortex ring (Phase 1 and 6) instead of a point above (Phase 5), which corresponds to the possible equilibrium position of bubbles trapped inside the vortex (see Section 5.1.2). Anyway, it is recommended to develop an experimental method which employs PIV for resolving the liquid velocity field, whereas the bubbles should be tracked with higher temporal resolution by using an additional high-speed camera. Experiments with low void fraction and particularly with bubble injection restricted to a small, selected number of needles are suggested in order to distinguish trapped bubbles from bubbles that move inside the vortex with higher velocity.

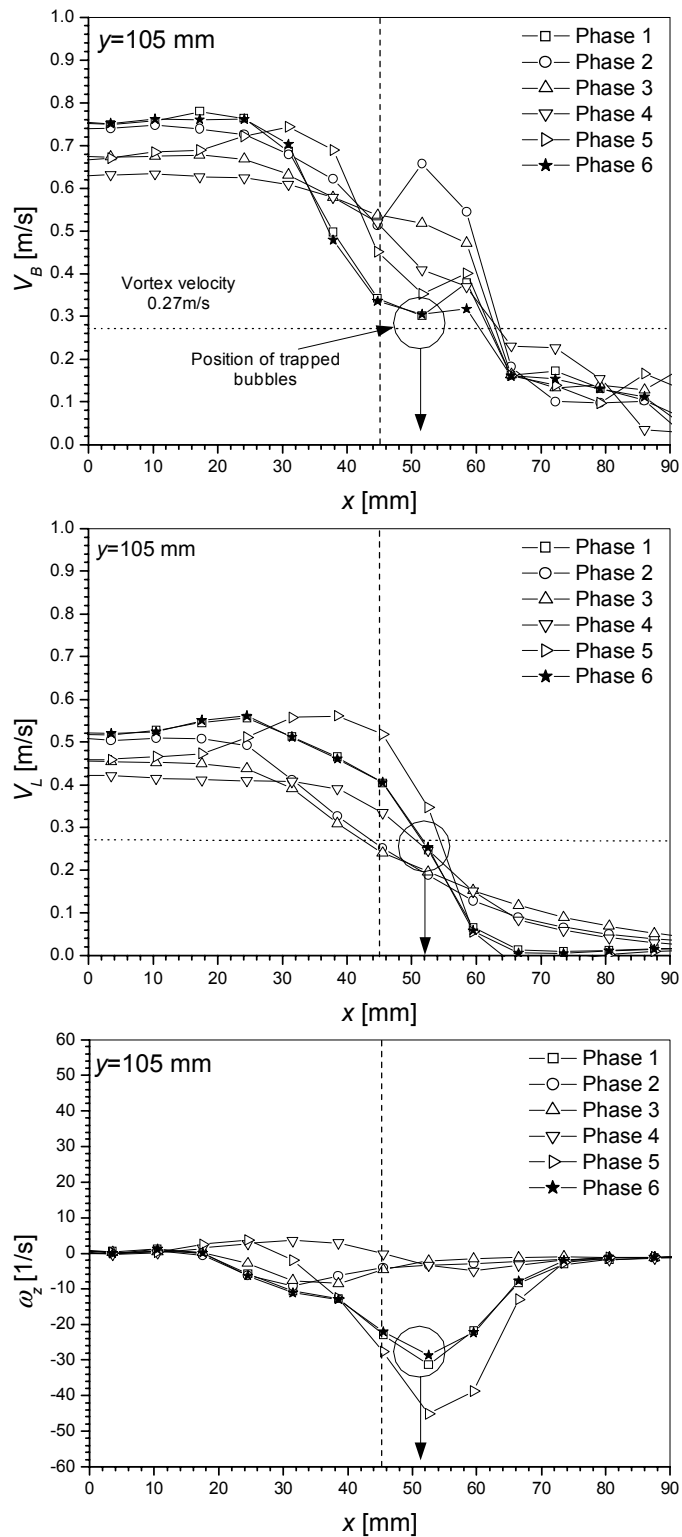


Figure (8.50): Profiles of vertical bubble and liquid velocity distributions at $y = 105 \text{ mm}$ during six different phases.

8.5 Downstream development and destruction of liquid and bubbly structures

This section contains experimental results obtained by *the vortex tracking method* applied for test condition *f3* further downstream between $y = 220$ to 400mm . Six phases were captured with a time between consecutive recordings of 66.7ms . The duration of the excitation period was 333.3ms , such that the sixth phase represents the beginning of a new excitation period. The data for the fourth phase, including phase-averaged velocities of bubbles and liquid, as well as azimuthal vorticity of the liquid are analyzed and presented in this section (see Figure (8.51)). The contour maps show the position and the size of the large vortices. The vortex centers of the first captured vortex ring are located at about 270mm from the nozzle exit.

Vortex tracking

Six consecutive phases, which show the locations of two vortex rings in the field of view are presented in Figure (8.52). The measured vortex ring velocity is about 0.37m/s , which is considerably higher than the value obtained close to the jet nozzle. The results illustrate the development and destruction of the vortex rings. The vorticity peak almost disappears at about $y = 405\text{mm}$ ($y/D = 4.5$), which means that vortex structures vanish at this location. This phenomenon also affects bubble distribution inside and in between the shear layer vortices. Gaussian velocity profiles and a relative velocity of about the value of the terminal bubble rise velocity characterize this region of the bubbly jet, that is dominated by buoyancy.

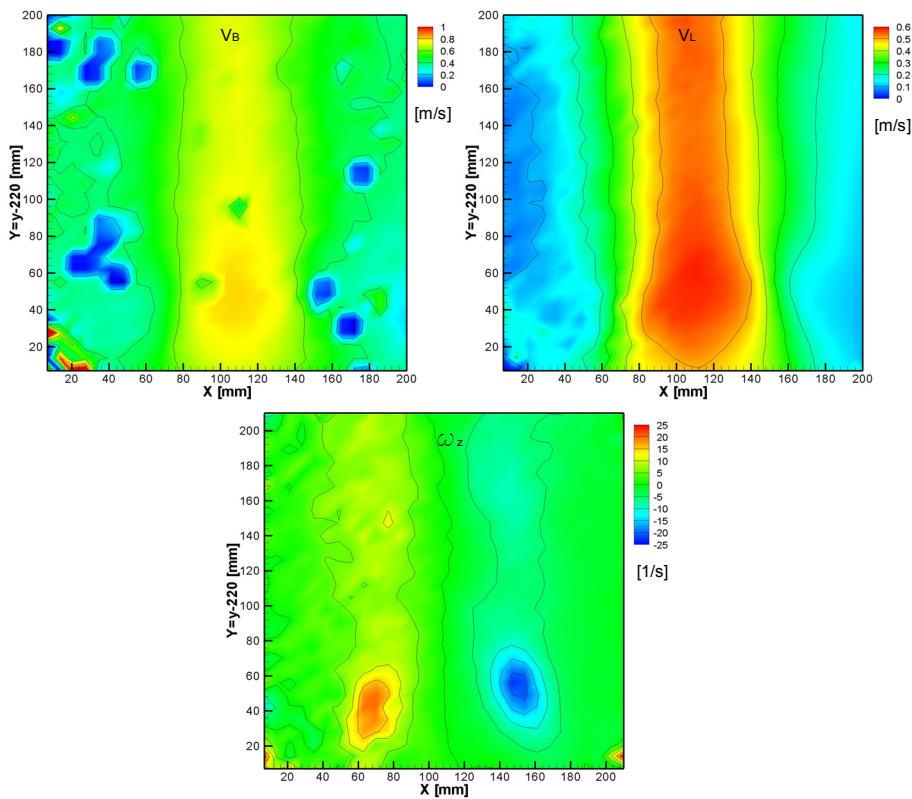


Figure (8.51): Phase-averaged vertical velocity fields of the bubbles (top-left), of the liquid (top-right) and azimuthal vorticity of the liquid (bottom).

8.5 Downstream development and destruction of liquid and bubbly structures

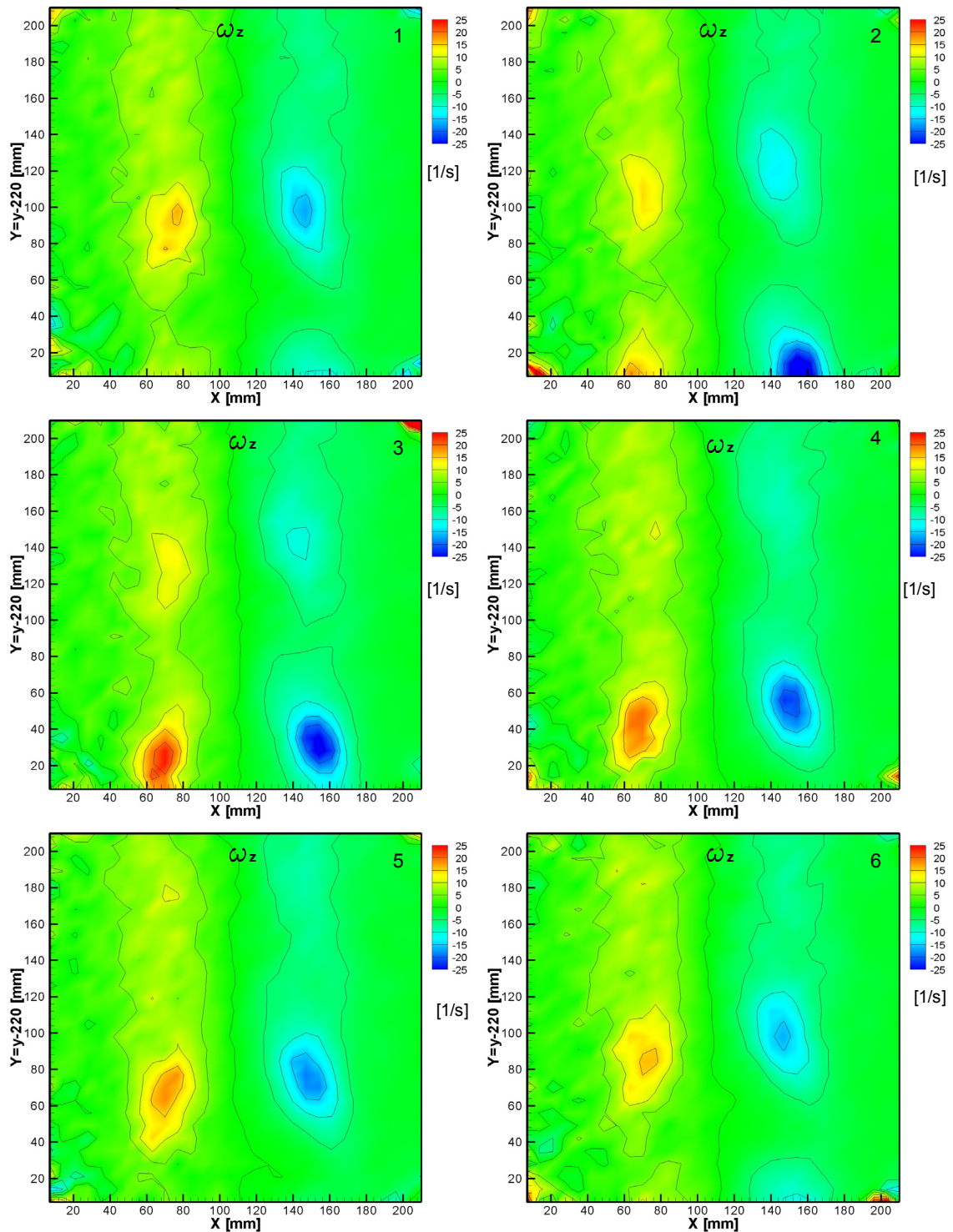


Figure (8.52): Consecutive phases of vortex ring movement obtained with the vortex tracking method at locations further downstream.

Bubble trapping condition

Experimental results for the velocity distribution of bubbles and liquid, as well as the vorticity of the liquid across the vortex rings which were situated at about 280mm and 390mm (Phase 4 in Figure (8.52)) are presented in Figure (8.53).

The phase-averaged vertical bubble velocity in the shear layer at $y = 283\text{mm}$ and at $x = 45 - 60\text{mm}$ lies between $0.37 - 0.5\text{m/s}$. The minimum is close to the vortex velocity so that trapping could have occurred. With a vortex radius of about 15mm and the terminal bubble rise velocity for 4mm bubbles of 0.24m/s , the Vortex Trapping parameter of 1.37 and the Vortex Froude number of 0.19 are smaller than required for bubble trapping ($\Gamma_\omega = 3.1$ and $Fr_\omega = 0.91$). Therefore trapping conditions are not satisfied at this location. The presented bubble and liquid velocity profiles also indicate that bubbles driven by buoyancy leave the vortex structures.

The phase-averaged vertical bubble velocity in the shear layer at $y = 381\text{mm}$ and $x = 50 - 60\text{mm}$ is about 0.46m/s . The phase-averaged vertical liquid velocity in the vortex center is smaller than the bubble velocity, which indicates that bubbles are no longer trapped inside this vortex ring. The measured peak vorticity created by the mean shear is about -9s^{-1} . With a vortex radius of about 32mm and the terminal bubble rise velocity for 4mm bubbles of 0.24m/s , the Vortex Trapping parameter of 1.2 and the Vortex Froude number of 0.07 are far below the smallest limits required for trapping ($\Gamma_\omega = 3.1$ and $Fr_\omega = 0.45$).

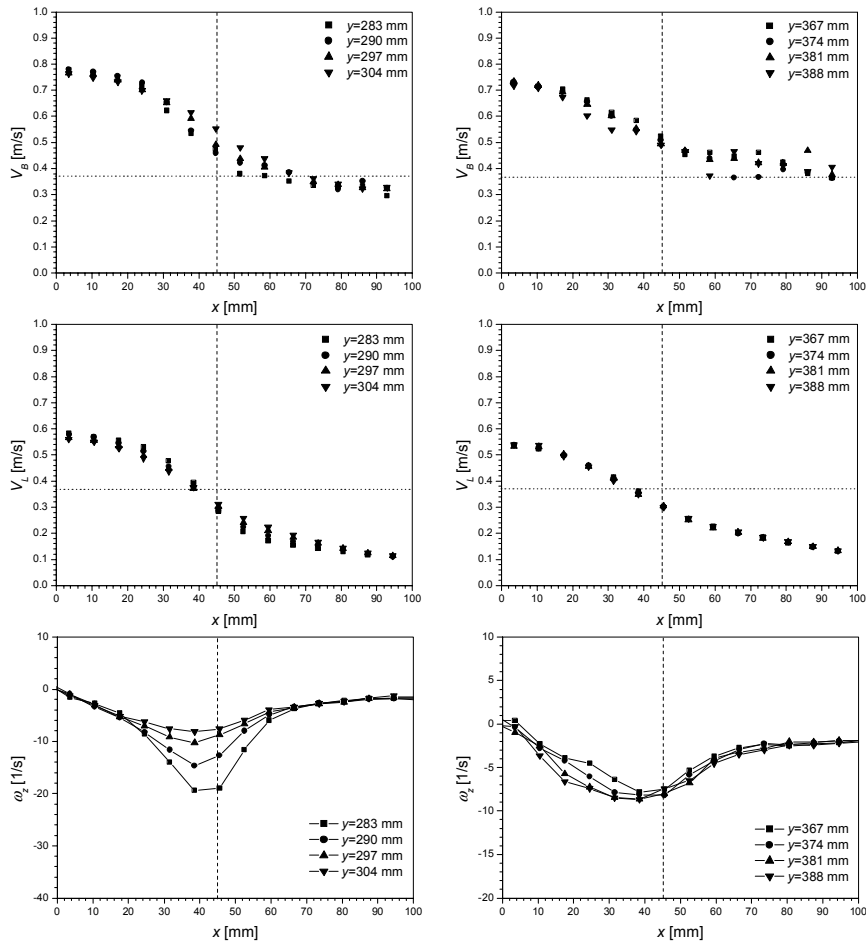


Figure (8.53): Phase-averaged velocity profiles of the bubbles and of the liquid and azimuthal vorticity profiles of the liquid at the elevations $y=283\text{-}304$ and $y=367\text{-}388$ mm from the nozzle exit.

8.6 Conclusions on bubble trapping

Based on results presented in this chapter the following conclusions can be drawn:

- Clear indication of bubble trapping inside coherent vortices is the formation of a bubble ring which travels at the same vertical velocity as the vortex ring. The trapping criteria formulated in Section 5.1.2 were approximately met in these cases (shown in summary in Table 8.2).
- In order to quantify this phenomenon it is necessary to estimate both vortex ring and bubble ring velocities.
- If the locations in the flow field where the phase-averaged vertical velocities of the bubbles are equal to the vortex ring or bubble ring velocity, they indicate positions of trapped bubbles.
- The phase-averaged velocities obtained by PIV of bubbles that are considered to be trapped may contain contributions of bubbles that travel at higher speed than the vortex ring velocity. Therefore it is recommended to study trapping phenomena simultaneously using PIV and a shadowgraphy technique, which employs an additional high-speed camera for tracking of the bubbles inside the vortices.
- Because of the decay of the coherent vortices and due to the secondary instabilities, the rings formed by trapped bubbles disintegrate at some distance downstream (shown in summary in Table 8.2).

Location	$y = 41mm$	$y = 140mm$
	$y/D = 0.45$	$y/D = 1.55$
Trapping Criteria (Section 5.1.2)	$\Gamma_\omega > 2.9$	$\Gamma_\omega > 3$
	$Fr_\omega > 1.4$	$Fr_\omega > 1.1$
Estimated parameters	$\Gamma_\omega = 2.7$	$\Gamma_\omega = 2.5$
	$Fr_\omega = 1.2$	$Fr_\omega = 0.77$
Drawn conclusions	Bubble ring is formed and travels with the same vertical velocity as the vortex ring.	The shape of the bubble ring is affected by the instabilities in the shear layer.

Location	$y = 283mm$	$y = 381mm$
	$y/D = 3.14$	$y/D = 4.23$
Trapping Criteria (Section 5.1.2)	$\Gamma_\omega > 3.1$	$\Gamma_\omega > 3.1$
	$Fr_\omega > 0.91$	$Fr_\omega > 0.45$
Estimated parameters	$\Gamma_\omega = 1.37$	$\Gamma_\omega = 1.2$
	$Fr_\omega = 0.19$	$Fr_\omega = 0.07$
Drawn conclusions	Trapping conditions are not satisfied and the bubble ring starts to disintegrate.	Bubble ring is fully disintegrated.

Table 8.2: *Trapping criteria and drawn conclusions.*

9 LIF visualization tests

The main motivation for conducting Laser Induced Fluorescence (LIF) experiments was to visualize bubble trapping inside large eddy structures, to obtain information on the size and development of these structures by comparing bubble velocity fields with instantaneous photographs of dye concentration fields, as well as to complete information presented in Chapter 8 regarding interactions and especially trapping of bubbles inside large eddy structures.

When using LIF for dye concentration measurements, one has to bear in mind that the emitted light intensity is proportional to the intensity of the laser light sheet illuminating the flow field, that has a non-uniform distribution, as it is attenuated in the fluid, especially in case of bubbly flow. The effect on the detected light intensity can be taken into account by conducting a complicated calibration procedure. Since the main purpose of this experiment is to visualize flow structures and especially bubble trapping, accurate information on dye concentration distribution is not needed.

Anyway, some of the image processing tools, that are applied in case of single-phase jets in order to demonstrate the main principles of the technique, can also be used in more advanced studies of dye concentration fields.

In general, the following phenomena can be studied:

Spreading of dye in the shear layer for single-phase and naturally-developing bubbly jets, effects of bubbles on shear layer development, visualization and tracking of large eddies for both single-phase and bubbly jets, visualization of bubble rings and their position inside large eddy structures, simultaneous observation of vortex and bubble ring movement, etc.

The single-phase flow regime investigated was *TTF2.VI.B*, whereas the triggered case was *f3*. More details about flow parameters, as well as PIV results for these cases, are presented in Chapter 8. In all cases investigated, dye was only added to the EF fluid (see Chapter 4), which mixes with surrounding fluid downstream of the jet nozzle and thus allows one to visualize the development of the mixing layer.

9.1 Single-phase naturally-developing jets

In order to extract information on the development of a shear layer and the distribution of a passive scalar (in this case, dye concentration), the images are processed by applying two different image operators for each pixel in a series of images:

1. The average-operator that calculates the average pixel value,
2. The max-operator that extracts the largest pixel value.

The sketch shown in Figure (9.1) illustrates the basic principle of image processing. The image operator is applied to high intensity pixel values (Pa and Pb) taken from the same location of two images. Therefore, the resulting pixel value Pn corresponds to the same location in the processed image.

The development of the shear layer for a single-phase jet is presented in Figure (9.2 a). The instantaneous photographic snapshot shows spreading of the fluorescent dye. It is obviously very difficult to identify large shear-layer vortices that are produced in case of naturally-developing

jets and, in particular, to estimate shape, diameter or dye concentration. On the other side, the instantaneous distribution of the dye in some regions of the shear layer indicates the existence of naturally-developed large structures. As concluded before, the production of shear layer vortices in case of naturally-developing flows is obviously a stochastic process, and therefore the systematic investigation of interactions between bubbles and vortices is difficult.

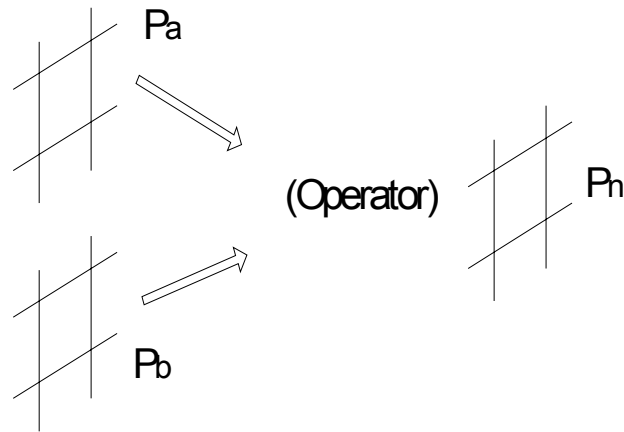


Figure (9.1): Basic principle of image processing.

Average Pixel Operator

The resulting picture obtained by applying both, the *Average Pixel Operator* and a thresholding procedure is presented in Figure (9.2 b). Since the operator was applied on 30 images acquired at $15Hz$, the resulting image is time-averaged. The chosen threshold value of 49 corresponds to the peak of the background light intensity obtained from a histogram ranging from 0 to 255. The average pixels which belong to the interval $[0 - 49]$ were replaced with zero values (black), whereas other intensities were kept as originally acquired and averaged. This kind of image processing operator only shows the downstream change of the light intensity emitted by the dye and is not an exact measure of its concentration.

The PIV experiments presented earlier that show decreasing variance of the liquid velocity downstream from the nozzle exit can also be used for visualizing the shear layer. The results of the LIF dye concentration field (a scalar map) and horizontal profiles of the pixel gray-scale values are presented in Figures (9.2 b) and (9.3), respectively. The PIV field of the variance of the vertical velocity (Figure (9.2 d)) gives similar pictures of the development of the shear layer. The PIV experiments can provide information on spreading, production and decay of turbulence in the shear layer, as well as on large eddy structures, whereas LIF dye concentration measurements can be rather used for visualization of the flow structures. The distribution of the laser light intensity must be taken into account if quantitative results have to be provided.

Estimates of the shear layer thickness (δ) obtained from the pixel gray-level distribution (Figure (9.3 top)) and from the variance of the vertical liquid velocity (Figure (9.3 middle)) are compared in Figure (9.3, bottom). These estimates are obtained from Gaussian approximations to the profiles of the form $e^{-\frac{4 \cdot (x-x_0)}{\delta^2}}$. By comparing photos of the instantaneous dye distribution in the shear layer and the scalar map of the variance of the vertical liquid velocity, one may conclude that the spreading of the passive scalar (dye) is different from the momentum spreading. Obviously, in order to study these phenomena in more detail, it is necessary to conduct extensive, well-controlled and carefully planned experimental investigations with both PIV and LIF techniques.

Max Pixel Operator

As expected, the image of the shear layer obtained by applying the *Max Pixel Operator* (Figure (9.2 c)) shows a slightly different development of the shear layer. The small white dots are caused by light emitted by seeding particles. Photos presented in Figure (9.2) show very similar development of the shear layer obtained after applying the Max Pixel Operator and of the shear layer illustrated in the scalar map of the variance of the vertical liquid velocity.

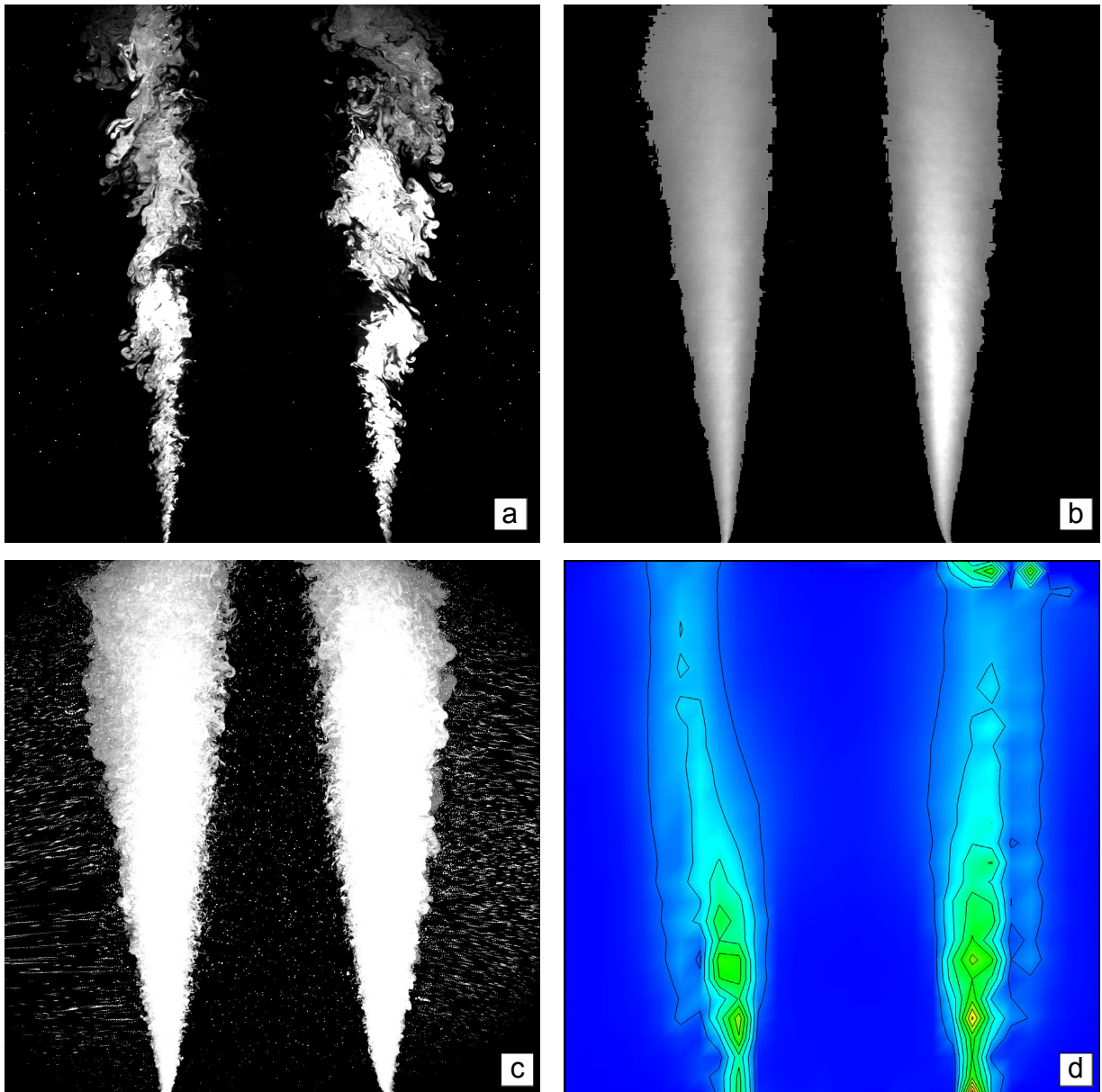


Figure (9.2): An instantaneous photo of the single-phase shear layer visualized by injecting fluorescent dye (a), a photo of the shear layer obtained by applying both, averaging and thresholding of the resulting image (b), a photo of the shear layer obtained by applying the Max Pixel Operator and thresholding the resulting image (c) and a scalar map of the variance of the vertical velocity obtained by PIV (d).

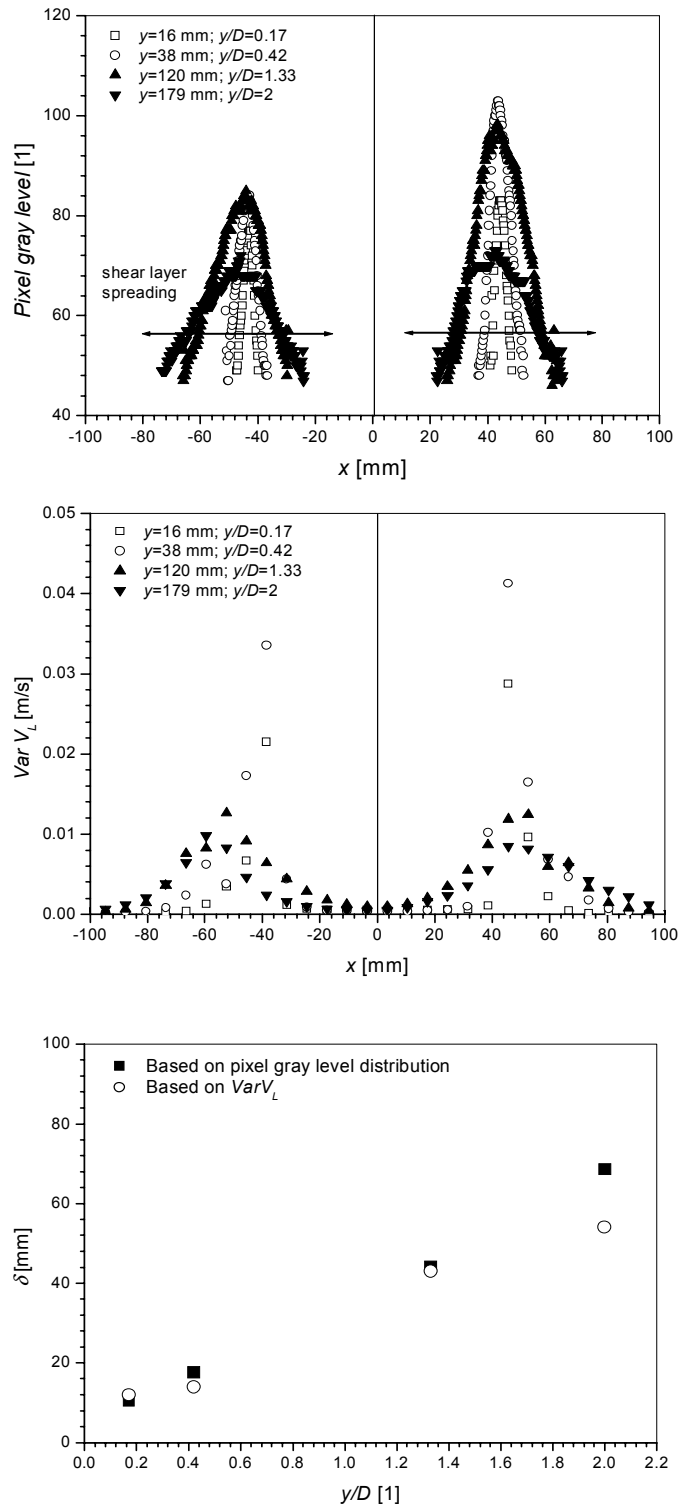


Figure (9.3): Pixel gray level distribution (top) and horizontal profiles of the standard deviation of the vertical liquid velocity (middle) show the development and spreading of the shear layer. The shear layer thickness estimated from the two sets of profiles presented is compared in the diagram at the bottom.

9.2 Naturally-developing bubbly jets

The evolution of the shear layer in the case of a naturally-developing bubbly jet is presented in Figure (9.4 b). If two instantaneous pictures of the shear layer for single-phase and bubbly jets are compared (Figures (9.4 a and b)), it is possible to notice different spreading of the dye in the shear layer, especially further downstream from the jet nozzle, also due to contraction of the bubbly jet caused by buoyancy. Obviously, the bubbles affect the development of the shear layer and the large vortices, as well as the spreading rate of the dye and interact with the structures in the shear layer. As mentioned before, the spreading rates in the inertial and transition region of bubbly jets may also be different. This phenomenon was, however, not studied during the current investigation.

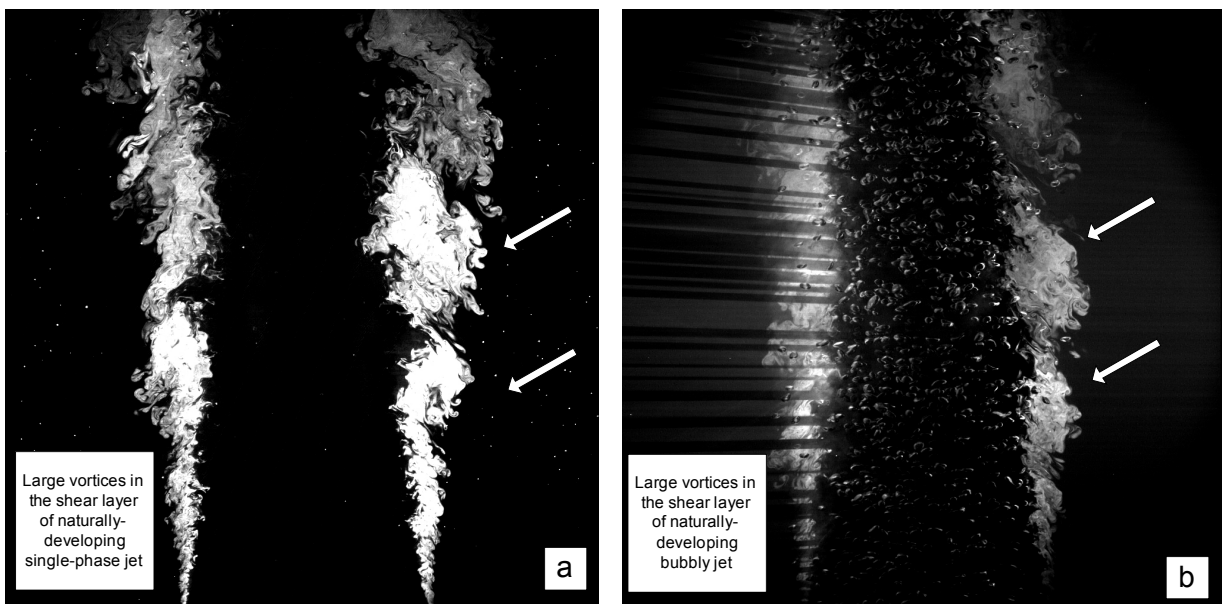


Figure (9.4): Photos of the shear layer of naturally-developing single-phase jet (a) and bubbly jet (b). White arrows show positions of large vortices.

9.3 Triggered bubbly jets

In general, dye concentration fields give information on vortex positions and size as well as distribution of dye concentration in the vortex structures. When illuminated by laser light, the injected dye emits light that also illuminates the bubbles in the flow field. Since the emitted fluorescent light and the laser light reflected from the bubbles have a similar effect as backlight, bubbles which are not located in the laser plane are also illuminated. Therefore, simultaneous information on bubble concentration in the laser plane cannot be obtained if it is not possible to discriminate the light reflected from the bubbles outside the laser plane.

The bubble trapping phenomenon, that is explored in detail in Chapter 8, is visualized here by using LIF and PIV techniques simultaneously. The light intensity distribution in the vortex rings (Figure (9.5)) shows structures that correspond to large vortices similar to those presented in the vorticity maps obtained by PIV (see Chapter 8).

Bubbles trapped inside these structures have the same velocity as the vortex rings. The results obtained by the *vortex tracking acquisition method* are presented in Figures (9.6) and (9.7).

Figure (9.6) shows six consecutive photos of the instantaneous dye concentration field, whereas six consecutive phases in Figure (9.7) are visualized by applying the *Max Pixel Operator* on 30 images. These results show that the fields of a passive scalar, i.e. the dye concentration, can be clearly distinguished and even tracked.

Comparison of the phase-averaged profiles of vertical and horizontal bubble velocity (Figure (9.8)) and the photo of an instantaneous dye concentration field (see Figure (9.5)) shows that bubbles move around the vortex center with coordinates $x = 50\text{mm}$ ($X = x + 108\text{mm}$) and $y \approx 80\text{mm}$. The vortex velocity is about 0.26m/s .

The sharp decrease of the vertical velocity of the bubbles for $x < -40\text{mm}$ and $x > 40\text{mm}$ indicates the domain where the bubble movement is determined by a local vortex. The x coordinate at which V_B equals the velocity of the vortex (see cross in Figure (9.5)) lies outside the vortex center ($x = 58\text{mm}$ and $X = 58 + 108 = 166\text{mm}$ in Figure (9.5)). This corresponds to trapped bubbles, for which the horizontal velocity U_B is near zero (see marked positions in Figure (9.8)).

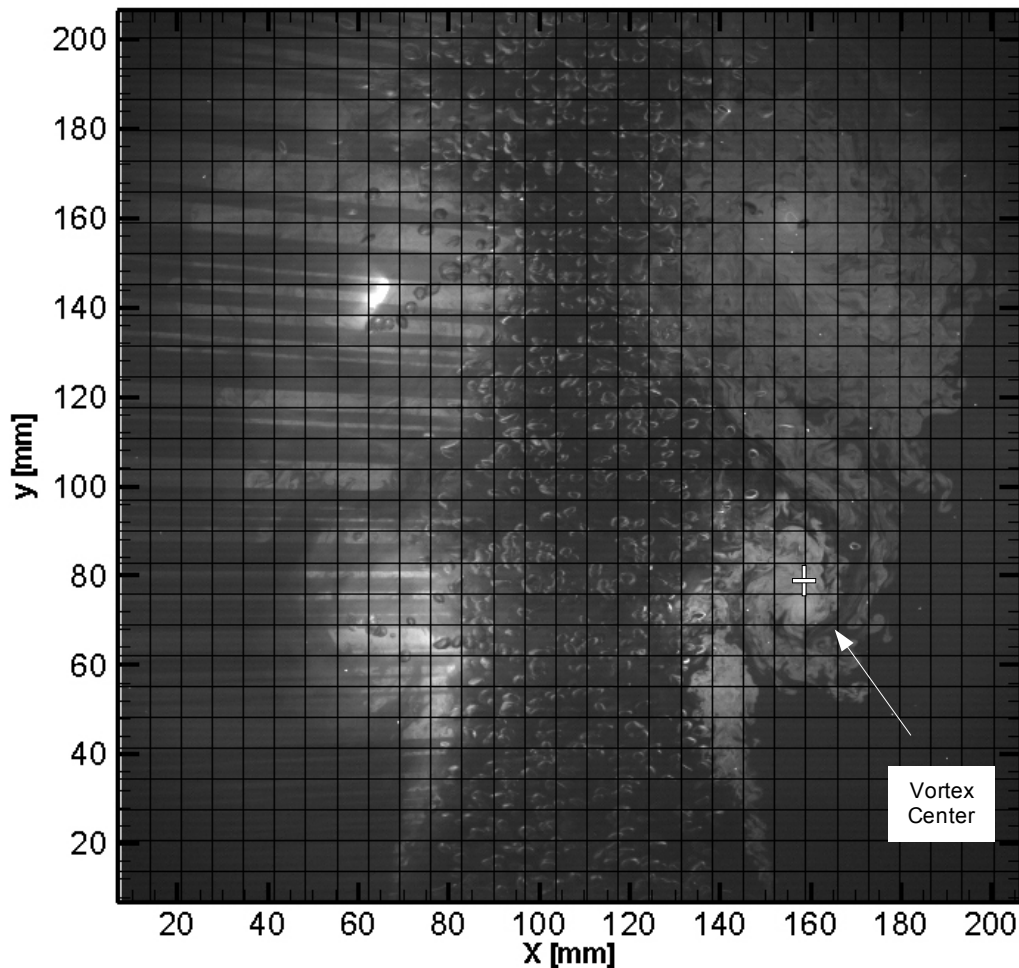


Figure (9.5): Photo of an instantaneous dye concentration field.

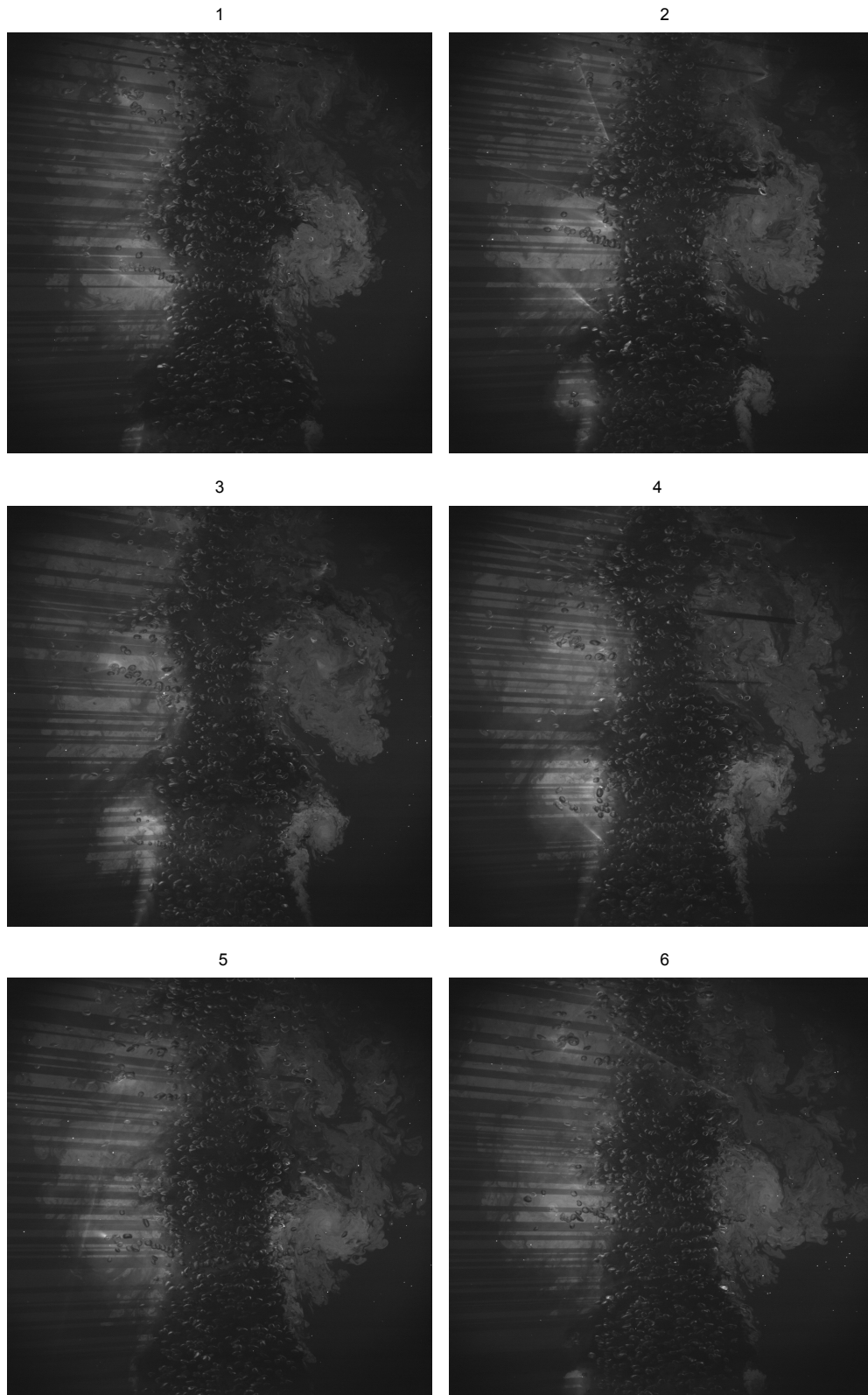


Figure (9.6): Six consecutive photos of the instantaneous dye concentration field. The time between two consecutive phase was 66.7 ms.

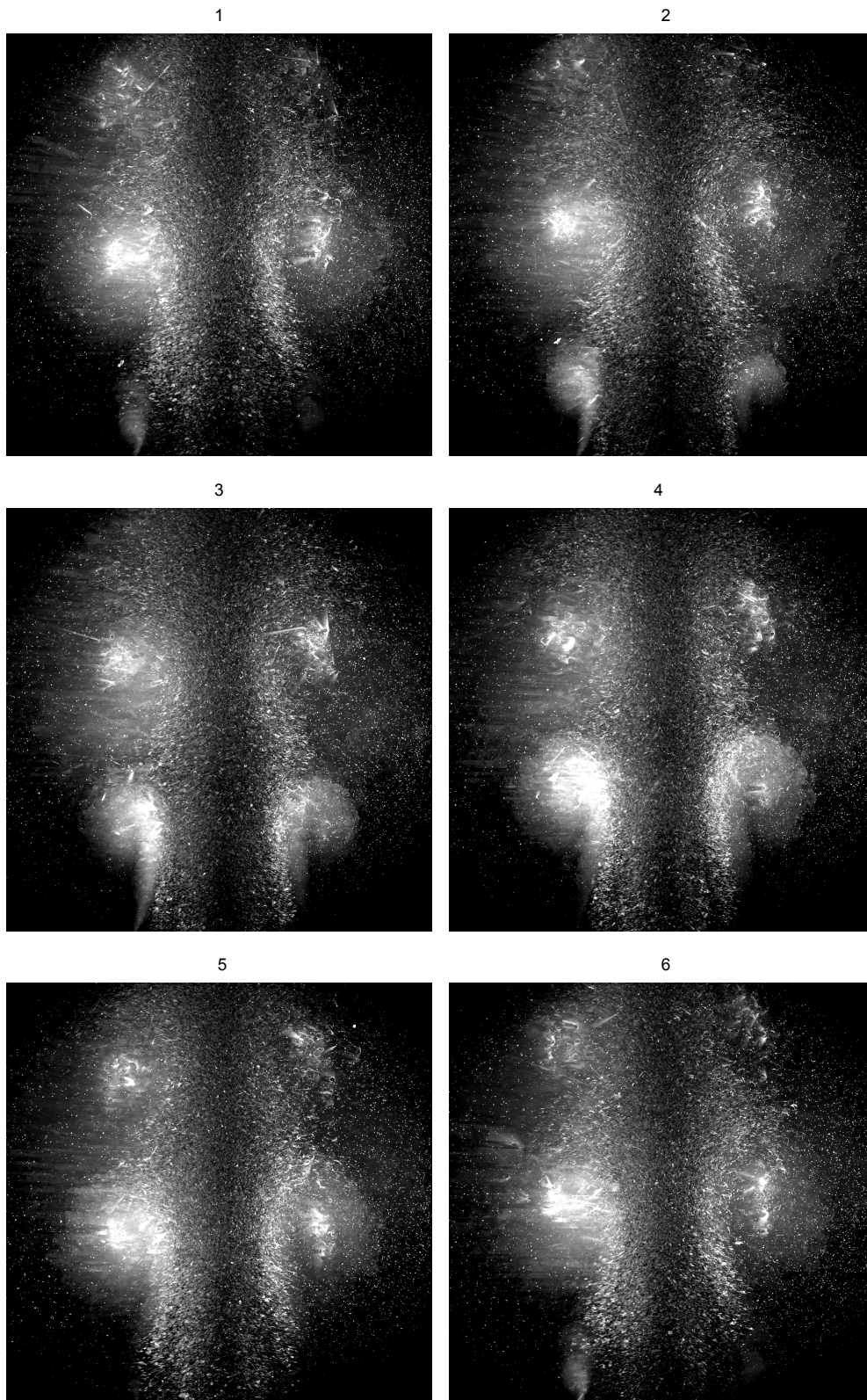


Figure (9.7): Six consecutive phases of the dye concentration field visualized by applying the Max Pixel Operator.

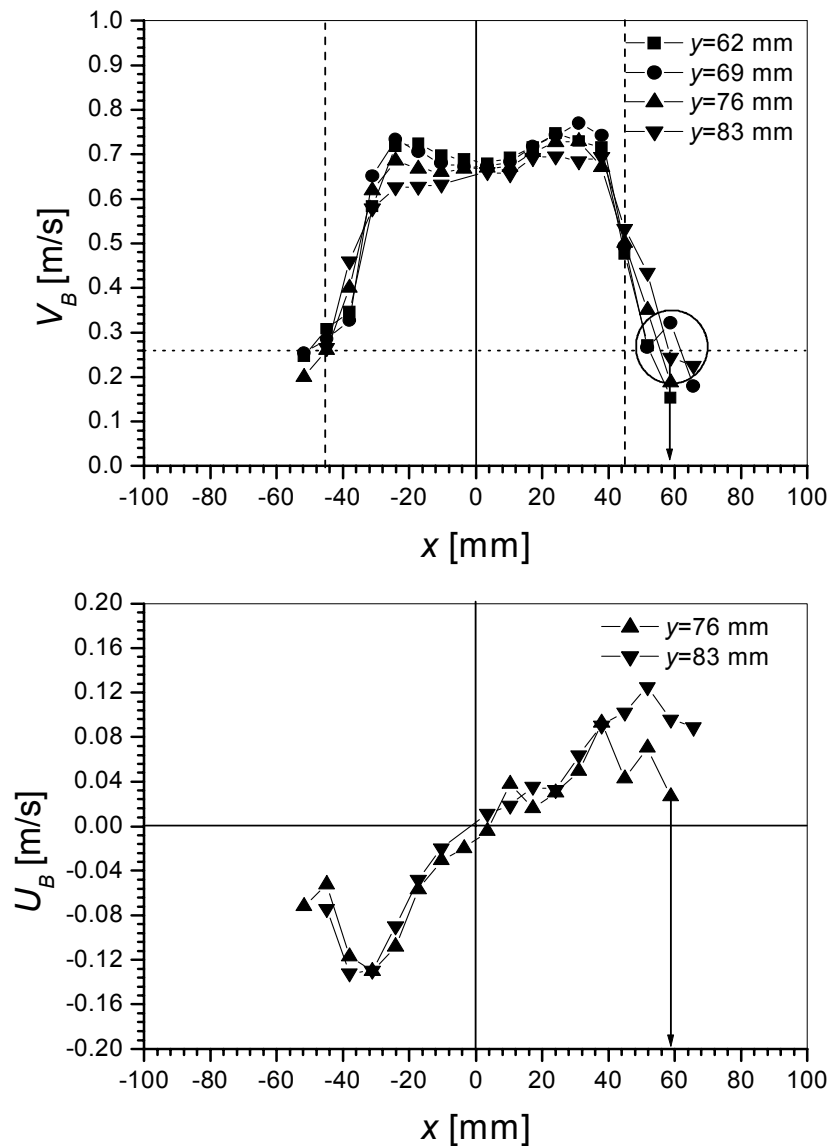


Figure (9.8): Profiles of vertical (top) and horizontal (bottom) bubble velocities through the visualised vortex ring.

The instantaneous photos of bubbles trapped inside vortices (vortex on the right side of photos shown in Figure (9.9) and the photo presented in Figure (9.10)) help to show real trajectories and positions of bubbles after they enter and move inside large vortex structures. For example, the bubble with the long shadow, located close to the center of the vortex is considered to be trapped. More advanced high-speed photographic techniques, that would allow tracking of bubbles inside large structures, would be required to provide sufficiently detailed data that could be compared with results of L-E computational methods and thus perhaps lead to further improvement of models of forces acting on bubbles. These were not possible within this project.

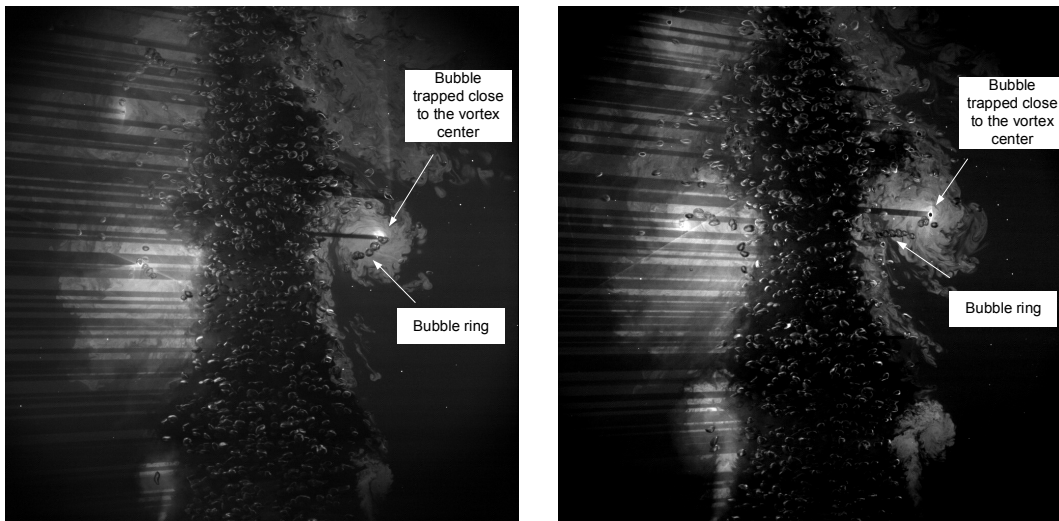


Figure (9.9): Photos of the vortex ring with bubble trapped close to the vortex center. The pictures, acquired at different times, show almost the same position of the vortex ring in the flow field and the trapped bubble close to the vortex center.

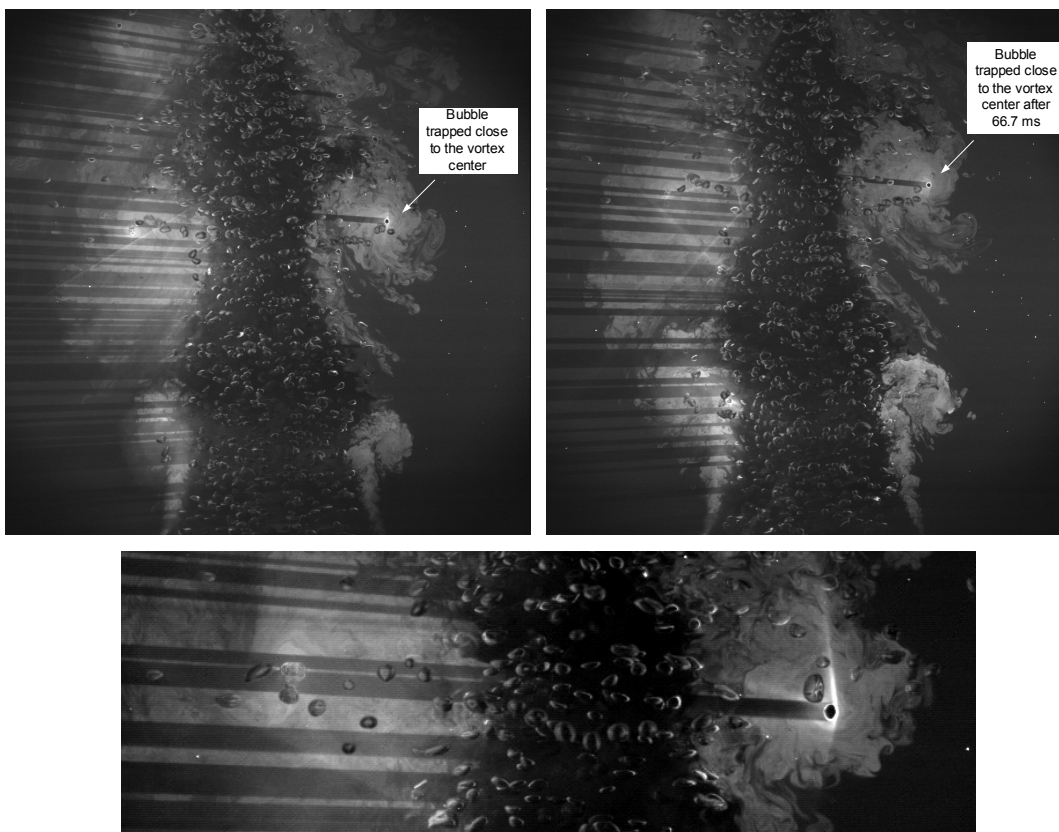


Figure (9.10): Photos of bubble trapped close to the vortex center at beginning and end of a time interval of 66.7 ms. The photo at the bottom represents the enlarged vortex ring with the trapped bubble as shown in the photo on the top-right side.

10 Some experimental results for dilute bubbly jets at low Reynolds number

In order to estimate the effect of the bubbles on the main flow properties such as: mean liquid velocity, standard deviation of the liquid velocity and kinetic energy of the liquid, experiments have been carried out with single-phase and *dilute bubbly jets* at various low Jet Reynolds numbers (i.e. low superficial liquid velocity at the nozzle exit). Monodisperse, uniform bubbles were used in this experiment. Furthermore, very small liquid flow rates inside the tubes were used in order to minimize the effects of the small jets on the mean flow properties. For dilute bubbly jets, feedback and bubble-bubble interactions do not play a significant role and, therefore, no attempt was made to measure and discuss the effect of the void fraction. Furthermore, measuring of the void fraction by means of DOS for dilute bubbly flows requires very long measurement times and carefully designed sensor tips as recommended by [34].

10.1 Test matrix

Table (10.1) shows the test matrix for low-Reynolds-number, naturally-developing, single-phase and very dilute bubbly jets (Figure (10.1)) with well-controlled bubble size that were experimentally investigated by PIV. Single-phase tests were also conducted at the same liquid flow rates, i.e. with $Q_G = 0NL/\text{min}$. Non-dimensional parameters such as the Jet Richardson and Jet Froude number as well as the non-dimensional quantities that characterize the flow regime show that the test with $Re_{jet,1}$ belongs to the class of *dilute bubbly plumes*, while the flows of the other tests can be considered as bubbly jets. The transition between jet and plume region is happening close to the nozzle exit. For the cases with $Re_{jet,3}$ and $Re_{jet,4}$, measurements at $y < 50mm$ lie in the inertial region of the bubbly jet, as the Jet Richardson number is about 1.8 and the non-dimensional distance ($\frac{y}{D} \cdot Ri_0$) at this elevation is less than 1. Measurements at $y > 100mm$ lie in the transition region.

Inlet parameters have been varied in order to change the Jet Reynolds number. All parameters presented were calculated by using the equations given in Chapter 5. The identification numbers in the test matrix indicate different jet flow conditions. The water level in the tank was $1200mm$ and the nozzle diameter $90mm$. Thermophysical properties for water and air are taken at $23^\circ C$. The bubble diameter was $2mm$.

In order to keep the parameters that determine the bubble formation equal for all tests, the liquid velocity inside the tubes was kept constant. This velocity is larger than the superficial jet velocity only for case $Re_{jet,1}$, whereas it is smaller for cases $Re_{jet,3}$ and $Re_{jet,4}$. In the single-phase cases, the tube flow thus produces jet turbulence only for $Re_{jet,1}$.

10.2 Experimental results and discussions

Assuming that the large turbulence scales introduced by the small jets have sizes in the range between the tube radius and one half of the tube pitch, i.e. about 2 to $6mm$, it is possible to resolve these structures by PIV if the size of the interrogation area is $16 \times 16 \text{ pixels}$ for

Test Name	1	2	3	4
Q_{Lin} [L/ min]	0.5	0.5	0.5	0.5
Q_{Lex} [L/ min]	4	8	15	20
Q_G [NL/ min]	0.1	0.1	0.1	0.1
Q_{Ltot} [L/ min]	4.5	8.5	15.5	20.5
Re_{jet}	1135	2144	3911	5172
ε_h [%]	2.38	1.27	0.7	0.53
ε_2 [%]	0.09	0.09	0.08	0.08
V_{Lin} [m/s]	0.02	0.02	0.02	0.02
V_{Gin} [m/s]	0.17	0.17	0.17	0.17
V_{jet} [m/s]	0.01	0.02	0.04	0.05
Ri_0	11.25	4.41	1.81	1.2
$\frac{y}{D} \cdot Ri_0; \frac{y}{D} = 0.5$	6.25	2.45	1	0.66
$\frac{y}{D} \cdot Ri_0; \frac{y}{D} = 1.12$	12.5	4.9	2	1.3

Table 10.1: Test matrix for experimental investigation of dilute, low-Reynolds-number bubbly jets. Corresponding single-phase tests were also conducted, i.e. with zero gas flow.

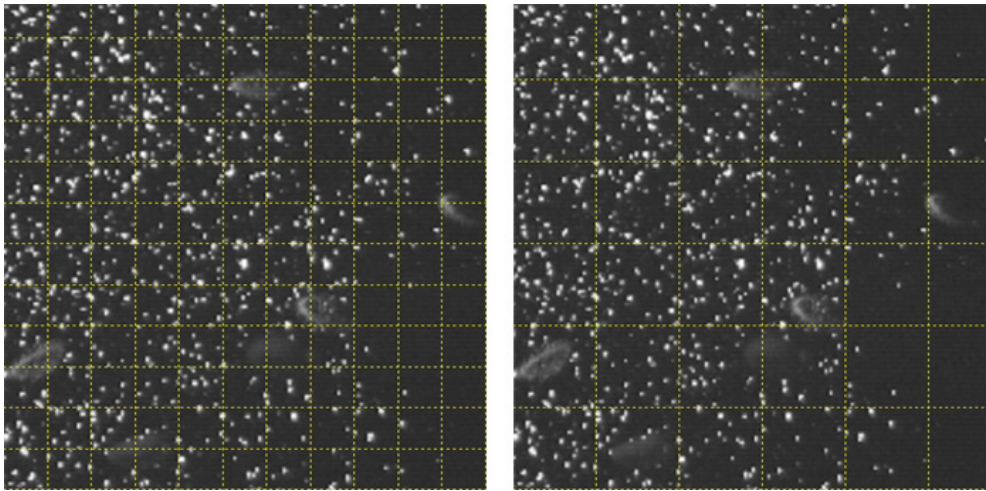


Figure (10.1): Snapshot of the flow field with dilute bubble concentration. The picture on the left shows 16x16 pixel-wide IAs, whereas the picture on the right shows 32x32 pixel-wide IAs.

a given resolution of $140\mu\text{m}/\text{pixel}$. In the case of dilute bubbly flow, it is preferable to use an interrogation area bigger than the bubble size, that is $32 \times 32 \text{ pixels}$. The two identical snapshots presented in Figure (10.1) show bubbles and seeding particles for a low-Reynolds-number dilute bubbly jet, using two different sizes of the interrogation area (the picture on the left is divided into IAs with $16 \times 16 \text{ pixels}$ and the picture on the right into IAs with $32 \times 32 \text{ pixels}$). The concentration of the seeding particles is adequate in both cases.

Downstream development of mean and turbulent properties

Scalar maps of the vertical velocity of the liquid and of its standard deviation are compared in the jet region for case $Re_{jet,3}$ in Figures (10.2) and (10.3).

The results presented show that even a small number of bubbles injected in a low-Reynolds number jet strongly affects the mean and turbulence properties of the flow. Jet shrinking caused by buoyancy forces can be observed in the near field of the jet.

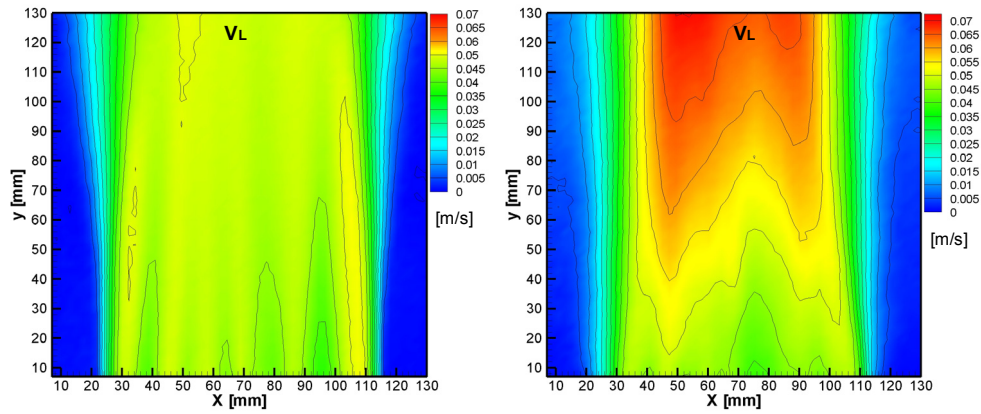


Figure (10.2): Scalar maps of the vertical velocity of the liquid for the single-phase (left) and the bubbly jet (right), $Re_{jet,3}$ case.

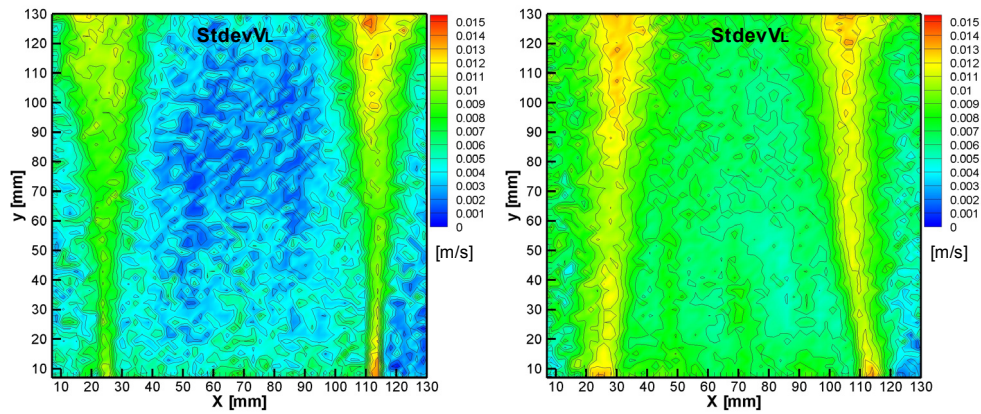


Figure (10.3): Scalar maps of the standard deviation of the vertical liquid velocity for the single-phase (left) and the bubbly jet (right), $Re_{jet,3}$ case.

The liquid-velocity profiles for the dilute bubbly jet at $Re_{jet,3}$ presented in Figure (10.4 a) shows the effects of bubbles on the mixing process and the development of the shear layer in both, the jet and the transition regions. In the region of inertia-dominated flow ($y/D < 0.5$), the effect of the bubbles on the mixing processes is much less pronounced than in the transition region ($y/D > 0.5$). The increment of the vertical velocity of the liquid indicates the acceleration of the flow due to the presence of bubbles. The shrinking of the jet presented in the scalar map in Figure (10.3), can be also observed by comparing the profiles of the standard deviation of the vertical liquid velocity, Figure (10.4 b).

Effects of the Jet Reynolds number

Profiles of mean velocities and kinetic energies of the liquid in bubbly flows are compared at $y/D = 1.12$ for the four Jet Reynolds numbers in Figures (10.5 a) and (10.5 b). Corresponding profiles for the single-phase jets with equal Re_{jet} can be found in Figures (10.7)

The kinetic-energy profile of the liquid for the single-phase case $Re_{jet,1}$ (Figure (10.5 a) at $y/D = 1.12$ is very broad. This flow regime appears to be almost laminar, but the shape of the

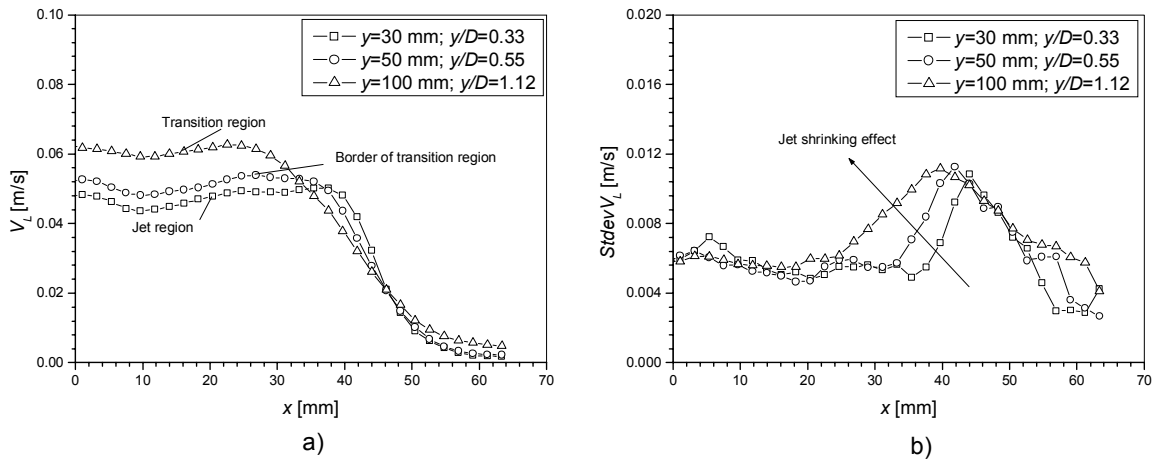


Figure (10.4): Downstream development of the profiles (vertical velocity of the liquid (a) and standard deviation of the vertical velocity (b)) for the dilute bubbly jet at $Re_{jet,3}$.

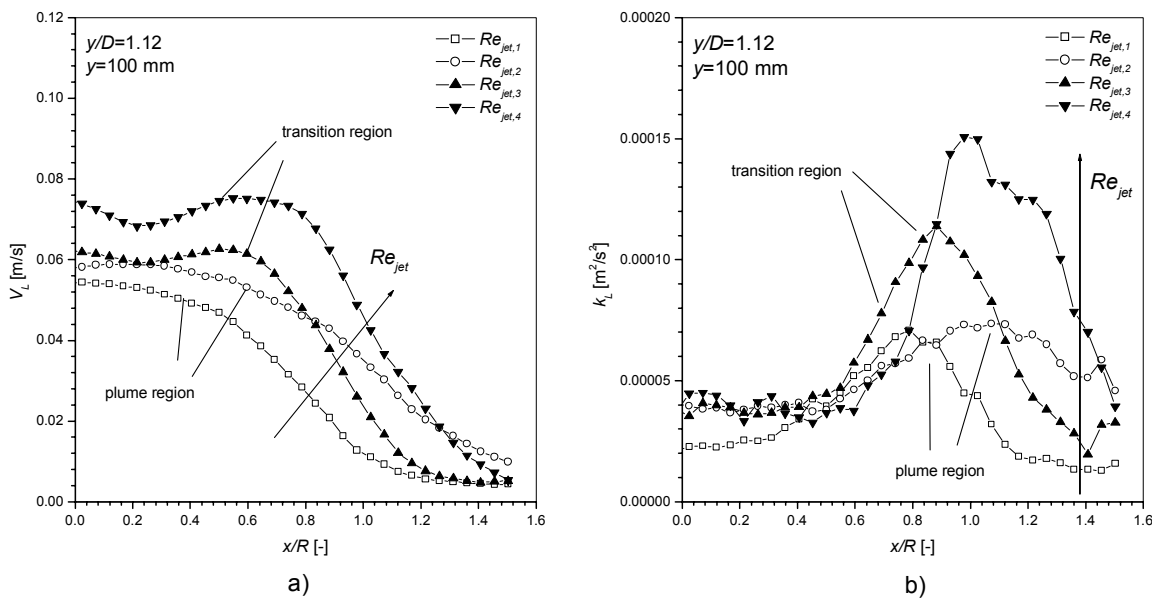


Figure (10.5): Vertical velocity of the liquid for the different cases (a) and kinetic energy of the liquid for the different cases (b).

velocity profile, which is close to Gaussian resembles that of a fully-developed jet. The tube jets produce perhaps more intense mixing than in the other cases, and therefore the asymptotic shape of the velocity profile is reached much faster. For the bubbly jet with $Re_{jet,1}$, the flow region at $y/D = 1.12$ belongs to the plume zone since the Richardson number (Ri_0) is about 11.2 and the criterion presented in Section 5.2 is fulfilled. Obviously, bubbles intensely modify the turbulence properties of the liquid in the bubbly plume region (Figure (10.7 b)).

For the higher Reynolds numbers, the profiles of mean velocities and kinetic energies in the single-phase jets are typical for the developing region, but bubbles also affect turbulence that is essentially produced by shear in single-phase jets. In these cases, the peak values of the kinetic

energy of the liquid in the shear layer are slightly smaller for bubbly flow (Figure (10.7 b)) than for single-phase flow.

Effects of bubbles on the profiles of mean velocity and kinetic energy of the liquid

From the mean normalized profiles of vertical velocity and kinetic energy of the liquid for single- and two-phase flow (some illustrations of dilute bubbly flows are presented in Figure (10.6)), which are compared at $y/D = 1.12$ in the jet region for four jet Reynolds numbers in Figure (10.7), the following conclusions can be drawn:

- Even though the void fraction is very low, the bubbles modify both the mean and the turbulence properties of the liquid jet.
- For lower Reynolds jet number, the borders of the transition and of the bubbly plume regions are reached closer to the nozzle exit. The velocity profiles already have a Gaussian shape, which is characteristic of buoyancy-dominated flows.
- For higher Jet Reynolds number, the bubbly plume region is reached further downstream. These regimes can be used for providing experimental data for validating turbulence models in both inertia and buoyancy-dominated flows. As shown in Chapter 6, it is expected that single-phase turbulence models are applicable in the near field of the jet.

General conclusions and recommendations for future work

Dilute bubbly jet and bubbly plume flows should be extensively investigated in order to provide a data base for developing and validating turbulence models. Due to the very low bubble concentration, other techniques such as LDA and HFA should also be applied for resolving liquid velocity fields, in order to provide data for spectral analysis and to investigate the effects of the bubble size on turbulence modulation.

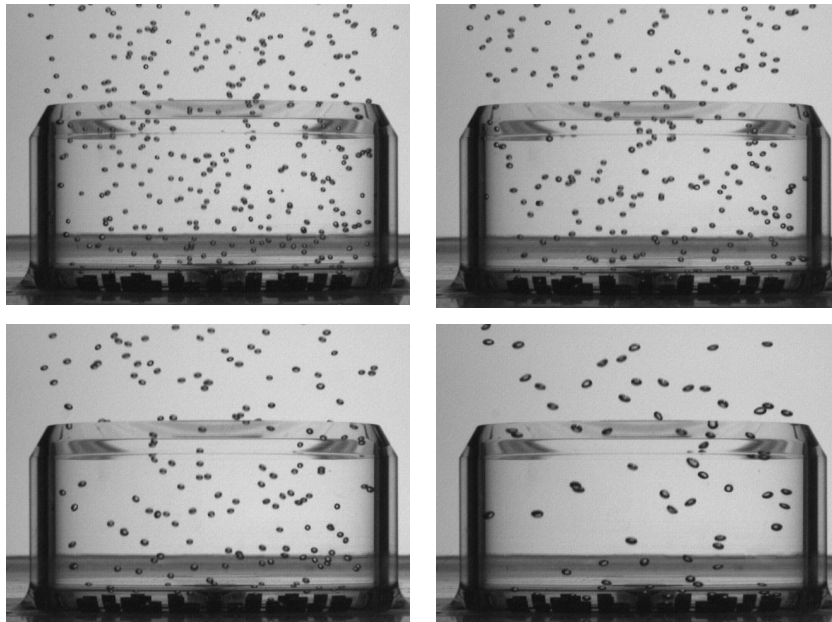


Figure (10.6): Photos of dilute bubbly flows with different bubble size generated in the gas/liquid injector by decreasing the liquid flow rate inside tubes (from top left to bottom right), while the gas flow rate was constant.

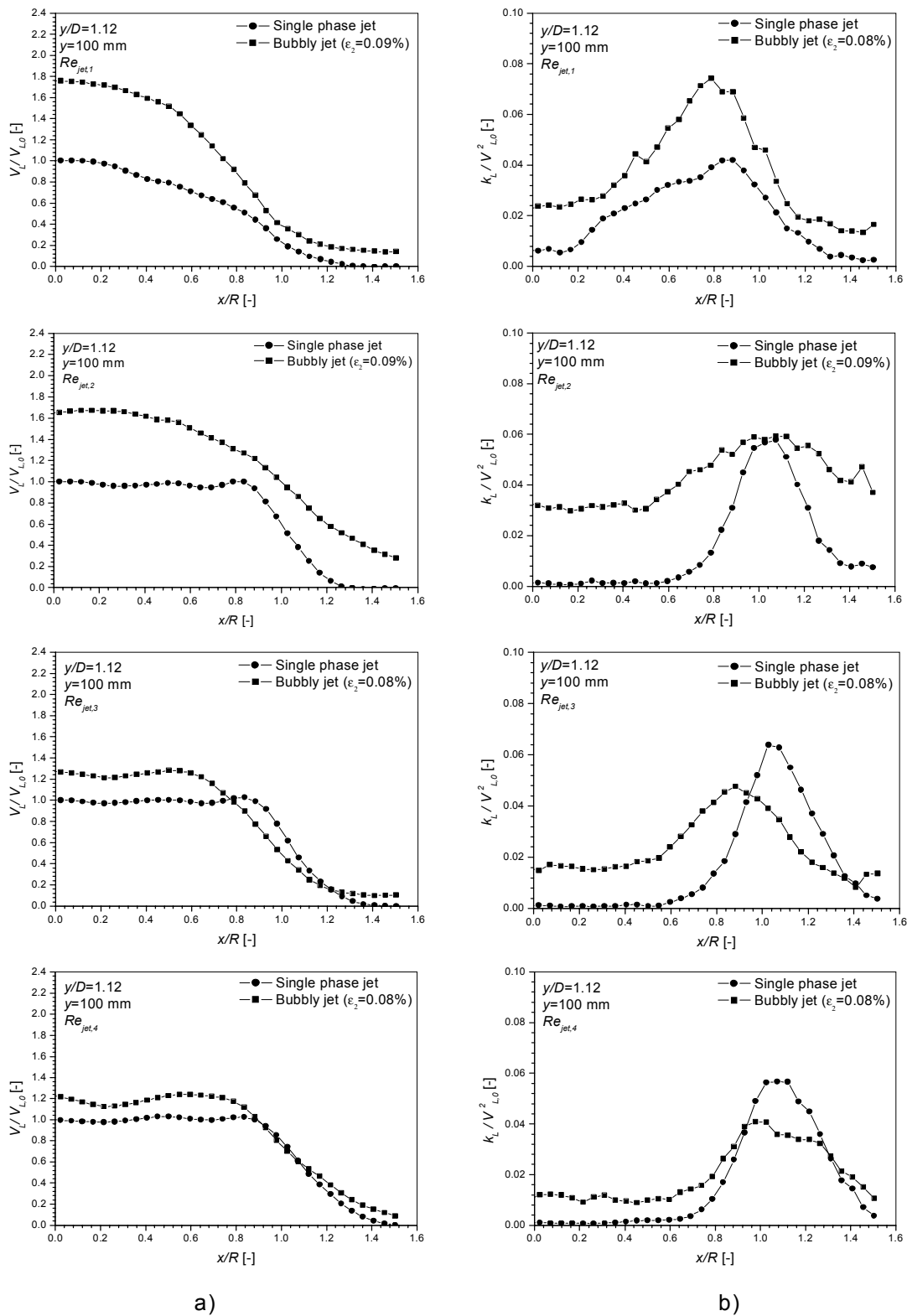


Figure (10.7): Comparison of the scaled velocity profiles (a) and of the scaled kinetic energy of the liquid (b) at $y/D=1.12$ between single-phase and bubbly jets.

11 Summary and conclusions

In order to improve physical insight into turbulent bubbly jet flows, the present experimental investigations have been carried out with a bubbly jet formed by injecting a water-bubble mixture vertically upward at the bottom of a large pool with stagnant water. A completely new experimental installation equipped with modern data and image acquisition systems, as well as systems for positioning the sensors and cameras were built.

The main goal of these investigations is to study the interactions between liquid and bubbles in turbulent *naturally-developing bubbly jet flows* as well as between large coherent structures of liquid and bubbles in *periodically-excited bubbly flows*.

In the case of naturally-developing jets, investigated first, the study of interactions between dispersed (bubbles) and the continuous phase (liquid) essentially yields only stochastic results. For a mechanistic investigation of fluid bubble interactions, it is, however, more informative to create large orderly structures by periodic excitation of the jet. This is achieved in a second series of experiments by modulation of the shear layer at the jet exit by means of a small external coaxial surging flow at controllable frequency and amplitude. The large coherent vortices formed in the shear layer of the jet affect bubble movement. Namely, when bubbles enter such vortices, they can be trapped if certain conditions are fulfilled. *Bubble trapping* actually means that bubbles reach an equilibrium position within the vortices and travel with them at the same vertical velocity. If bubbles reach such a position in the vortices, a bubble ring is formed.

For the naturally-developing bubbly jet flows, where the measurement of statistical properties and of the spatial distribution of local stochastic parameters is the main objective, a number of experiments have been carried out to study the effects of flow parameters and inlet conditions. In particular, the influence of flow parameters (bubble size, void fraction, Jet Reynolds number, etc.) on jet development, bubble dispersion, turbulent properties and entrainment have been studied.

In industrial applications, it is important to design apparatuses and to control flow characteristics in such a way that processes perform optimally. These characteristics include the liquid-phase velocity distribution and turbulence and gas-liquid interfacial properties for mass, momentum and heat exchange. The results presented can be helpful for the qualitative understanding of the physical processes involved and the tuning of computational tools that are needed for design of industrial processes.

11.1 Characteristics of naturally-developing turbulent bubbly jets

In the first series of tests, the effects of bubble size and concentration on turbulence, velocity and void distributions, shear-layer spreading rates, mixing, characteristic length scales and velocity correlations have been studied. However, these measurements provide results only on statistical properties and the spatial distribution of local stochastic variables.

In order to show the effect of bubbles on jet flow, it was necessary to also perform experiments with single-phase jets with comparable inlet conditions to those of the bubbly jets in the developing region using PIV as the main experimental technique. These PIV data were compared

with data obtained by HWA [6] in order to check important PIV settings such as the size of the interrogation area and the time between two laser shots. The results are used as reference data for studying the effects of parameters such as void fraction and Jet Reynolds number.

To study the effects of bubble size on turbulent properties of the liquid and to support various numerical approaches, the experimental investigations should be performed on dilute bubbly flows by experimental techniques that allow simultaneous measurements of velocity and concentration fields. If simultaneous measurements of the stress term, that appears for instance in the LES model, of the bubble and liquid velocity fields as well as of the void fraction or bubble concentration fields can be performed by a special experimental technique, it will be possible to correlate data and to validate empirical closure models that can be directly included into numerical simulations. Unfortunately such a technique is not developed yet, but simultaneous PIV measurements with advanced image analyses will certainly open another chapter in exploring complex two-phase flow phenomena.

Effect of bubbles on entrainment and on the liquid velocity

The objective of these investigations is to quantify the augmentation of entrainment in the inertial and transition regions of *the bubbly jet*. Most data found in the literature relate to the far field of the flow, where nearly asymptotic conditions prevail.

Comparisons of experimental data for single-phase cases and bubbly jets (flow condition *TF3.VI*) show that entrainment is indeed enhanced due to the presence of bubbles. The void fraction effect on entrainment varies in different regions of the jet.

In the region of inertia-dominated flow, the effect of the bubbles on mixing is much less pronounced than in the transition region, where the entrainment mechanism is much more efficient due to the buoyancy effect.

Turbulence properties of the jet and effect of bubbles

Based on the experimental results presented, the following conclusions can be drawn:

- Turbulent fluctuations of the single-phase jet with internal liquid flow in the injector tubes are stronger than those of the jet without internal flow due to the higher turbulence level at the nozzle exit, which is induced by the liquid jets from the tubes. This effect is especially pronounced in the case of small Jet Reynolds numbers. For higher Jet Reynolds numbers, the enhancement of turbulence is weak, since the liquid velocity inside the tubes is the same as that of the external flow for all three Re_{jet} numbers.
- Due to the bubble drift, turbulence intensities of the bubbly jets are higher than those of the single-phase jets in both, the inertial and the transition regions.
- The joint effects of bubbles and inlet turbulence are more pronounced in case of low Reynolds number jets. This can be concluded by comparing vertical velocity profiles. In the inertial region of the jet, the velocity profiles already have Gaussian shape. In case of higher Reynolds jet number, profiles are still flat in the inertial region;
- In the inertial region of the bubbly jet, the shear layer is shifted toward the jet centerline, which means contracting or shrinking of the jet due to its acceleration. This effect is more pronounced in the case of higher Jet Reynolds number.
- In the transition region of the bubbly jets, the vertical velocity profiles have a Gaussian shape, the entrainment is enhanced due to the presence of bubbles, and shear layer turbulence decays.

Testing of simplified turbulence models

Some of the basic concepts such as the mixing-length model of Prandtl, the $k - L$ model and two-equation models like the $k - \varepsilon$ have been tested. In experimental work on bubbly jets and plumes, most data found in the literature relate to the far field of the flow, where nearly asymptotic conditions prevail. The models are applied to own experimental results, first in relation to the single-phase jets and then subsequently to the bubbly jets.

For all single-phase cases, very good agreement was found between algebraic Reynolds stress expressions that are based on turbulence models and the stress term measured by PIV in the near field close to the nozzle exit.

In the region of the inertia-dominated part of the bubbly jet ($y/D = 1.12$), the above-mentioned $k - L$ model was tested for four flow regimes: two different Jet Reynolds numbers, while the void fraction was also varied to examine bubble effects on jet turbulence. Since the effect of buoyancy in this region is relatively small compared to that of inertial forces, it is realistic to assume that existing single-phase models might work well, as actually shown. This is reasonable to expect, since the liquid-phase turbulence is mainly driven by shear in the near jet region. In the case of a bubbly jet with a void fraction of about 2%, the situation is not dramatically changed.

Further downstream, where the effect of the buoyancy forces starts to dominate the flow, bubbles significantly influence the turbulence of the liquid phase and also affect the shear-induced turbulence in the mixing layer. No attempt was made to decompose the total kinetic energy into contributions due to shear-induced turbulence and pseudo turbulence.

Experimental results for dilute, low-Reynolds-number, bubbly jets

In order to estimate the effect of the bubbles on the main flow properties such as: *mean liquid velocity, standard deviation of the liquid velocity fluctuations and kinetic energy of the liquid*, experiments have been carried out with dilute bubbly jets at various low Jet Reynolds numbers (i.e. low superficial liquid velocity at the nozzle exit). Monodisperse, uniform bubbles were used in these experiments. Furthermore, very small liquid flow rates inside the injector tubes were used in order to minimize the effects of the small jets created by the tubes on the mean flow properties.

The development of the vertical velocity profiles shows the effects of bubbles on entrainment and the development of the shear layer in both, the jet and transition regions of the dilute bubbly jet.

In the region of inertia-dominated flow, the effect of the bubbles on entrainment is much less pronounced than in the transition region where buoyancy forces start playing more important role.

An increment of the vertical velocity of the liquid indicates the acceleration of the flow due to the presence of bubbles. Shrinking of the jet can be observed either in the scalar-map figures of the standard deviation of the vertical liquid velocity or by comparing the diametrical profiles of the standard deviation of the vertical liquid velocity.

11.2 Interactions between bubbles and large vortices

The bubble trapping phenomenon, which can also occur in naturally-developing jets, was one of the main issues of this work and was investigated in a second series of tests. Trapping criteria were thoroughly discussed and bubble trapping could be experimentally verified. In the experiments with naturally-developing bubbly jets, it was not possible to fulfill the trapping conditions, which required higher values of Froude number and Trapping parameter. The Jet Reynolds number could have been increased either by installing a more powerful pump or a smaller jet nozzle. The former was not done because of lack of time and the latter for the following reasons. In general, the size of the large eddy structures generated in the shear layer is affected by the size of the nozzle. With smaller nozzles, smaller structures are produced. It is, however, preferable to achieve a high ratio of the size of large vortices to that of bubbles in order to study the interaction between bubbles and vortices. Further, the appropriate PIV settings, such as dimension of the field of view, camera resolution and size of the interrogation area must be carefully chosen in order to optimally resolve flow structures.

Experimental data obtained for test *TF3.VI* by DOS and PIV show that there are individual bubbles which have velocities equal and even smaller than the mean velocity of the liquid measured at the same position in the shear layer. This result indicates that individual bubbles might be trapped inside large structures and travel with a velocity that corresponds to the velocity of these structures. The process is obviously and clearly stochastic, therefore a systematic observation of interactions between bubbles and large eddy structures is difficult and requires the simultaneous detection of bubbles and velocity fields by combining, e.g., photographic techniques with PIV in the case of naturally-developing jets. In addition, it is obviously very difficult to obtain information on size and development of the large eddy structures in naturally-developing flows, as well as to quantify the interaction between bubbles and the large vortices that are formed in the shear layer. In general, for correlating bubble and liquid velocities with void fraction, it is necessary to develop new or to improve existing experimental techniques for the simultaneous measurement of these quantities. In reality, the simultaneous PIV measurements that were applied during this study represent a very first, basic step as they resolve only velocity fields in two-phase flow. Processing of the complicated images for obtaining information on bubble concentration inside the interrogation area could, however, be a tempting task for future investigations.

The trapping condition could however be fulfilled by triggering the jet by a periodical surging flow, imposed at the nozzle exit, that produces a concentration of the shear layer vorticity in coherent large-scale ring structures. This method allows one to control the trapping conditions by varying the amplitude and frequency of the surging flow. These parameters affect the maximum vorticity and the shape of the vortices and therefore also the Vortex Froude number and the Vortex Trapping parameter.

The main objectives of the second set of experimental investigations were: to vary trapping conditions at the jet exit, to develop an experimental procedure for tracking both liquid and bubbly structures in order to study interactions between them and to quantify bubble trapping inside large vortices that are formed in the shear layer.

In order to fulfill these objectives, the following phase-averaged quantities were simultaneously measured and computed from the data: the azimuthal liquid vorticity field, vertical velocity of the liquid and bubbles and vertical velocity of both the vortex ring and of the bubble ring. The azimuthal liquid vorticity field provides information on the size, shape and position of large vortices in the flow field, as well as the maximum vorticity at the vortex center. These data were used to calculate the Vortex Trapping parameter and the Vortex Froude number and to check

whether the simplified condition for bubble trapping was fulfilled or not. Furthermore, data at different phases within the triggering periods could be acquired, phase-averaged and analyzed.

The tests show that the triggering amplitude and frequency influence the maximum vorticity at the vortex centers and therefore the velocity of the liquid circulating around vortex axes. If the amplitude is increased, the inertial force acting on bubbles is enhanced and the trapping condition is reached. If the triggering amplitude is small and the values of the Vortex Trapping parameter and of the Vortex Froude number are below the minima for trapping, the bubbles can escape the vortices. These bubbles are dispersed by shear layer turbulence. This situation usually happens in all cases further downstream, i.e. at about $y/D = 4$. The triggering experiments are done with a fixed amplitude, while the excitation modes that correspond to $St = 0.3, 0.6$ and 0.8 are investigated.

It is important to emphasize that the flow field conditions change downstream. This influences the development of the large structures and the trapping condition. Therefore, the results are systematically presented for different positions of the flow structures in the field.

The downstream variation of the Vortex Trapping parameter and of the Vortex Froude number for a given excitation frequency showed that trapping conditions could not be maintained beyond $y/D > 3.5$; the bubbles escaped from the vortex rings and were dispersed by large structures in the surrounding fluid. This phenomenon happened in the transition region where the buoyancy force starts to dominate the flow, but buoyancy need not to be the main cause of this phenomenon. In general, the relation between different forces acting on bubbles in the downstream directions change, and this affects bubble agglomeration inside large structures and distribution of the bubbles in the shear layer.

Also, a comparison of tests performed with naturally-developing single phase jets and bubbly jets shows that excitation of the flow increases turbulence properties at the jet axis, as well as in the shear layer.

11.3 Suggestions for future work

In order to complete and extend experimental results and to create a data base for validating CFD codes the following steps are recommended:

- Extension of the test matrix (higher flow velocities, more powerful water loop and/or smaller size nozzles) in order to achieve higher values of the Jet Froude number and of the Trapping parameter in case of naturally developing bubbly jets.
- Development of techniques for simultaneous PIV and void fraction measurements.
- Detailed investigation of the differences between transport of bubbles, fluid momentum and passive scalars (dye) in natural bubbly jets.
- In order to provide an extensive data base on the *effect of bubbles on entrainment*, the velocity and void fraction profiles for various flow regimes of bubbly as well as single-phase jets should be measured and integrated for various flow conditions and at a larger number of axial levels in inertial, transitional and buoyancy-dominated regions of bubbly jets. The experimental data could be presented in the form used by Papanicolaou [46] in case of vertical buoyant single-phase jets, where the local Richardson number ($Ri(y)$) is plotted versus the non-dimensional distance from the jet exit (y/l_M). This kind of information for two-phase jets does not yet exist in the literature.
- For the investigation of pseudo-turbulence, it is recommended to analyze dilute bubbly jets with well-defined and controllable bubble sizes for laminar and turbulent liquid flow condi-

tions and to systematically compare data with single-phase experiments in different regions of bubbly jets. Also, with the above-mentioned technique for the simultaneous measurement of velocities and void fraction, correlations between liquid and bubble velocities with the void fraction could be obtained. This kind of information for two-phase jets also does not yet exist.

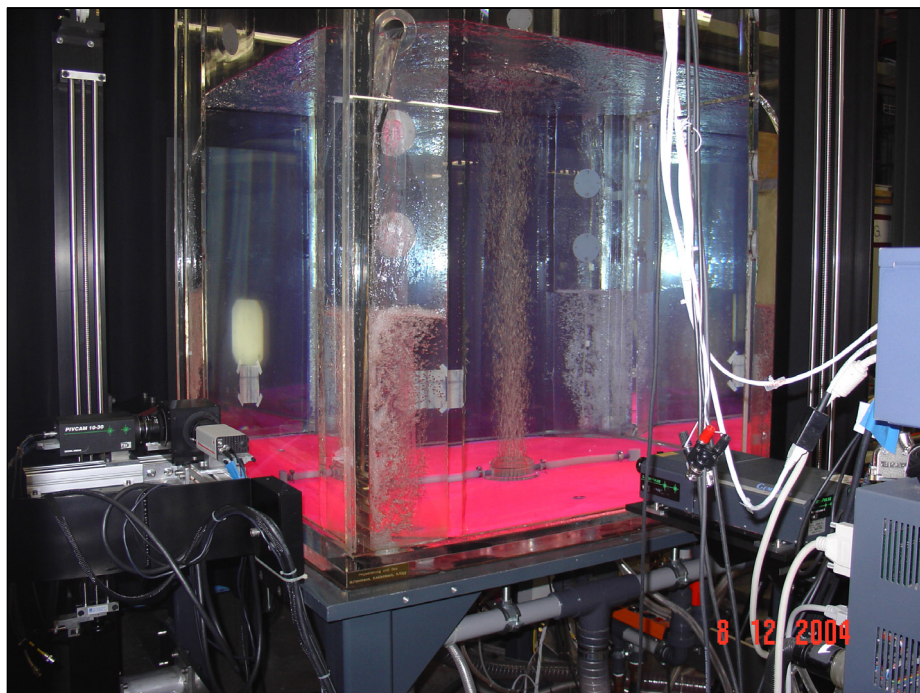
- To develop an image acquisition procedure for the simultaneous tracking of bubbles and vortices. Experimental data for different flow conditions can be very useful for validating Lagrangian-Eulerian (L-E) methods and the models of different forces acting on bubbles.
- Excitation of subharmonics which are responsible for vortex pairing. Study of effects of bubbles on vortex pairing phenomena in an axisymmetric mixing layer.
- Triggered LIF visualization tests (position, size and velocity of large-scale structures, difference between bubble field and dye concentration). Dye should be injected into the shear layer and/or the jet flow.

The bubbly-jet experimental installation, that was built as a part of this work can be easily modified, equipped with additional experimental techniques and used for various single-phase and two-phase experiments. This installation and the methods developed can make further useful contributions to the exploration of bubbly jet flows and the further development of CMFD.

A Experimental facility



From here to ...



Experimental facility equipped with the PIV system.

A.1 Water loop, air supply and list of instruments

The schematic diagram of the bubbly-jet experimental facility is shown in Figure (A.1). Tests are performed in a tank, which is connected via the injector (description is given in Chapter 4) to the water loop and the regulated air supply. The list of instruments embedded in the water loop and the air supply are shown in Tables (A.1) and (A.2), respectively.

The total liquid flow rate is adjusted by valves $VM0017$ and $VM0018$, the internal liquid flow rate by valve $VM0015$, the external liquid flow rate by valve $VM0014$ and the gas flow rate by the mass flow controllers $FM0001$ and $FM0002$. Controlling the cooling water flow rate through the heat exchanger regulates the water temperature in the loop.

Instrument	Function
$TF0002$	External water temperature before entering injector
$TF0003$	Temperature indicator for controlling loop temperature (controlling cooling water flow rate)
$TF0004$	Internal water temperature before entering injector
$PG0004$	External water pressure before entering injector
$FM0003$	Internal water flow rate before entering injector
$FM0004$	External water flow rate before entering injector
$FM0005$	Total water flow rate before entering injector
$PG0004$	Water pressure after pump
$PG0005$	Cooling-water pressure
$FM0006$	Cooling-water flow rate
$PG0003$	Internal water pressure before entering injector
$TF0005$	Water temperature at storage tank outlet

Table (A.1): Instruments embedded in the water loop.

Instrument	Function
$TF0001$	Air temperature before entering injector
$PG0001$	Air pressure before pressure reducer
$PG0002$	Air pressure before entering injector
$FM0001$	Regulating and indicating air flow rates (0 – 30Nl/min)
$FM0002$	Regulating and indicating air flow rates (0 – 1Nl/min)

Table (A.2): Instruments embedded in the air supply.

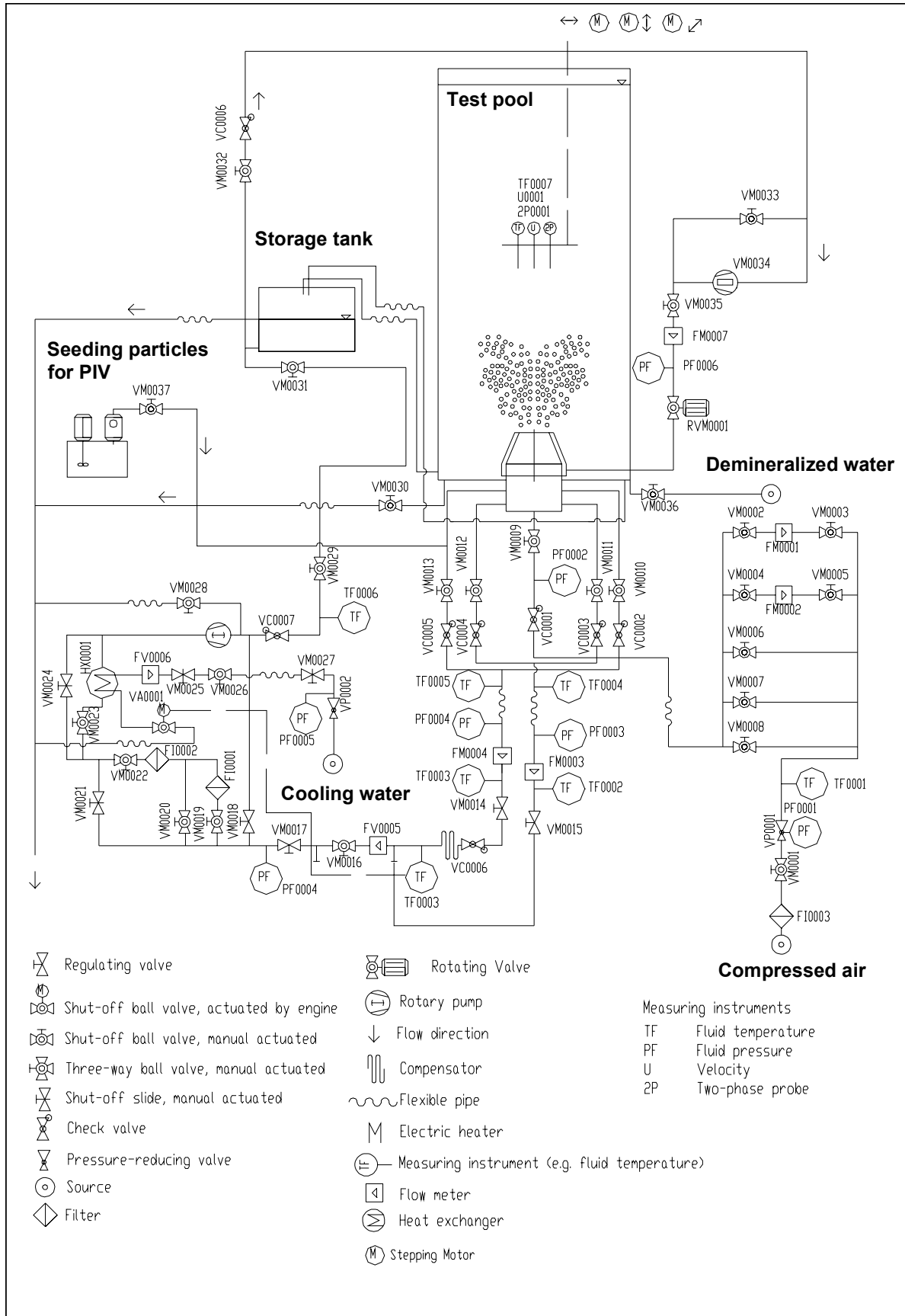


Figure (A.1): Bubbly-jet experimental installation: piping and instrumentation diagram.

A.2 Tank and traversing system

The square Plexiglas tank (Figure A.2) used for the bubbly jet experiment is 2200mm high and 1200mm wide. The injector (Chapter 4) is mounted at the bottom of the tank and connected to the water and air supply pipes. Four downcomers are created in the four corners of the tank with a triangular cross section as shown in Figure (A.2). There are in total 7 flanges for each outlet manifold. The water level in the tank is regulated by closing the flanges of the downcomer below the selected water level. The following water level heights: 600, 800, 1000, 1200, 1400, 1600 and 1800 mm can be obtained. The maximum water level in the tank, which can be achieved when all flanges are closed, is 2100mm .

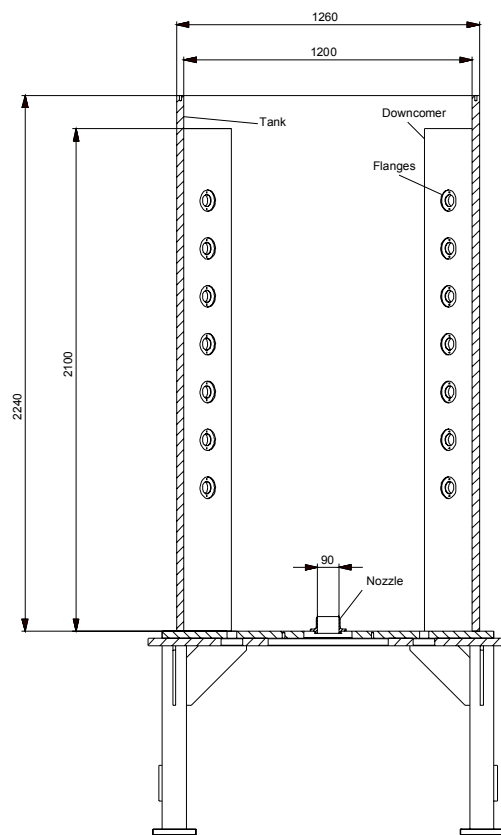


Figure (A.2): *Experimental tank.*

The injector nozzle and the triggering nozzle (Figure A.3) are mounted in the center of the pool bottom and can be easily exchanged or replaced. The height of the nozzle that was most frequently used for the naturally-developed as well as the triggered jet experiments is 70mm . The nozzle diameter is 90mm . In addition, two other nozzles with 40 and 60mm inner diameter have been fabricated in order to achieve higher values of the Trapping parameter and of the Froude number. These nozzles have not been used.

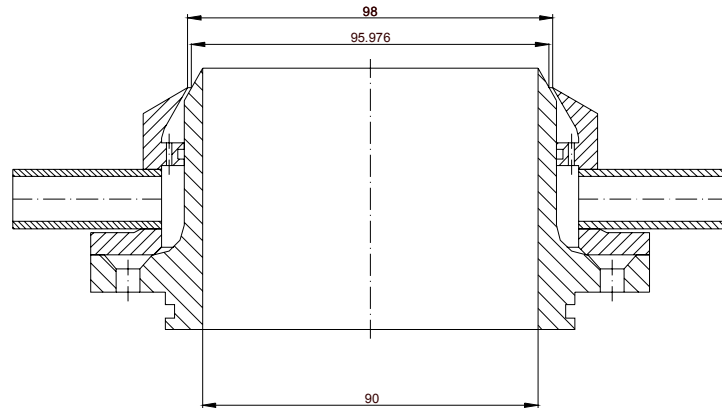


Figure (A.3): *Triggering nozzle.*

A traversing system is used to position local sensors and calibration targets for photographic and PIV measurements. Equipped with three stepper motors, limit switches and supports for sensors and targets, the three-axes traversing system was mounted at the top of the tank. The positioning accuracy achieved with the stepper motors is $\pm 0.1\text{mm}$. The system was designed to cover more than 90% of the entire pool cross-section. The telescopic arm used to carry local sensors was designed for minimal oscillations and maximal flexibility. High mechanical system stability is necessary, especially in the case of high jet velocities. The range of vertical elevations which can be covered with the telescopic arm is from 0mm to 700mm , measured from the nozzle exit.

Before measurements or optical calibrations, it is necessary to define the reference position of the traversing system relative to the nozzle exit.

The complete experimental system, designed to provide flexibility, by easy exchangeability of important components, enables the performance of a wide range of experiments for exploring two-phase flow phenomena.

A.3 System for triggering large vortices

One of the main tasks was to create large orderly structures in bubbly jets with controllable frequency and amplitude in order to provide well-defined conditions for studying the interactions between the dispersed and the continuous phase in bubbly jet flow. Bubble movements, interactions with large eddy structures and feedback effects on the continuous phase can be systematically observed in the case of triggered jets, where generation of large orderly vortices with controllable frequency and phase can be accomplished.

This was achieved by modulation of the shear layer at the jet exit by injecting periodic water surges through the coaxial annular nozzle at the jet exit (shown in Figure (A.3)). The water flow can be modulated by a rotating valve installed in the triggering loop, as shown in Figure (A.1).

A fast response flow meter (PROMAG 50P, Endress+Hauser) is used for measuring the periodically-modulated liquid flow rate. The variation of the liquid flow rate is acquired on a PC configuration composed for process control and presented in Figure (A.5). The data acquisition speed

is approximately an order of magnitude higher than for the other process data. The flow meter settings have to be specially adjusted in order to enable flow rate scanning with adequate speed. The rotating valve (Figure A.4) is driven by a stepping motor. By adjusting the rotation speed of the valve, the frequency of excitation is varied. The excitation amplitude is varied by adjustment of the total liquid flow rate through the rotating valve. The triggering flow does not contain bubbles.

The synchronization of PIV and image acquisition equipment with flow excitation was obtained by an encoder mounted on the stepper motor shaft. The TTL (Transistor to Transistor Logic) pulses from the encoder, produced with a period corresponding to a full rotation of the motor shaft, externally trigger the PIV system. Since the valve opens twice during one full rotation, the excitation frequency is two times the triggering frequency.

In addition, a sophisticated system for manipulation of encoder signals was developed in order to vary the phase shift between excitation signal and triggering signal for data acquisition.

The signal from the encoder attached on the shaft of the motor, which corresponds to one full rotation of the shaft, is used as the signal for triggering another TTL signal.

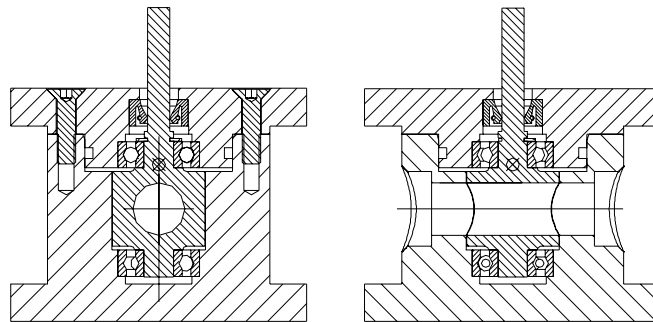


Figure (A.4): Rotating valve.

A.4 Process control and data acquisition systems

The schematic shown in Figure (A.5) describes the hardware and software for process control and data acquisition and processing. Two personal computers, PC1 (Pentium 2, 512kB RAM, Windows 2000) and PC2 (Pentium 4, 512kB RAM, Windows 2000) are used during the experiments for the following tasks:

1. Measuring and monitoring process data: air flow rates, liquid flow rates and liquid and air temperatures;
2. Positioning the sensors for point (local) measurements such as double optical sensor and thermocouple via stepping motors;
3. Positioning the optical target;
4. Driving the rotating valve;
5. Image acquisition, analyzing and processing;
6. Data acquisition, analyzing and processing.

A third personal computer PC3 (Pentium 4, 1GB RAM, Windows XP) is used for the PIV measurements, together with the following equipment: laser, synchronizer, CCD cameras and beam splitter.

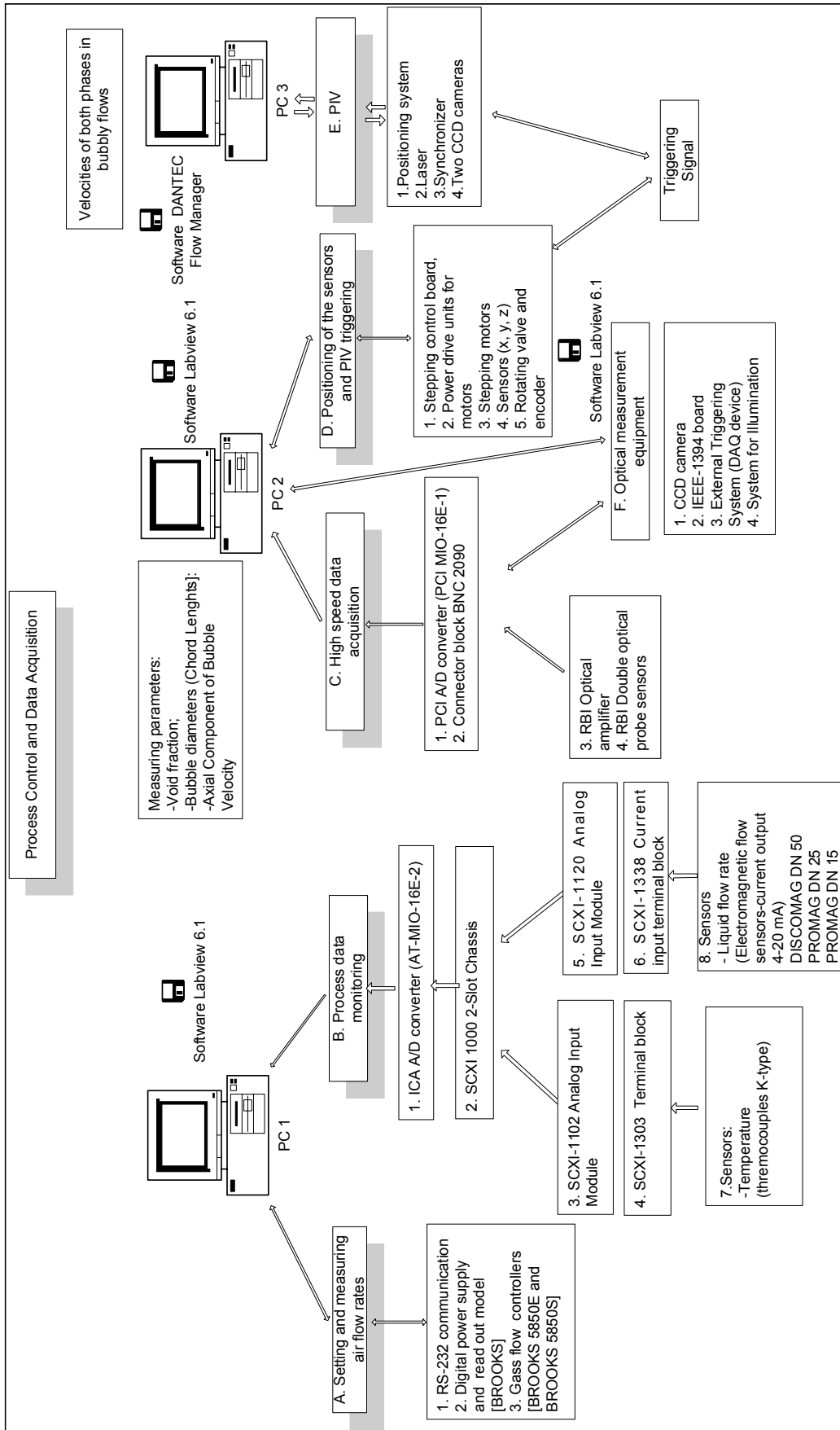


Figure (A.5): Process control and data acquisition schematic.

A.4.1 Process Data Acquisition

Monitoring and acquiring process data, like fluid temperatures and flow rates, require much slower sampling rate than signals from double optical sensors. A low-speed data acquisition system, where different inputs like thermocouple voltages and flow meter voltage or current outputs are transformed into physical values such as temperatures and flow rates, is used. These analog signals are translated into digital signals with a 12-bit AD-converter card (AT-MIO-16-E21, National Instruments). This device can operate at any sampling frequency up to $500kSamples/s$. The analog input range can be selected from ± 0.05 to $\pm 10V$ at 64 single-ended channels. Digital data are monitored and saved directly to the computer hard disk.

The air flow rates are measured and controlled with Brooks flow meters (5850E and 5850S). Flow rate adjustment is done via a Euro Card Module (Brooks Instruments). The output voltage signal is also monitored and transformed into flow rate data by using calibration curves that relate output voltage signal from 0 to $5V$ to flow rate. The measurement procedure allows flow rate readings within an error margin of $\pm 2\%$ of the full-scale reading.

The liquid flow rates (internal and external flow) are measured by electromagnetic flow meters (PROMAG 50P, Endress+Hauser). The output current is induced in a conductive fluid moving in an outer alternating magnetic field. The signals from liquid flow meters are connected to the SCXI-1338 (National Instruments) Sensor Terminal Block. Signals are then amplified in the SCXI-1120 (Thermocouple Input Module, National Instruments). Each of 8 isolation amplifiers can be programmed for input ranges of $\pm 2.5 mV$ to $\pm 5V$. Each channel also includes programmable low-pass filter electronics that can be configured for $4Hz$ or $10kHz$. The current output is measured and transformed to flow rate data by calibration curves that relate the output current signal of 4 to $20mA$ to flow rate. The flow rate readings lie within an error of $\pm 0.5\%$.

The liquid and air temperatures are measured with K-type thermocouples. The thermocouples are connected to the SCXI-1303 Isothermal Sensor Terminal Block (National Instruments). Thermocouple signals are then amplified in the SCXI-1102 Thermocouple Input Module. Each of the 32 instrumentation amplifiers can be programmed for input ranges of $\pm 100mV$ to $\pm 10V$. Each channel also includes a fixed $2Hz$ low-pass filter. This module can read the cold-junction compensation sensor (thermistor) located on each analog input channel. The measured cold-junction sensor voltage is added to the voltage measured by the thermocouples and converted into temperature. Voltage readings and temperatures from all thermocouples were checked with a "FLUKE" calibration device with a reference signal at $23^{\circ}C$. The absolute system accuracy of SCXI-1102 modules with a PCI-MIO-16E-1 (National Instruments) converter measuring a K-type thermocouple at $23^{\circ}C$ is about $\pm 0.6-1^{\circ}C$. Accuracy of the cold junction sensor on the SCXI 1303 (National Instruments) from $15^{\circ}C$ to $30^{\circ}C$ is $0.5^{\circ}C$ and reproducibility is $0.35^{\circ}C$. Taking into account all these considerations, the total temperature measurement error is about $\pm 1^{\circ}C$. The data analysis and processing software package was developed with LabVIEW (National Instruments).

A.4.2 High-speed data acquisition

Acquisition of the analog signals from the DOS is done with a 12-bit AD converter (PCI-MIO-16E-1). A shielded connector block with signal-labeled BNC connectors is used to interface the analog signals from sensor tips. The acquisition device can stream data to the disk at up to $1.25MSamples/s$. Digitalized signal data are stored directly on the hard disk, so that the amount of data stored is limited only by the free hard disk space. For example, scanning the

2 channels, with the sampling rate of $100kSamples/s$ for 10 minutes, produces $240MB$ binary data stored directly on the hard disk. The signal-processing software packages [28], developed with LabVIEW, are used to pre-process raw data and to reduce the size of the files, so that they can be analyzed after the experiments.

A.4.3 Photographic measurements

To get the shapes and dimensions of bubbles and of coherent structures, their positions in the field of view, as well as to perform possible tracking and observations of flow patterns for bubbly flow etc., the optical measurement system was configured to separate image acquisition from image processing and analyzing. The image acquiring and analyzing software package was developed in LabVIEW and Image Vision Library (National Instruments). The snap, sequence and grab image acquisition options were used with a BASLER 301f progressive-scan fire-wire camera, which supports the $640 \times 480 pixels$ format with $8bits/pixel$ and frame rates of 3.75; 7.5; 15; 30 and $60frames/s$. Furthermore, the camera supports a predefined set of image sizes, while operating in the so-called Scalable Image Format 7.

Timing of the files was done with a high-precision timer code (LabVIEW) National Instruments), which uses the processor of a PC to keep track of time. Furthermore, a DAQ device used for high-speed data acquisition, together with two counters implemented in it, was used for measuring the time needed for execution of some LabVIEW program parts, especially loops for performing image acquisitions. The same device was used as external source for triggering the camera and the flash lamp. The generated TTL signal with counters located on the DAQ board allows triggered grab acquisition in the range from 1 up to almost $60Hz$. The maximum possible frame rate of $60frames/s$ is achieved with sequence acquisition. The total number of saved frames depends on the RAM size, i.e. total number of allocated buffers in the memory. For lower frame rates, carefully programmed loops can successfully control transfer of images from buffers in the RAM memory to the computer hard disk.

A.4.4 System for positioning the sensors (DOS, Thermocouple and PIV cameras)

A traversing system was primarily designed for moving local sensors as well as a calibration target, but its electronics were used in addition for controlling the stepper motor connected to the rotating valve. The personal computer PC2 with installed stepper control board (DCX-PCI300, Precision Micro Control Corporation) and three DCX-MC360 stepper motor control modules were used for operating both the traversing system and the rotating valve. Each motor was connected to a power drive unit, which supplies the motors with variable current intensity. The nominal current for driving the motors can be selected depending on the expected load. The operating program, which is written in LabVIEW, controls the motor speed and the number of motor steps i.e. displacement. The stepper motors operate in the quarter-step mode and 200 steps result in one full revolution of the motor shaft.

A.4.5 System for feeding the installation with seeding particles

The system for feeding the flow with seeding particles is schematically presented in Figure (A.1). The 100l barrel with a dosing pump and a mixer is connected to the water loop via a small ball valve. The pulsating frequency can be directly regulated by the dosing pump electronics.

A.5 Experimental investigation of bubble formation

The injector used in the experiments is described in Sections 4.1 to 4.3. In order to produce bubbly jets with uniform but variable bubble sizes, injectors with one and four needles were developed and tested in a small experimental set-up (see Figure (A.6)). Bubbles are formed by continuously injecting air through the needle into the parallel water flow (the internal liquid flow). The effects of geometrical parameters, such as diameter of tube and needle, length of tube and needle together with liquid velocity inside the tube (internal liquid flow), air flow rate and external liquid flow rate, on bubble diameters and shapes were experimentally investigated.

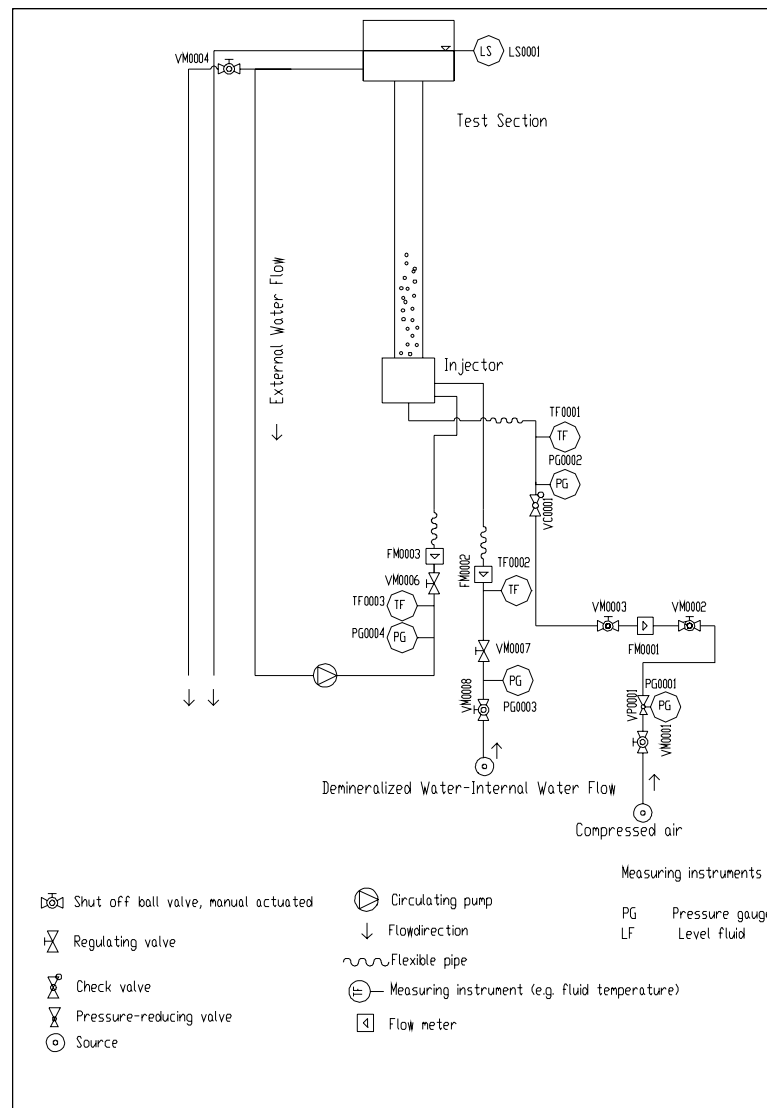


Figure (A.6): Experimental installation for investigating bubble formation.

Air is injected through the bottom of the injector. Air pressure, temperature and flow rate were measured. Fresh demineralized water was used as internal liquid flowing through the tubes of the injector, while the external liquid flow was maintained by a centrifugal pump. The overflow from the collecting tank on the top of the test section was drained. Water temperature as well as external and internal water flow rates were measured during each run. Bubble sizes were measured by taking photographs with a digital camera and an electronic flash light. A ruler

installed in the test section was used for calibration. Furthermore, tubes located in the middle of the test section were used for checking calibration data. Details about injector configuration and tube/needle design are given in Chapter 4.

Experimental investigations were carried out with the following configurations shown in Figure (4.3) in Section 4.1:

- Single tube-needle configurations with external/internal diameters:
 1. Tube size: 4/3mm; Needle size: 0.8/0.6mm
 2. Tube: 3.5/2.5mm; Needle size: 0.8/0.6mm
 3. Tube: 4/3mm; Needle size: 0.5/0.3mm
 4. Tube: 3.5/2.5mm; Needle size: 0.5/0.3mm
 5. Tube: 3/2mm; Needle size: 0.3/0.2mm

- Four in-line tube-needle configurations:
 6. Tube size: 1.5/1.2mm; Needle size: 0.33/0.2mm
 7. Tube: 4/3.4mm; Modified Needle: Part 1 is 0.33/0.2mm and Part 2 is 1/0.6mm
 8. Tube: 4/3.4mm; Needle size: 0.3/0.2mm
 9. Tube: 4/3.4mm; Needle size: 1/0.4mm

After obtaining stable and homogeneous bubble formation from the nozzles, photographs and movies were taken for each flow regime. The most homogeneous bubbles were formed with the single tube-needle configuration No.1 and with the four-in-line tube-needle configuration No. 7. Furthermore, experimental results showed that the dimensions of the needle, especially the inner diameter, play an important role and affect the bubble size.

The needle with 0.6mm inner diameter performed best for producing uniform bubble sizes between 1 and 4mm. Configuration No. 7 was chosen for the final tests.

The pictures shown in Figure (A.7) give snapshots of different flow regimes producing uniform bubbles. The size of bubbles is controlled by adjusting the flow rates of the gas and internal liquid. Very large bubbles are generated by pure air injection in the capillary with no water flow in the tube, while clusters of smaller bubbles are produced by increasing the internal liquid flow (shown in Figure (A.8)).

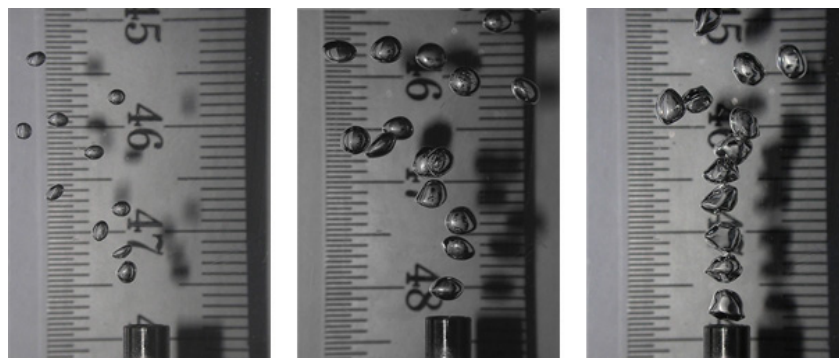


Figure (A.7): Uniform bubble formation from injector tubes.

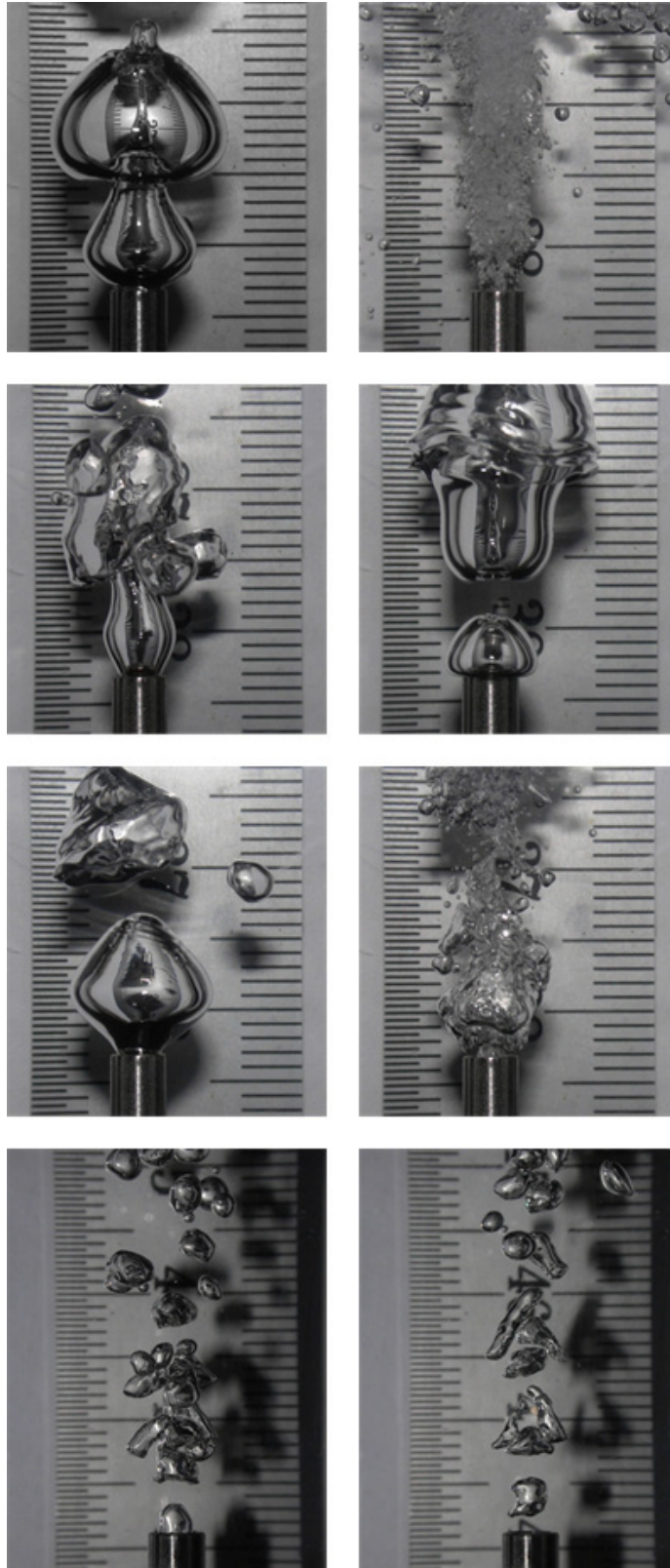


Figure (A.8): *Characteristic regimes of non-uniform bubble formation.*

The injector, which is described in Sections 4.1 to 4.3, is included in the EU/USA patent application [42].

B Experimental procedure

Figure (B.1) shows the flow chart for a test with the basic steps and functions, which are controlled by programs written in LabVIEW.

To measure process data with PC 1, the LabVIEW program *Procdata* was developed. A test starts by setting up the liquid level in the tank, adjusting sensor electronics, moving the sensor to a defined position in the tank, setting up the air flow rates, adjusting the internal and external water flow rate in the injector, monitoring process data and the bubbly-jet development until boundary conditions and a steady state operating mode are reached. In the case of triggered experiments, additional test settings for the excitation frequency and triggering flow rate are selected. The encoder signal is used to trigger the PIV system.

During the experiments, air and liquid flow rates are continuously saved to the hard disk of PC1. High-speed data acquisition with DOS is run with a separate LabVIEW program and the data are saved on PC 2. After pre-processing, the raw DOS data are deleted from the hard disk. The pre-processed data are saved to the hard disk of PC2. Having finished with point measurements, images of bubbles and flow structures are acquired by the digital camera and saved to the hard disk of PC2.

Subsequently, measurements with the PIV system are started and data are transferred and saved to the storage system of computer PC 3.

The measurement procedure is repeated until all data are acquired and saved for each experimental location in the tank and investigated flow regime.

Appendix B Experimental procedure

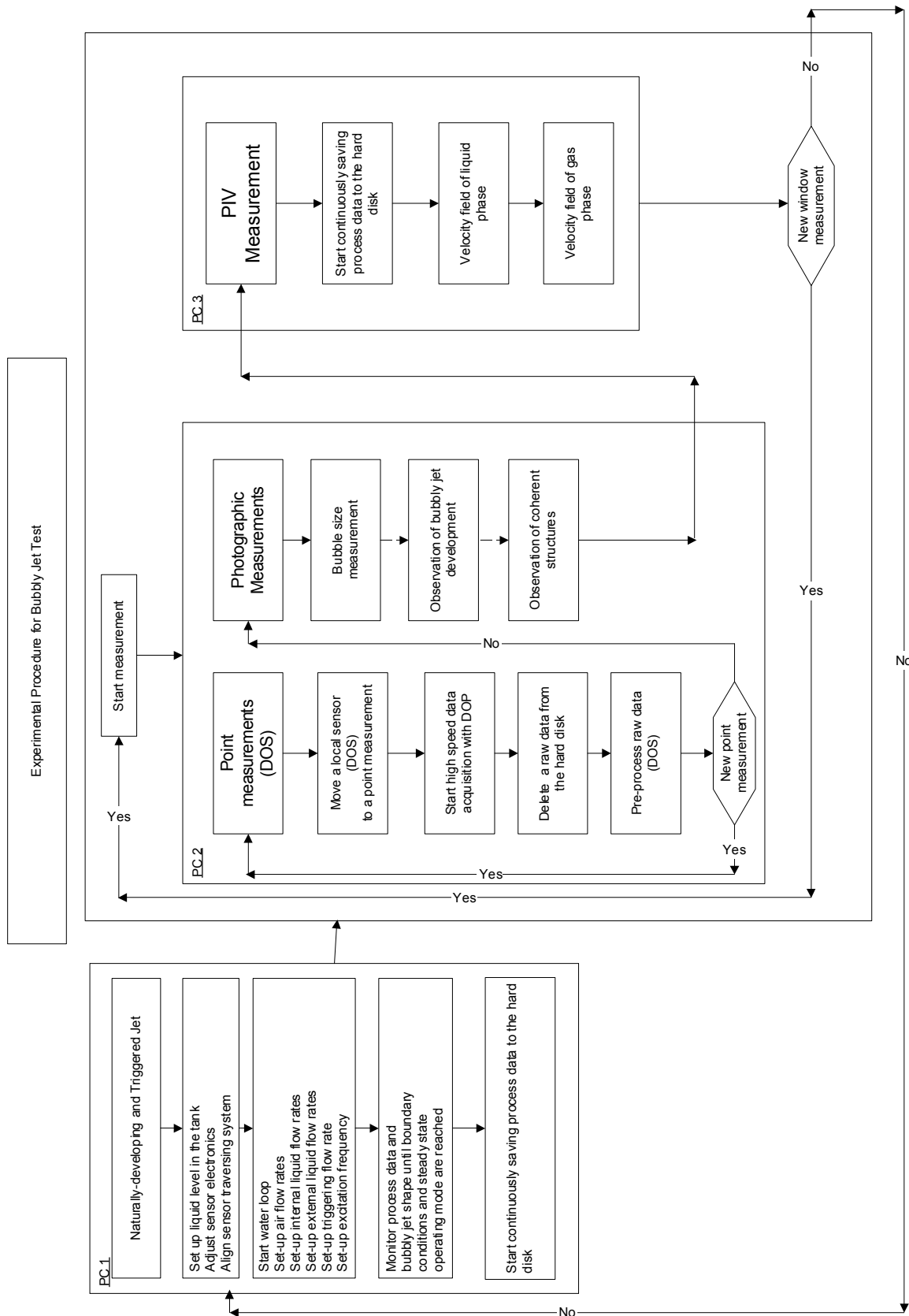


Figure (B.1): Experimental procedure.

C Testing and calibration of the Double Optical Sensors (DOS)

C.1 Testing for accuracy, reproducibility and absence of systematic errors

In order to check reproducibility and accuracy of results as well as absence of systematic errors in DOS measurements, systematic testing according to the test matrices presented below was carried out for different flow conditions i.e. void fractions and bubble sizes. All performed tests can be classified into the following groups:

1. Comparison of the air flow rate obtained by integrating the DOS local measurements ($\dot{V}_{air,DOS}$) with the measurements of the flow meter ($\dot{V}_{air,AFC}$) was performed for each profile obtained (all tests);
2. Testing of reproducibility: three sequences were acquired at a chosen elevation and flow condition in single test.

Furthermore, in an attempt to further extend the range of tested flow regimes to different dispersed-phase concentration ranges, i.e. *dilute* (no feedback), *weakly dilute* (with feedback on the continuous fluid) and *concentrated* (with interactions between bubbles), the test cases presented in Tables (C.1, C.2 and C.3) were also investigated.

C.2 Comparison of volumetric flow rates

The procedure for comparing $\dot{V}_{air,DOS}$ and $\dot{V}_{air,AFC}$ presented here was applied for checking the void fraction measurements with the DOS at the jet exit (shown in Figure C.1), as well as further downstream. Both tips of the DOS sensor were used for the void fraction measurements. Volumetric flow rates determined with DOS were compared with volumetric flow rate measurements performed with the mass flow meter, considering the pressure at the jet exit.

Assuming axisymmetry of velocity and void fraction profiles, the volumetric flow rate ($\dot{V}_{air,DOS}$) was calculated from the local void fraction and the vertical bubble velocity measurements as follows:

$$\dot{V}_{air,DOS} = A \cdot \langle j_{air}^{DOS} \rangle_A = 2\pi \cdot \int_0^{\infty} \varepsilon(r) \cdot V_B(r) \cdot r dr \quad (11.1)$$

The volumetric flow rate injected into the tank ($\dot{V}_{air,AFC}$) has been obtained from the measured air flow rate (\dot{Q}_{air}) considering the pressure at the injector exit:

$$\dot{V}_{air,AFC} = A \cdot \langle j_{air}^{DOS} \rangle_A = \frac{p_N}{T_N} \cdot \frac{T_0}{p_0} \cdot \dot{Q}_{air} \quad (11.2)$$

with

A , injector cross-section area,

T_0, p_0 , temperature and pressure at injector exit.

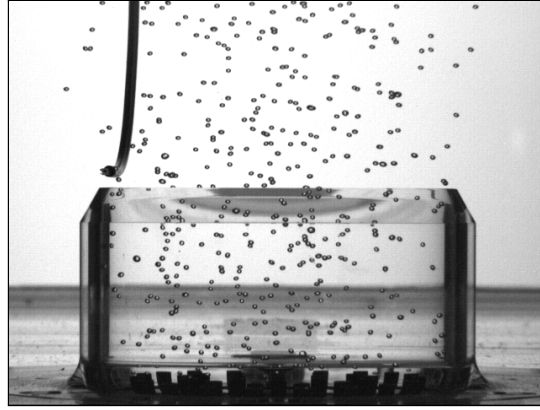


Figure (C.1): Vertically oriented DOS tips at the jet exit.

C.2.1 Test conditions

Tests were conducted for a range of void fractions that can be characterized as dilute, weakly dilute and dense. Tests T1.1-T1.4 can be considered as typical flow conditions with intermediate void fraction in the range 1 – 2% (*weak feedback*) and bubble diameter of about 3mm. The gas flow rate was kept constant as well as the internal liquid flow rate, but the external liquid flow rate, i.e. the non-dimensional parameters, void fraction and bubble velocities were varied. The water level in the tank was 600mm.

Test Number	T1.1	T1.2	T1.3	T1.4
ε_h [%]	5.95	3.12	2.12	1.6
ε_2 [%]	2.05	1.59	1.28	1.08
V_{jet} [m/s]	0.14	0.27	0.4	0.53
\dot{Q}_{Lin} [L/min]	14	14	14	14
\dot{Q}_{Lex} [L/min]	38	88	138	188
\dot{Q}_G [NL/min]	3	3	3	3
\dot{Q}_{Ltot} [L/min]	52	102	152	202
Re_{jet}	13119	25734	38349	50963
Fr_{jet}	0.02	0.08	0.18	0.32
Γ	0.52	1.03	1.53	2.04
St	0.04	0.079	0.118	0.156
V_{Lin} [m/s]	0.09	0.06	0.66	0.66
V_{Gin} [m/s]	4.99	4.99	4.99	4.99

Table (C.1): Experimental matrix for DOS testing (weakly dilute bubbly jets).

Tests T1.5-T1.8 cover the domain of low void fraction ($< 0.1\%$) (*no feedback*) and small bubbles ($\sim 1.2mm$). The nozzle diameter was 90mm, and the water level in the tank 1200mm.

Optical probe measurements were done at $y = 3mm$ from the nozzle exit.

Test Number	T1.5	T1.6	T1.7	T1.8
ε_h [%]	0.32	0.1	0.32	0.1
ε_2 [%]	0.08	0.05	0.08	0.05
V_{jet} [m/s]	0.09	0.28	0.09	0.28
\dot{Q}_{Lin} [L/ min]	10	10	16	16
\dot{Q}_{Lex} [L/ min]	24	98	18	92
\dot{Q}_G [NL/ min]	0.1	0.1	0.1	0.1
\dot{Q}_{Ltot} [L/ min]	34	108	34	108
Re_{jet}	8587	27248	8578	27248
Fr_{jet}	0.01	0.09	0.01	0.09
Γ	0.27	0.87	0.23	0.73
St	0.033	0.105	0.039	0.124
V_{Lin} [m/s]	0.47	0.47	0.75	0.75
V_{Gin} [m/s]	0.17	0.17	0.17	0.17

Table (C.2): Experimental matrix for DOS testing (dilute bubbly jets).

Tests T1.9-T1.12 can be considered as typical of flow conditions with high void fractions $> 3.5\%$ (with strong feedback) and bubble diameter of about $4mm$. The gas flow rate was kept constant, but the external liquid flow rate, i.e. the non dimensional parameters, void fraction and bubble velocities were varied. The water level in the tank was $600mm$.

Test Number	T1.9	T1.10	T1.11	T1.12
ε_h [%]	17.4	9.71	6.73	5.15
ε_2 [%]	5.99	4.92	4.07	3.45
V_{jet} [m/s]	0.14	0.27	0.4	0.53
\dot{Q}_{Lin} [L/ min]	14	14	14	14
\dot{Q}_{Lex} [L/ min]	38	88	138	188
\dot{Q}_G [NL/ min]	10	10	10	10
\dot{Q}_{Ltot} [L/ min]	52	102	152	202
Re_{jet}	13119	25734	38349	50963
Fr_{jet}	0.02	0.08	0.18	0.32
Γ	0.52	1.03	1.53	2.04
St	0.04	0.079	0.118	0.156
V_{Lin} [m/s]	0.09	0.06	0.66	0.66
V_{Gin} [m/s]	16.62	16.62	16.62	16.62

Table (C.3): Experimental matrix for DOS testing (dense bubbly jets).

Tables (C.4) and (C.5) compare $\dot{V}_{air,DOS}$ and $\dot{V}_{air,AFC}$ in case of dilute bubbly jets. All data for the upstream DOS channel lie within an error band of $0/ - 30\%$, but results obtained with the downstream channel in case of low void fraction and small bubble diameter ($1.2mm$) show very strong deviations of up to 62% . Therefore, considering also the size of the sensor tip, bubbles are more effectively detected by the upstream sensor tip, which gives more reliable measurements.

A comparison of $\dot{V}_{air,DOS}$ and $\dot{V}_{air,AFC}$ for the bubbly jet flow regimes presented in the test matrices Table (C.1) and (C.3) for weakly dilute and dense flow regimes, respectively, shows

Appendix C Testing and calibration of the Double Optical Sensors (DOS)

Test	$\dot{V}_{air,DOS}[Ndm^3/min]$	$\dot{V}_{air,AFC}[Ndm^3/min]$	$\dot{V}_{air,DOS} - \dot{V}_{air,AFC}/\dot{V}_{air,AFC}[\%]$
Test 1.1	0.082	0.096	-15.2
Test 1.2	0.095	0.096	-1.3
Test 1.3	0.068	0.096	-29.6
Test 1.4	0.084	0.096	-12.5

Table (C.4): Optical sensor testing results for upstream tip (dilute bubbly jets).

Test	$\dot{V}_{air,DOS}[Ndm^3/min]$	$\dot{V}_{air,AFC}[Ndm^3/min]$	$\dot{V}_{air,DOS} - \dot{V}_{air,AFC}/\dot{V}_{air,AFC}[\%]$
Test 1.1	0.057	0.096	-40.5
Test 1.2	0.089	0.096	-7.0
Test 1.3	0.036	0.096	-62.5
Test 1.4	-	0.096	-

Table (C.5): Optical sensor testing results for downstream tip (dilute bubbly jets).

good agreement at different vertical levels in the tank. The maximum error is +18%. Results obtained from the upstream probe are presented in Table (C.6) for the weakly dilute bubbly jets, and Table (C.7) for the dense bubbly jets.

Test	$\dot{V}_{air,DOS}[Ndm^3/min]$	$\dot{V}_{air,AFC}[Ndm^3/min]$	$\dot{V}_{air,DOS} - \dot{V}_{air,AFC}/\dot{V}_{air,AFC}[\%]$
Test 1.1, $y = 3mm$	3.1	3.0	1.4
Test 1.1, $y = 25mm$	3.1	3.0	0.6
Test 1.1, $y = 50mm$	3.3	3.0	8.3
Test 1.1, $y = 100mm$	3.3	3.0	7.4
Test 1.1, $y = 300mm$	3.2	3.0	6.5
Test 1.2, $y = 3mm$	3.6	3.0	17.3
Test 1.2, $y = 25mm$	3.1	3.0	1.5
Test 1.2, $y = 50mm$	3.5	3.0	16.2
Test 1.2, $y = 100mm$	3.2	3.0	6.1
Test 1.2, $y = 300mm$	3.1	3.0	0.9
Test 1.3, $y = 3mm$	3.5	3.0	15.6
Test 1.3, $y = 25mm$	2.9	3.0	-5.1
Test 1.3, $y = 50mm$	3.3	3.0	7.1
Test 1.3, $y = 100mm$	3.3	3.0	9.9
Test 1.3, $y = 300mm$	3.3	3.0	8.5
Test 1.4, $y = 3mm$	3.1	3.0	1.9
Test 1.4, $y = 25mm$	2.7	3.0	-10.1
Test 1.4, $y = 50mm$	2.9	3.0	-3.9
Test 1.4, $y = 100mm$	3.2	3.0	5.3
Test 1.4, $y = 300mm$	3.2	3.0	4.8

Table (C.6): Optical sensor testing results for upstream tip (weakly dilute bubbly jets).

These tests were performed for the bubble size range from 1mm up to 4mm and void fractions from 0.1% up to 5%. In general, they have shown fairly good agreement between $\dot{V}_{air,DOS}$ and $\dot{V}_{air,AFC}$ with a maximum error of $\pm 20\%$, which belongs to the state-of-the-art for bubbly-flow experiments. Similar comparisons of results found in the literature are reported by Kubasch [28] and Cartellier [2]. Kubasch obtained mean errors within an error band $\pm 25\%$ and Cartellier from $\pm 2\%$ up to -30% and $+40\%$.

Test	$\dot{V}_{air,DOS}[Ndm^3/min]$	$\dot{V}_{air,AFC}[Ndm^3/min]$	$\dot{V}_{air,DOS}-\dot{V}_{air,AFC}/\dot{V}_{air,AFC}[\%]$
Test 1.9, $y = 3mm$	8.8	9.0	-2.4
Test 1.9, $y = 25mm$	8.7	9.0	-3.0
Test 1.9, $y = 50mm$	8.6	9.0	-4.5
Test 1.9, $y = 100mm$	8.5	9.0	-5.0
Test 1.9, $y = 300mm$	9.4	9.0	4.8
Test 1.10, $y = 3mm$	9.9	9.0	9.6
Test 1.10, $y = 25mm$	9.8	9.0	9.4
Test 1.10, $y = 50mm$	9.7	9.0	8.2
Test 1.10, $y = 100mm$	9.6	9.0	7.1
Test 1.10, $y = 300mm$	9.9	9.0	10.2
Test 1.11, $y = 3mm$	8.8	9.0	-2.7
Test 1.11, $y = 25mm$	9.0	9.0	-0.2
Test 1.11, $y = 50mm$	10.1	9.0	12.3
Test 1.11, $y = 100mm$	9.4	9.0	4.2
Test 1.11, $y = 300mm$	8.7	9.0	-2.9
Test 1.12, $y = 3mm$	8.4	9.0	-6.1
Test 1.12, $y = 25mm$	8.6	9.0	-4.7
Test 1.12, $y = 50mm$	9.5	9.0	5.9
Test 1.12, $z = 100mm$	8.6	9.0	-4.5
Test 1.12, $z = 300mm$	9.5	9.0	5.8

Table (C.7): Optical sensor testing results for upstream tip (dense bubbly jets).

C.3 Adjustment of DOS parameters

C.3.1 The offset value (λ)

The parameter used for adjusting the threshold of the DOS signal in order to discriminate air signals and water signals is called the offset value (λ). Optimum threshold settings obtained from various experiments with optical sensors are presented by Cartellier [2]. Since these settings are highly scattered (the offset value $\lambda = 0.1 - 0.5$), it is recommended to calibrate and check each sensor. Kubasch [28] analyzed the void fraction at the centerline of a bubbly plume with different offset values. As reference value he assumed $\lambda = 0.05$ (5% of span). He showed that the mean bubble residence time depends little on the threshold value.

Test T1.1 with a water level in the tank of $1200mm$ was used for investigating the effect of varying the offset value (λ). This test is actually chosen because of two void peaks at $r \equiv x = \pm 20mm$ shown in Figure (C.2). The offset setting (λ) influences the void fraction measurement, because it slightly changes the bubble arrival and detachment times. These changes depend on many factors such as: sampling rate, sensor sensitivity, electronic adjustments etc. In principle, the higher threshold value delays the measured bubble arrival time, which means that bubble residence time and resulting void fraction decrease. The sampling rate also plays a role, since it is desirable to obtain good resolution of the rising and falling edge. Furthermore, it must be stressed that a higher offset value reduces the error due to detected "spurious bubbles", which originates from electronic noise in the sensor signal. In principle, there are two sources of false signals: pre-signals arriving in front of a bubble signal and electronic noise in the rising or falling edge. Electronic noise, especially in the falling edge, was evidently observed. It very strongly affects the number of detected bubbles, but not that much the void fraction, since the "virtual" residence times are much smaller than the real ones. All these errors are actually corrected by the *modified threshold method* [28]. This method is introduced in order to reduce the number of cases where sensor signals are misinterpreted due to pre-signals and electronic

noise. It compares the time interval between the detachment of a first bubble and the arrival of a following bubble with the correction time [28]. If the time interval is less than the correction time, the two bubbles are considered to be merged. This method still does not solve the problem when several peaks due to electronic noise occur, for example, in the falling edge. It can be that the real and the first next "virtual" bubble are merged, but the same rule is applied for the next two spurious bubbles, they would be registered as another, obviously spurious bubble.

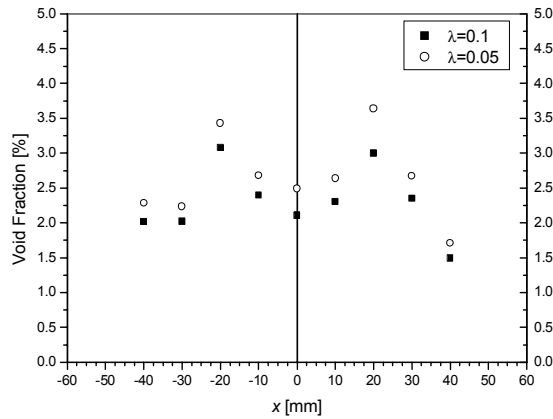


Figure (C.2): Comparison between void measurements obtained with different offset values.

Analysis of data from the sensor calibration and checking tests is performed with two values of (λ) i.e. 0.05 and 0.1. Their influence on the data obtained from the upstream sensor tip is shown on Figure (C.2). The higher offset value results in a relative void fraction decrement of 14%. Obtained profiles are integrated (as it is explained above) and compared with injected gas flow rates. The result obtained with $\lambda = 0.1$ for the upstream tip shows an error of 3% and with the downstream tip 25%, while in case of $\lambda = 0.05$ the error band obtained for the upstream tip is $\pm 18\%$ and $\pm 14\%$ for the downstream tip. Anyhow, the two void peaks exist in both cases. Finally, in order to reduce the error due to detected "spurious bubbles" the offset value of $\lambda = 0.1$ was chosen.

C.3.2 The correction time

As mentioned above the correction time represents the minimum time for distinguishing detachment of a bubble and arrival of a following bubble at the sensor tip. For our tests the correction time was set to $0.2ms$. Since the correction time is much smaller than the bubble residence time, it does not seriously affect the void fraction measurement, but the total number of counts will certainly be reduced.

C.3.3 The bubble velocity

Measured bubble times of flight are taken into account in the calculation of the time-averaged vertical bubble velocity if the following conditions are fulfilled:

- the bubble velocity lies within a prescribed range:

$$V_{B\min} < V_B < V_{B,\max}, \text{ i.e. } \frac{\Delta y_{tips}}{V_{B,\max}} < \Delta t_{fl} < \frac{\Delta y_{tips}}{V_{B,\min}}$$

- the relative difference between the bubble residence times at the two DOS tips must be below a certain limit:

$$|\Delta t_{res}| = \left| \frac{t_{res,us} - t_{res,ds}}{t_{res,us}} \right| < |\Delta t_{res}|_{lim}$$

For the experiments presented, bubbles within the velocity range $0.1m/s$ to $2m/s$ were considered for the vertical bubble velocity calculations. $|\Delta t_{res}|_{lim}$ was set to 0.2. The setting of $|\Delta t_{res}|$ virtually does not affect the vertical bubble velocity measurement. In these experiments, about 65% of the bubble signals are considered for the vertical bubble velocity measurement. It is important to emphasize that the selected value of $\Delta t_{min} = \frac{\Delta y_{tips}}{V_{B,max}}$ can affect the calculated average bubble velocity, but has no influence on the void measurement.

These filtering conditions must be chosen very carefully in order to avoid systematic errors. The comparison between the results obtained by integration method and the local void and vertical bubble velocity measurements can obviously reveal the presence of systematic errors. In order to check and estimate the range of the vertical bubble velocity and especially the upper limit, a statistical analysis was carried out for flow regime *TF3V1* (details about flow regime are shown in Chapter 6), with the highest water jet superficial velocity at $y = 200; 350mm$ and $x = 0mm$. The results are presented on Figure (C.3). The distribution of the vertical bubble velocity is Gaussian. Since the bubble velocity at two different vertical locations in the jet center falls into the range $0.4 - 1.8m/s$, the filtering conditions mentioned above are properly chosen.

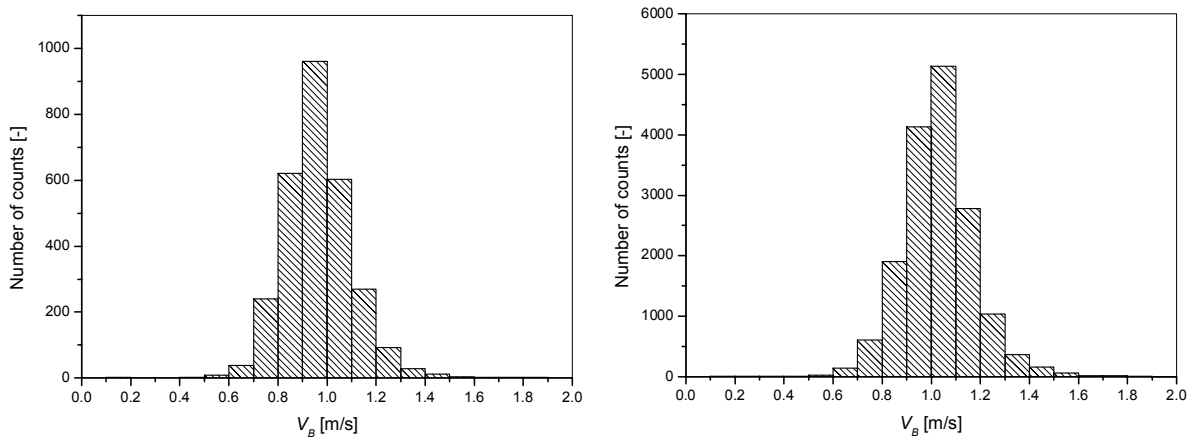


Figure (C.3): Bubble vertical velocity for test *TF3V1*, point at $y = 200mm$ and $x = 0mm$ (left) and point $y = 350mm$ and $x = 0mm$ (right).

C.3.4 Testing of reproducibility

Testing of the reproducibility of the experimental results was done for flow regime T1.1. The offset parameter was $\lambda = 0.1$. Three data sequences were acquired with intervals of a few days and analyzed. Flow conditions were changed and re-adjusted in between. The experimental results presented on Figure (C.4) show very good agreement for both sensor tips.

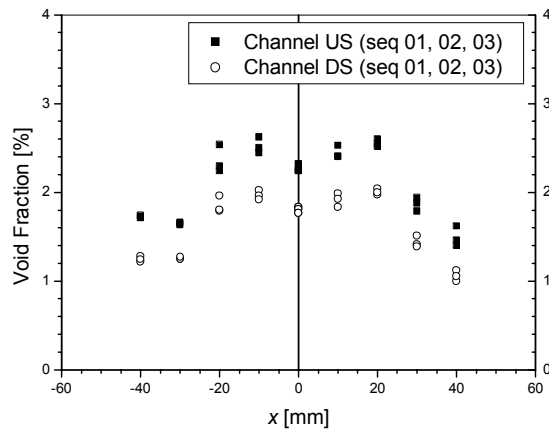


Figure (C.4): Testing of DOS measurements reproducibility.

C.3.5 Selection of measuring time

The required measurement time depends on the bubble density and the bubble velocity, because the total number of counted bubbles determines the statistical accuracy.

Figure (C.5) shows the dependence of the resulting void fraction and vertical bubble velocity on measuring time for a point located in the jet center. The statistical analysis was done for flow regime *TF3VI* (see Chapter 6 for details about flow regime) at $y = 350\text{m}$ and $x = 0\text{mm}$. The total measuring interval of 1800s was divided into smaller intervals of 1s such that, for every measurement time, averages of all preceding intervals could be formed. The development of mean values shows that measurement times can be much smaller than 1800s . Taking into account the sampling rate and the amount of memory needed to store the data, the total measuring time for centerline points was usually 300s . For points located at the jet boundaries the total measurement time in case of naturally-developing jets was 600s . In case of periodically triggered jets, where phase-averaged void fractions and velocities were determined, the total measurement time for points in the shear layer was about 3600s .

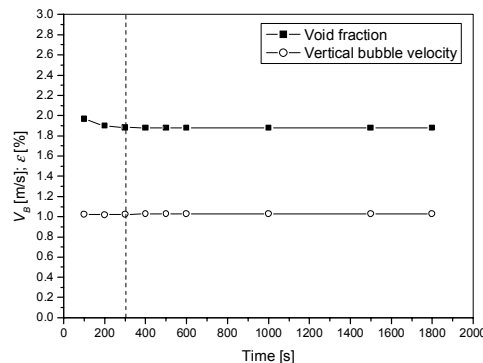


Figure (C.5): Dependency of the void fraction (a) and of the vertical bubble velocity (b) on measuring time.

D Particle Image Velocimetry (PIV)- Settings and error estimates

The basic principles of the standard PIV measurement technique and some details about PIV configurations are briefly explained in Chapter 3. The emphasis will be laid here on details of the configuration used to perform simultaneous PIV and Shadowgraphy measurements, especially for triggered jets. Also, the effects of important parameters, such as the time between two laser shots, which should be carefully chosen and optimized during PIV measurements, will be discussed in Section D 3.1. Finally, the effects of using filtering functions, called here window functions, on velocity measurements will be illustrated in Section D 3.2.

D.1 General adjustment of PIV system

A New-Wave-Research-Minilaser double-cavity Nd:YAG laser with an output of $150mJ$ per pulse and a pulse duration of $10ns$ was used as light source. The wavelength of the emitted laser light is $532nm$. The thickness of the laser light sheet was estimated from the trace on photo paper obtained after performing the adjustment procedure with different combinations of cylindrical and spherical lenses. It was in the range of 1.5 to $2mm$.

Images were captured by an $8bit$ cross-correlation CCD camera (Kodak MegaPlus ES 1.0) with a resolution of $1k \times 1k$ pixels. The fields of view (FV) of both cameras were carefully adjusted that the position of the axis of the $90mm$ nozzle (i.e. the jet axis) was in the middle of both FVs. Two different dimensions of the FV were used, $138 \times 138mm$ and $220 \times 220mm$. Therefore the corresponding resolution was 140 and $220\mu m$ per pixel, respectively. A calibration procedure was performed before and after conducting PIV experiments. The interrogation area used usually was 64×64 pixels with 50% overlap. If the minimum particle displacement which can be measured by cross-correlation [9] is about 0.1 pixel, the dynamic range of the velocity measurement corresponding to a maximum particle displacement of 25% of the IA size is equal to 160.

A special beam splitter was used for observing the same FV with both two CCD cameras. Because of geometric aberration of the camera lenses and mirrors used in the beam splitter, it is not possible to achieve 100% match between the two FVs. The distortion causes points that are away from the lens' optical center to appear further away from the center than they really are. Small shifts are acceptable.

The standard cross-correlation procedure [9], followed by the application of a peak validation criterion and a simple velocity range filtering, was used for obtaining velocity data. The ratio between the signal peak relative to the noise peak of $1.2 - 1.3$ was applied as the peak validation procedure, whereas the following criteria for filtering of the velocities were used in the inertial region of the jet:

$$-0.4 \cdot V_{\max} \leq U \leq 0.4 \cdot V_{\max}$$

$$-0.35 \cdot V_{\max} \leq V \leq 1.75 \cdot V_{\max}$$

where the maximum mean velocity of the liquid was estimated as

$$V_{\max,L} = V_{jet} + 0.1[m/s] \cdot \varepsilon[\%]$$

and of the bubbles as

$$V_{\max,B} = V_{jet} + 0.1[m/s] \cdot \varepsilon[\%] + 0.25[m/s]$$

The coefficient $0.1m/s$ was found experimentally. The value of $0.25m/s$ corresponds to the terminal bubble rise velocity of $3mm$ bubbles.

More details on the selection of the time interval between two laser pulses as well as on window filtering functions are presented in Appendix D.3.1 and D.3.2.

A statistical analysis of PIV results requires an ensemble consisting of a large number of vector maps. Depending on the flow conditions, on the basic PIV settings and, especially, on the quality of feeding the flow with seeding particles, the number of rejected vectors per single vector map may vary during the measuring time. For the experiments with naturally-developing jets, performed at the constant acquisition frequency of $15Hz$, 1024 image maps were acquired. The theoretical statistical errors for the mean value, standard deviation and for the variance can be estimated by the following equations, respectively [64]:

$$\frac{\varepsilon(V_{mean})}{V_{mean}} = \frac{StdevV/V_{mean}}{\sqrt{N}}$$

$$\frac{\varepsilon(StdevV)}{StdevV} = \frac{1}{2} \cdot \frac{\varepsilon(VarV)}{VarV}$$

$$\frac{\varepsilon(VarV)}{VarV} = \sqrt{\frac{2}{N}}$$

Assuming that 50% of the total vectors are accepted for a point in the shear layer (i.e. $N = 512$), the theoretical statistical error of the mean velocity is less than 2% for a standard deviation of 30% and about equal to the resolution error of the PIV measurement. The theoretical statistical error of the variance is less than 10%.

An example of time-dependent data for a point in the shear layer at $X = 25.6mm$ ($x = -43.4mm$) and $y = 59.8mm$ (Figure D.1) illustrates raw data obtained after applying cross-correlation and the peak validation procedure. The outliers obviously have nonrealistic velocity values and are eliminated by the range validation procedure. After applying range validation, 966 of 1000 vectors are used for calculating the mean value. These results are obtained for flow case *TF2VI* (more details are presented Chapter 6).

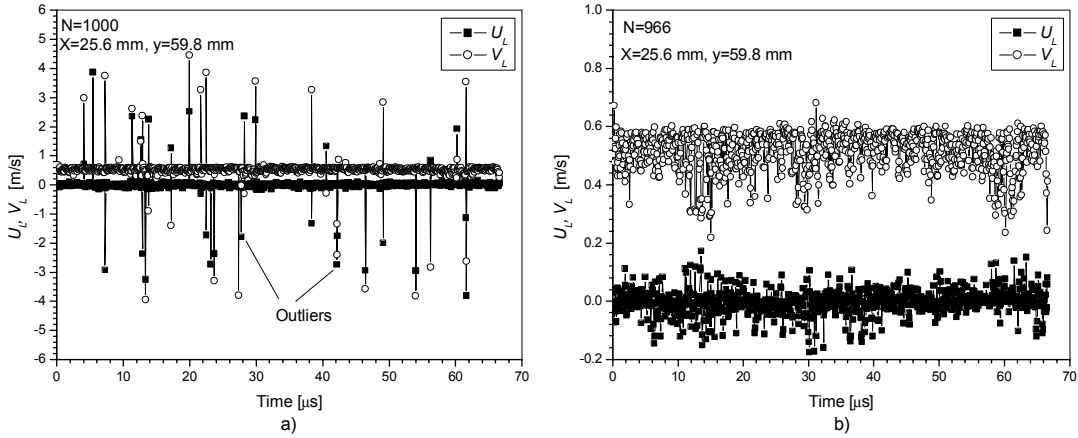


Figure (D.1): Time dependent data for a point in the shear layer.

The azimuthal vorticity fields ($\omega_{z_{i,j}}$) were obtained from the velocity fields by applying the following differential operators:

$$\omega_{z_{i,j}} = \left(\frac{dV}{dx} \right)_{i,j} - \left(\frac{dU}{dy} \right)_{i,j}$$

$$\left(\frac{dV}{dx} \right)_{i,j} \approx \frac{V_{i+1,j} - V_{i-1,j}}{2 \cdot \Delta X}$$

$$\left(\frac{dU}{dy} \right)_i \approx \frac{U_{i,j+1} - U_{i,j-1}}{2 \cdot \Delta Y}$$

The velocity vectors were sampled on a two-dimensional evenly-spaced grid (ΔX , ΔY), which is defined by the size of the interrogation areas and by using 50% overlap. Since the velocity data are disturbed by noise, i.e. they contain a certain measurement uncertainty, the vorticity fields also have a corresponding measurement uncertainty [48]. The error of the vorticity is of the same order of magnitude as that of the velocity.

D.1.1 Acquisition scheme

In order to obtain velocity and vorticity fields at various phases within the triggering periods, i.e. at different positions of the vortices, a data acquisition scheme (Figure (D.2)) has been chosen that is synchronized with the excitation. The data acquired in the described way yield information on deformations, size modifications and velocity of the vortex ring. PIV acquisition is started by a periodic external signal from the encoder, which covers two excitation periods since the rotating valve opens twice during a full revolution. The PIV records are acquired with higher frequency. Thus N_{ep} shots per excitation period are captured, allowing phase-averaging at N_{ep} different times within the excitation period to be performed.

The signal from the encoder, emitted at every rotation of the stepping motor, is used as the triggering signal to start PIV image acquisition (Figure (D.2a)). The excitation frequency being two times higher than the rotating frequency (Figure (D.2b)). The N_{ep} PIV recordings (double frames) within the excitation period are acquired at constant, but higher frequency (schematic shown in Figure (D.2c)). Since the production of large vortices and PIV acquisition are synchronized, it is possible to track coherent structures in the flow field and to obtain phase-averaged

velocity fields. The following settings were applied:

- for the excitation frequency of $1Hz$, 12 recordings during the excitation period were acquired with the frequency of $12Hz$ (time between recordings was $83.3ms$),
- for the excitation frequency of $2Hz$, 6 recordings during the excitation period were acquired with the frequency of $12Hz$ (time between recordings was $83.3ms$),
- for the excitation frequency of $3Hz$, 5 recordings during the excitation period were acquired with the frequency of $15Hz$ (time between recordings was $66.7ms$).

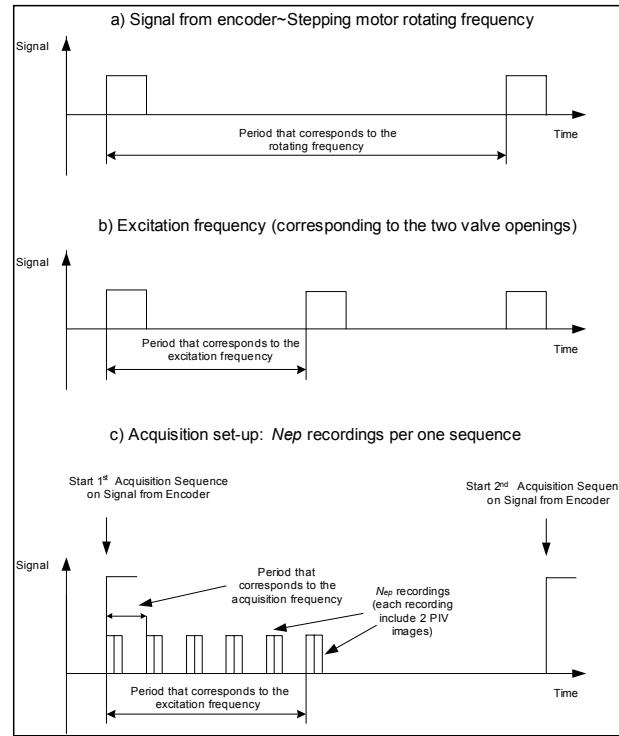


Figure (D.2): Acquisition scheme.

List of PIV settings

The objectives of the various set-ups used were:

Set-up 1 (Interrogation area 64×64 ; scanning frequency $15Hz$; total number of images was $N_{ai}=1024$)

- to obtain the mean azimuthal vorticity field and to observe mean-velocity profiles in the shear-layer.

Set-up 2 (Interrogation area 64×64 ; PIV acquisition triggered by the encoder signal; total number of images per phase used for phase-averaging was $N_{ai}=512$)

- to obtain the phase-averaged azimuthal vorticity field and velocity profiles,
- to determine the size and position of the vortices for the observed phases.

Set-up 3 (Interrogation area 64×64 ; PIV vortex tracking by triggered acquisition; total number of images per phase used for phase-averaging was $N_{ai}=256$)

- to obtain data for different phases i.e. positions of the vortices in the flow field in order to see deformations, size modifications and velocity of the vortex pair.

Set-up 4 (Interrogation area 64×64 ; Simultaneous PIV and image acquisition (shadowgraphy) triggered by the encoder signal; total number of images per phase used for phase-averaging was $N_{ai}=512$)

- to obtain "simultaneous" pictures with trapped bubbles in vortex rings, the position and the velocity of the bubble ring and phase-averaged bubble velocity fields. The second frames of double images taken with the PIV camera for resolving the liquid velocity field were illuminated by the flashing backlight. Since the backlight illumination introduces a certain noise to the PIV images, they should be pre-processed before applying the standard PIV cross-correlation algorithm. An in-depth analysis of the PIV images illuminated with the backlight illumination is presented in Section D.2.

Set-up 5 (Interrogation area 64×64 ; separate PIV and image acquisition (shadowgraphy) triggered by the encoder signal; The acquisition is separated into two parts. The first part contains only images illuminated by the laser light, whereas the second part contains the images illuminated by laser and back-light, total number of images per phase used for phase-averaging was $N_{ai,part1}=512$ and $N_{ai,part2}=256$)

- in order to avoid adding noise to the PIV images, the acquisition was split into two parts. Images acquired without backlight illumination ($N_{ai,part1}$) were used to estimate velocity fields, whereas images with backlight illumination ($N_{ai,part2}$) provided information on positions of bubble rings. Since the flow conditions were not changed, the data obtained in this way could be compared.

D.2 Analysis of PIV images illuminated by backlight

This section contains a comparison of the PIV results for a chosen phase (see Figures (D.3)-(D.4)), which were acquired with and without backlight. Flow condition is *TT F2V1.B-f3-Phase10* (see Chapter 8). In order to check the applicability of the method described as *Simultaneous PIV and Shadowgraphy*, results obtained after pre-processing of the PIV images that are illuminated by the backlight are compared with results obtained by applying the usual processing algorithm of standard PIV images. In addition, the standard cross-correlation algorithm is also applied without any pre-processing of the images.

Pre-processing of the captured PIV images illuminated by the backlight means thresholding based on the histogram of pixel values. All pixels outside the range between a lower (115) and an upper value (255) are set to 0, while the values inside the specified range are kept. After thresholding, the cross-correlation algorithm is applied.

Phase-averaged profiles across the vortex of the vertical liquid velocity and the standard deviation of its fluctuations are presented in Figure (D.3).

Phase-averaged profiles across the vortex and scalar maps of the azimuthal vorticity of the liquid in the shear layer are presented in Figures (D.4).

Position, size and maximum vorticity do not differ significantly between the cases. If the standard PIV algorithm is applied to pictures that are illuminated with uniform backlight but not pre-processed (thresholded) only the standard deviation of the velocity is affected.

Appendix D Particle Image Velocimetry (PIV)-Settings and error estimates

The results show that the described acquisition method can be successfully applied to study interactions between bubbles and large eddy structures. It is a very useful technique to simultaneously observe bubble and vortex rings during experiments. Special attention must be paid to a careful adjustment of the backlight intensity, which must be strong enough for the observation of bubble rings, without, however, producing such a high background noise that would affect PIV cross-correlation evaluations.

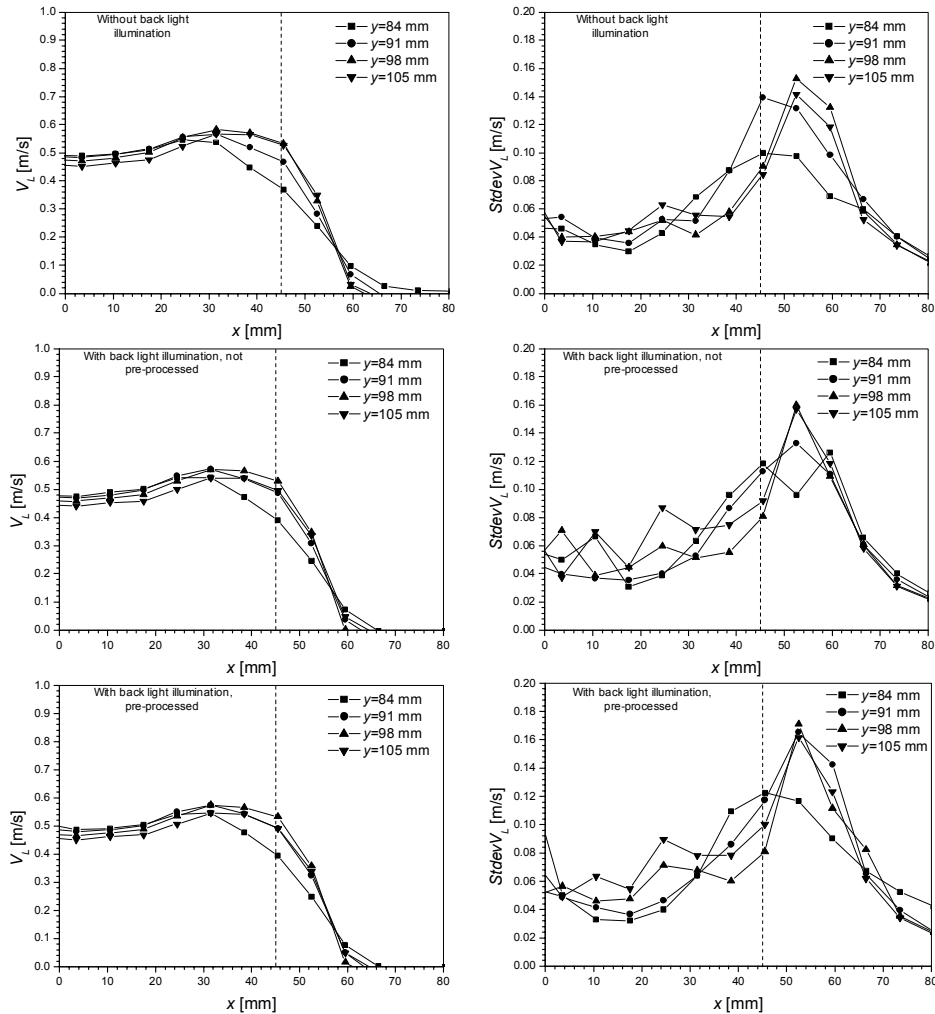


Figure (D.3): Horizontal profiles of phase-averaged vertical velocity (left) and standard deviation of vertical velocity (right) obtained with PIV images that are/are not illuminated by backlight (see explanation in diagrams).

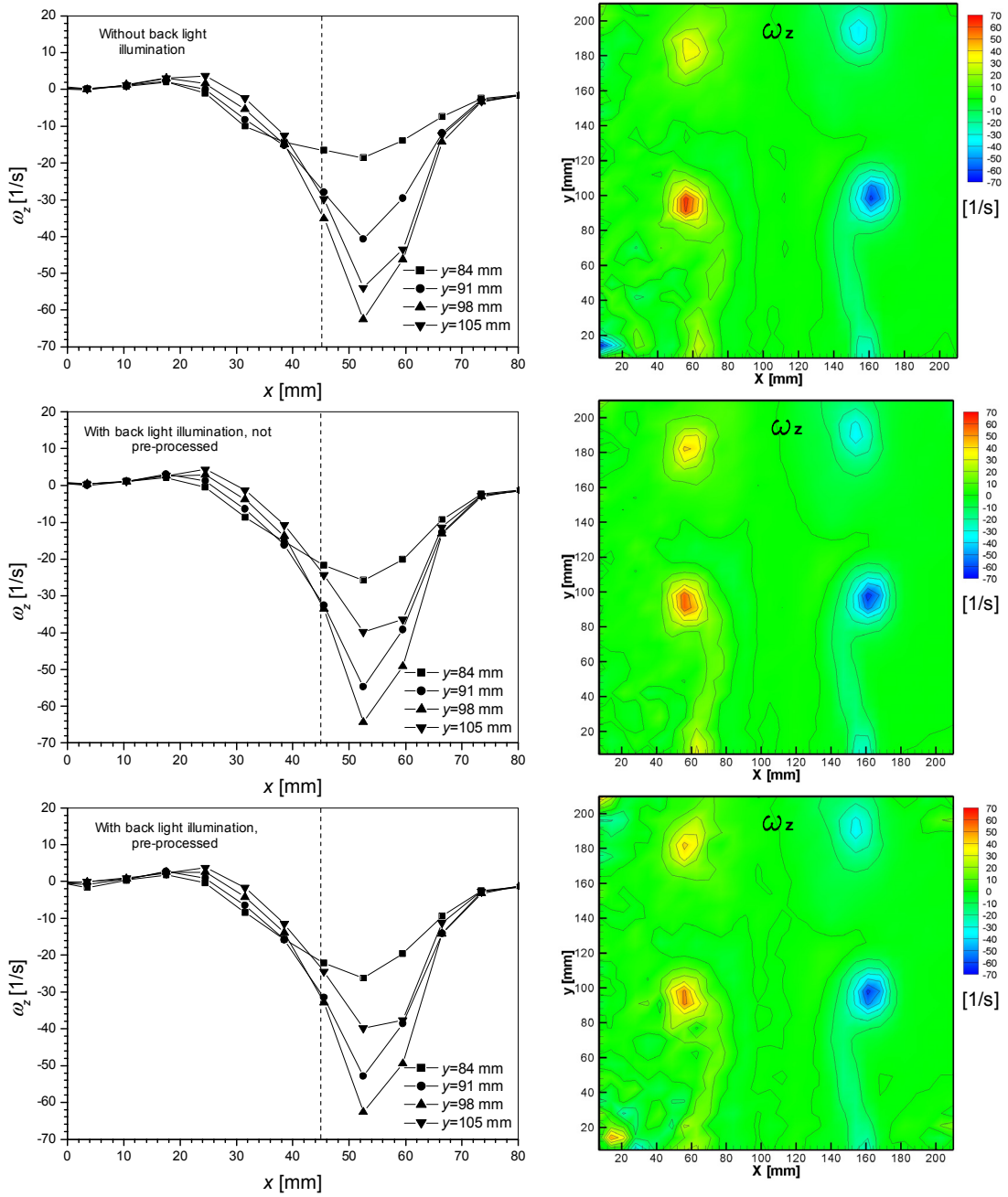


Figure (D.4): Profiles (left) and scalar maps (right) of phase-averaged azimuthal vorticity of liquid obtained with PIV images that are/are not illuminated by backlight (see explanation in diagrams).

D.3 Effects of PIV parameters on time-dependent velocity profiles and *rms* values

D.3.1 Time between laser pulses

The very first and most important parameter that must be optimized during PIV measurements is the time interval between the two successive laser light pulses. As it is nicely illustrated by Raffel in [48], the measured image displacement contains a certain resolution error, which increases rapidly with decreasing pulse separation time. On the other side, increasing the separation time between laser pulses leads to loss of pairs due to too-large particle displacement. This practically means that an optimum separation time should be determined. In many cases, prior knowledge of mean and turbulent flow quantities, as well as the void fraction in the case of bubbly flow, can be used to improve the result of the evaluation.

In order to investigate the effect of important PIV parameters, such as the time between laser pulses, on the experimental error, the following tests were conducted for a single-phase jet (index *L* is dropped, but index *mean* used) with $V_{jet} = 0.18m/s$, and without internal flow inside the injector tubes. The time between the two laser pulses was systematically varied between $10\mu s$ and $10ms$.

For the selected field of view the optical resolution of $1pixel$ corresponded to $140\mu m$, and the size of the chosen interrogation area was 32×32 pixels. The recommended maximum particle displacement is about 25% of the size of the interrogation area, which in our case means $8pixels$. Since, the cross-correlations are calculated by using so-called window functions (in our case Gaussian window, $k_{win} = 1$ [9]), the seeding particles near the edge of the interrogation area are suppressed. In that case, the maximum recommended displacement is 17.7% of the interrogation area, which in our case means $5.6pixels$. Usually, the general recommendation is to use the 64×64 interrogation area instead of 32×32 when applying window functions.

The feeding of the seeding particles was done with an injection system identically operated during all experiments. The seeding density was adjusted in such a way that there were on average at least 5 particles per interrogation area for cross-correlation.

Eight sets of data were acquired with the following PIV settings:

$\Delta t = 10\mu s; 100\mu s; 1000\mu s; 2000\mu s; 2800\mu s; 4000\mu s; 5000\mu s$ and $10000\mu s$.

Table (D.1) presents the average particle displacement in pixels calculated with the chosen times between laser pulses and a maximum vertical velocity component of $0.2m/s$ ($V_{mean} + 0.1 \cdot V_{mean}$).

Case	1	2	3	4	5	6	7	8
$\Delta t[\mu s]$	10	100	1000	2000	2800	4000	5000	10000
$\Delta x[pixel]$	0.014	0.14	1.42	2.8	4	5.71	7.14	14.3
Recommended: $\Delta x[pixel]$	5.6							

Table (D.1): The time between laser pulses and corresponding particle displacement.

Experimental Results

Profiles of the mean liquid velocity profiles and standard deviation of the vertical velocity as well as a scalar maps of a standard deviations of the vertical velocity component (i.e. *rms* values) are systematically presented in Figures (D.5), (D.6) and (D.7), respectively. The profiles are measured at $y = 19.2mm$ from the nozzle exit and the scalar maps show the full PIV window.

D.3 Effects of PIV parameters on time-dependent velocity profiles and rms values

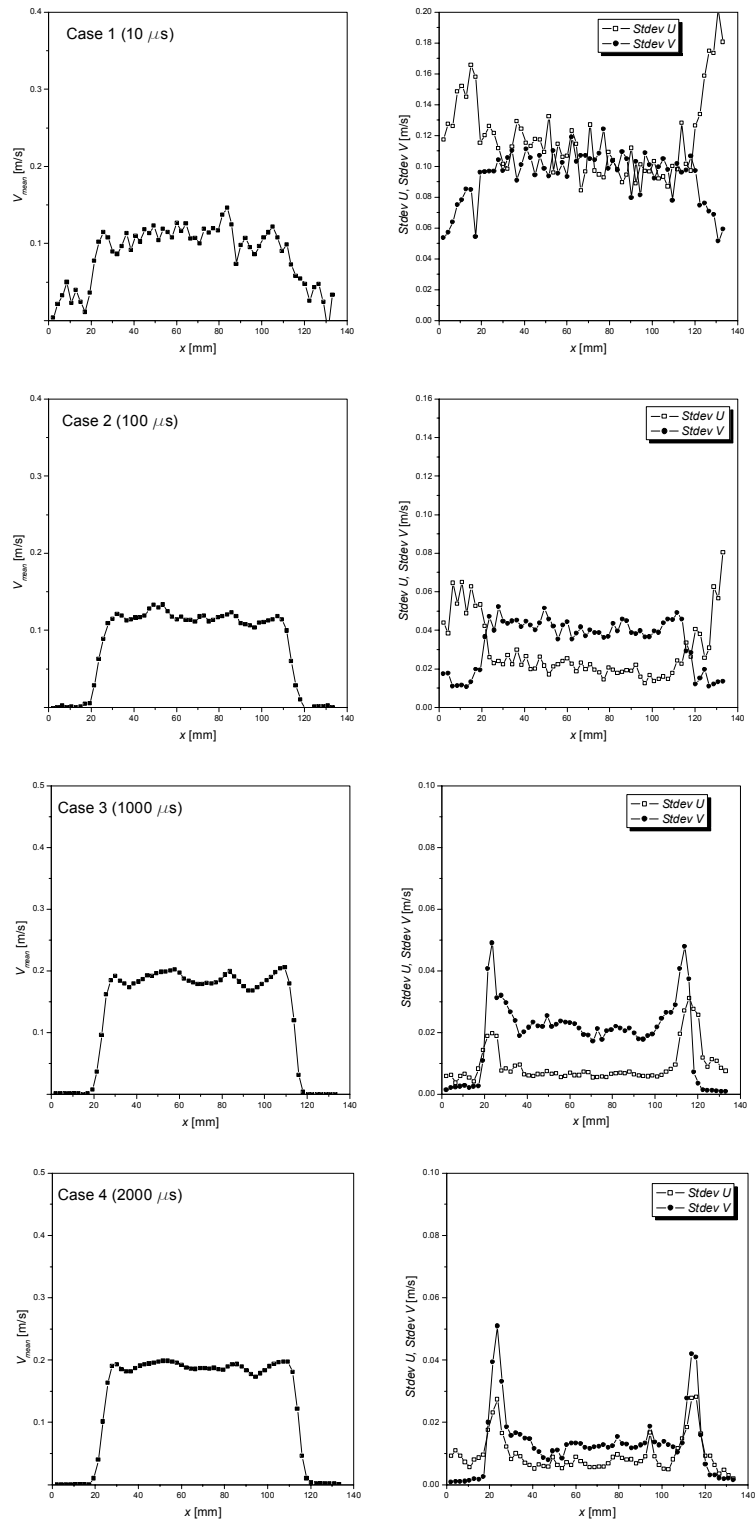


Figure (D.5): Horizontal profiles of vertical velocity of the liquid (left) and standard deviation of vertical liquid velocity (right) obtained with different settings for the time between two laser pulses.

Appendix D Particle Image Velocimetry (PIV)-Settings and error estimates

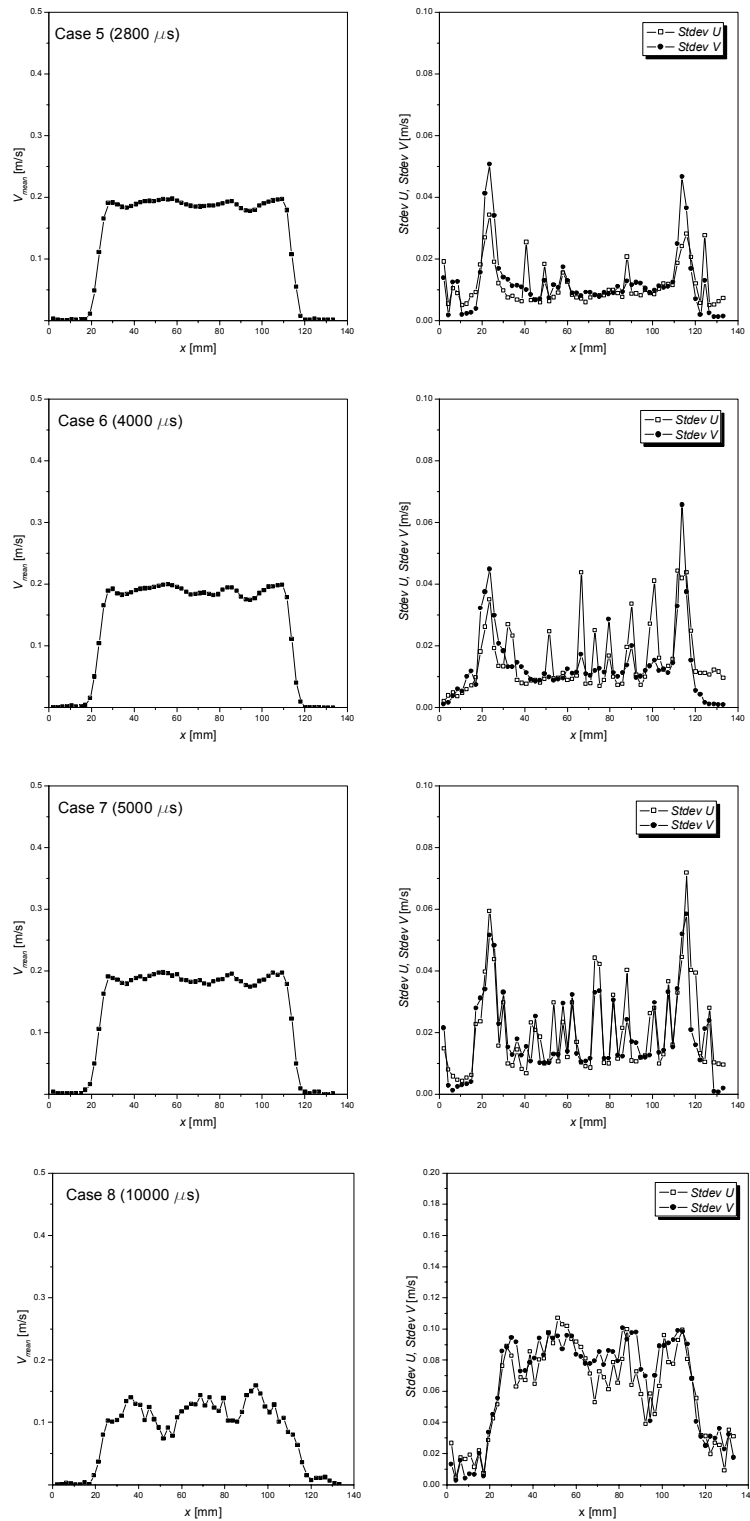


Figure (D.6): Horizontal profiles of vertical velocity of the liquid (left) and standard deviation of vertical liquid velocity (right) obtained with different settings for the time between two laser pulses.

D.3 Effects of PIV parameters on time-dependent velocity profiles and rms values

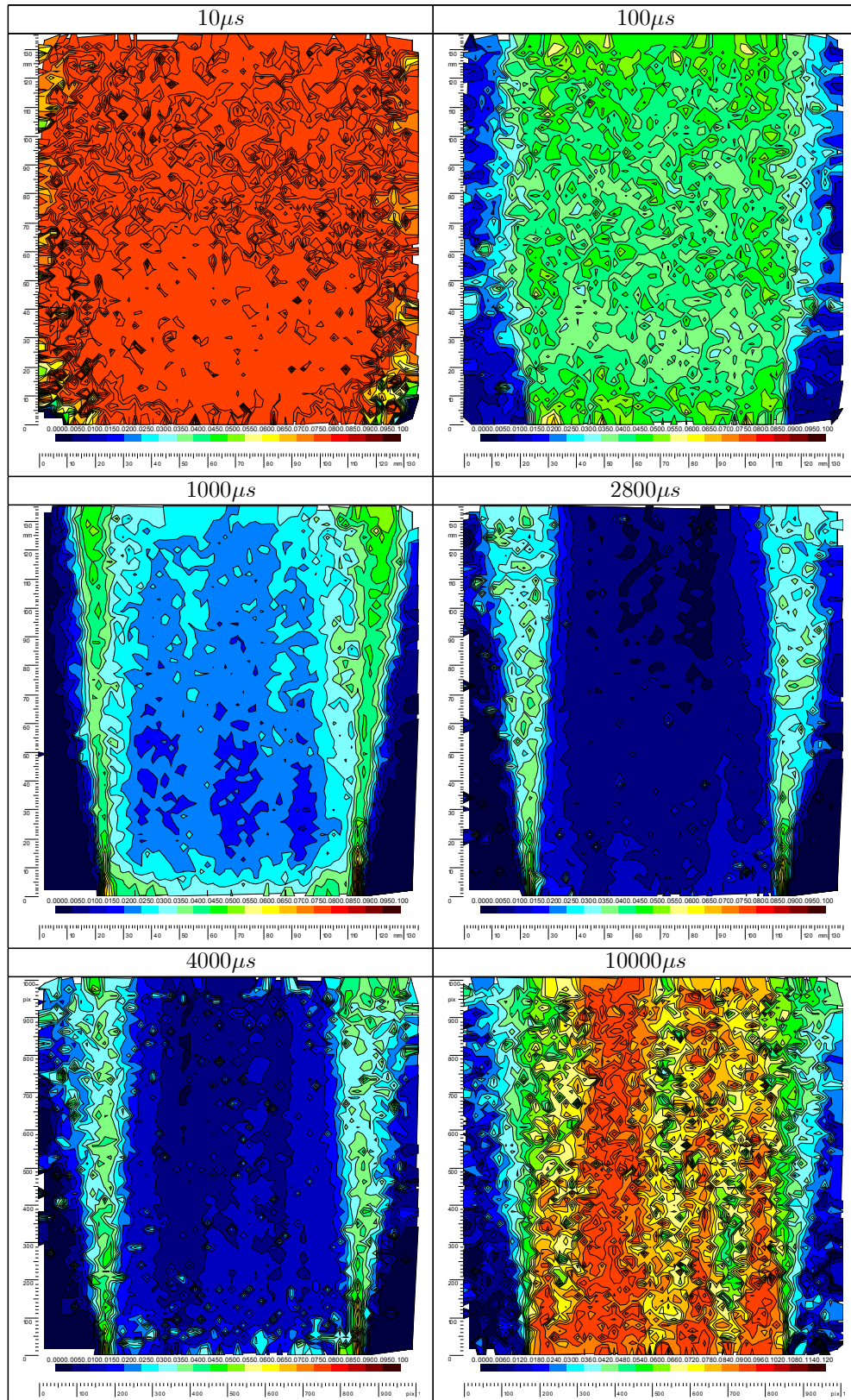


Figure (D.7): Scalar maps of rms values of the vertical velocity component for different times between laser pulses.

The results show that the optimum profiles of mean velocity and *rms* values are obtained for cases 4 and 5 with relative particle displacement of about 10% of the interrogation area. This optima are characterized by a minimum contribution of noise.

It is, however, not obvious that a result like that obtained for Case 3 is not correct. It just shows relatively high intensity for *StdevV* inside the jet compared to Cases 4 and 5. One must now take into account the resolution power of the PIV method, which is about 0.1pixel for optimum conditions [9], [48]. The corresponding noise for case 3 is

$$(StdevV^2)_{noise} = \left(\frac{\Delta x_{res}}{\Delta t} \right)^2 \approx \left(\frac{14\mu m}{1ms} \right)^2 \approx 2 \cdot 10^{-4} \frac{m^2}{s^2}$$

whereas $(StdevV^2)_{noise} = 1 \cdot 10^{-4} \frac{m^2}{s^2}$ in Cases 4 and 5. Summing up the energy $(StdevV^2)_{noise}$ for Case 3 and the value obtained from the PIV measurement for case 4 (see Figure D.5) should give an estimate for *StdevV* in Case 3 of $1.73 \cdot 10^{-2} \frac{m}{s}$. Since the noise should not depend on V_{mean} , this analysis shows that only the variation of the velocity in the IA is expected to play a role. The peaks in the central part of profiles in Case 7–8 are probably caused by measurements that are out of range.

The reason why cases 6 and 7 provide less good profiles (rough profiles) is due to the very large time applied between laser shots, which is out of the recommended range.

Comments:

In cases of extremely small or extremely large relative particle displacement within IAs, the mean velocity components are not correctly predicted and velocity *rms* values reach non-realistic values. In general, properly chosen times between laser pulses and seeding concentration will result in good estimates of space-averaged velocity profiles and *rms* values.

D.3.2 Application of the window function

A window function is the weighting or filtering function that is applied in order to suppress particles at the boundaries of the interrogation area, that lead to phantom particles and correlations after applying FFT [9]. The intensity of the recorded pixels is multiplied with a factor between 0 and 1 depending on the pixel position within the interrogation area. This means that particles in the center of the interrogation area will contribute more to the calculated velocity.

Two cases were chosen from the previous analysis in order to investigate the effect of the interrogation area size and application of the window function.

Results in Figures (D.8) and (D.9) show that in the case of short intervals between laser pulses ($1ms$), omission of the Gaussian filter has virtually no effect. But using the larger IA leads to slightly smaller *rms* values of horizontal and vertical velocity components.

In experiments with large intervals between laser pulses ($5ms$), and small IA, application of window filtering suppresses particles at the boundaries of IAs, which may affect the signal-to-noise ratio. Results also show that the Gaussian window function does not help. On the other side, the use of this window function in case of large IA only yields good results for the standard deviations.

From these results one must conclude that it is more difficult to find the optimum value for the case of small IA, and the application of a larger IA is recommended if the resulting loss of spatial resolution and the additional filtering of the fluctuating quantities can be accepted. For the analysis of PIV data during our experimental research, the interrogation area of $64 \times 64\text{pixels}$ and the Gaussian window function were used.

D.3 Effects of PIV parameters on time-dependent velocity profiles and rms values

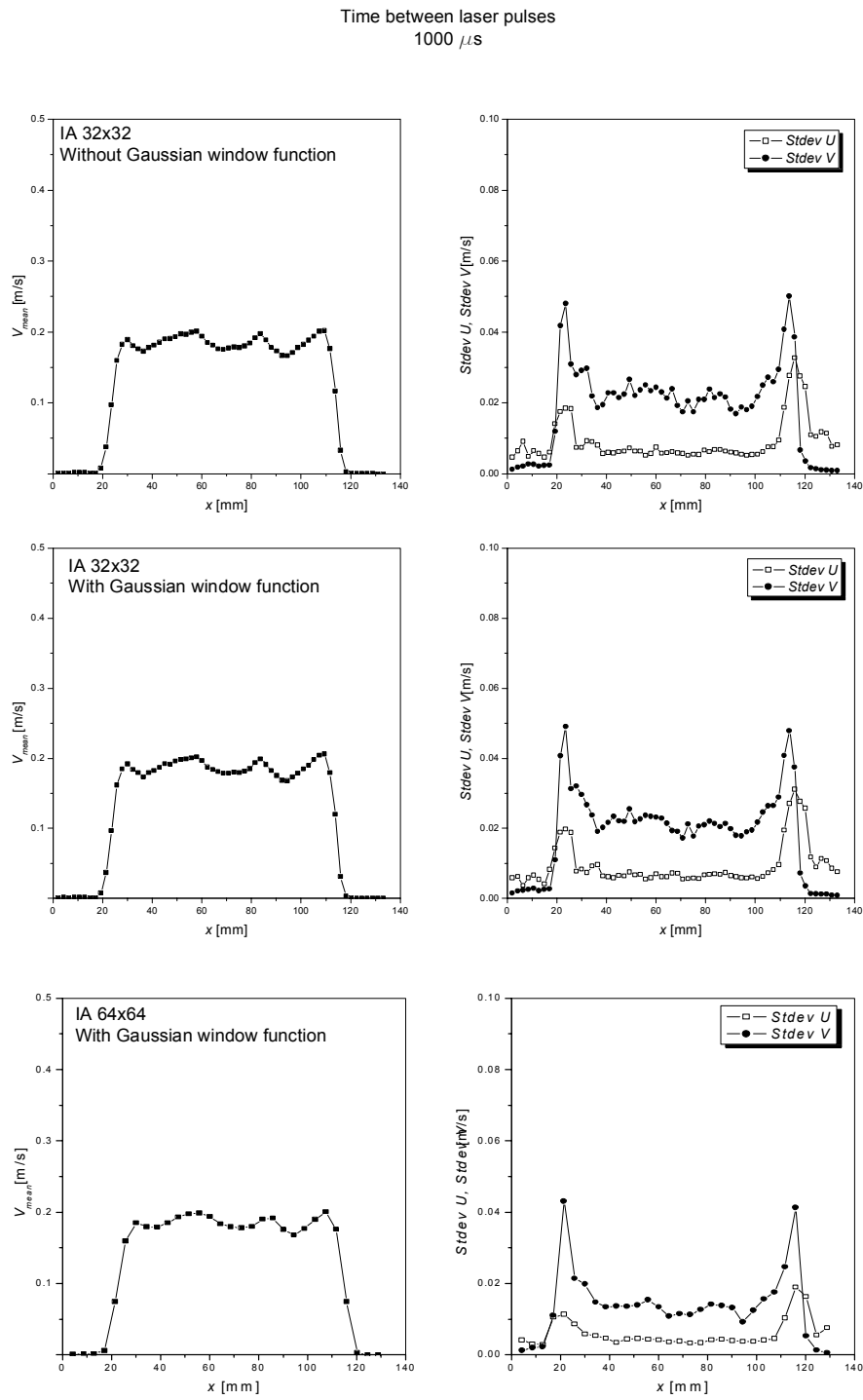


Figure (D.8): Testing the effect of Gaussian window function.

Appendix D Particle Image Velocimetry (PIV)-Settings and error estimates

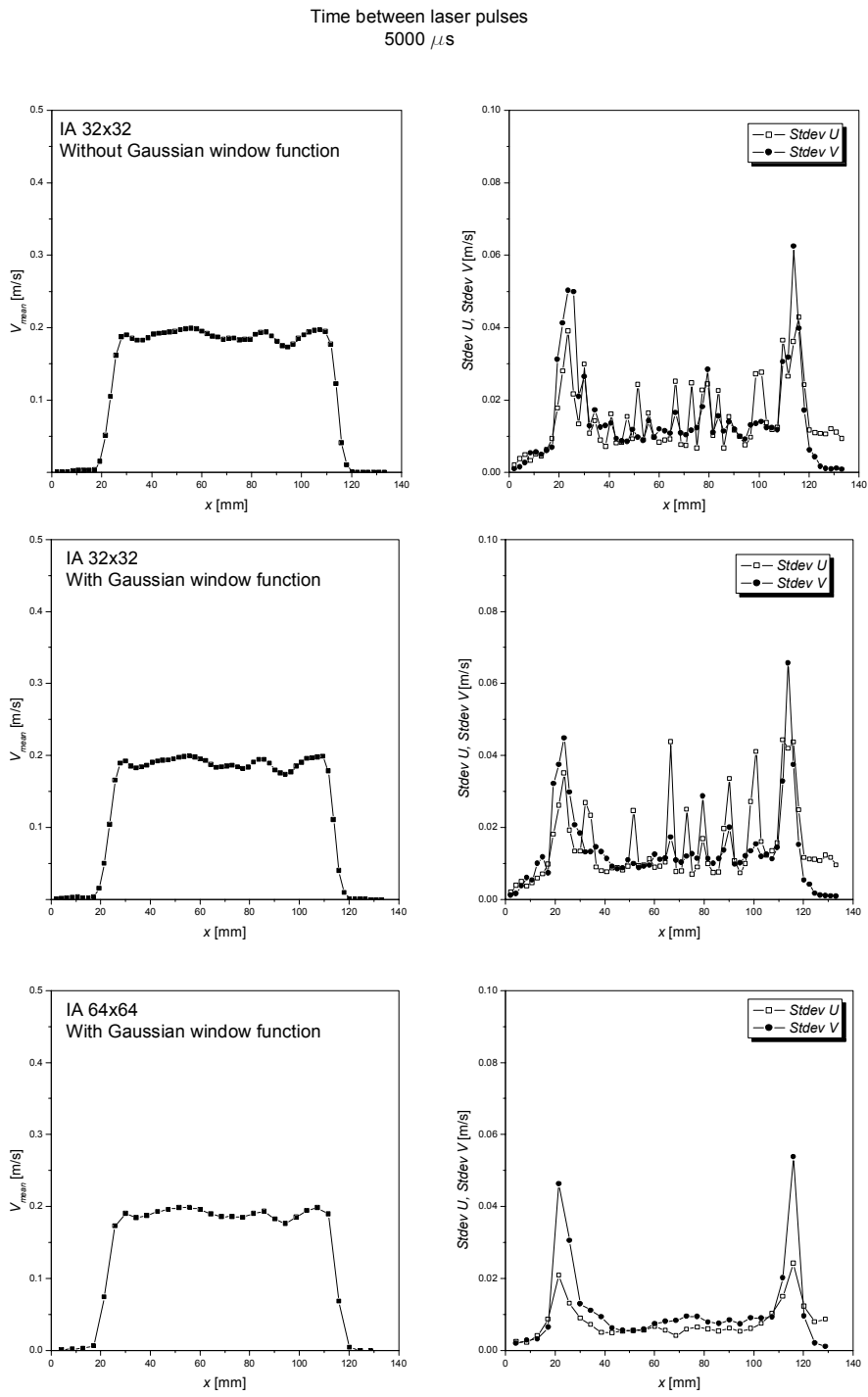


Figure (D.9): Testing the effect of Gaussian window function.

D.3.3 Testing of reproducibility

In order to test reproducibility of the PIV measurements, the following test (denoted here as Experiment D) was repeated four times at $y = 305\text{mm}$ from the nozzle exit for flow case *TF1V1* (for more details see Chapter 6), i.e. for a naturally-developing jet with $Re_{jet} = 17761$ and void fraction $\varepsilon_2 = 1.9\%$. Results are presented in Figure (D.10).

The PIV setting for Experiment D were:

- Interrogation area 32×32 ;
- Total number of acquired images $N_{ai} = 1024$;
- Sampling frequency 15Hz ;
- Time between two laser pulses $600\mu\text{s}$.

Satisfactory agreement was found for mean vertical velocities of the bubbles and for standard deviations of the vertical bubble velocity, although the differences between the results of mean velocities of the liquid and the standard deviations of the vertical liquid velocity were distinctly larger. The reason for different results of experiments D1-D4 is related to the total measurement time. If very slow movements of the bubbly jet with characteristic times scales of the order of the total measurement time of 68s exist, they can cause the profiles of average velocities to become biased. The slow movements can be the result of instabilities of the flow pattern prevailing in the water tank.

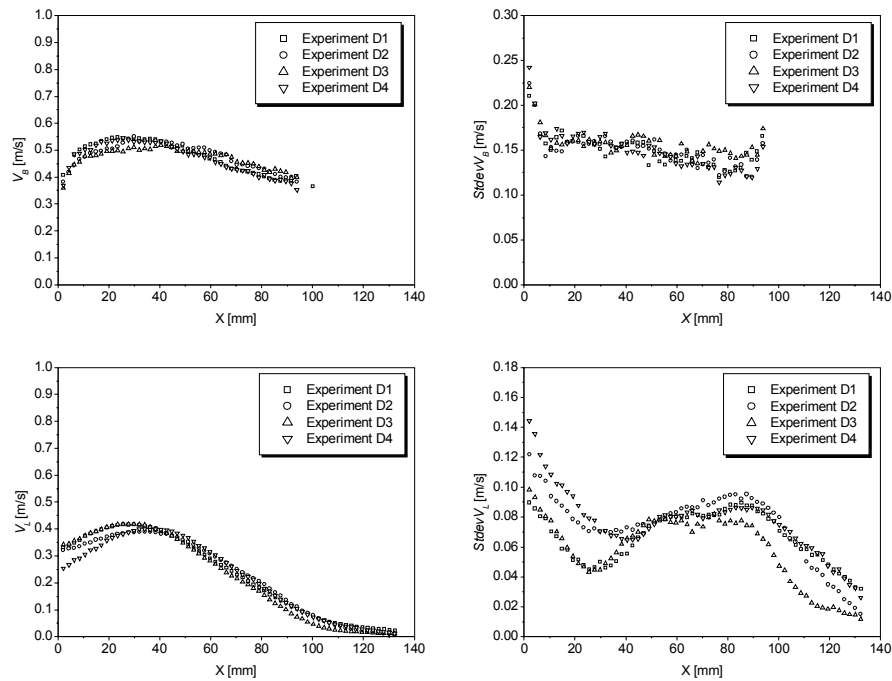


Figure (D.10): Testing of reproducibility of PIV measurement (top-bubbles, bottom-liquid phase).

Bibliography

- [1] AUTON, T. R., HUNT, J. C. R., AND PRUD'HOMME, M. The force exerted on a body in inviscid unsteady non-uniform rotational flow. *J. Fluid Mech.*, Vol. 197 (1988), pp. 241–257.
- [2] CARTELLIER, A., AND ACHARD, J. Local phase detection probes in fluid/fluid two-phase flows. *Rev. Sci. Instruments*, Vol. 62(2) (1991), pp. 279–302.
- [3] CHAHED, J., ROIG, V., AND MASBERNAT, L. Eulerian- Eulerian two-fluid model for turbulent gas-liquid bubbly flows. *Int. J. of Multiphase Flow*, Vol. 29 (2003), pp. 23–49.
- [4] CHEN, C. J., AND RODI, W. *Vertical Turbulent Buoyant Jets - A Review of Experimental Data*. Pergamon Press, 1980.
- [5] CLIFT, R., GRACE, J., AND WEBER, M. *Bubbles, Drops and Particles*. Academic Press, 1978.
- [6] CROW, S. C., AND CHAMPAGNE, F. H. Orderly structure in jet turbulence. *J. Fluid Mech.*, Vol. 48 (1971), pp. 547–591.
- [7] CROWE, C. T., GORE, R. A., AND TROUTT, T. R. Particle dispersion by coherent structures in free shear flows. *Part. Sci. Technol.*, Vol. 3 (1985), pp. 149.
- [8] CROWE, C. T., TROUTT, T. R., AND CHUNG, J. N. Numerical models for two-phase turbulent flows. *Ann. Rev. Fluid Mech.*, Vol. 28 (1996), pp. 11–43.
- [9] DANTEC. *Flow Manager Software and Introduction to PIV Instrumentation*. Dantec Dynamics, 2000.
- [10] DECKWER, W. *Bubbly Column Reactors*. John Wiley and Sons, 1992.
- [11] DELNOIJ, E., KUIPERS, J. A. M., AND VAN SWAAIJ, W. P. M. Dynamic simulation of dispersed gas-liquid two-phase flow: effect of column aspect ratio on the flow structure. *Chem. Eng. Sci.*, Vol. 52, No. 21/22 (1997), pp. 3759–3772.
- [12] DELNOIJ, E., LAMMERS, F., KUIPERS, J., AND VAN SWAAIJ, W. Dynamic simulation of dispersed gas-liquid two-phase flow using a discrete bubble model. *Chemical Engineering Science*, Vol. 52, No. 9 (1997), pp. 1429–1458.
- [13] DREW, D. A., AND PASSMAN, S. L. *Theory of Multicomponent Fluids*. Springer, 1991.
- [14] DUDUKOVIC, M. P., LARACHI, F., AND MILLS, L. P. Multiphase reactors-revisited. *Chemical Engineering Science*, Vol. 54 (1999), pp. 1975–1995.
- [15] EAMES, I., AND MAGNAUDET, J. The motion of high-Reynolds-number bubbles in inhomogeneous flows. *Ann. Rev. Fluid Mech.*, Vol. 32 (2000), pp. 659.
- [16] GEBHART, B. *Buoyancy-Induced Flows and Transport*. Hemisphere Publishing Corporation, 1988.
- [17] GORE, R. A., AND CROWE, C. T. Effect of particle size on modulating turbulence intensity. *Int. J. of Multiphase Flow*, Vol. 222 (1989), pp. 279–285.
- [18] GORE, R. A., AND CROWE, C. T. Modulation of turbulence by a dispersed phase. *Trans. ASME J. Fluids Eng.*, Vol. 113 (1991), pp. 304–307.
- [19] HUERRE, P., AND MONKEWITZ, P. A. Absolute and convective instabilities in free shear layers. *J. Fluid Mech.*, Vol. 159 (1985), pp. 151–168.
- [20] HUSSAIN, A. K. M. F. Coherent structures, reality and myth. *Phys. Fluids*, 26

- (1983), pp. 2816–2850.
- [21] HUSSAIN, A. K. M. F., AND ZAMAN, K. B. M. Q. Vortex pairing in a circular jet under controlled excitation, Part 2, Coherent Structure Dynamics. *J. Fluid Mech.*, Vol. 110 (1980), pp. 493–544.
- [22] HUSSAIN, A. K. M. F., AND ZAMAN, K. B. M. Q. The preferred mode of the axisymmetric jet. *J. Fluid Mech.*, Vol. 110 (1981), pp. 39–71.
- [23] IGUCHI, M., OKITA, K., NAKATANI, T., AND KASAI, V. Structure of turbulent round bubbling jet generated by premixed gas and liquid injection. *Int. J. of Multiphase Flow*, Vol. 23 (1997), pp. 249–262.
- [24] IGUCHI, M., UEDA, H., AND UEMURA, T. Bubble and liquid flow characteristics in a vertical bubbling jet. *Int. J. of Multiphase Flow*, Vol. 21 (1995), pp. 861–873.
- [25] JOSHI, J. B. Computational flow modelling and design of bubble column reactors. *Chemical Engineering Science*, Vol. 56 (2001), pp. 5893–5933.
- [26] JOSHI, J. B., VITANKAR, V. S., KULKARNI, A. A., DHOTRE, M. T., AND EKAMBRA, K. Coherent flow structure in bubble column reactors. *Chemical Engineering Science*, Vol. 57 (2002), pp. 3157–3183.
- [27] KITAGAWA, A., MURAI, Y., AND YAMAMOTO, F. Two-way coupling of Eulerian-Lagrangian model for dispersed multiphase flows using filtering functions. *Int. J. of Multiphase Flow*, Vol. 27 (2001), pp. 2129–2153.
- [28] KUBASCH, J. *Bubble hydrodynamics in large pools*. ETH-Zuerich, Doctoral Dissertation ETH Nr. 14398, 2001.
- [29] KUMAR, S., NIKITOPOULOS, D., AND MICHAELIDES, E. Effect of bubbles on the turbulence near the exit of a liquid jet. *Experiments in Fluids*, Vol. 7 (1989), pp. 487–494.
- [30] LAIN, S., BRÖDER, D., AND SOMMERFELD, M. Experimental and numerical studies of the hydrodynamics in a bubble column. *Chem. Eng. Sci.*, Vol. 54, No. 21 (1999), pp. 4913–4920.
- [31] LAÍN, S., BRÖDER, D., SOMMERFELD, M., AND GÖZ, M. F. Modelling hydrodynamics and turbulence in a bubble column using the Euler Lagrange procedure. *Int. J. of Multiphase Flow*, Vol. 28, No.8 (2002), pp. 1381–1407.
- [32] LANCE, M., AND BATAILLE, J. Turbulence in the liquid phase of a uniform bubbly air-water Flow. *J. Fluid Mech.*, Vol. 222 (1991), pp. 95–118.
- [33] LANCE, M., AND ET AL. Experimental study of turbulent bubbly shear flows. *Chem. Eng. Comm.*, Vol. 141-142 (1996), pp. 51–70.
- [34] LE CORRE, J., AND ISHII, M. Numerical evaluation and correction method for multi-sensor probe measurement techniques in two-phase bubbly flow. *Nuclear Engineering and Design*, Vol. 216 (2002), pp. 221–238.
- [35] LEGENDRE, D., AND MAGNAUDET, J. The lift force on a spherical bubble in a viscous linear shear flow. *J. Fluid Mech.*, Vol. 368 (1998), pp. 81–126.
- [36] LOPEZ DE BERTODANO, M., LAHEY JR, R., AND JONES, O. Development of a $k-\epsilon$ Model for Bubbly, Two-Phase Flow. *Trans. ASME*, Vol. 116 (1994), pp. 128–134.
- [37] LOTH, E., AND CEBRZYNSKI, M. S. Modulation of shear layer thickness due to

- large bubbles. *Int. J. of Multiphase Flow*, Vol. 21(5) (1995), pp. 919–927.
- [38] MARTINEZ-BAZAN, C., AND LASHERAS, J. Turbulent dispersion of bubbles in a plane, free shear layer. *Experimental Thermal and Fluid Science*, Vol. 25 (2001), pp. 437–445.
- [39] MASTORAKOS, E., SHIBASAKI, M., AND HISHIDA, K. Mixing enhancement in axisymmetric turbulent isothermal and buoyant jets. *Experiments in Fluids*, Vol. 20 (1996), pp. 279–290.
- [40] MAXEY, M. R., AND RILEY, J. J. Equation of motion for a small rigid sphere in a non-uniform flow. *Phys. Fluids*, Vol. 26 (1983), pp. 883–889.
- [41] MAXWORTHY, T., GNANN, C., KÜRSTEN, M., AND DURST, F. Experiments on the rise of air bubbles in clean viscous fluids. *J. Fluid Mech.*, Vol. 321 (1996), pp. 421–441.
- [42] MILENKOVIC, R., AND FEHLMANN, M. *Gas/liquid injector, Mass and/or heat transfer apparatus and method for mass and/or heat enhancement*. EP-Patent Application No. 2003P19217EP (F-5125). Paul Scherrer Institut (PSI) and ETH Zürich, 2004.
- [43] MILLELI, M. *A numerical analysis of confined turbulent bubble plumes*. ETH-Zuerich, Doctoral Dissertation ETH Nr. 14799, 2002.
- [44] NADAOKA, K., NIHEI, Y., AND YAGI, H. Grid-averaged Lagrangian LES model for multiphase turbulent flow. *Int. J. of Multiphase Flow*, Vol. 25, No. 8 (1999), pp. 1619–1643.
- [45] PAN, Y., DUDUKOVIC, M. P. R., AND CHANG, M. Dynamic simulation of bubbly flow in bubble columns. *Chemical Engineering Science*, Vol. 54 (1999), pp. 2481–2489.
- [46] PAPANICOLAOU, P. N., AND LIST, E. J. Investigations of round vertical turbulent buoyant jets. *J. Fluid Mech.*, Vol. 195 (1988), pp. 341–391.
- [47] PFLEGER, D., GOMES, S., GILBERT, N., AND WAGNER, H. G. Hydrodynamic simulations of laboratory scale bubble columns fundamental studies of the Eulerian-Eulerian modelling approach. *Chemical Engineering Science*, Vol. 54 (1999), pp. 5091–5099.
- [48] RAFFEL, M., WILLERT, C., AND KOMPENHANS, J. *Particle Image Velocimetry-A Practical Guide*. Springer, 1998.
- [49] RIGHTLY, P. M., AND LASHERAS, J. C. Bubble dispersion and interphase coupling in a free shear layer. *J. Fluid Mech.*, Vol. 412 (2000), pp. 21–59.
- [50] RODI, W. *Turbulent Buoyant Jets and Plumes*. Pergamon Press, 1982.
- [51] RODI, W. *Turbulence Models and Their Application in Hydraulics- A State of the Art Review*. International Association for Hydrolic Research, 1984.
- [52] ROIG, V., SUSANNE, C., AND MASBERNAT, L. Experimental investigation of a turbulent bubbly mixing layer. *Int. J. of Multiphase Flow*, Vol. 24 (1998), pp. 35–54.
- [53] SENE, K., HUNT, J., AND THOMAS, N. The role of coherent structures in bubble transport by turbulent shear flows. *J. Fluid Mech.*, Vol. 259 (1994), pp. 219–240.
- [54] SOCOLOFSKY, S., CROUNSE, B., AND ADAMS, E. Multi-phase plumes in uniform, stratified, and flowing environments. *Environmental Fluid Mechanics-Theories and Applications*, Ch. 3 in , H. Shen, A. Cheng, K.-H. Wang, and M.H.

- Teng eds., ASCE/Fluids Committee* (2001), pp. 241–257.
- [55] SOKOLOCHIN, A., AND EIGENBERGER, G. Applicability of the standard $k-\varepsilon$ turbulence model to the dynamic simulation of bubble columns: Part I. Detailed numerical simulations. *Chemical Engineering Science*, Vol. 54 (1999), pp. 2273–2284.
- [56] SPURK, J. H. *Stroemungslehre*. Springer, 1987.
- [57] STANLEY, K. N., AND NIKITPOULOS, D. E. Bubble measurements in a gas-liquid jet. *Chem. Eng. Comm.*, Vol. 143 (1996), pp. 1–22.
- [58] STEWART, C. W., AND CROWE, C. T. Bubble dispersion in free shear flows. *Int. J. of Multiphase Flow*, Vol. 19(3) (1993), pp. 501–507.
- [59] SUN, T., AND FAETH, G. Structure of turbulent bubbly jets-methods and centerline properties. *Int. J. of Multiphase Flow*, Vol. 12 (1986), pp. 99–114.
- [60] SUN, T., AND FAETH, G. Structure of turbulent bubbly jets-phase property profiles. *Int. J. of Multiphase Flow*, Vol. 12 (1986), pp. 115–126.
- [61] TOMIYAMA, A., TAMAI, H. C., ZUN, I., AND HOSOKAWA, S. Transverse migration of single bubbles in simple shear flows. *Chemical Engineering Science*, Vol. 57 (2002), pp. 1849–1858.
- [62] TROSHKO, A. A., AND HASSAN, Y. A. A two-equation model of turbulent bubbly flows. *Int. J. of Multiphase Flow*, Vol. 27 (2001), pp. 1965–2000.
- [63] TSI. *PIV Manual*. TSI, 2000.
- [64] ULLUM, U., SCHMIDT, J. J., LARSEN, P., AND MCCLUSKEY, D. Statistical analysis and accuracy of PIV data. *Journal of Visualization*, Vol. 1, No. 2 (1988), pp. 205–216.
- [65] YADIGAROGU, G., ANDREANI, M., DREIER, J., AND CODDINGTON, P. Trends and needs in experimental and numerical simulation for LWR safety. *Nuclear Engineering and Design*, Vol. 221 (2003), pp. 205–223.
- [66] ZAMAN, K. B. M. Q., AND HUSSAIN, A. K. M. F. Vortex pairing in a circular jet under controlled excitation, Part 1, General Jet Response. *J. Fluid Mech.*, Vol. 101 (1980), pp. 449–491.

Curriculum Vitae

Name: Rade Ž. Milenković

Nationality: Serbian

Date/place of birth: 24.06.1970, Belgrade, Serbia.

Education:

1977-1985 Primary School, Serbia.

1985-1989 Secondary School, Experimental Physics, Serbia.

1989-1994 Engineering studies at University of Belgrade, Faculty of Mechanical Engineering, Department of Process Engineering.

1994-1996 Post graduate studies at University of Belgrade, Faculty of Mechanical Engineering, Department of Process Engineering, Group for Heat and Mass Operations and Apparatuses.

1999 Master of Science Thesis defended at University of Belgrade, Faculty of Mechanical Engineering, Department of Process Engineering.

2001-2005 Doctoral studies at ETH Zürich (Nuclear Engineering Laboratory, LKT) while employed at Paul Scherrer Institut (Thermalhydraulics Laboratory, LTH), Villigen, Switzerland.